AN EXPLORATION OF INTER-STELLAR GAS AND ITS ROLE IN GALAXY ASSEMBLY OVER COSMIC TIME

A Dissertation

Presented to the Faculty of the Graduate School

of Cornell University

in Partial Fulfillment of the Requirements for the Degree of

Doctor of Philosophy

by

Riccardo Pavesi

May 2019

AN EXPLORATION OF INTER-STELLAR GAS AND ITS ROLE IN GALAXY ASSEMBLY OVER COSMIC TIME

Riccardo Pavesi, Ph.D.

Cornell University 2019

The key physical processes driving galaxy formation and evolution are controlled by gas and, in particular, the process of star formation from cold, dense gas is not well understood since it depends upon the gas cooling ability, its dynamical state and complex feedback processes. Galaxies were observed to form stars much more rapidly in the past ($\sim$ 10 – 11 billion years ago), which may be due to larger gas reservoirs or more efficient star formation processes. While previous studies have identified large molecular gas reservoirs in a few pre-selected star-forming galaxies, an unbiased survey for molecular gas is necessary to provide robust statistical constraints to the gas content of galaxies at the peak epoch of cosmic star formation. Taking advantage of the improved frequency coverage, sensitivity and bandwidth of the upgraded Very Large Array we have carried out the first unbiased survey by performing a deep-field blind search for CO(1–0) line emission at $z \sim 2 - 3$ and CO(2–1) line emission at $z \sim 5 - 7$, targeting CO(1–0) which is the most commonly used tracer of the cold, dense molecular gas which fuels star formation. Having detected the first CO(1–0)-selected galaxies at high redshift, we have used their luminosity and abundance to provide robust statistical constraints to the CO luminosity function at $z \sim 2$–3, finding conclusive evidence for a much higher gas mass content relative to galaxies in the local Universe. This finding suggested that evolution in the mechanisms of star formation may not be the dominant contribution to the high

observed star formation rates, but rather large amounts of available cold gas. In order to explore how this finding may apply to even higher redshift, we have also achieved the first detection of CO emission in "normal" galaxies at $z > 5$ (in the first billion years of cosmic time) together with far-infrared fine structure line tracers of the atomic and ionized gas using the sensitive Atacama Large (sub-)Millimeter Array. We found that early galaxies appear to be extremely gas rich, relative to their stellar content, and to display comparable star formation efficiency to typical lower redshift "normal" galaxies. However, the interstellar medium in a fraction of such galaxies also appears to be strongly affected by lower metallicity, affecting the phase structure of the interstellar medium, and the usefulness of CO as a tracer of molecular gas.

BIOGRAPHICAL SKETCH

Riccardo Pavesi grew up in Parma, Italy, graduating from the Liceo Scientifico G. Marconi in 2008 while spending a good amount of time in the countryside near Mulazzano and the Appennini mountains. He received his Bachelor of Arts (BA) and Master of Mathematics (MMath) from the University of Cambridge, UK in 2012, studying Theoretical Physics. After joining Cornell University as a Physics graduate student, he joined the Theoretical High Energy Physics group led by Prof. Csaba Csaki and worked on beyond-the-Standard-Model phenomenology model-building for a year and a half, leading to the publication of his first paper (arXiv:1310.4504; Csáki et al. 2014). Inspired by the possibility to further our understanding of Dark Matter through Astrophysics, he subsequently joined the Galaxy Evolution group led by Prof. Dominik Riechers in the Astronomy Department where he carried out the research contained in this thesis.

This work is dedicated to Lydia. It would not have been possible without her constant support.

ACKNOWLEDGEMENTS

Many people have contributed to the success of my graduate research, and I am extremely grateful to all of them for their help and their support along the way. Without their encouragement and collaboration this thesis research would not have been possible, and my graduate experience would have been completely different. Although the following list is very incomplete, I would like to specifically acknowledge the contribution of each of the following to my thesis work.

- Lydia Thompson — The unwavering support and steady encouragement from my wife Lydia have been essential to the success of my research, as well as to most other accomplishments and happiness I have experienced
- My parents and my grandfather — My family has always been there to inspire me and to help me, successfully overcoming the distance that separates us. Their presence has been key to my success and my strength over the years, they have shaped me as a scientist as much as a person
- Melissa, Clay, Claire and Ross — Lydia's family has been an invaluable presence in the years of my Ph.D. and I want to thank them for always being there to believe in me, support me and being interested in my research
- Martha Haynes and Riccardo Giovanelli — Martha and Riccardo have been encouraging me in my endeavors and my astronomy career since I was in High School. They are one of the main reasons I came to Cornell and their words and counsel have been central to shaping the direction of my graduate school years
- Dominik Riechers — I thank my advisor Dominik for all his help and his teachings. I have learned a lot from Dominik over the years, he helped me get started in Astronomy after transferring from a different field and

taught me so much about "making" science, scientific writing, and public speaking. His cheerfulness in the face of difficulty have been inspiring to me.

- Chelsea Sharon — Chelsea has been an excellent mentor, and has been really important to my growth, especially during the early phase of my astronomy career. Her advice and her incredible willingness to make time to talk to me about any aspect of my work (from astronomy to the most minute details of the tools and methods), even during her busiest periods have been an inspiration for me.

- Gordon Stacey and his research group — I have learned so much interesting science from Gordon, he has been an endless source of expertise and of cheer. His enthusiasm (and sometimes his stress) are extremely contagious and have often set the mood on our corridor. Chuck and Thomas have been such a great, constant presence in the corridor and in my daily life, and I thank them both for our nice chats over the years and for their presence in my days.

- Andreas Faisst — My collaboration with Andreas has always been really instructive and enjoyable, both remotely and in person. I thank him for hosting me at Caltech, for the great time I had there, and for his invaluable help in establishing a network within the broader astronomical community. Andreas has believed in me, pushed my contribution to the attention of many astronomers and has been a real collaborator.

- Henrik Spoon, Shami Chatterjee, Jamie Lloyd, Greg Sloan — Henrik has always been there for me, ready to listen when I needed that, and to support me with encouraging words. Shami, Jamie and Greg have been the companions of many coffee hours and chats over lunch. I thank them all

for the insightful conversations about science, the friendly comradery and the politics.

- Tom Loredo — When I joined the astronomy department I did not enjoy probability and statistics very much. Tom is single-handedly responsible for making me passionate about these topics, and teaching me most of what I know about them. His enthusiasm for Bayesian thinking and his theoretical perspective on data work is extremely contagious and has inspired me greatly. I owe him how I was able to find enjoyment working with data both in this research and in my future career in Data Science.
- Amit Vishwas — Of all the people whose dear friendship I have treasured over these years, Amit is notable for many reasons: for how much astronomy he has taught me, for his constant belief in my ability to carry out this research and for willingness to sharing the hardest parts of graduate school with me. Amit's friendship has also been precious for his willingness to hang out, do fun stuff in and around Ithaca and for the awesome time when he hosted us in Portland!
- Avani Gowardhan — Since the day Avani asked me about joining our group at Cornell she has always been a wonderful friend and fellow group member. I have learned so much from talking to Avani and chatting in her office. Without her indomitable spirit and energy, going through the hardest parts of graduate school would not have been the same.
- Greg Douthit — Greg has been a wonderful friend and office mate in the last years of my Ph.D. He is undoubtedly one of the best physicists I have met during my time at Cornell, and I have really enjoyed all of our conversations and out time together over the years. I particularly appreciate his ability to simultaneously stoke my ego, and keep me humble and I look

forward to the day when he will appreciate himself as much as I appreciate him.

- Cody Lamarche, Paul Corlies, Matt Hankins and Sam Birch — I have valued their friendship over the years greatly, and have particularly enjoyed our lunch times together every day. Their sense of humor and kindness are inspiring to me. Their passion for science, steadiness and appreciation for what is really important has helped me stay calm through countless graduate school days.
- Carlos Gomez Guijarro and Daisy Leung — Carlos and Daisy have been good friends and fellow "high redshift fans". I have enjoyed our time together greatly, I treasure our conversations, and I have much appreciated their important contribution to my research and my development.
- Luke Leisman and Mike Jones — Luke and Mike have been excellent role model grad students for me and friends. I have greatly enjoyed going to the VLA summer school with Luke (and our unexpected road trip across Texas), our softball games, as well as the fun hiking with Mike. They have been great fellow grad students, an inspiration to contribute to the life of the department, and always extremely helpful in making me feel welcome in the astronomy department, and in the extra-galactic group.
- Everett Schlawin — Everett was such a great office mate and friend to me. He did not only help me start in astronomy (e.g., when all I was doing was read a lot of papers, and books), but he also inspired me to go backpacking and to enjoy Ithaca-life fully, and was always such an inspiration for me as a junior grad student with his passion and steadiness. He also contributed to my motivation and success in outreach through GRASSHOPPR and general desire to share the passion.

- Jeremy Hodis — I thank Jeremy for all our great time together, for our ability to commiserate about grad school and life, and helping each other feel that we were not alone.
- All the other astronomy graduate students and postdocs — There are too many to thank individually, but they have all been wonderful companions in this journey. Our social and academic events together have been so much fun, and you have all contributed to making my graduate school experience so excellent.
- Marco Farina and Mario Martone — Thanks for being excellent friends, for all the great advice, for listening to me in the time of need, and for hosting me at your places and meeting up all the time.
- Csaba Csaki — I thank Csaba for initiating me to scientific research, for spending lots of time teaching me exciting Physics, for creating a welcoming group environment and for communicating to me his faith in my abilities
- Flip Tanedo — Flip was my first role model at Cornell, a real mentor to junior grad students. He convinced me to come to Cornell, he warmly welcomed me to the group and he was responsible for creating the inclusive and wonderful environment we had in the theory group in those years. Flip also showed me the Ithaca farmers market for the first time, as soon as I arrived, which immediately became a lifelong passion of mine.
- All the countless collaborators on my papers (most of whom I have, sadly, never met) — Your advice has always been kind and instructive, I have appreciated your help and collaboration very much and I wish I could have had more meaningful interactions with you all.

- Rachel Bean and Michael Niemack — Finally, I want to thank Rachel and Mike for being wonderfully supportive special committee members, for reading this thesis and for their encouragement and contribution to my Ph.D. over the years.

We acknowledge support from the National Science Foundation under grant number AST-1614213 to Cornell University and through award SOSPA3-008 from the NRAO.

TABLE OF CONTENTS

LIST OF TABLES

LIST OF FIGURES

CHAPTER 1

INTRODUCTION

1.1 In the beginning all was Dark Matter and Gas...

In this thesis, we use observations of gas tracers in primordial galaxies to explore how star formation in those galaxies turned gas into stars and assembled the galaxies we observe in the Universe today. We carry out the most detailed statistical characterization of the abundance of cold, dense gas which fuels star formation at the peak epoch of galaxy assembly and we push the frontier of star formation studies to some of the first galaxies at the end of the Epoch of Reionization.

1.2 The cosmological role of galaxy evolution

The Universe we see around us is made up of galaxies. Galaxies appear to be the unit building blocks of all observable structures (e.g., galaxy groups, clusters, filaments and voids) and also represent the physical scale at which physical processes are not determined solely by gravity[1]. The study of galaxy evolution therefore represents the key step in the understanding of the Universe on the largest scales. The current cosmological model of ΛCDM (cold dark matter with a cosmological constant; e.g., Planck Collaboration et al. 2018) suggests that Dark Matter underlies all these structures, and represents the majority of the existing matter by mass. Since Dark Matter may not be observed directly,

[1]Galaxy clusters also display important non-gravitational physics, but we include their study in the study of galaxy evolution due to their strong links.

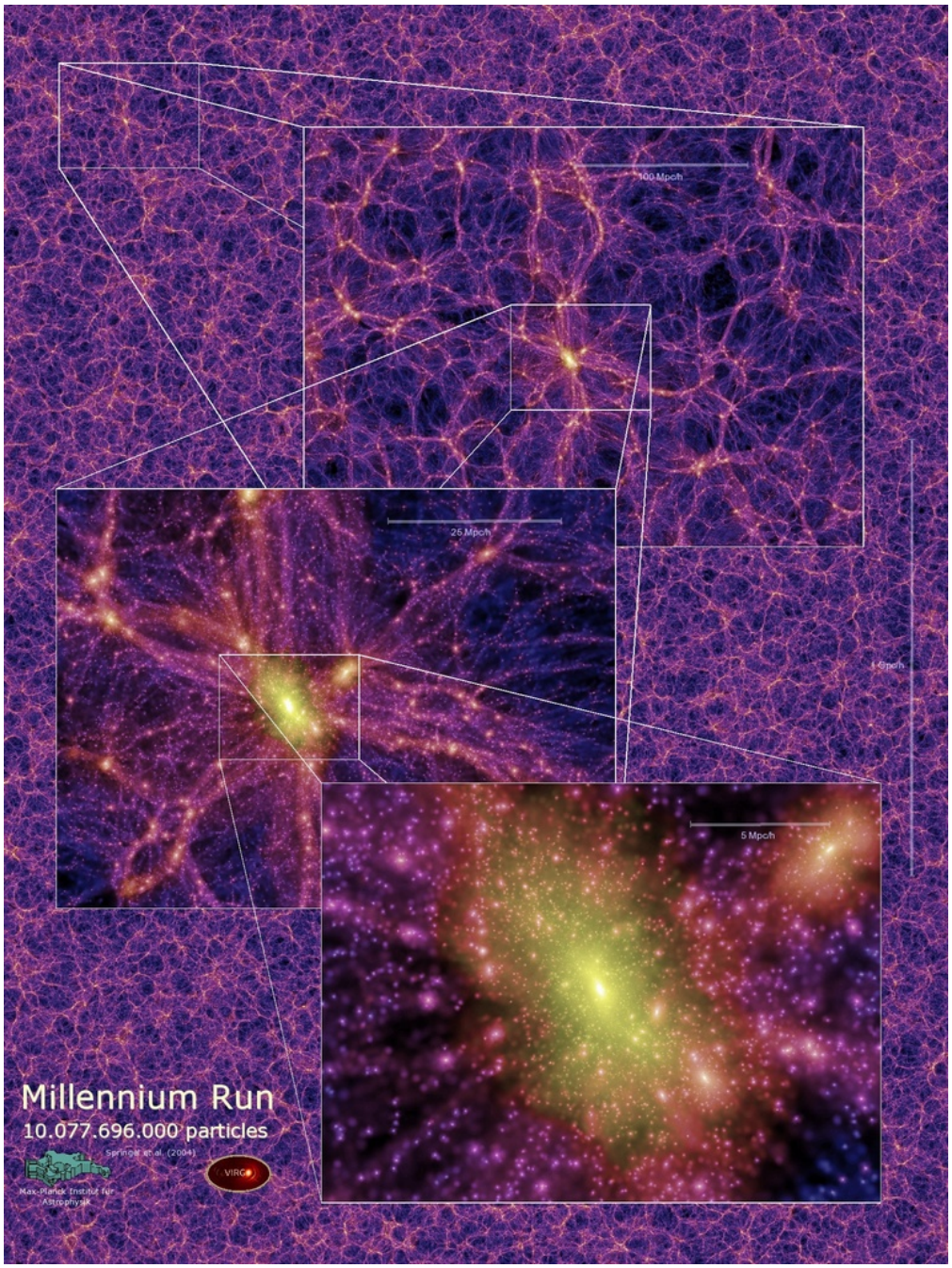

Figure 1.1: Millennium Simulation snapshot showing the filamentary structure of the dark matter distribution (color coded by density), which cannot be directly observed but dominates the Universe by mass. Dark matter provides the backbone of cosmological structure formation, but all we can see in the Universe is galaxies and the "dense" gas associated with them (with the exception of a few probes of the tenuous intergalactic medium; IGM). To study the underlying dark matter, and to explore the Universe on the largest scales we have to understand the processes of galaxy formation and evolution. Figure from the Millennium Simulation project (Springel et al., 2005).

currently most of the constraints to its properties derive from a detailed analysis and understanding of the observable, baryonic components of galaxies (Figure 1.1; e.g., Sofue & Rubin 2001). Crucially, in order to push the predictive power (and hence falsifiability) of the standard cosmological model beyond the linear perturbation regime (e.g., Hu & Dodelson 2002) we need to include models of the baryonic physics taking place in and around galaxies (e.g., Ferraro 2015). The two main, complementary approaches to gaining a deeper and more accurate understanding of these processes are the direct investigation of the smaller scale physical processes (within galaxies, down to the length-scale of individual stars or star clusters) which may be observed in the local Universe (Milky Way and neighboring galaxies) and the constraints to the formation and evolution of galaxy populations, which are observable as we peer into the furthest observable reaches of the Universe. In this thesis we follow the second approach, while utilizing the techniques and striving for addressing the questions which are commonly the prerogative of the former approach. In particular, we try to bridge the gap between statistical studies of galaxy evolution and internal structure by focusing on those probes which are most sensitive to the local physical processes driving the evolution, such as the conditions of the inter-stellar medium and their relationship to star formation.

1.3 Cosmic history, cosmic epochs and cosmic puzzles of galaxy assembly

One of the main successes of high redshift galaxy surveys has been the measurement of the cosmic star formation history (the average star formation rate per

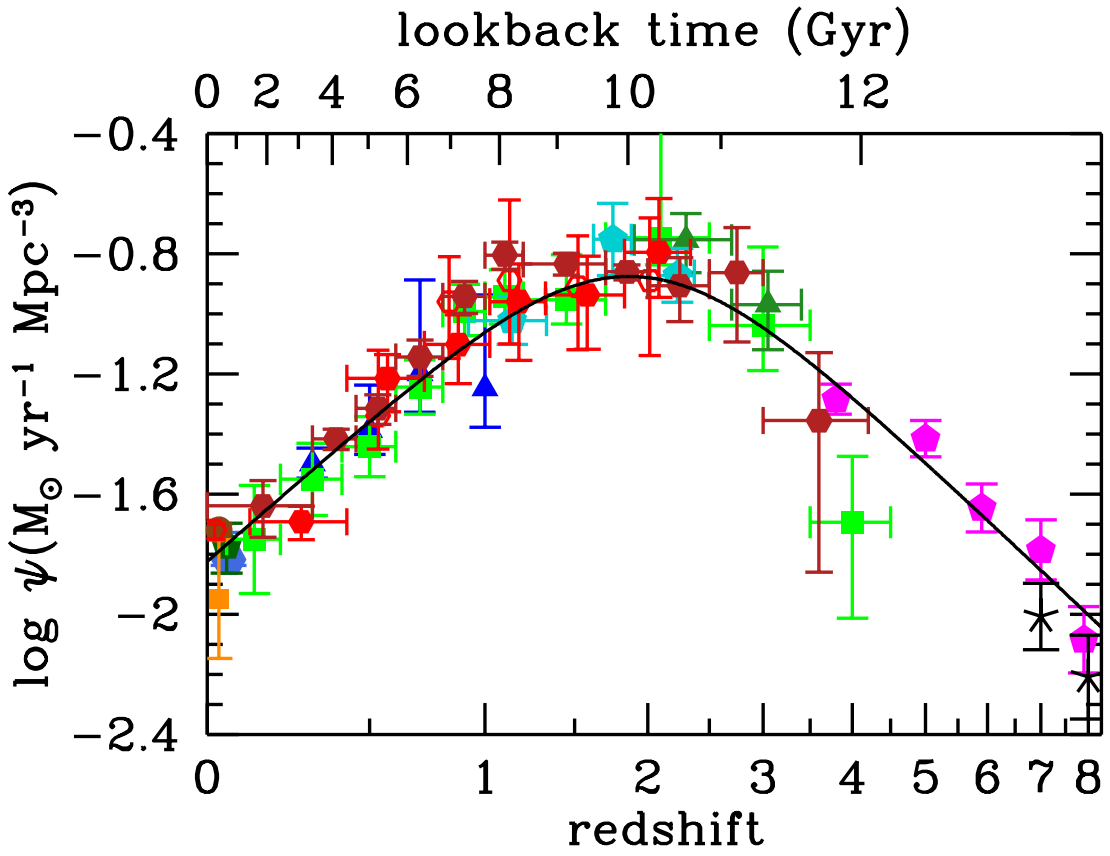

Figure 1.2: Observational constraints to the cosmic density (per comoving volume) of star formation rate taking place in galaxies as a function of redshift, illustrating the history of cosmic star formation. The observed Star Formation History of the Universe shows three main epochs of galaxy assembly: the Early Growth phase of rapid build-up, the "cosmic noon" peak epoch when massive galaxies formed most of their stellar mass, and the subsequent epoch of steady decrease, when galaxies started appearing the way they do now. Figure from the review by Madau & Dickinson (2014).

comoving volume as a function of redshift, Figure 1.2) based on measurements of ultra-violet (UV) and infrared (IR) galaxy luminosity functions at different redshifts (e.g., Madau & Dickinson 2014). While the emitted UV light from a stellar population is a good tracer of the recent star formation rate because it is only produced by hot O and B stars which have a short and approximately fixed lifetime (essentially counting how many stars were born in the last ~100 Myr; Kennicutt & Evans 2012) a large fraction of this UV light is absorbed by dust

in the inter-stellar medium and re-radiated in the far infrared (FIR) as thermal emission (e.g., Kennicutt & Evans 2012). Although the cosmic star formation history only captures the spatial average, and is agnostic to the contribution from galaxies of different sizes, it suggests the presence of three main cosmic epochs, during and following the end of reionization (at $z \sim 6-7$, 800–900 Myr after the Big Bang; e.g., Fan et al. 2006). There is evidence for a steady rise in the rate of galaxy assembly through star formation since at least $z \sim 10$ (e.g., Bouwens et al. 2015) up to $z \sim 3$ (~2 Gyr after the Big Bang; Madau & Dickinson 2014), which we refer to as the epoch of early galaxy growth. Then the star formation history peaked approximately between $z \sim 3$ and $z \sim 1$ (~2–6 Gyr after the Big Bang), reaching a very fast pace of star formation and assembling the majority of the stellar mass we see in galaxies today during the "cosmic noon" (Madau & Dickinson, 2014). Since then, the average star formation taking place in galaxies has been declining steadily, decreasing by a factor ~ 20 up to the present time (13.8 Gyr after the Big Bang; Planck Collaboration et al. 2018). Cosmological models of structure formation also predict that gas and dark matter accretion histories may be characterized by a peak at $z \sim 2$ (e.g., Dekel et al. 2013), and thus suggest that gas accretion may be the main driver of galaxy assembly. This general shape may be understood through the following simplified model: as dark matter halos grow more massive their stronger gravitational pull produces a faster gas inflow, while the late time decrease is likely due to the expansion of the Universe, which causes a drop in the density of the intergalactic gas supply. While the general trend may be understood based on these general physical principles, the quantitative details of the assembly history (in particular the rapid late time decrease) remain difficult to reproduce by current theoretical models (e.g., Somerville & Davé 2015; Furlong et al. 2015; Donnari et al.

2019). Gas accretion is indeed a complex process, as it involves shocks, a variety of cooling mechanisms, a density increase of several orders of magnitude, and phase transitions from ionized to atomic and then molecular, for the gas to become available for star formation. The difficulty in quantitatively reproducing this cosmic evolution suggests that the average star formation history may bear the imprint of the complex interplay of gas accretion, star formation and feedback, therefore representing an important observational constraint (e.g., Lilly et al. 2013).

1.4 The role of the inter-stellar medium in galaxy evolution

Although massive galaxies in the local Universe are dominated by their stars by mass, their evolution has predominantly been shaped by the gas component. The latest cosmological simulations of galaxy formation show (e.g., Popping et al. 2014b), in agreement with observations (e.g., Tacconi et al. (2010); Daddi et al. (2010a)), that massive galaxies used to be very gas rich, with dense gas reservoirs at least as massive as the stellar component at the peak epoch of cosmic star formation. These massive and highly turbulent gas reservoirs were the result of the balancing between inflowing gas, cooling from the halo in the form of cold streams and accretion from the intergalactic medium (IGM; Dekel et al. 2009b), rapid star formation locking gas into long lived stars and intense gas outflows powered by stellar and active galactic nuclei (AGN) feedback (e.g., Silk & Rees 1998; Springel & Hernquist 2003; Hopkins et al. 2012). These gas processes, therefore, control galaxy evolution (Figure 1.3). The physical and chemical conditions of the gas may also affect the efficiency or the mechanisms of star formation. For example, gas metallicity is thought to play an important

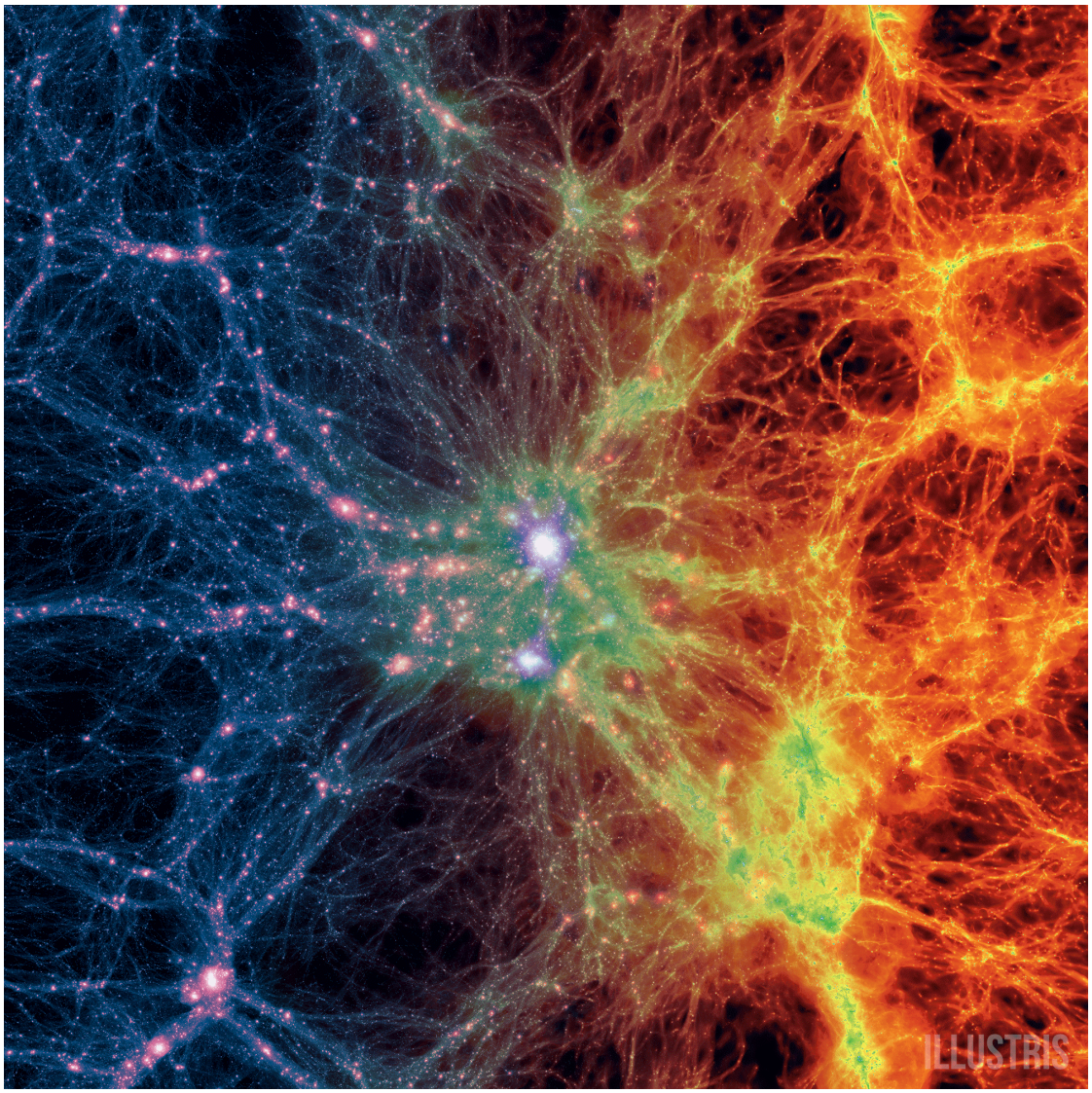

Figure 1.3: Large scale projection through the Illustris volume at $z = 0$, centered on the most massive cluster, 15 Mpc/h deep. Shows dark matter density (left) transitioning to gas density (right). Cosmological simulations show that galaxy formation results from the interplay of inflowing gas, rapid star formation and intense gas outflows powered by stellar and active galactic nuclei (AGN) feedback. These gas processes control galaxy evolution. Image credit to "Illustris Collaboration".

role in setting the gas cooling timescale and may therefore affect the efficiency with which gas can collapse, radiate its energy away and reach the high density necessary for star formation (e.g., Myers et al. 2011; Krumholz 2013). Clearly the gas density in the galaxy disk may also play an important role, although it is yet unclear whether there are thresholds for star formation and how they might relate to the ambient density (e.g., Krumholz & Thompson 2007; Krumholz et al. 2009; Krumholz 2012). Stellar feedback includes all those stellar life processes which inject energy or matter into the inter-stellar medium (ISM), such as winds, outflows and jets during protostar phases, winds and ionizing radiation from massive stars, and finally supernovae (e.g., Hopkins et al. 2012). AGN feedback represents all those processes by which an AGN injects energy into a galaxy such as jets, intense radiation driving powerful winds and strong ionizing radiation fields (e.g., Fabian 2012). These feedback processes [2] are invoked by galaxy evolution models to explain the varying efficiency of dark matter halos in assembling the stellar component of galaxies (Figure 1.4; e.g., Somerville & Davé 2015). Besides the large uncertainty regarding feedback and its role in controlling the gas supply and physical state, the main single uncertainty in galaxy evolution is due to our poor understanding of star formation (e.g., Silk & Mamon 2012). The subject of what controls star formation in galaxies, over cosmic time, will be central to this thesis.

[2] Or other factors such as strangulation from interrupted gas supply, potentially due to a virial shock in the most massive halos (e.g., Peng et al. 2015).

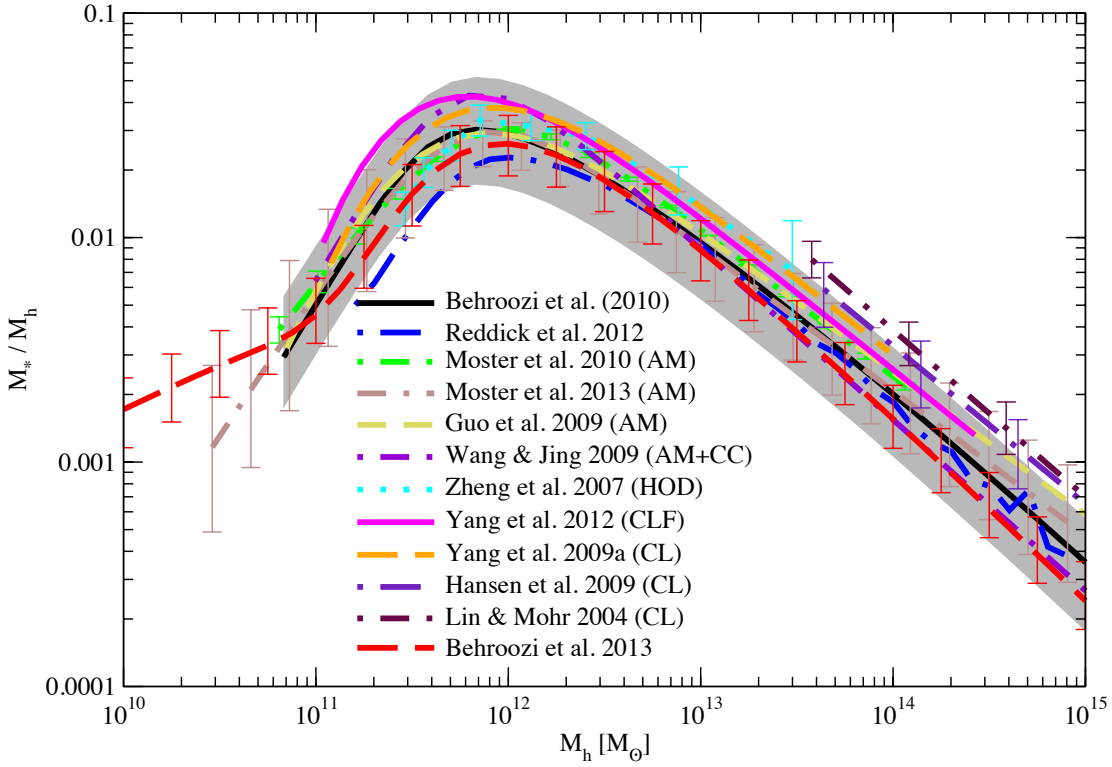

Figure 1.4: A crucial element in galaxy evolution is the link between dark matter halos and the galaxies they host. Here shown is the relative mass of halos (M_h) and the associated galaxy stellar mass (M_*) showing a "peak" efficiency for halos in forming stars at $M_h \sim 10^{12}\, M_\odot$. The mechanisms shaping this curve are still poorly understood. Figure taken from Behroozi et al. (2013).

1.5 Brief review of the ISM structure and physics

The inter-stellar medium (ISM) is predominantly composed of hydrogen and helium gas. Metals are present in trace amounts both in gas form, and in solid form which is referred to as dust (e.g., Spitzer 1978; Draine 2011). Additional, and less understood, components of the ISM are magnetic fields and cosmic rays. The gas is found in a variety of phases within individual galaxies. The gas surrounding galaxies is called the halo (not to be confused with the dark matter halo, which galaxies are presumably embedded in), while further from the galaxy it is called the circumgalactic and intergalactic medium (CGM and IGM).

In these regions the gas is ionized and in a very low density state. As gas density increases, the collisional recombination rate increases. When this rate matches the ionization rate due to the UV radiation field, hydrogen can recombine and become atomic (e.g., Osterbrock & Ferland 2006). In the Milky Way, approximately half the volume is filled by a hot ionized medium with $n < 0.01\,\mathrm{cm}^{-3}$ and $\mathrm{T}_K > 10^5\,\mathrm{K}$, and half is filled by some combination of warm ionized medium (WIM) and warm neutral medium (WNM) with $n \sim 0.1-1\,\mathrm{cm}^{-3}$ and $\mathrm{T}_K > 1000\,\mathrm{K}$ (Cox, 2005). The neutral gas is subject to a thermal instability that would predict segregation into the warm neutral and cold neutral media (CNM), the latter with $n > 10\,\mathrm{cm}^{-3}$ and $\mathrm{T}_K < 100\,\mathrm{K}$ (Field et al., 1969), although a large amount of gas appear to have properties which would be expected to be unstable. The cold ($\mathrm{T}_K < 100\,\mathrm{K}$) phases are the only plausible sites of star formation because pressure would halt the gravitational collapse (Kennicutt & Evans, 2012), while the warmer phases may provide the raw material for the cold phases, perhaps through anisotropic "cold" flows (Dekel & Birnboim, 2006).

Galaxies in the local Universe have very extended atomic hydrogen (HI) reservoirs, observable through emission of the 21 cm hyper-fine atomic transition (e.g., Haynes et al. 2018). The densest regions of the ISM allow the formation of hydrogen molecules through a phase transition controlled by "self-shielding" of the hydrogen molecule energy levels. In local galaxies, molecular gas (with density $n \sim 10^4 - 10^5\,\mathrm{cm}^{-3}$) appears to take the form of Giant Molecular Clouds (GMCs) and a Central Molecular Zone (CMZ) in the galactic nuclear regions (e.g., Heyer & Dame 2015). However, higher redshift galaxies appear to be very rich in molecular gas, which may sometimes take the form of giant molecular disks, making up most of the galaxy by mass (e.g., Daddi et al. 2010a). The dense, atomic boundary regions surrounding molecular clouds are referred to

as photo-dissociation regions or photon-dominated regions (PDR) because the micro-physical processes are dominated by the highly energetic Far-UV photons (Hollenbach & Tielens, 1997; Wolfire et al., 2003).

Complex thermodynamic processes set the density structure of the ISM. Heating in the PDR is dominated by the photo-electric effect on dust grains while deep in the molecular region it is dominated by cosmic rays. Gas cooling is generally dominated by line emission from FIR fine-structure lines and by CO lines deep in the molecular cloud. This fact makes such lines extremely valuable tracers of the physical conditions of the ISM (e.g., Stacey et al. 1991; Kaufman et al. 1999).

Gas metallicity is expected to play an important role in affecting the ISM structure and physical properties because it affects the hardness and intensity of the radiation emitted by stars, it affects the efficiency of gas cooling and the dust abundance which, among other effects, is central to the shielding of CO molecules which are the second most abundant molecule and the primary tracer of the molecular medium (e.g., Bolatto et al. 2013). Low metallicity stars have hotter photospheres due to changes in their atmosphere and low metallicity suppresses mass loss from massive stars. It is also believed that low metallicity may lead to the existence of a new binary evolution process named "quasi-homogeneous evolution" (QHE; Yoon & Langer 2005; Cantiello et al. 2007; Eldridge et al. 2011; Eldridge & Stanway 2012) in which the more massive star over-flows its Roche lobe and dumps mass onto the secondary, which (because of weak winds inherent to lower stellar metallicity) accretes gas rapidly and spins up to high rotational velocity, causing it to become fully mixed. Such stars can burn all of their H to He, last up to 3 times longer on the main se-

quence than a single star of the same mass, would not produce stellar winds, and become progressively hotter as they evolve away from the main sequence. QHE could produce sources of extreme-UV (EUV) radiation that would mimic classical Wolf-Rayet stars, but would be much longer lived, would require less massive progenitors, and may be not have the emission features of C or N (e.g., Steidel et al. 2016).

Although the ISM structure is relatively well characterized in the Milky Way and in local galaxies due to an abundance of available probes, the structure of the ISM at high redshift is much more poorly constrained due to limited sensitivity of current observatories. In particular, in the next sections we will see that a few mid-sized surveys (tens to hundreds of galaxies) have started investigating the ISM at the "cosmic noon" epoch $z \sim 1-3$, while the typical ISM properties are almost unconstrained at $z > 3$, leaving open the possibility of strong variations.

1.6 A galaxy-scale view of star formation

The process of star formation is one of the most complicated and least understood important astrophysical processes shaping our Universe. The problem has been approached observationally and theoretically with a variety of probes and over a wide range of scales and no consensus theory has been able to fully predict the effect of large and small-scale environmental variables to star formation. We here briefly summarize the galaxy-wide, observational approach to star formation studies (for a review, see Kennicutt & Evans 2012). The Jeans instability which is responsible for the gravitational collapse leading to star for-

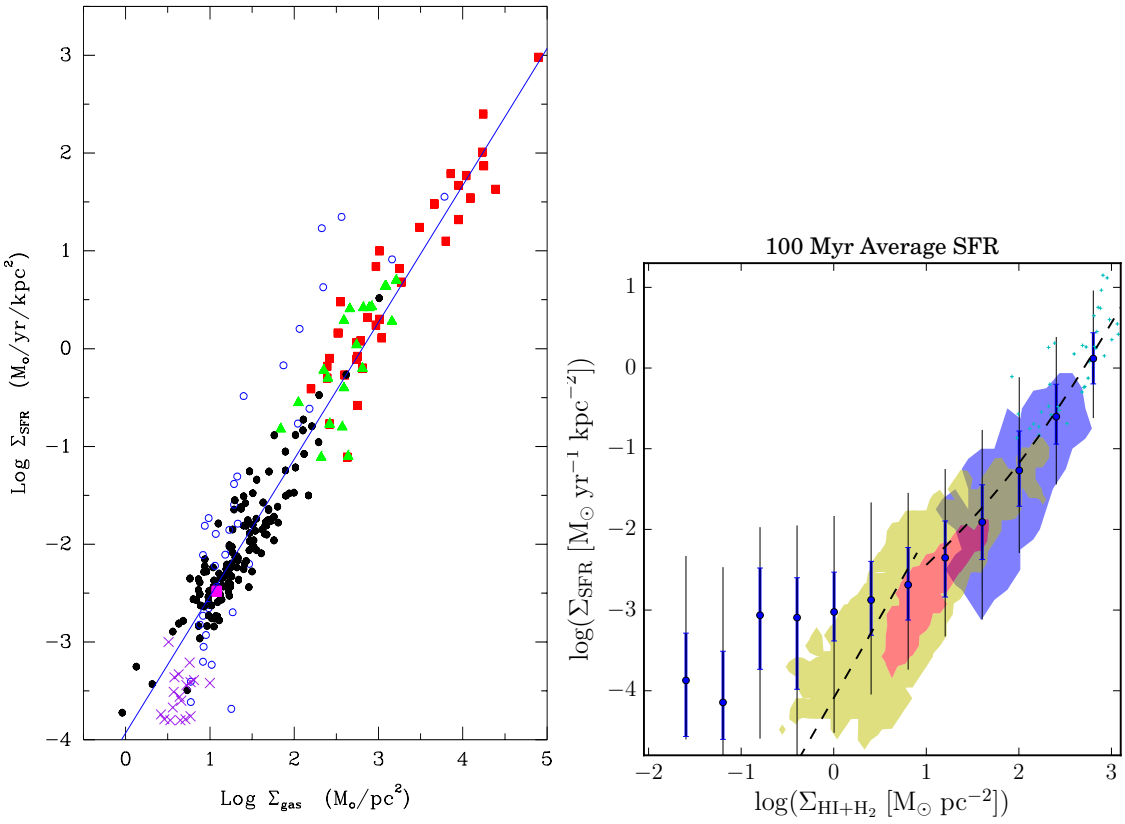

Figure 1.5: Relationship between the star formation rate surface density and the gas mass surface density in observed galaxies (left) and simulations (right). A power-law dependence of star formation activity as a function of cold, dense gas mass surface density has been measured (star formation law) and was approximately reproduced by galaxy formation simulations. Since this correlation holds over scales $\gtrsim$ 100pc, it might arise from large scale self-regulation although the micro-physics of star formation could play an important role as well (e.g., Orr et al. 2018). Figures from Kennicutt & Evans (2012); Orr et al. (2018).

mation suggests that low temperature and high gas density are necessary to initiate collapse. Therefore, star formation takes place in the densest regions of the ISM, where most matter is in molecular form (e.g., Krumholz et al. 2009; Krumholz 2012). A major open question is whether star formation may arise in atomic gas, perhaps in local dwarf galaxies or in low metallicity primordial galaxies where the formation of molecules may have been hindered by the low dust abundance (e.g., Krumholz 2013). The rate of star formation in a galaxy

is typically measured by tracing the emission from the most massive, hot stars expected to have a short (10–100 Myr) and constant lifetime and inferring the total rate of star formation (SFR) by extrapolating through the assumption of an Initial Mass Function (IMF; the stellar mass distribution function at formation; e.g., Bastian et al. 2010). The emission from hot stars is typically measured either through estimates of the UV luminosity or by the Hα line luminosity which is emitted by the ionized gas surrounding hot stars (Osterbrock & Ferland, 2006). However, star formation takes place in gas-rich and dusty environments, and therefore a large fraction of the stellar emission is typically absorbed by dust and re-radiated as thermal emission in the FIR (Kennicutt & Evans, 2012). The total measure of SFR typically requires summing the obscured (proportional to the FIR luminosity) and the unobscured (proportional to the UV luminosity) components, however in most massive, actively star-forming galaxies the obscured contribution is largely dominant and the SFR may be estimated based on the total FIR luminosity (Kennicutt & Evans, 2012). The amount of dense gas in a sufficiently large region of a galaxy (typically 100 pc to a few kpc) correlates with the SFR in that region because this gas provides the fuel for star formation. A relationship was put forth by Schmidt (1959), suggesting that SFR per unit volume should be a power law of the gas density per unit volume over sufficiently large scales. This Schmidt star formation law was observationally investigated in the Milky Way and local galaxies, through the observable surface density of star formation and the molecular gas surface density (Kennicutt, 1998a). A fairly tight correlation was found in this Σ_{SFR}-Σ_{gas} plane, suggesting a power-law index of $\sim$ 1.4 although with significant systematic uncertainty due to the calibration of the tracers on both axes (Figure 1.5). Often in extragalactic studies at high redshift the resolution of our observations does not allow re-

solving the star forming regions, and therefore integrated gas mass and SFR are compared instead. A similar relationship has been found to hold for integrated quantities, although the physical interpretation may not be identical since the quantities are now extensive (i.e., scale with the galaxy overall mass; e.g., Carilli & Walter 2013). The ratio of SFR and gas mass, or of their surface densities, is a measure of the efficiency of star formation (SFE) and is an inverse timescale which is referred to as the gas depletion time. This timescale is typically of order $\sim$ 1 Gyr in local, star-forming galaxies, although the non-linearity of the star formation law implies that it varies as a function of gas surface density or of galaxy gas mass (e.g., Leroy et al. 2013). The power-law index of ~1.5 has a particularly simple interpretation, because it derives from the reasonable assumption of taking the typical timescale to be proportional to the free-fall timescale (which is inversely proportional to the square root of the local gas density) to within a constant efficiency. This assumption is therefore found to hold reasonably well, for efficiencies of order ~2%, although detailed studies have found that such efficiencies vary as a function of galaxy type, location within the galaxy and as a function of gas surface density (Utomo et al., 2018).

It is unclear whether all galaxies and galaxy regions follow a universal star formation law or whether there are multiple "modes" of star formation. In particular, starburst galaxies appear to show high star formation for their gas masses (Figure 1.6; e.g., Daddi et al. (2010b)). However, since they also display the highest gas surface densities this may be due to the non-linear character of the "normal" star formation law. Furthermore, there is evidence that measuring the molecular gas mass in such starbursts (similarly to the nuclear regions of star-forming galaxies) may require a different calibration of the typical observables (CO line luminosity; e.g., Carilli & Walter 2013). It is therefore difficult to

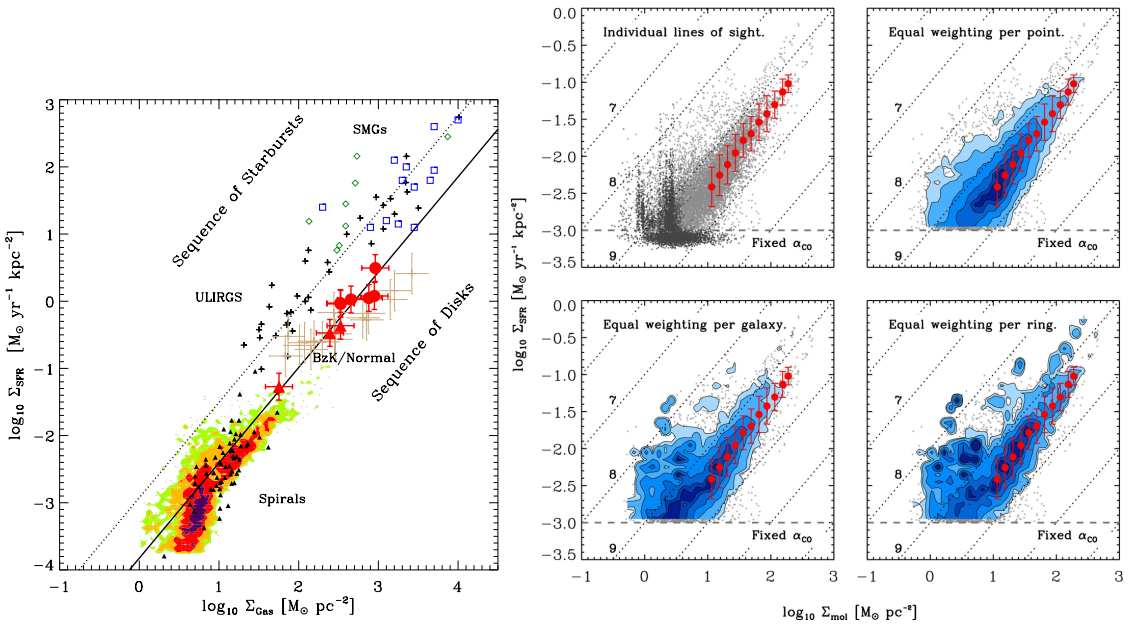

Figure 1.6: Observed relationship between the star formation rate and gas mass surface densities. (Left) There is some evidence that starburst galaxies may be characterized by a higher efficiency of star formation per unit gas mass relative to MS galaxies, both locally and at high redshift (Daddi et al., 2010b). (Right) Local studies using resolved CO emission line surveys from samples of tens of galaxies have shown that the star formation law appears to hold within individual galaxies, and may not show large galaxy-to-galaxy variation, at least for "normal", local, star-forming galaxies (Leroy et al., 2013). Figures from Daddi et al. (2010b); Leroy et al. (2013).

separate the effects of the starburst, or of the high gas density, on the gas tracers from the effect on the star formation law itself. Alternatively, Daddi et al. (2010b) have suggested a second mode of star formation with a consistent offset from the star formation law of "normal" galaxies, which may be due to a higher fraction of dense gas, within the molecular medium. Although starbursts are typically defined as regions of elevated star formation activity, a physically motivated definition would require an elevated star formation efficiency per unit gas mass. Alternatively, the term has been used to refer to galaxies which lie above the "typical" relationship between stellar mass and star formation rate (the star-forming main sequence, to be introduced in the following section).

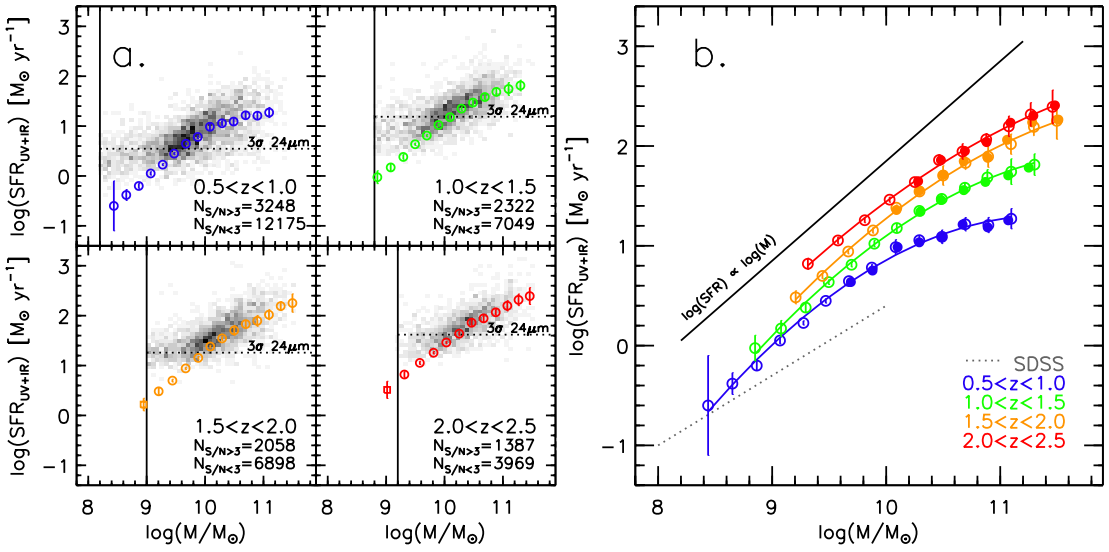

Figure 1.7: Star-forming galaxies in both the local Universe and high redshift show a correlation between stellar mass and SFR, the star-forming galaxy Main Sequence (MS). The figure shows the observed redshift evolution of this correlation using large samples of galaxies at $0.5 < z < 2.5$, and comparing them to the $z \sim 0$ measurements by SDSS. The main property of redshift evolution for the Main Sequence has been shown to be a consistent, smooth decrease of the SFR normalization over cosmic time, and potentially a flattening of the high-mass end (e.g., Speagle et al. 2014a; Whitaker et al. 2014). Figure from Whitaker et al. (2014).

There is evidence that such galaxies with elevated star formation for their stellar mass may also show shorter galaxy-wide gas depletion times, and thereby connecting them to the former definition (Silverman et al., 2015, 2018; Genzel et al., 2015; Scoville et al., 2016, 2017a; Tacconi et al., 2018).

1.7 Brief review of "normal" galaxies over cosmic time

Massive galaxies in the local Universe may be separated into passive ellipticals, star-forming spirals and a few irregulars and transition galaxies (e.g., Hubble 1926; Baldry et al. 2004, but Eales et al. 2018). In the current work we only focus

on star-forming galaxies because they are rich in inter-stellar matter and because they are responsible for the observed stellar mass buildup. Star-forming galaxies further back in time look less and less like spiral galaxies and more like irregular, clumpy disks, at least when observed through their optical emission (e.g., Elmegreen et al. 2007, 2009). Furthermore, *Herschel* showed that massive galaxies at $z \sim 1-3$ were forming stars much more intensely than lower redshift star-forming galaxies (e.g., Magnelli et al. 2013). These changes are likely to be the consequence of a strong evolution in their makeup: whereas the gas mass in local spirals is only $\lesssim$10% of the mass, it typically grows to ~50% or more by $z \sim 2-3$ as we will see in the next sections. The morphology and dynamics of these gas-rich disks is therefore dominated by their ISM and, potentially, by the strong gas inflows and outflows which are expected to be comparable in mass rate to the observed star formation rates. Some of these conclusions were reached by deep field studies with the *Hubble* Space Telescope (*HST*), and through color selection of galaxies to identify photometric redshifts (photo-z, Grogin et al. 2011; Koekemoer et al. 2011; Momcheva et al. 2016). Galaxy populations which were selected through such techniques were then followed-up in the mid-IR and FIR to estimate SFRs (e.g., Lutz et al. 2011; Elbaz et al. 2007, 2011; Daddi et al. 2007; Rodighiero et al. 2010; Wuyts et al. 2011; Oliver et al. 2012; Magnelli et al. 2013), and sometimes by spatially resolved spectroscopy of the Hα emission tracing the ionized gas, which has provided the largest samples of kinematic information at high redshift (e.g., Förster Schreiber et al. 2006, 2009; Wisnioski et al. 2015; Förster Schreiber et al. 2018). One of the main results from such surveys was the characterization of the correlation between stellar mass and SFR in star-forming galaxies, sometimes called the star-forming galaxy Main Sequence (MS, Figure 1.7;e.g., Brinchmann et al. 2004; Noeske et al.

2007; Elbaz et al. 2007; Daddi et al. 2007; Pannella et al. 2009). Although this observed correlation may show significant scatter (e.g., Speagle et al. 2014b), it has been interpreted as an important constraint to galaxy evolution models. It may provide evidence for a secular mode of galaxy growth, possibly due to smooth accretion from the IGM and hinting to the importance of self-regulation in galaxy-scale star formation (e.g., Davé et al. 2012a). Passive galaxies at any redshift lie below the MS, while a population of galaxies lying above the MS is sometimes named "starburst" population. It is unclear whether there may be a gap or a smooth transition to starbursts above the MS, although no conclusive evidence for such a gap has been discovered (e.g., Rodighiero et al. 2011; Caputi et al. 2017). Perhaps the main finding of such studies was the measurement of a substantial redshift evolution in the normalization of the Main Sequence, increasing in SFR by a factor of ~ 30 between $z = 0$ and $z \sim 2$ (e.g., Daddi et al. 2007; Speagle et al. 2014a; Whitaker et al. 2012, 2014). **This finding suggested that "normal" galaxies of a fixed stellar mass were forming stars much more intensely at $z \sim 2-3$, and that the peak in the cosmic SFR density is due to an overall increase in the SFR for the whole population of Main Sequence galaxies, rather than increased prevalence of starburst galaxies (e.g., Rodighiero et al. 2011)**. Galaxies with high rates of star formation (both massive MS galaxies and lower mass galaxies lying above the MS) generally display a high degree of dust obscuration, making them bright FIR and sub-mm sources while making their optical emission difficult to detect (e.g., Blain et al. 2002a, for a review). This galaxy population was therefore discovered through sub-mm telescopes and has been variously named sub-mm galaxies (SMGs) or dusty star-forming galaxies (DSFGs; e.g., Casey et al. 2014a for a review). The physical properties of such massive, star-forming galaxies may not therefore be investigated through

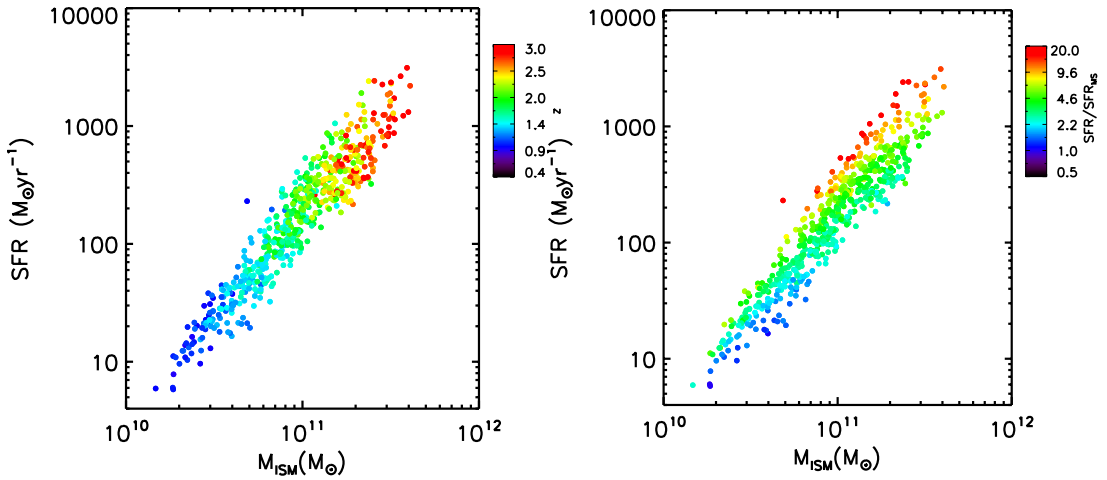

Figure 1.8: Using the dust continuum emission on the Rayleigh-Jeans tail, Scoville et al. (2017a) have estimated ISM masses for large samples of galaxies at $z \sim 0.5 - 3$. Here we show the observed correlation between ISM mass and star formation rate for their sample, color coded by redshift (left) and offset from the Main Sequence (right). Scoville et al. (2017a) find a correlation between ISM mass and SFR in agreement with the star formation law, with an increase in both the gas mass fraction and the star formation efficiency toward higher redshift. They also find increasingly higher efficiency for starburst galaxies above the MS. Figure from Scoville et al. (2017a).

optical spectroscopy because the majority of their star formation activity is completely obscured by dust, but rather through sub-mm spectroscopy which is less affected by dust extinction.

1.8 Tracers of the molecular gas in galaxies

As we will explore in more detail in the next chapter, the best established tracer of molecular gas mass and properties is the CO rotational line ladder. In particular, the ground level transition CO(1–0), is the best tracer of the total molecular gas mass because it is independent of level population excitation (e.g., Carilli & Walter 2013). However, observations of CO(1–0) are time consuming at high

redshift due to its moderate brightness and therefore alternative approaches to measuring the gas mass have been developed. The most widespread approach uses long-wavelength dust emission as a tracer for the total gas mass (Scoville et al., 2016, 2017a). The method relies on the assumption of a constant dust-to-gas mass ratio, that the Rayleigh-Jeans tail of the dust emission is dominated by cold dust with an approximately fixed emissivity power-law index, that the cold dust faithfully traces the bulk of the gas distribution and that the cold dust temperature is always ~ 25 K. Nonetheless, this method has been shown to provide an estimate, although uncertain, in local galaxy samples and may hold at least for a subset of luminous high redshift galaxies (Eales et al., 2012; Scoville et al., 2013; Bourne et al., 2013; Groves et al., 2015; Scoville et al., 2016). However, a significant downside to this method lies in relying on a dust continuum measurement which (although on the Rayleigh-Jeans tail and therefore less sensitive to the total FIR luminosity than near the peak) is unavoidably correlated to the FIR luminosity and hence the SFR. After all, the dust emission is re-radiated stellar radiation and therefore this tracer makes it difficult to reliably investigate the relationship between gas mass and star formation (the star formation law). This method has been applied to characterize the ISM content of FIR-selected galaxies (through *Herschel*) in mid-sized samples (a few hundreds) at $z \sim 1-3$ (Scoville et al., 2016, 2017a), and the findings are in general agreement with the CO-based studies which we will discuss next (Figure 1.8; e.g., Tacconi et al. 2018).

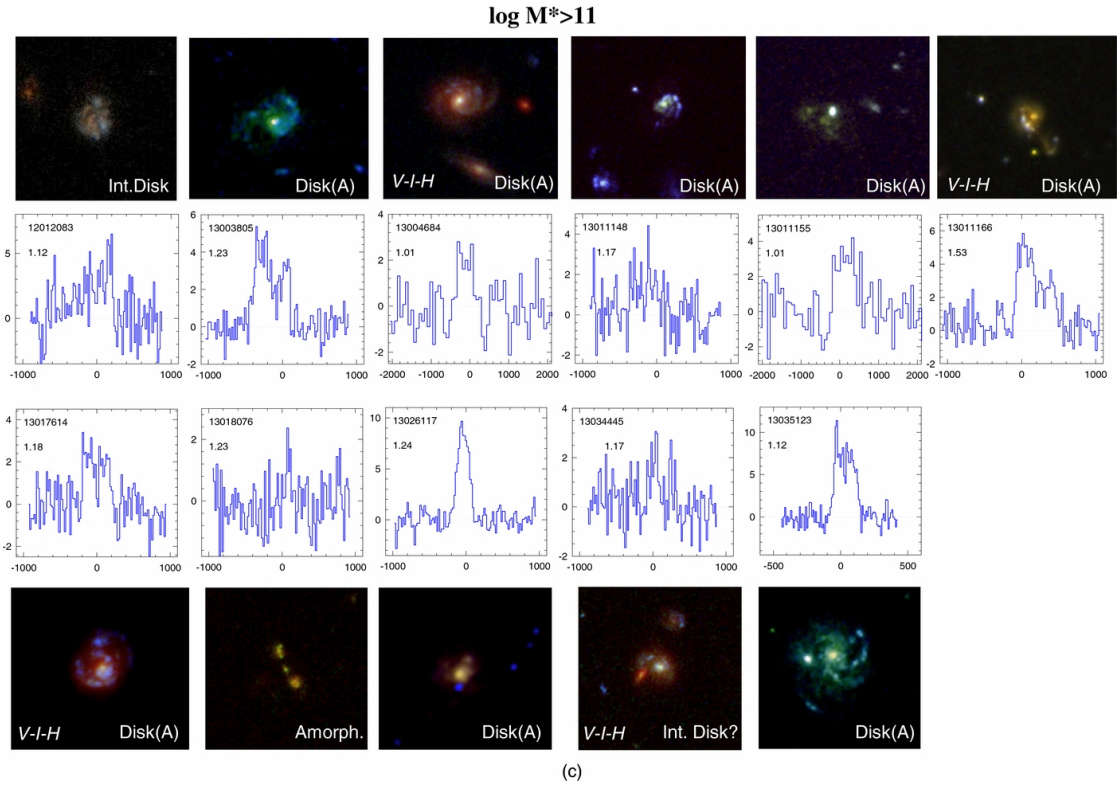

Figure 1.9: Targeted observations of CO(3–2) line emission have revealed massive molecular gas reservoirs in $z > 1$ galaxies selected through *HST* deep fields, corresponding to rest-frame UV emission (e.g., Tacconi et al. 2013). Although such studies have been crucial to understanding optically selected populations at the peak epoch of cosmic star formation, they might miss gas rich galaxies if they are largely dust obscured. Here shown *HST/WFC3* imaging and CO(3–2) line detections for the most massive sub-sample targeted by the PHIBSS survey. Figure from Tacconi et al. (2013).

1.9 Unbiased surveys versus targeted studies

In order to understand what drives the elevated star formation rate observed in "normal" galaxies at $z > 0$, CO studies of the molecular gas content have been carried out targeting typical MS galaxies (e.g., Daddi et al. 2008; Aravena et al. 2010a; Daddi et al. 2010a,b; Riechers et al. 2010a; Aravena et al. 2012; Tacconi et al. 2013; Aravena et al. 2014; Genzel et al. 2015; Daddi et al. 2015; Bolatto et al. 2015; Spilker et al. 2016; Tacconi et al. 2018), and highly FIR luminous galaxies

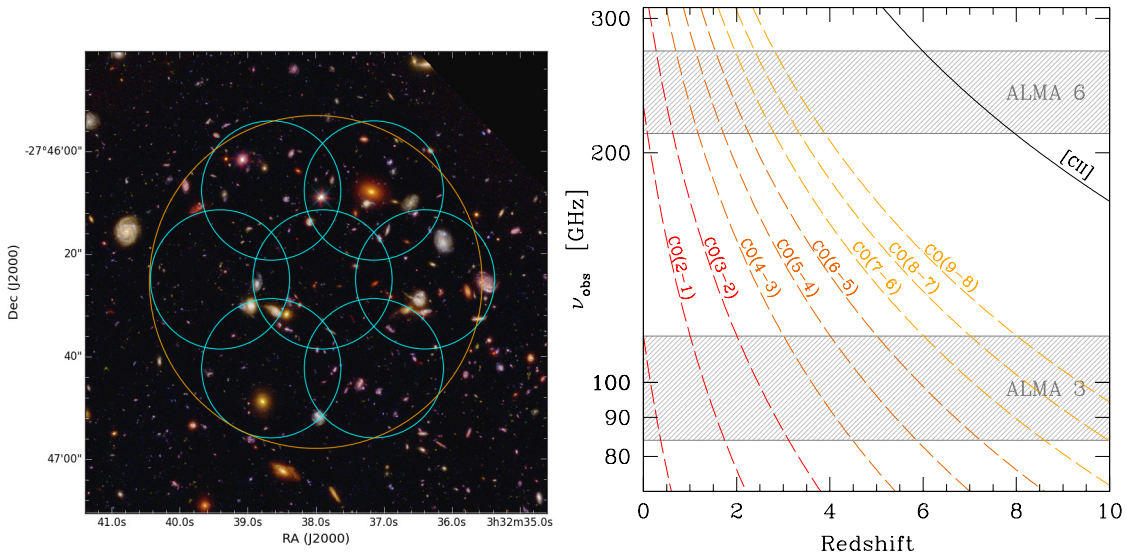

Figure 1.10: CO deep fields have just started exploring the cold gas content in galaxies at $z > 1$ in an unbiased way (e.g., Decarli et al. 2014a; Walter et al. 2016; Decarli et al. 2016a). The limited field of view of one of the first such blind surveys is shown, to the left, overlaid on the *HST* image of the H-UDF. However, sub-mm interferometers such as ALMA can only target mid-*J* CO lines at high redshift (redshift range accessible for different CO transitions shown, to the right), which may not be an accurate tracer of the cold molecular gas reservoir. Figure from Walter et al. (2016).

which predominantly lie above the MS (see Carilli & Walter 2013 for a review). Such targeted studies have found increasing molecular gas fraction toward high redshift at least up to $z \sim 3$, which appears to be the main driver of the increased SFR at a fixed stellar mass with redshift (Tacconi et al., 2010; Daddi et al., 2010a). Furthermore, MS galaxies at high redshift appear to approximately follow the low redshift star formation law relating gas mass per unit surface area to SFR per unit surface area and starburst galaxies at high redshift may be compatible with the elevated SFR per unit gas mass which is observed in local starbursts (e.g., Daddi et al. 2010b; Genzel et al. 2010). Mid-sized samples of CO(3–2) measurements such as the IRAM Plateau de Bure HIgh-z Blue Sequence Survey (PHIBSS) have suggested that the increased gas availability may not be entirely responsible for the elevated SFR but that the star formation efficiency may also

be slightly elevated by a factor $\sim 2-3$ relative to $z \sim 0$ (with gas depletion timescales of ~ 500 Myr on the MS, Figure 1.9; Tacconi et al. 2013; Genzel et al. 2015; Tacconi et al. 2018).

These studies have used sensitive sub-mm and radio interferometers to measure CO line emission from pre-selected galaxies which were discovered either through optical color selection or through their FIR emission. These selection techniques have selective completeness and may lead to biases which are poorly characterized due to our limited knowledge of the high redshift galaxy population. For example, optical surveys may miss galaxies completely if they are dusty due to the strong obscuration of their UV/optical emission, while the FIR selection is preferentially sensitive to galaxies with high SFR, and such studies may be biased against gas-rich galaxies with lower SFR. In order to complement such studies, it is necessary to use selection techniques which are sensitive to the gas mass directly such as CO deep field surveys. In particular, a measurable quantity of great interest consists in the CO luminosity function, i.e., the distribution of CO(1–0) line luminosity emitted per unit comoving volume, over cosmic time. This is directly related to the molecular gas mass function of galaxies, describing the cosmic volume density of galaxies as a function of their gas mass, as a function of redshift. The first such CO deep field study was a pilot study with the Plateau de Bure Interferometer (now NOEMA), which resulted in the first CO selected galaxies and the first constraints to the CO luminosity function (Decarli et al., 2014a; Walter et al., 2014). Following this first pilot study, the Atacama Large (sub)Millimeter Array (ALMA) has allowed carrying out a much deeper CO deep field as part of the ALMA Spectroscopic Survey in the Hubble Ultra Deep Field (ASPECS, Figure 1.10) program and providing deeper, more accurate constraints to the CO luminosity function (e.g., Walter et al. 2016; De-

carli et al. 2016a). Interferometers such as NOEMA and ALMA are sensitive to mid-J CO lines, that are related to CO(1–0) through an excitation factor which appears to vary from galaxy to galaxy by a factor of a few (Figure 1.10). Therefore, a CO selection based on mid-J CO lines such as CO(3–2) may still be biased toward selecting galaxies with higher CO excitation than average, rather than tracing the cold molecular gas mass without bias. In particular, CO excitation is related to conditions of gas density and temperature which are determined by star formation, e.g., CO(5–4) appears to accurately trace the warm, directly star-forming gas rather than the bulk molecular reservoir. Therefore a deep field survey targeting CO(1–0), uniquely made possible by the upgraded Very Large Array (VLA), is needed in order to eliminate the excitation bias of previous CO deep field surveys. We carried out the first such study as part of the CO Luminosity Density at High-z (COLDz) survey, which is the main subject of this thesis.

1.10 Normal galaxies at the end of reionization: ISM structure and gas phases

As previously described, the ISM properties of "normal" galaxies have been constrained to some degree during the "cosmic noon", up to $z \sim 3$. However, the conditions at higher redshift are only poorly constrained due to the faintness of the emission from such galaxies. The main techniques to select galaxies at such high redshift consist in the Lyman break galaxy color selection (LBG) and, narrow band filters allow selecting Lyman Alpha Emitters (LAEs) at the specific redshift which places the Lyα line within the narrow band (e.g., Par-

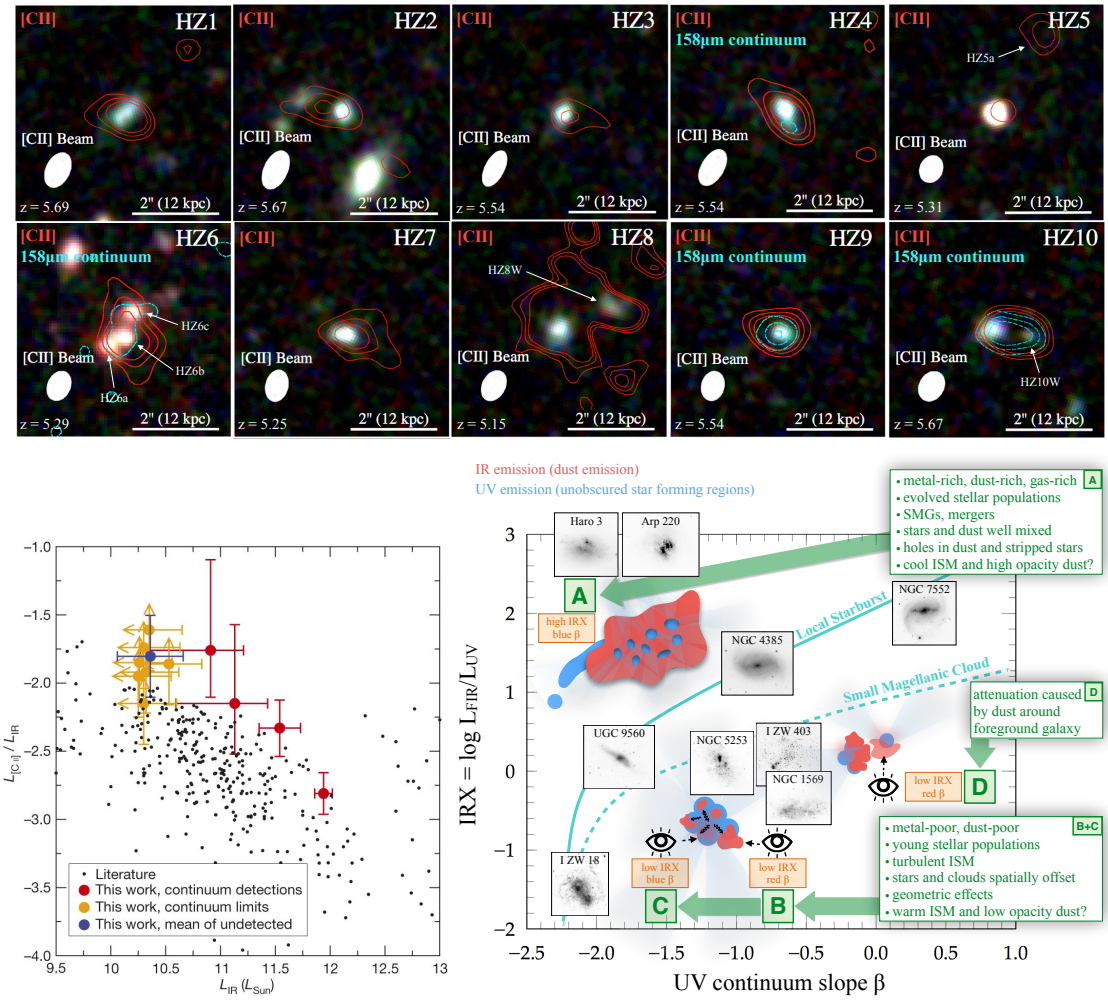

Figure 1.11: ALMA allows observing the ISM in "normal" galaxies at $z > 5$ for the first time (Riechers et al., 2014a; Capak et al., 2015). Capak et al. (2015) carried out the first sample study of [CII] in MS galaxies at $z = 5 - 6$, finding bright [CII] relative to the dust continuum. At the top, [CII] and dust continuum shown as contours, overlaid on *HST*/WFC3 imaging. At the bottom left, observed offset of the [CII]/IR ratio of the $z > 5$ sample relative to local galaxies. This is evidence of an evolution in the ISM properties of massive galaxies, suggesting that the first billion years of cosmic time is the time of formation for such galaxies. The dust properties may be different, perhaps due to lower metallicity, or the dust geometry in relation to recent star formation as shown by Barišić et al. (2017); Faisst et al. (2017). At the bottom right, the possible interpretations of different IR-properties for the $z > 5$ galaxy sample. Figures from Capak et al. (2015); Faisst et al. (2017).

tridge & Peebles 1967; Ouchi et al. 2003, 2005, 2008). The lack of survey telescopes sensitive to the rest-frame infrared emission (both the near-IR, tracing the stellar component and the FIR tracing the obscured star formation) also precludes any completeness in our census of star-forming galaxies at $z \gtrsim 3-4$. Although *HST* and ground based optical surveys have yielded fairly large catalogs of such high-z candidates, studies of their ISM conditions typically require spectroscopy, and may only be obtained for limited samples due to current sensitivity of optical telescopes (e.g., Hasinger et al. 2018). Some of the most recent results in this field have shown that, at this epoch, the composition of the interstellar medium in common, low mass galaxies may begin to show an evolution toward lower metallicity (e.g., Masters et al. 2016; Faisst et al. 2016a; Harikane et al. 2018). At the same epoch, statistical studies constraining the ratio of SFR to stellar mass have shown that this rises steeply toward the early Universe, implying that the first billion years of cosmic time ($z > 5$) may have been a time of unprecedented growth for galaxies (Faisst et al., 2016b). In the near future, the *James Webb* Space Telescope (JWST) will provide the level of detail on the conditions in these galaxies which is now available for galaxies at the "cosmic noon", but ALMA is already opening the way by exploiting the diagnostic power of FIR fine-structure lines. In particular, the [CII] line at 158 μm is one of the most luminous lines because it is one of the main coolants of the neutral ISM, and has been observed up to $z > 7$ in both "normal" galaxies, quasars and luminous starburst galaxies. The first detection of [CII] in a "normal" galaxy in the first billion years of cosmic time demonstrated the possibility of using ALMA for the task and was achieved by targeting an overdensity of galaxies, an early proto-cluster, surrounding a major starburst at $z \sim 5.3$ (Riechers et al., 2014a). Capak et al. (2015) carried out the first sample study targeting [CII] and the ad-

jacent dust continuum in ten "normal", Main Sequence galaxies at $z = 5 - 6$ which are representative of the typical selection techniques used at these redshifts (Figure 1.11). Although these observations found luminous [CII] lines showing intense star formation, the dust continuum was fainter than expected both relative to [CII] and to the UV luminosity. This faint dust emission suggests an evolution in the dust properties affecting these massive ($M_* \sim 10^{10}\,M_\odot$) galaxies potentially related to lower metallicity, a different radiation environment or a different structure of the ISM in relation to star formation (Capak et al., 2015; Barišić et al., 2017; Faisst et al., 2017).

1.11 The pivotal role of metallicity: a potential for very new galactic labs

The importance of metallicity (the abundance of heavy elements in the ISM) as a physical quantity in probing galaxy formation stems from the ability to trace the cumulative imprint of generations of stars, which enrich the gas starting from an essentially pristine IGM (of very low metallicity). Therefore, gas metallicity probes what fraction of the ISM in a galaxy has been freshly accreted, rather than having been enriched by previous episodes of star formation (e.g., Finlator & Davé 2008; Finlator 2017). It complements some of the information which may be derived from stellar mass and SFR measurements, and uniquely carries information on the "maturity" of a galaxy, i.e., the level of enrichment of its ISM rather than recent accretion. In addition to probing the interplay of gas accretion, star formation and outflowing enriched gas, metallicity is also expected to strongly influence the conditions for star formation possibly affecting

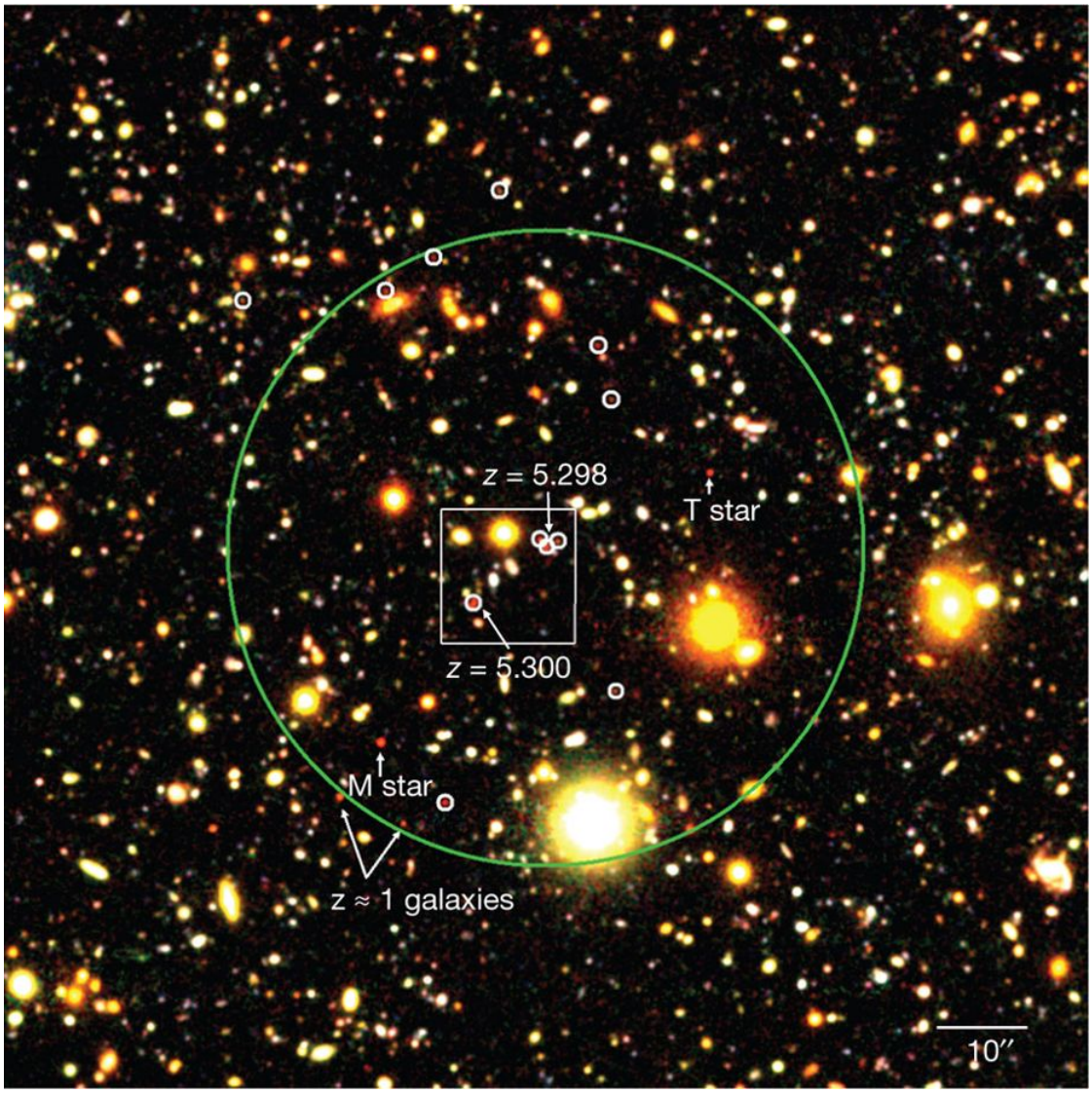

Figure 1.12: A rich, massive proto-cluster at $z \sim 5.3$ was identified as an overdensity of LBG dropout galaxies around the extreme starburst AzTEC-3 (*HST* image above), in the COSMOS field (Riechers et al., 2010b; Capak et al., 2011). Such beacons of high redshift star formation have provided some of the first "labs" to explore the different ISM conditions in "normal" galaxies, and their luminous neighbors (e.g., Riechers et al. 2014a). Figure from Capak et al. (2011).

the IMF and the star formation law, the stellar structure and evolution and the abundance and properties of the dust in the ISM (e.g., Clark et al. 2008; Dopcke et al. 2013). Although local dwarf galaxies provide a lab into low metallicity star-forming conditions (e.g., Rubio et al. 2015), assembling galaxies in the early Universe are expected to differ in significant ways, mainly due to their environment and due to the different cosmological setting (Figure 1.12). In addition, it is believed that abundant, low-mass star-forming galaxies may be responsible for causing reionization to take place (ending at $z \sim 6$). Characterizing the physical processes responsible for this important phase transition of the intergalactic medium represents the next frontier of high redshift studies because it may hold clues to new fundamental physics phenomena. In order to start characterizing the drivers of reionization we need to gain a more accurate understanding of the sources, i.e., the production of UV photons by massive stars in early galaxies and the ISM which these photons need to escape in order to ionize the IGM.

1.12 The role of cosmic overdensities in early galaxy assembly: massive proto-clusters

A key piece of the early galaxy assembly puzzle appears to be galaxy clustering and the role of early proto-clusters in shaping the formation history of massive galaxies. One of the main lessons that cosmological hydro-dynamical simulations have taught us is that we should not think of galaxies as closed systems but rather as constantly exchanging a large fraction of their gas with, and injecting energy into their surrounding environment (e.g., Muratov et al. 2015; Sparre et al. 2017; Hayward & Hopkins 2017). It is therefore natural to infer

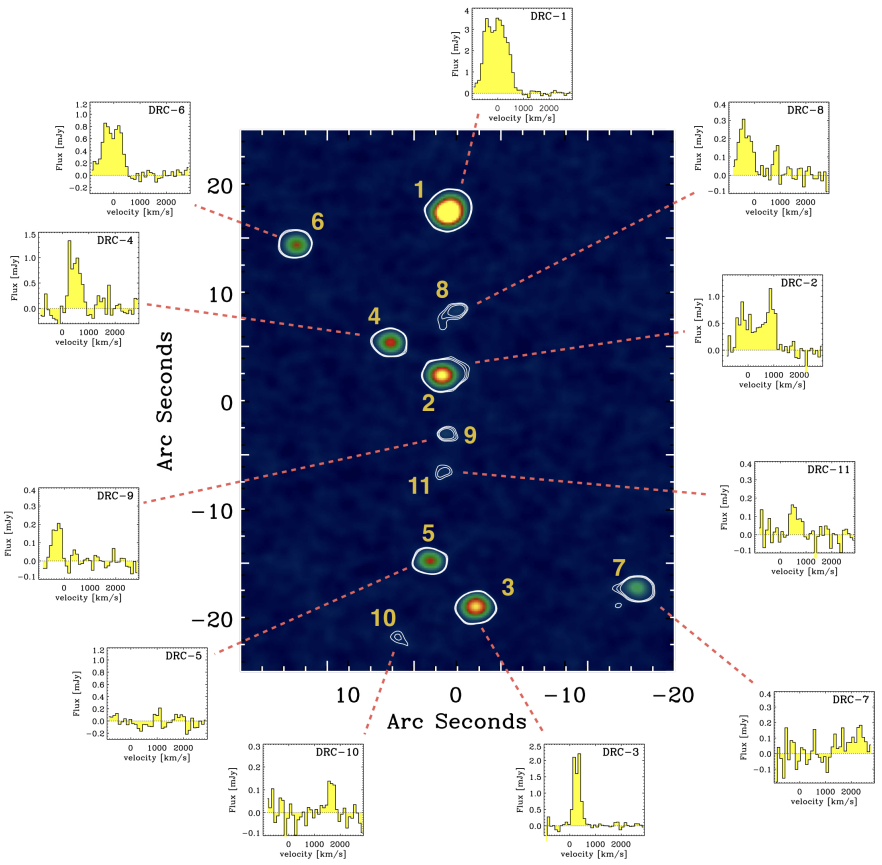

Figure 1.13: A rich proto-cluster of dusty star-forming galaxies at $z \sim 4$ shown in dust continuum emission and the [CII] line emission which demonstrated that the different galaxies are at the same redshift, and therefore physically associated. Proto-clusters of massive star-forming galaxies at $z > 4$ may be more prevalent than expected since they are being discovered at a surprisingly high rate. This suggests that galaxy clustering, especially for the most massive galaxies, may play a larger role in early star formation than anticipated. Figure from Oteo et al. (2017a).

that galaxy assembly in an overdense proto-cluster environment may strongly affect, among others: the gas composition and cooling, the star formation self-regulation, the dynamical gas conditions and the ionizing photons escape fraction.

While it has been known for decades that large scale dark matter structures form hierarchically from the gravitational growth of smaller seed overdensities,

it may not have been immediately obvious that galaxy formation would "start out" in the most massive halos, which are also the most strongly clustered ones. While the early galaxy formation efficiency of dark matter halos is still not well understood, recent theoretical work suggests that proto-clusters may have dominated star formation in the first ~ 2 billion years of cosmic time (Chiang et al., 2013, 2017). This is due to the fact that the fraction of the cosmic volume occupied by all future (proto)clusters increases by nearly three orders of magnitude from $z = 0$ to $z = 7$. More importantly, most models suggest that early galaxy formation may be dominated by the central regions of the most massive overdensities, and that star formation may evolve inside-out to galaxies in lower density environments (Chiang et al., 2017). This might be a consequence of a weakening of feedback in the most massive halos, relative to lower redshift. These may be crucial, observable predictions of structure formation in the early Universe. A quantification of the fraction of star formation in different environments as a function of cosmic time will be an important cosmological probe in the era of wide-area surveys (e.g., LSST, WFIRST). Of relevance here, the physical processes associated with the "central" galaxy forming in a proto-cluster, which may be a DSFG at least during part of its life, may strongly affect the evolution of such proto-clusters, both by enriching the intra-cluster medium and by providing energy input through winds and radiation (Figure 1.13; where multiple DSFGs are associated in a proto-cluster). In our final chapter of this thesis, we present the serendipitous discovery of one of the brightest, highest redshift star-forming galaxies known to date which may help shed light on such early proto-cluster environments. We identified this galaxy in our data thanks to its close proximity to a "normal" galaxy in our sample, and we find these galaxies to be in physical association. In this final chapter, we speculate on the impli-

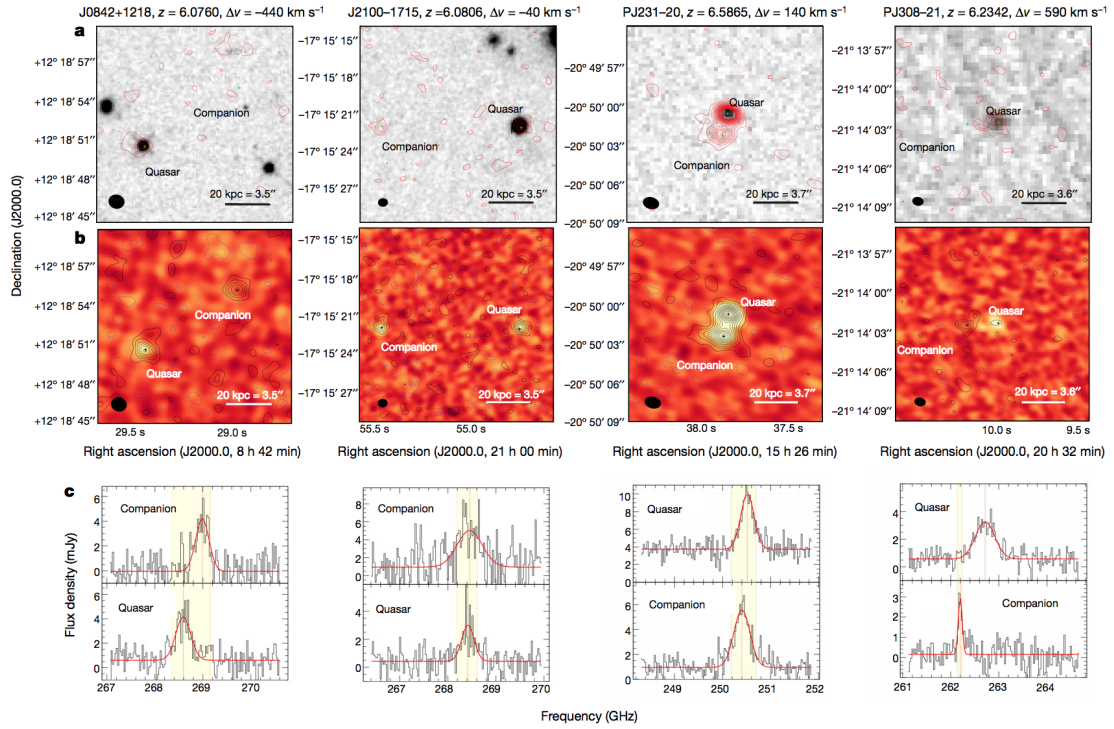

Figure 1.14: Serendipitous discoveries of massive starbursting galaxies appear more common than expected, even though the ALMA field of view only probes the immediate neighborhood of galaxies at high redshift (e.g., Pavesi et al. 2018a). Four out of 25 quasars observed by ALMA in a survey at $z > 6$ have resulted in additional, highly star-forming companion galaxies within few tens of kpc from the quasars (Decarli et al., 2017). Figure from Decarli et al. (2017).

cations of this connection and the connection found by recent results in several other systems (e.g., Capak et al. 2011; Riechers et al. 2014a; Decarli et al. 2017; Oteo et al. 2017b; Marrone et al. 2018), and whether the ISM in these galaxies may be affected by one another potentially shining light on such important, often neglected, aspect of early galaxy formation (Figure 1.14).

CHAPTER 2

METHODS AND TOOLS

The main diagnostics for studying different phases of the ISM is the luminosity of emission lines from molecules, atoms and ions. In this section we briefly describe the lines of interest for this study, their connection to ISM physical properties and define some of the derived quantities used in the following. We also briefly describe the main observatories used and introduce some of the main statistical methods employed.

2.1 The CO line transitions

Molecular Hydrogen (H_2) is by far the most abundant molecule in the Universe and dominates the ISM in regions of active star formation due to the low temperature and high density required for gravitational collapse. However, molecular hydrogen in this cold phase is not directly observable in emission because the lowest lying excited energy level corresponds to a transition energy equivalent to a 28.2 μm photon, which requires a temperature of ~510 K for collisional excitation. The high energy level separation is due to the low mass of the Hydrogen atom, implying a low moment of rotational inertia and hence a high energy associated with each additional quantum of angular momentum. The symmetry of the Hydrogen molecule also produces a zero electric dipole moment, but the lower rate of electric quadrupole transitions would not hinder observability if such states were excited. Indeed warm molecular Hydrogen in shocked regions emits bright rotational and ro-vibrational lines in the near and mid-IR. Carbon and oxygen are among the most abundant elements after Hy-

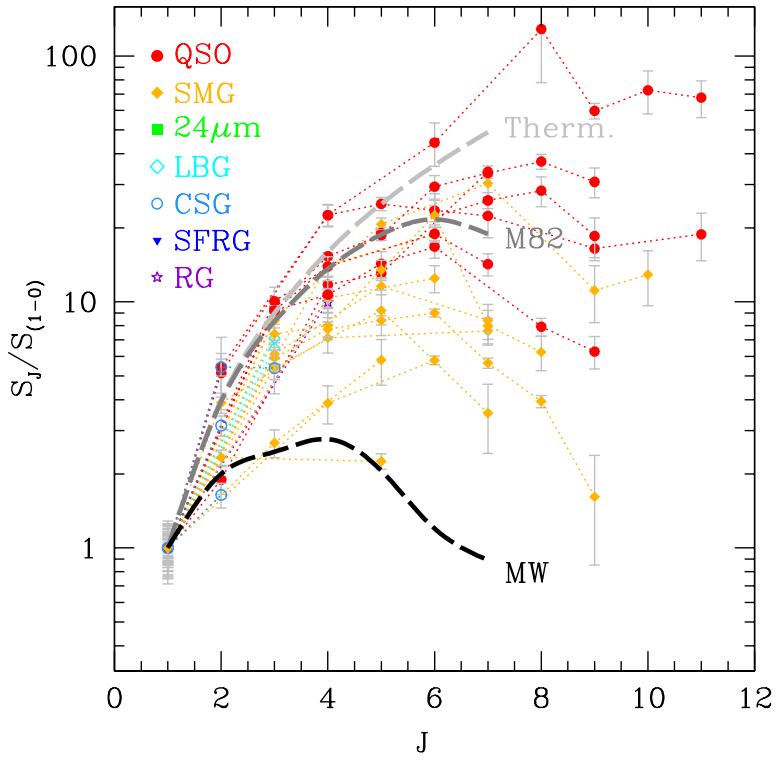

Figure 2.1: The CO spectral line energy distribution (SLED) shows a wide range of excitation conditions in different galaxy populations. While the luminosity of the CO(1–0) line is the best tracer of the molecular gas mass in galaxies, the relative brightness of higher J levels shown here is determined by the prevalence of higher density and temperature in the molecular gas, characteristic of active star formation or AGN activity. Figure from Carilli & Walter (2013).

drogen and Helium, and the CO molecule is prevalent in the conditions which are typical of molecular clouds. CO has a weak permanent dipole moment and a ground rotational transition with a low excitation energy of $h\nu/k \sim 5.53$ K. With such low energy and critical density (see next paragraph, further reduced by radiative trapping due to its high typical optical depth), CO is easily collisionally excited even in cold molecular clouds (Carilli & Walter, 2013). In addition, the line wavelength of 2.6 mm for the J=1–0 transition of CO lies in a fairly transparent atmospheric window so it has become the workhorse tracer of the bulk distribution of H_2 in our Galaxy and beyond (Bolatto et al., 2013).

The rotational lines of CO form a linearly spaced ladder in frequency since the quantized rotation energy is (to zeroth order):

$$E_{\rm rot} = \frac{J(J+1)\hbar}{2I} \text{ where } J = 0, 1, 2, ... \tag{2.1}$$

The electric dipole selection rule implies that $\Delta J = \pm 1$ for all allowed transitions and the line frequency is therefore:

$$\nu(J \rightarrow J-1) = \frac{\hbar J}{2\pi I} \text{ where } J = 1, 2, ... \tag{2.2}$$

Implying that the rotational spectrum is composed of lines at frequencies which are multiples of the ground level CO(1–0) transition frequency of ~115.27 GHz. We refer to CO(1–0) and CO(2–1) as low-J levels, CO(3–2) up to approximately CO(6–5) as mid-J levels and high-J levels beyond that. All other molecular transitions (such as vibrational) lie at significantly higher frequency in the mid-IR regions of the spectrum. The excitation energy of successive rotational energy levels therefore increases quadratically with the quantum number, showing that higher J lines are predominantly excited in warmer and denser molecular gas, which is typically more closely associated with ongoing star formation (Figure 2.1). Density of the molecular medium plays an important role in CO excitation of the higher energy levels because a large fraction of the molecular medium is not dense enough (relative to a "critical density" for a level transition[1]) for thermodynamic equilibrium to occur (i.e., the excitation rate due to collisions is not balanced by collisional but rather by radiative de-excitation) and the population of the mid-J and especially high-J levels does not follow a Boltzmann distribution (Figure 2.1).

[1]The critical density for CO(1–0) is 2200 cm^{-3} and increases as J^3 for higher J lines.

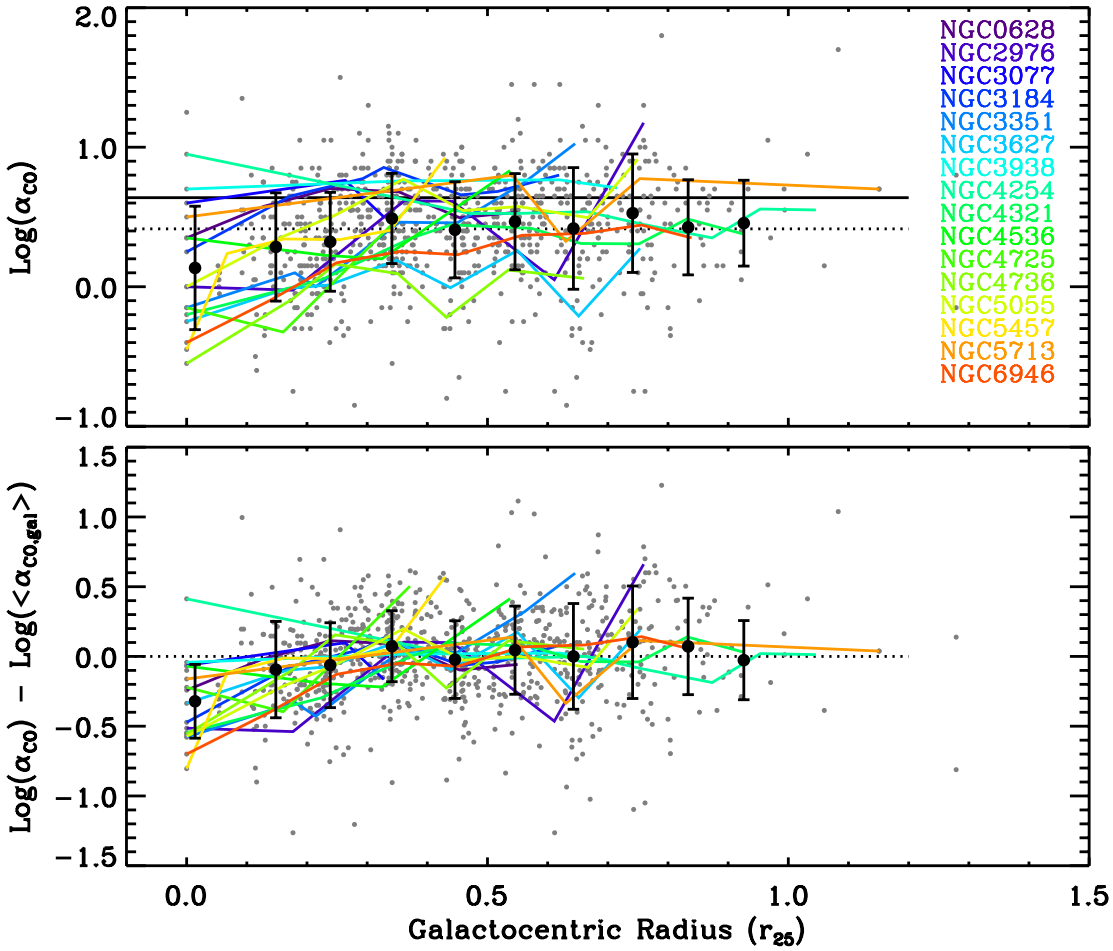

Figure 2.2: The α_{CO} gas mass-to-light ratio shows a surprising degree of consistency in local galaxies, both among different galaxies (top) and within individual galaxies (bottom). Sandstrom et al. (2013a) show that α_{CO} is approximately constant within most galaxies in their sample, and that central galactic regions appear to exhibit lower α_{CO}, as expected based on the increasing importance of the stellar potential to the gas dynamics. Figure from Sandstrom et al. (2013a).

2.2 CO as a tracer of molecular gas mass

2.2.1 Line luminosity definitions

First, let us introduce the definitions of two quantities traditionally used to express line "luminosities" for radio emission lines. The first one is just the con-

ventional expression of luminosity as the radiated power from line emission, obtained by integrating the emitted flux over the line frequency width as follows:

$$L_{\rm line} \equiv 4\pi D_L^2 (1+z)^{-1} \nu_r / c \int S_\nu d{\rm v} \simeq 1.04 \times 10^{-3}\, L_\odot \, \frac{S_\nu \Delta {\rm v}}{\rm Jy\,km\,s^{-1}} \, \frac{D_L^2}{\rm Mpc^2} \, \frac{\nu_{\rm obs}}{\rm GHz} \qquad (2.3)$$

where the velocity integrated line flux $S_\nu \Delta {\rm v}$ is the result of the integral and D_L is the luminosity distance. However, sometimes radio astronomers use an alternative definition partly due to historical reasons:

$$L'_{\rm line} \equiv \frac{c^3}{8\pi k_B \nu_r^3} \, L_{\rm line} \simeq 3.25 \times 10^7 {\rm K\,km\,s^{-1}\,pc^2} \, \frac{S_\nu \Delta {\rm v}}{\rm Jy\,km\,s^{-1}} \, (1+z)^{-3} \, \frac{D_L^2}{\rm Mpc^2} \, \frac{\rm GHz^2}{\nu_{\rm obs}^2}. \qquad (2.4)$$

The main advantage of the latter definition, which only differs by a factor of ν_r^3, comes from canceling out the prefactor in Planck's formula. Therefore, lines coming from energy levels which are thermally populated (i.e., follow a Boltzmann distribution) are expected to produce the same $L'_{\rm line}$ line luminosity. Since thermal population is generally an upper limit on the population obtained from collisional excitation (barring optical depth effects and pumping from other energy levels) CO rotational lines generally show a non-increasing $L'_{\rm line}$ line luminosity as a function of J-level.

2.2.2 The CO conversion factor

The standard methodology to use CO(1–0) luminosity measurements to measure integrated gas masses simply posits an approximate direct proportionality between the two, $M_{\rm gas} = \alpha_{\rm CO}\, L'_{\rm CO}$. The justification for this is somewhat complicated and is primarily inspired by empirical practice: within the regimes where it has been tested so far, this appears to hold with moderate, mainly systematic

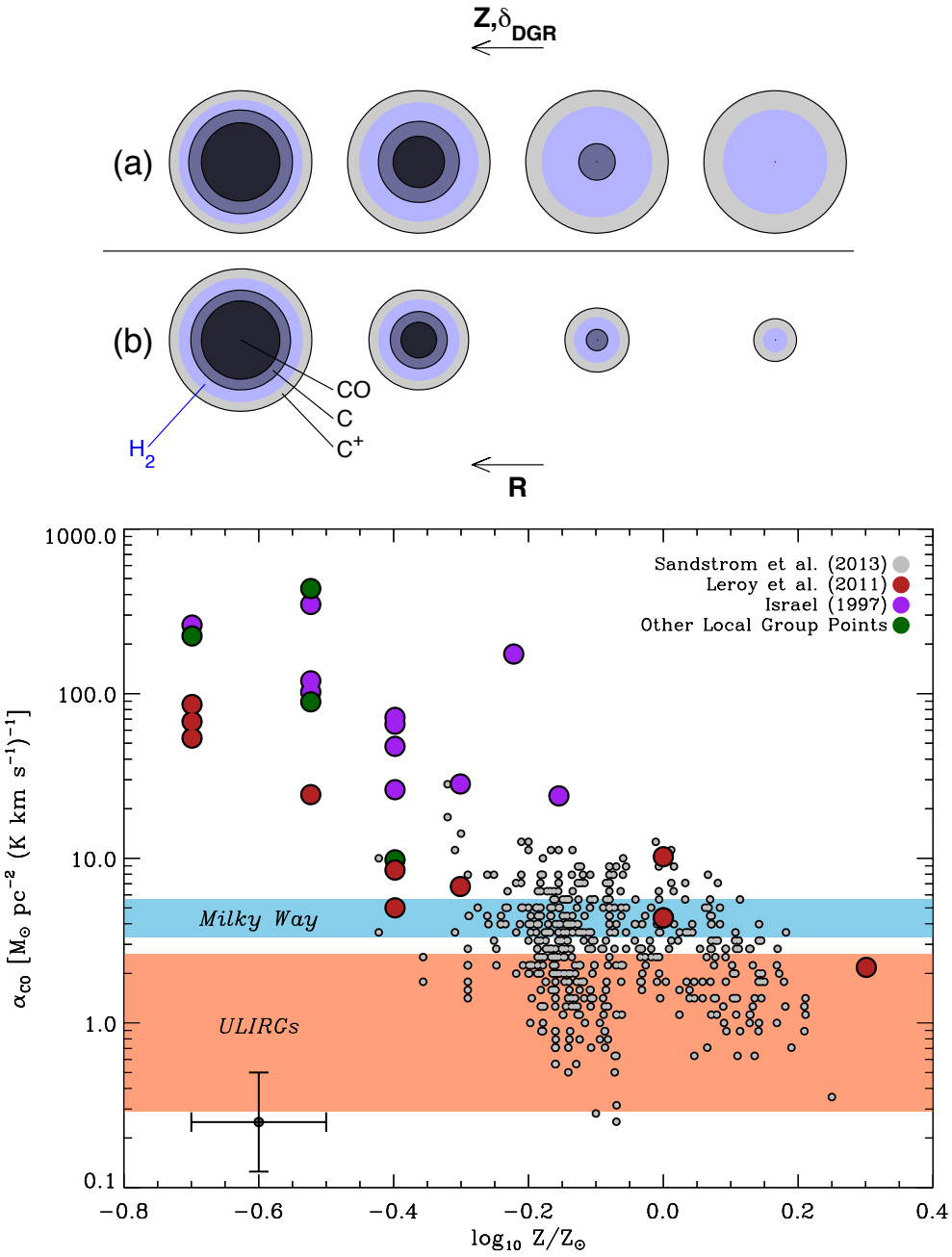

Figure 2.3: Metallicity strongly affects the α_{CO} conversion factor due to the progressive shrinking of the CO-emitting region relative to the molecular hydrogen region, with decreasing metallicity due to reduced dust shielding from the FUV field. The dependence of α_{CO} on metallicity appears to be very steep in local galaxies, and can make CO difficult to observe in high redshift galaxies, if their ISM is increasingly dust or metal-poor. Figures from Bolatto et al. (2013).

and understandable, variations (Figure 2.2). In particular within the Milky Way molecular clouds the $\alpha_{\rm CO}$ mass-to-light ratio appears to be approximately constant and multiple independent constraints deriving from dynamical estimates, gamma rays and dust emission suggest a value of $\sim 4.3\,M_\odot\,(\mathrm{K\,km\,s^{-1}pc^2})^{-1}$ (Bolatto et al., 2013). We here note that the emission from CO(1–0) is consistently optically thick except along very low column density lines of sight, and therefore the velocity dispersion plays an important role in determining the line luminosity. The theoretical justification for an approximately constant $\alpha_{\rm CO}$ comes from noticing that the line specific flux emitted by the $\tau \sim 1$ cloud surface is approximately set by the excitation temperature which is approximately the gas kinetic temperature, and does not vary substantially in different cold gas clouds in the Milky Way and local galaxies. Then virial equilibrium for molecular gas clouds implies that $M_{\rm vir} \propto R\sigma^2$ and supersonic turbulence implies $R \propto \sigma^2$. Together, these approximate relations imply that the integrated line luminosity from a virialized cloud is approximately proportional to its virial mass. Then we assume that the CO line emission from a galaxy is just the additive superposition of the emission from individual "clouds" (neglecting overlapping lines of sight) and therefore the total luminosity provides a measure of the total gas mass. The result is mostly a cloud-counting measure, weighted by an estimate of individual cloud masses (Bolatto et al., 2013). As this argument shows, the $\alpha_{\rm CO}$ ratio is expected to show some dependence on the gas physical conditions such as temperature, density and dynamical state. In particular, local ultraluminous infrared galaxies (ULIRGs), which are extreme galaxies in the local Universe characterized by very compact starburst regions, appear to show a lower $\alpha_{\rm CO} \sim 0.8\,M_\odot\,(\mathrm{K\,km\,s^{-1}pc^2})^{-1}$, potentially due to the lack of virialization and the dominant external potential felt by the compact molecular zones set

by a stellar component (Bolatto et al., 2013). Furthermore, we have so far assumed that molecular gas is always accompanied by CO emission but this is strongly violated in practice. The formation of CO molecules is quite independent from the formation of H_2 molecules and, in particular, is strongly dependent on the abundance of dust for shielding against a dissociating FUV field. Indeed, dust deficient molecular environments commonly observed in metal-poor dwarf galaxies show a lack of CO molecules, requiring a rapidly increasing column density of molecular gas in order to allow CO formation and therefore strongly increasing the necessary $\alpha_{\rm CO}$ factor (e.g., Bolatto et al. 2013; Figure 2.3). Nonetheless, converting observed CO luminosity to molecular gas masses assuming an approximately constant factor appears to work well, in practice, over a wide range of environments (e.g., Bolatto et al. 2013).

2.3 Far-IR fine-structure lines

Although CO lines are excellent tracers of the molecular medium, ALMA is also sensitive to the bright atomic FIR fine-structure lines, which are predominantly tracers of the ionized and atomic medium (Figure 2.4). The commonly observed FIR lines are emitted by carbon, (C) nitrogen (N) and oxygen (O), the most abundant metals in the ISM with abundances of ~ 3, ~ 1 and $\sim 6 \times 10^{-4}$ relative to hydrogen, respectively (Stacey, 2011). The ground state energy level of these atoms and their ions are split by the spin-orbit coupling perturbation, producing multiplets of two levels for atoms/ions with one or five valence electron in the outer p orbital and of three levels for atoms/ions with two or four valence electrons. Among these elements, the O, O^{++}, C, C^{+}, N^{+} and N^{++} ionizations states have ground term split into fine-structure levels that emit photons in the FIR

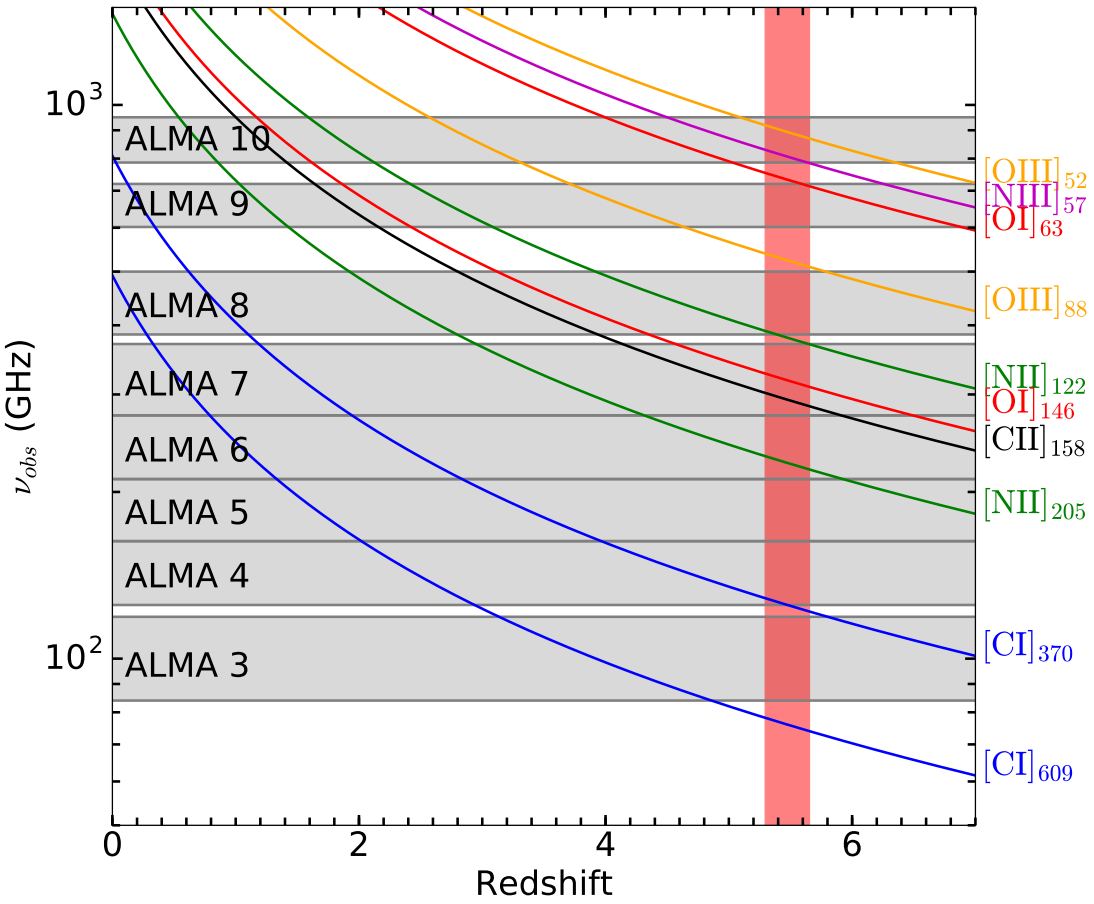

Figure 2.4: Redshift coverage of all ALMA bands for the most common FIR fine-structure lines. The red band shows the redshift range of interest $z \sim 5-6$, targeted by our studies.

range (Stacey, 2011). Since their wavelength is larger than the typical dust grain size, these photons are largely unaffected by dust absorption, in contrast to their optical counterparts (except in the depths of starburst/ULIRG nuclei). These fine-structure lines are forbidden by electric dipole selection rules (no change in the electronic configuration) and therefore decay by magnetic dipole transitions, with much longer decay rates. Therefore, they are generally optically thin due to the small spontaneous emission rates and hence are only weakly affected by

self-absorption. Furthermore, the energy levels emitting these lines lie within a few hundred Kelvin of the ground state, so that they are easily collisionally excited by electrons, hydrogen atoms and molecules. These properties make these FIR fine-structure lines particularly luminous, and often are the main coolants of several gas phases of the ISM, making them excellent probes of the physical conditions of the gas and tracers of the energy sources (e.g., radiation field from nearby stars, AGN, cosmic rays, X-rays or interstellar shocks).

2.4 Brief overview of fine-structure lines as ISM probes

The ionization energy of the hydrogen atom is 13.6 eV, so species requiring more than 13.6 eV photons to form will be found exclusively within HII regions (O^{++}, N^{+}, N^{++}), while those with ionization energy less than 13.6 eV (O, C) will be found exclusively in neutral (hydrogen) gas clouds. The first ionization energy of carbon is only 11.3 eV and the second ionization is 24.4 eV so that the C^{+} ion is found in both neutral and ionized hydrogen gas (Stacey, 2011).

2.4.1 Ionized gas lines

Fine-structure lines provide one of the best density probes of the ionized ISM. In particular, the [NII][2] line pair (at 205μm and 122 μm) has only slightly different excitation energies, but different de-excitation rates giving the two transitions a different critical density (48 and 310 cm^{-3}, respectively). Therefore, in the den-

[2]While ions are indicated by superscripts (e.g., N^{+}), emission lines from such ions are typically indicated using a roman numeral notation, with I indicating neutral species and subsequent numbers referring to higher, positive ionization states (e.g., [NII]).

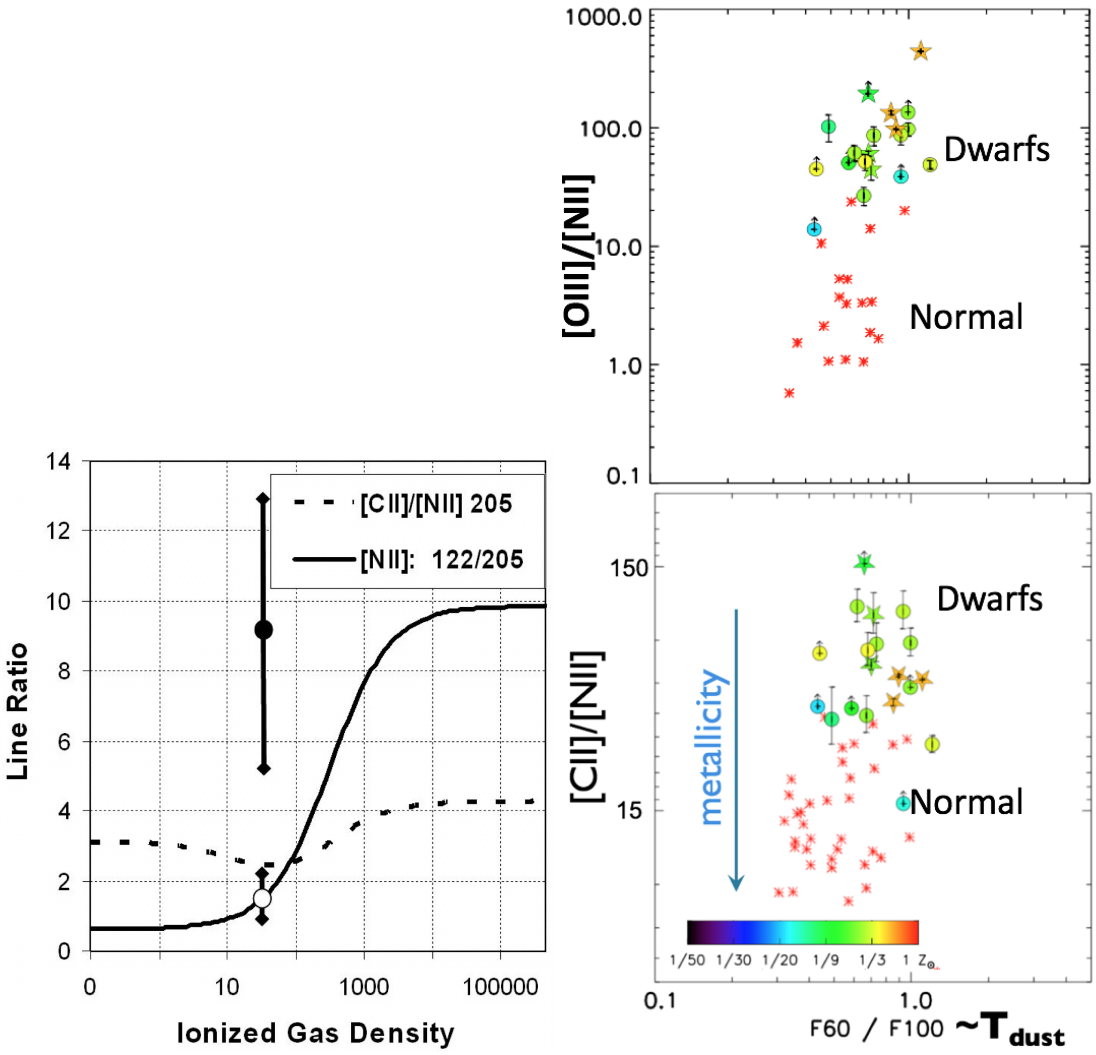

Figure 2.5: Left: Ionized gas density dependence of the ratios of [NII] 205μm, 122μm and [CII] lines. While the ratio of the two [NII] lines is an excellent probe of gas density, the [CII]/[NII] 205μm ratio which we have studied in a sample of galaxies at $z > 5$, is insensitive to density making it an accurate tracer of the fraction of [CII] coming from ionized rather than neutral phase. Right: Local dwarf galaxies show a significant offset in the [CII]/[NII] line ratio, relative to local "normal" galaxies, due to low-metallicity. Figure adapted from (Cormier et al., 2015). The fainter [NII] emission is the result of higher intensity and hardness of the radiation field (resulting from the lower metallicity), as evidenced by the brighter [OIII] observed in dwarfs. Therefore, most of the nitrogen in the ionized gas may be in the higher ionization state of N^{++}, rather than N^{+}. Figures from Oberst et al. (2006); Cormier et al. (2015).

sity regime between these critical densities the lower transition is thermalized (hence density insensitive) while the upper transition excitation keeps increasing with density toward thermalization making the line ratio an accurate probe of ionized gas density (Figure 2.5). For the lines arising from ionized gas, the level excitation potentials are much less than the ionized gas temperature ($\sim 10^4$ K) so that level excitation is insensitive to gas temperature. The ionized gas lines are also probes of the intensity and hardness of the radiation field, which may be produced by AGN or by stars of different surface effective temperature. The most massive main-sequence stars have the highest surface temperatures, so they dominate the interstellar UV field. While it takes 14.5 eV to form N^+, produced by a stellar surface temperature of $\sim 33,000$ K, the further ionization to N^{++} requires 29.6 eV photons, only produced by $\sim 39,000$ K stellar photosphere and O^{++} requires 35 eV photons to form (Stacey, 2011). Therefore the [NIII]/[NII] line ratio is indicative of hardness and intensity of the radiation field.

2.4.2 Neutral gas lines

Moving away from the sources of ionizing radiation the gas transitions from being almost completely ionized (the HII region) to almost completely neutral, and the neutral region near this edge is referred to as a photo-dissociation or photon-dominated region (PDR; e.g., Tielens & Hollenbach 1985). Beyond this atomic phase, where the physical and chemical processes are dominated by the intense FUV field ($6 < h\nu < 13.6$ eV), the gas may transition to a higher density, colder phase which allows for the formation of molecular hydrogen. The majority of the fine-structure emission from the PDR is coming from the warmer

regions closer to the radiation source, given by the depth to which photons can penetrate and ionize carbon forming C^+. This depth is typically determined by extinction of FUV photons by dust, implying that dust-poor conditions lead to larger C^+ regions and smaller neutral C and CO regions beyond that, as we saw in previous sections. Within the PDR gas heating is provided by the photoelectric ejection of electrons from dust grains. The heating efficiency is affected by grain charge, which is itself controlled by hydrogen gas density and the intensity of the FUV field, and ranges in the 0.1 to 1%. The rest of the FUV energy deposited goes to heating the dust. The primary coolant within the PDR is provided by the collisional excitation and emission in the [CII] line at 158 μm and [OI] at 63 and 146 μm. The CO line emission, especially in the mid to high-J levels is also an important coolant and becomes the dominant coolant further into the molecular cloud. Since [CII] may often be considered the primary coolant of the gas in the PDR and the FIR continuum emission is often predominantly emitted in the same regions, the [CII]/FIR luminosity ratio measures the gas heating efficiency which is itself a probe of the FUV intensity in the PDR (e.g., Hollenbach & Tielens 1997).

Both the [CII] line emission, and a fraction of the FIR dust emission also receive contributions from the ionized regions. In order to diagnose this contribution to the [CII] emission from the ionized gas, the [NII] 205 μm provides an ideal tool. Indeed, the [NII] 205 μm transition has similar critical density for excitation by electrons as [CII] and has comparable further ionization potential making the two ions located within the same region of HII gas. Hence, the [CII]/[NII] line ratio from ionized gas is only a function of the assumed C/N abundance ratio and may be used to measure the fraction of [CII] coming from ionized rather than neutral gas (e.g., Oberst et al. 2006; Figure 2.5). In this thesis

we have used such line ratio to probe, for the first time, the physical state of the ionized and neutral gas in "normal" galaxies at $z > 5$, in the first billion years of cosmic time.

2.5 The tools of the trade: the VLA and ALMA

There are few telescopes which are sensitive enough, or have the frequency coverage necessary to observe the molecular CO lines and the FIR fine-structure lines from the "normal" galaxies at high redshift which are the subject of this thesis. The currently existing facilities are divided into two main categories: (sub-)millimeter telescopes typically observing mid-J CO lines and FIR fine-structure lines at high redshift (typically in bands at 850 μm, 1, 2 and 3 mm), and radio telescopes operating at the centimeter wavelengths which are capable of observing low-J CO lines at high-z. Currently, only interferometers have the necessary collecting area required to achieve the sensitivity to observe emission from "normal" galaxies at $z > 1$. In addition, single dish telescopes suffer from spectral baseline instability implying that the zero-flux level needs to be subtracted out over time and so cannot measure faint signals with high reliability. In contrast, interferometers are blind to such baseline instability because the gain fluctuations across different receivers are independent and therefore average out from the signal correlation, which is the key observable. Furthermore, interferometers naturally provide the higher resolution (thanks to longer baselines) which is necessary to measure emission region sizes form high redshift galaxies and sometimes allows resolving the emitting structure over a few resolution elements (synthesized beams), providing important kinematic information for the emitting gas. This kinematic information is important because

Figure 2.6: The current thesis research has made use of the two most sensitive radio and (sub)millimeter interferometers on Earth: the Very Large Array (VLA) and the Atacama Large (sub)Millimeter Array (ALMA) shown here. Image credit National Radio Astronomy Observatory (NRAO).

the gas dynamics probe the gravitational potential of galaxies. While the spectral information is directly measured by the interferometer or single-dish using a heterodyne detection system, the spatial information provided by the interferometer is contained in the signal differences measured by different telescope pairs as a function of the pairwise separation vector (baseline; separation between telescopes for each possible pair). The reason why the antenna separation introduces differences in the cross-correlation of the measured signal comes from the angular dependence of the phase delay between the two antennas. This is, in basic terms, the mechanism at the root of the ability of an interferometer to infer spatial information on the emission from the sky. Since the inferred spatial emission distribution is obtained through a Fourier transform of the signal as a function of baseline vector components, the long baselines measure the high spatial frequency content of the sky emission while short baselines measure the low spatial frequency modes of the emission (Figure 2.7).

The interferometers utilized in this thesis are NSF's Karl G. Jansky Very Large Array (VLA) in New Mexico, USA for the low-frequency, radio measurements and the Atacama Large (sub)Millimeter Array (ALMA) in Chile for the high-frequency (sub-)millimeter wavelength observations. The only additional observatory reaching sufficient sensitivity to allow such studies is the NOrthern Extended Millimeter Array (NOEMA) at the Plateau de Bure in the French Alps. Although we did not utilize data from this third observatory in the current thesis, additional follow-up studies are underway taking advantage of its unique capabilities (very wide bandwidth, allowing simultaneous coverage of multiple lines).

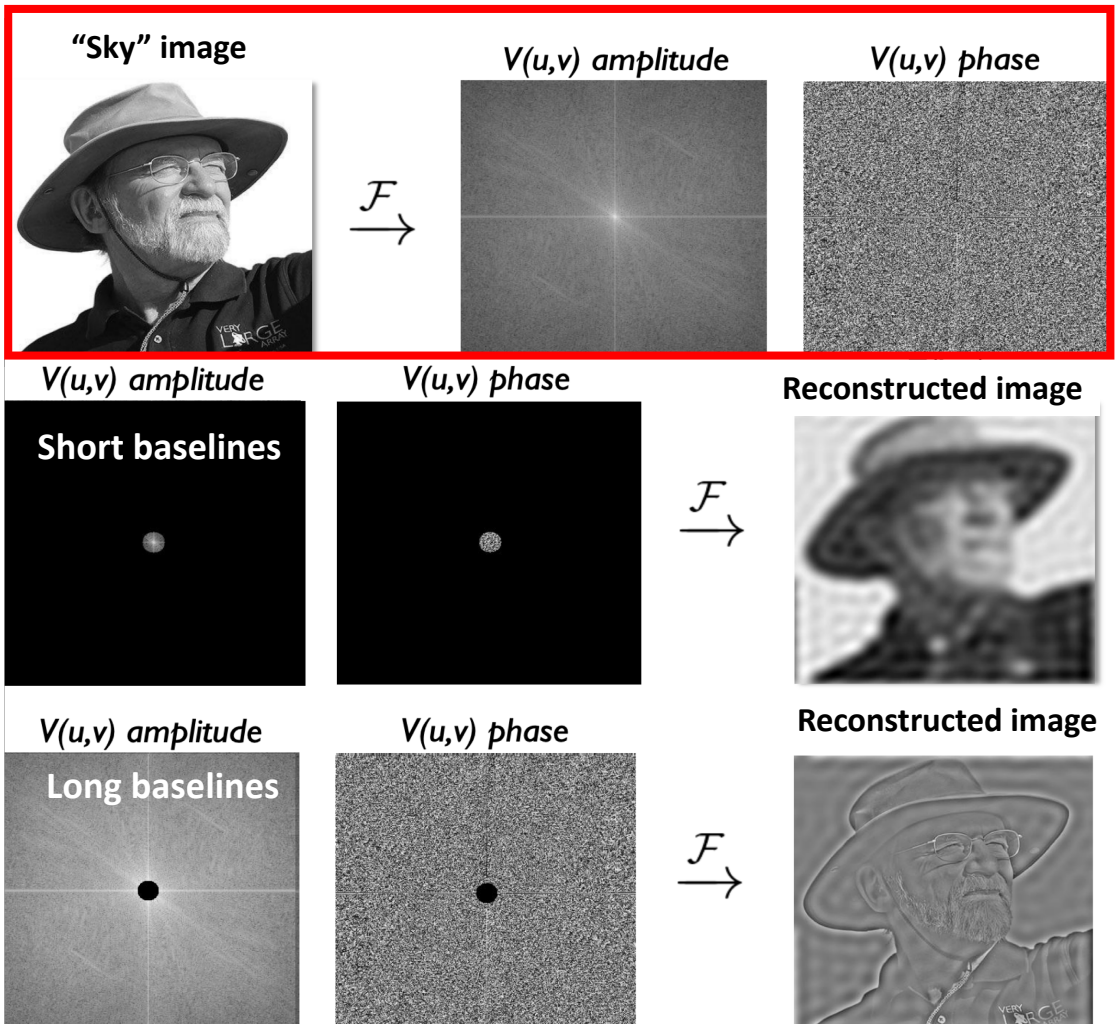

Figure 2.7: Although the 2D Fourier transform of an image (e.g., sky emission) contains the full information content of the image, an interferometer only measures a the emission over a subset of all possible baselines, therefore limiting the spatial features which can be reconstructed. This example illustrates how short baselines (near the origin) contain information on the large-scale emission structure (essentially a smoothed version). On the other hand, the long baselines are only sensitive to the edges, the sharp features, therefore missing larger scale structures completely. Image credit D. Wilner.

2.6 Bayesian modeling. An application to interferometric data

In multiple parts of this thesis we have applied Bayesian approaches to the statistical analysis, and we here review the basics and terminology of such methods (e.g., Gregory 2010). In the Bayesian approach to data analysis, we aim to construct a probabilistic model approximating the data-generating process. We interpret probabilities for events as representing our uncertain state of knowledge. Therefore we calculate probability distributions of model parameters, which are interpreted as a quantification of the available information on the underlying processes. Although the underlying physical processes are themselves stochastic in nature, we often simplify our "physical model" by assuming a deterministic relationship between model parameters and some underlying objective state of nature of which we have imperfect observations. Therefore we often limit the stochastic approach to the second component of the data-generating process, the "measurement". All inference requires limiting the space of possible models under examination by making assumptions, and we will assume a parametric model in the following for simplicity. In this setting, Bayes' theorem helps us relate probabilistic outputs from our model to model constraints by conditioning on the observed data:

$$P(\theta|D) = \frac{P(D|\theta)\,P(\theta)}{\sum_\theta P(D|\theta)\,P(\theta)}, \tag{2.5}$$

where θ represents the set of parameters, D represents the observed data, $P(\theta|D)$ represents the probability of the specific parameter values corresponding to reality given the observed data (called the posterior probability), $P(D|\theta)$ represents the the output of the probabilistic model, i.e., the probability of observing such data, given the specific parameter value (called the likelihood of the parameters), $P(\theta)$ is the prior probability of the specific model parameters, i.e., the dis-

tribution reflecting our prior information and expectation on the values of the parameters before making the measurement. The sum in the denominator is just a normalization (corresponding to the overall probability of observing the data within the framework of the chosen model) and the sum runs over all allowed values of the parameters.

In this thesis work we have applied this framework several times, in different contexts, but we here discuss one specific application for illustration and for its wide applicability in future studies [3]. Interferometric data targeting spectral line emission such as [CII] from a high redshift galaxy naturally provides rich three dimensional information (two spatial dimensions in the plane of the sky and one spectral dimension corresponding to velocity along the line of sight) constraining the kinematics of the emitting gas. This gas emission is often widespread across a significant fraction of the galaxy extent and probes the total gravitational potential, providing information on the total matter content in galaxies (dark matter, stellar and gas content). In order to infer probabilistic estimates of dynamical quantities such as a rotation curve we have developed a technique to model such observations in generality within a Bayesian framework. We have used existing tools such as `KinMS` (Davis et al., 2013) to model optically thin emission from a rotating disk (including gas dispersion and arbitrary brightness profiles and rotation curves) together with possible unresolved (point-source) emission and continuum emission with elliptical Gaussian spatial profiles. We have then used different existing tools such as utility functions from `UVMCMCFIT` (Bussmann et al., 2016) or the optimized code `Galario` (Tazzari et al., 2018) to derive the expected visibilities (i.e., the measurements of the interferometer) for a given model if observed in the same conditions as our

[3]The code for our implementation of this method is freely available online at https://github.com/pavesiriccardo/UVmodeldisk

data (essentially a Fourier transform relationship). By assuming a Normal distribution of the observed visibilities with empirically determined noise we may then compute the likelihood of any model parameters by calculating the "χ^2" value. We have used two different approaches to use such likelihood estimates to derive posterior samples which describe the inferred probability distribution for the model parameters. The first model is based on Markov Chain Monte Carlo (MCMC) sampling making use of the popular package `emcee` (Foreman-Mackey et al., 2013), while the second approach is based on Nested Sampling making use of `Multinest` (Feroz et al., 2009). The latter approach was usually preferable because it does not require initialization choices (it is sometimes difficult to determine if MCMC chains have converged or are still affected by the starting point), it has automatic criteria to determine convergence within a prescribed accuracy, appears to require comparable computing time and guarantees that the full parameter space specified by the prior will be explored allowing for multiple maxima of the posterior.

CHAPTER 3

THE CO LUMINOSITY DENSITY AT HIGH-Z (COLDZ): SURVEY DESCRIPTION AND ANALYSIS

3.1 Context

As shown in the previous chapters, in order to advance our understanding of the cosmic history of galaxy assembly through star formation we need a better characterization of the cosmic history of gas in galaxies, because cold gas directly fuels star formation. To achieve a census of molecular gas in galaxies at the "cosmic noon", the epoch of fastest galaxy assembly, targeted studies are not sufficient because they may not sample the distribution of gas masses uniformly. Blind searches are therefore needed, directly selecting galaxies based on their cold, molecular gas mass and potentially finding galaxies with larger gas masses than expected based on their star formation activity or stellar mass. CO(1–0) line emission is the best tracer of molecular gas mass, and has been calibrated in local galaxies and at high redshift achieving a substantial degree of consistency (e.g., Carilli & Walter 2013). In this chapter, we describe the first CO(1–0) deep field blind search at high redshit, covering the redshift range $z = 2 - 2.8$, carried out with the Very Large Array (VLA). This survey was made possible by the VLA upgrade completed in ~2012–2013, which added sensitive new Ka band receivers covering our frequency range of interest (30–39 GHz), greatly upgraded the correlator enabling much wider bandwidth and improved sensitivity, making this search possible by simultaneously observing the full 8 GHz covering the full redshift range. In this chapter we describe the survey observations, the data calibration and imaging, the line search algorithms, the

results of the blind CO line search, the CO line candidate properties and the analysis of the results from stacking our measurements at previously known galaxy positions.

This chapter was previously published in the *Astrophysical Journal* as: Pavesi, R., et al., 2018, ApJ, 864, 49 in collaboration with Chelsea Sharon, Dominik Riechers, Jacqueline Hodge, Roberto Decarli, Fabian Walter, Chris Carilli, Emanuele Daddi, Ian Smail, Mark Dickinson, Rob Ivison, Mark Sargent, Elisabete da Cunha, Manuel Aravena, Jeremy Darling, Vernesa Smolčić, Nick Scoville, Peter Capak and Jeff Wagg.

3.2 Abstract

We describe the CO Luminosity Density at High-z (COLDz) survey, the first spectral line deep field targeting CO(1–0) emission from galaxies at $z = 1.95 - 2.85$ and CO(2–1) at $z = 4.91 - 6.70$. The main goal of COLDz is to constrain the cosmic density of molecular gas at the peak epoch of cosmic star formation. By targeting both a wide (~51 arcmin^2) and a deep area (~9 arcmin^2), the survey is designed to robustly constrain the bright end and the characteristic luminosity of the CO(1–0) luminosity function. An extensive analysis of the reliability of our line candidates, and new techniques provide detailed completeness and statistical corrections as necessary to determine the best constraints to date on the CO luminosity function. Our blind search for CO(1–0) uniformly selects starbursts and massive Main Sequence galaxies based on their cold molecular gas masses. Our search also detects CO(2–1) line emission from optically dark, dusty star-forming galaxies at $z > 5$. We find a range of spatial sizes for the

CO-traced gas reservoirs up to $\sim$ 40 kpc, suggesting that spatially extended cold molecular gas reservoirs may be common in massive, gas-rich galaxies at $z \sim 2$. Through CO line stacking, we constrain the gas mass fraction in previously known typical star-forming galaxies at z = 2–3. The stacked CO detection suggests lower molecular gas mass fractions than expected for massive Main Sequence galaxies by a factor of $\sim 3-6$. We find total CO line brightness at $\sim$ 34 GHz of $0.45 \pm 0.2\,\mu$K, which constrains future line intensity mapping and CMB experiments.

3.3 Introduction

Although the process of galaxy assembly through star formation is believed to have reached a peak rate at redshifts of z = 2–3 (i.e., ~10–11 billion years ago), the fundamental driver of this evolution is still uncertain (Madau & Dickinson, 2014). In order to understand the physical origin of the cosmic star formation history (i.e., the rate of star formation taking place per unit comoving volume), we need to quantify the mass of cold, dense gas in galaxies as a function of cosmic time, because this gas phase controls star formation (Kennicutt & Evans, 2012). In particular, the evolution of the cold gas mass distribution can provide strong constraints on models of galaxy formation by simultaneously measuring the gas availability and, through a comparison to the star formation distribution function, the global efficiency of the star formation process (see Carilli & Walter 2013 for a review). In this work, we carry out the first fully "blind" deep-field spectral line search for CO(1–0) line emission, arguably the best tracer of the total molecular gas mass at the peak epoch of cosmic star formation, by taking advantage of the greatly improved capabilities of NSF's Karl G. Jansky Very

Large Array (VLA).

To date, observations of the immediate fuel for star formation, i.e., the cold molecular gas, have mostly been limited to follow-up studies of galaxies that were pre-selected from optical/near-infrared (NIR) deep surveys (and hence based on stellar light) or selected in the sub-millimeter based on dust-obscured star formation as sub-millimeter galaxies (SMGs; for reviews see, e.g., Blain et al. 2002b; Casey et al. 2014b). In particular, optical/NIR color-selection techniques (e.g., "BzK", "BM/BX"; Daddi et al. 2004; Steidel et al. 2004) have explored significant samples of massive, star forming galaxies at z ~1.5 to 2.5 (Daddi et al., 2008, 2010a; Tacconi et al., 2010, 2013) and the sub-mm selection has been particularly effective in identifying the most highly star-forming galaxies at this epoch for CO follow-up (e.g., Bothwell et al. 2013). Although such targeted CO studies are fundamental to explore the properties of known galaxy populations, they need to be complemented by blind CO surveys that do not pre-select their targets, which may potentially reveal gas-dominated and/or systems with uncharacteristically low star formation rate missed by other selection techniques.

Targeted CO studies have found more massive gas reservoirs at $z \sim 2$ compared to local galaxies. Cold molecular gas is therefore believed to be the main driver for the high star formation rates of normal galaxies at these redshifts (e.g., Greve et al. 2005; Daddi et al. 2008, 2010a,b; Tacconi et al. 2010; Genzel et al. 2010; Bothwell et al. 2013). Recent studies have claimed tentative evidence for an elevated star formation efficiency, i.e., star formation rate generated per unit mass of molecular gas, at $z \sim 2$ compared to local galaxies (e.g., Genzel et al., 2015; Scoville et al., 2016; Schinnerer et al., 2016; Scoville et al., 2017a; Tacconi et al., 2018). Such an elevated star formation efficiency could be related to massive,

gravitationally unstable gas reservoirs. The interstellar gas content of galaxies therefore appears to be the main driver of the star formation history of the Universe, during the epoch when galaxies formed at least half of their stellar mass content (e.g., Madau & Dickinson 2014). Although targeted molecular gas studies currently allow to observe larger galaxy samples more efficiently than blind searches, their pre-selection could potentially introduce an unknown systematic bias. Critically, such studies may not uniformly sample the galaxy cold molecular gas mass function. The best way to address such potential biases, and thus, to complement targeted studies, is through deep field blind surveys, in which galaxies are directly selected based on their cold gas content. Although some targeted CO(1–0) deep studies have previously been attempted (most notably Aravena et al. 2012 and Rudnick et al. 2017), these studies have typically targeted overdense (proto-)cluster environments. Hence, a blind search approach, to sample a representative cosmic volume is needed, in order to assess the statistical significance of such previous studies.

CO(1–0) line emission is one of the most direct tracers of the cold, molecular inter-stellar medium (ISM) in galaxies[1]. Its line luminosity can be used to estimate the cold molecular gas mass by means of a conversion factor ($\alpha_{\rm CO}$; see Bolatto et al. 2013 for a review). Although other tracers of the cold ISM have been utilized to date, including mid-J CO lines and the dust continuum emission, these are less direct tracers because they require additional, uncertain conversion factors (e.g., CO excitation corrections and dust-to-gas ratios). Specifically, while the ground state CO(1–0) transition traces the bulk gas reservoir, mid-J CO lines such as CO(3–2) and higher-J lines are likely to preferentially trace the fraction of actively star-forming gas. Hence, their brightness requires addi-

[1]In this work, CO always refers to the most abundant isotopologue ^{12}CO

tional assumptions about line excitation, in order to provide a measurement of the total gas mass. Furthermore, different populations of galaxies may be characterized by significantly different CO excitation conditions (e.g., BzK, SMGs and quasar hosts; Daddi et al. 2010b; Riechers et al. 2006a, 2011a,b; Ivison et al. 2011; Bothwell et al. 2013; Carilli & Walter 2013; Narayanan & Krumholz 2014), which also show considerable individual scatter (e.g., Sharon et al. 2016).

Long-wavelength dust continuum emission has been suggested to be a measure of the total gas mass, and is utilized to great extent in recent surveys with ALMA to investigate large samples of far-infrared (FIR)-selected galaxies (Eales et al., 2012; Bourne et al., 2013; Groves et al., 2015; Scoville et al., 2016, 2017a; Decarli et al., 2016a). Nonetheless, there remain substantial uncertainties in the accuracy of the calibration for this method at high redshift especially below the most luminous, most massive sources.[2] Another caveat to using FIR continuum emission instead of CO comes from the finding that the dust emission measured by ALMA may not always trace the bulk of the gas distribution. This is made clear by the small sizes of the dust-emitting regions compared to the star forming regions and the gas as traced by CO emission (e.g., Riechers et al. 2011c, 2014a; Ivison et al. 2011; Simpson et al. 2015; Hodge et al. 2016; Miettinen et al. 2017; Chen et al. 2017a).

Disentangling the causes for the observed increased star formation activity at $z \sim 2$ is not straightforward, since an increased availability of cold gas may be difficult to distinguish from increased star formation efficiency due to the uncertainty in deriving gas masses, for representative samples of galaxies.

[2]The dust continuum method to determine gas masses may be affected by the metallicity dependence of the dust-to-gas ratio (Sandstrom et al., 2013a; Berta et al., 2016), by trends in dust temperature with redshift (e.g., Magdis et al. 2012a), or with galaxy population (e.g., Faisst et al. 2017).

Now, thanks to the unprecedented sensitivity and bandwidth of the VLA and the Atacama Large (sub-)Millimeter Array (ALMA), CO deep field studies can be carried out efficiently, and these are ideal to address such potential selection effects. Previous deep field studies, with the Plateau de Bure Interferometer (PdBI; now the NOrthern Extended Millimeter Array, NOEMA) in the HDF-N (Decarli et al., 2014a; Walter et al., 2014) and ALMA in the HUDF (ALMA SPECtroscopic Survey in the Hubble Ultra-Deep Field Pilot or ASPECS-Pilot, Walter et al. 2016; Decarli et al. 2016a), have provided the first CO blind searches covering mid-J transitions such as CO(3–2)[3], which are accessible at millimeter wavelengths. These studies have yielded crucial constraints on the molecular gas mass function at $z \sim$ 1–3, subject to assumptions on the excitation of the CO line ladder to infer the corresponding molecular gas content.[4] They have found broad agreement with models of the CO luminosity evolution with redshift by finding an elevated molecular gas cosmic density at $z > 1$ in comparison to $z \sim 0$, but they may suggest a tension with luminosity function models at $z \gtrsim 1$ by finding a larger number of CO line candidates than expected (Decarli et al., 2016a).

In order to more statistically characterize the molecular gas mass function in galaxies at z = 2–3 and 5–7 than previously possible, while avoiding some of the previous selection biases, we have carried out the COLDz survey[5] a blind search for CO(1–0) and CO(2–1) line emission using the fully upgraded VLA[6].

[3]The ASPECS-Pilot survey simultaneously covered the CO(2–1) line in the redshift range z ~1.0–1.7, the CO(3–2) line at z ~2.0–3.1, and higher-J CO transitions at higher redshift.

[4]A key challenge in these studies is the uncertainty in assigning candidate emission lines to the correct CO transition, in cases where the redshift of the observed line candidates is not independently known.

[5]The COLDz survey data, together with complete candidate lists, and analysis routines may be found online at coldz.astro.cornell.edu.

[6]The recently expanded VLA, with its new Ka-band detectors, the new 3-bit samplers, the simultaneous 8 GHz bandwidth, and its improved sensitivity, for the first time, enables carrying out this survey study.

The main objective of this survey is to constrain the CO(1–0) luminosity function at $z = 2$–3, which provides the most direct census of the cold molecular gas at the peak epoch of cosmic star formation free from excitation bias, and based on a direct selection of the cold gas mass in galaxies. As such, the COLDz survey is highly complementary to millimeter-wave surveys like ASPECS and targeted studies. The CO(1–0) intensity mapping technique explored by Keating et al. (2015, 2016) is complementary to our approach. Intensity mapping offers sensitivity to the aggregate line emission signal from galaxies, but only measures the second raw moment of the luminosity function (therefore not distinguishing between the characteristic luminosity and volume density). While the intensity mapping technique allows to cover significantly larger areas of the sky, it does not directly measure gas properties of individual galaxies, and is therefore complementary to direct searches such as COLDz.

In a previous paper (Lentati et al. 2015; Paper 0) we have described a first, interesting example of the galaxies identified in this survey. In this work, we describe the survey, present the blind search line catalog, analyze the results of line stacking, and outline the statistical methods employed to characterize our sample. In the next chapter, we present the analysis of the CO luminosity functions and our constraints on the cold gas density of the Universe at $z = 2$–7 (Riechers et al., 2018).

In Section 4 of this chapter, we describe the VLA COLDz observations, the calibration procedure and the methods to mosaic and produce the signal-to-noise cubes. In Section 5, we describe our blind line search through Matched Filtering in 3D. In Section 6, we present our "secure" and "candidate" CO line detections in both the deeper (in COSMOS) and wider (in GOODS-N) fields. In

Table 3.1: COLDz Observations Summary.

Field	Pointing	D configuration	D→DnC configuration	DnC configuration	DnC→C configuration
Baseline range (m)		40–1000	40-2100	40–2100	40–3400
COSMOS	1–7	82 hr	—	11 hr	—
GOODS-N	1–7	13 hr	—	—	—
GOODS-N	6	—	—	3 hr	—
GOODS-N	8–14	15 hr	—	—	—
GOODS-N	15–21	15 hr	—	—	—
GOODS-N	22–28	14 hr	1.4 hr	—	—
GOODS-N	29–35	—	3 hr	12 hr	—
GOODS-N	36–42	—	—	11 hr	3 hr
GOODS-N	43–49	14 hr	—	1.3 hr	—
GOODS-N	50–56	10.5 hr	—	3.5 hr	—
GOODS-N	57	2 hr	—	—	—

Note: We list the total, on-source time in different array configurations, for all pointings in each group combined.

Section 7, we utilize stacking of galaxies with previously known spectroscopic redshifts, to provide strong constraints on their CO luminosity. In Section 8, we derive constraints to the total CO line brightness at ~34 GHz. In Section 9, we discuss the implications of our results in the context of previous surveys. We conclude with the implications for future surveys with current and planned instrumentation. In Appendix A, we describe a parallel search for formaldehyde absorption lines against the CMB carried out on the COLDz data. A more detailed characterization of the complete candidate sample is presented in Appendix B.

In this work we adopt a flat, ΛCDM cosmology with $H_0 = 70\,\mathrm{km\ s^{-1}\ Mpc^{-1}}$ and $\Omega_M = 0.3$ and a Chabrier IMF.

3.4 Observations

In order to constrain both the characteristic luminosity, $L^*_{\rm CO}$, or "knee" of the CO(1–0) luminosity function and the bright end, we have optimized our observing strategy following the "wedding cake" design, to cover a smaller deep area and a shallower, wide area. We have used the wide-band capabilities of the upgraded VLA to obtain a continuous coverage of 8 GHz in the Ka band (PI: Riechers, IDs 13A-398; 14A-214) in a region of the COSMOS field (centered on the dusty starburst AzTEC-3 at $z = 5.3$ as a line reference source, Capak et al. 2011; Riechers et al. 2014a) and in the GOODS-N/CANDELS-Deep field, in order to take advantage of the availability of excellent multi-wavelength data (Grogin et al., 2011; Koekemoer et al., 2011; Giavalisco et al., 2004).

The COSMOS data form a 7-pointing mosaic (center: R.A.=10h 0m 20.7s, Dec.=2°35'17") with continuous frequency coverage between 30.969 GHz and 39.033 GHz. The GOODS-N data form a 57-pointing mosaic (center: R.A.=12h 36m 59s, Dec.=62°13'43.5") with continuous coverage between 29.981 GHz and 38.001 GHz (Figs. 3.1,3.2). The total on-source time was approximately 93 hrs in the COSMOS field and 122 hrs in the GOODS-N field. The frequency range targeted in this project covers CO(1–0) at z = 1.95–2.85 and CO(2–1) at z = 4.91–6.70, such that the space density of CO(2–1) line emitters is expected to be smaller than for CO(1–0) (Fig. 3.1; e.g., Popping et al. 2014b, 2016). Both the large redshift spacing and the expected redshift evolution of the space density of CO emitters lessens the severity of the redshift ambiguity in our survey compared to previous studies.

At 34 GHz the VLA primary beam can be described as a circular Gaussian

with FWHM~80″, so our pointing centers were optimized to achieve a sensitivity that is approximately uniform in the central regions of the mosaics by choosing a spacing of 55″ (< 80″/ $\sqrt{2}$) in a standard hexagonally packed mosaic (Condon et al., 1998). During each observation, we targeted a set of 7 pointings in succession, alternating through phase calibration. We performed pointing scans at the beginning of each observation, with additional pointing observations throughout for observations longer than 2 hours. Most of the COSMOS and GOODS-N data were taken in the D configuration of the VLA. Some of the observations, especially for the GOODS-N pointings, were fully or partially carried out in DnC configuration, in re-configuration from D to DnC (D→DnC) and in re-configuration from DnC to C (DnC→C). Pointings are named sequentially from GN1 to GN57 (groups of GN1–7, GN8–14 etc. were observed together; Table 3.1).

The total area imaged, down to a sensitivity of ~ 30% of the peak, in COSMOS is 8.9 arcmin^2 at 31 GHz and 7.0 arcmin^2 at 39 GHz. In GOODS-N the total area is 50.9 arcmin^2 at 30 GHz and 46.4 arcmin^2 at 38 GHz. The correlator was set-up in 3-bit mode, at 2 MHz spectral resolution (corresponding to ~ 18 km s^{-1} at 34 GHz), to simultaneously cover the full 8 GHz bandwidth for each polarization (Fig. 3.1). Tuning frequency shifts between tracks, and sometimes in the same track, were used to mitigate the edge channels noise increase in order to achieve a uniform depth across the frequency range (Table 2).

3.4.1 COSMOS observations

The dataset in the COSMOS field consists of 46 dynamically scheduled observations between 2013 January 26 and 2013 May 14, each about 3 hours in duration. Flux calibration was performed with reference to 3C286, and J1041+0610 was observed for phase and amplitude calibration. Three frequency tunings offset in steps of 12 MHz were adopted to cover the gaps between spectral windows and to obtain uninterrupted bandwidth.

3.4.2 GOODS-N observations

The GOODS-N dataset consists of 90 observations between 2013 January 27 and 2014 September 27, each about 2 hours in duration. Pointing 6, which covers the 3 mm PdBI pointing of the CO deep field in Decarli et al. (2014a) in the HDF-N, was observed both as part of the 1–7 pointing set, and in two additional, targeted observations to achieve better sensitivity. Pointing GN57 was observed for 3 hours (127 min on source) in D-array configuration on 18 December 2015, in order to follow up the most significant negative line feature in GN1–56 (see Appendix A for details). J1302+5748 was used for phase calibration, and the flux was calibrated by observing either 3C286 (in 7 observations) or in reference to the phase calibrator (in the remaining observations). An average phase calibrator flux at 34 GHz of S=0.343 Jy and spectral index of −0.2 was assumed in the observations in 2013 and S=0.21 Jy and spectral index of −0.6 was assumed in 2014, as regularly measured in the tracks where a primary flux calibrator was observed. Based on track-to-track variations of the calibrator flux, we estimate a ∼20% total flux calibration uncertainty. The spectral setup employed uses two

Table 3.2: Lines, Redshift Ranges and Volumes Covered by COLDz.

Transition	ν_0 [GHz]	z_{min}	z_{max}	$\langle z \rangle$	Volume [Mpc^3]
		COSMOS			
CO(1–0)	115.271	1.953	2.723	2.354	20,189
CO(2–1)	230.538	4.906	6.445	5.684	30,398
		GOODS-N			
CO(1–0)	115.271	2.032	2.847	2.443	131,042
CO(2–1)	230.538	5.064	6.695	5.861	193,286

Notes: The comoving volume is calculated to the edges of the mosaic, and does not account for varying sensitivity across the mosaic, which is accounted for by the subsequent completeness correction. The average redshift is cosmic volume weighted.

dithered sets of spectral windows, with a relative shift of 16 MHz, in order to fully cover the 8 GHz bandwidth available without gaps.

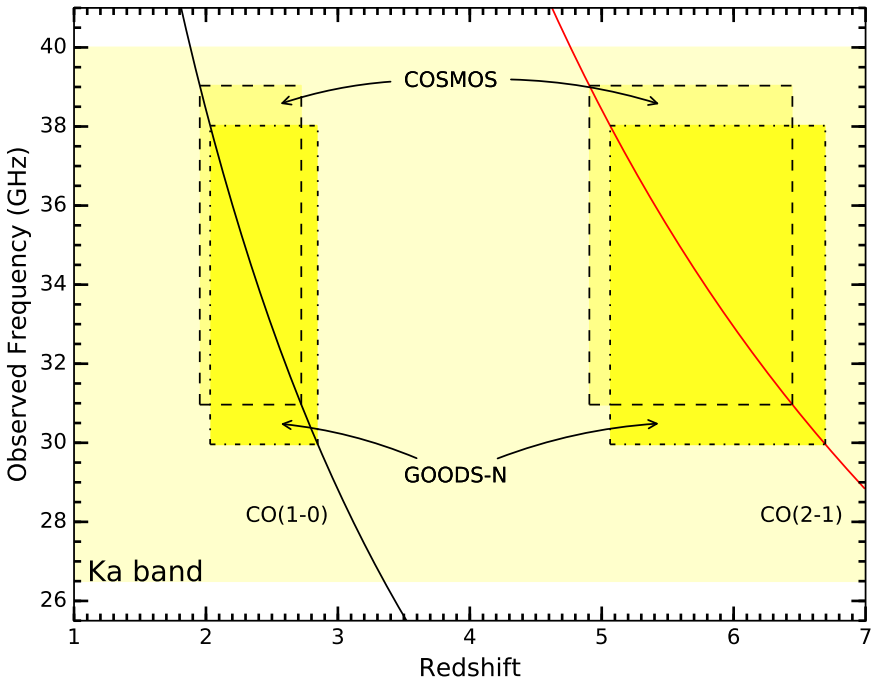

Figure 3.1: Frequency coverage of the VLA COLDz survey, in the Ka band. The frequency range covers CO(1–0) at z = 1.95–2.85, and CO(2–1) at z=4.91–6.70.

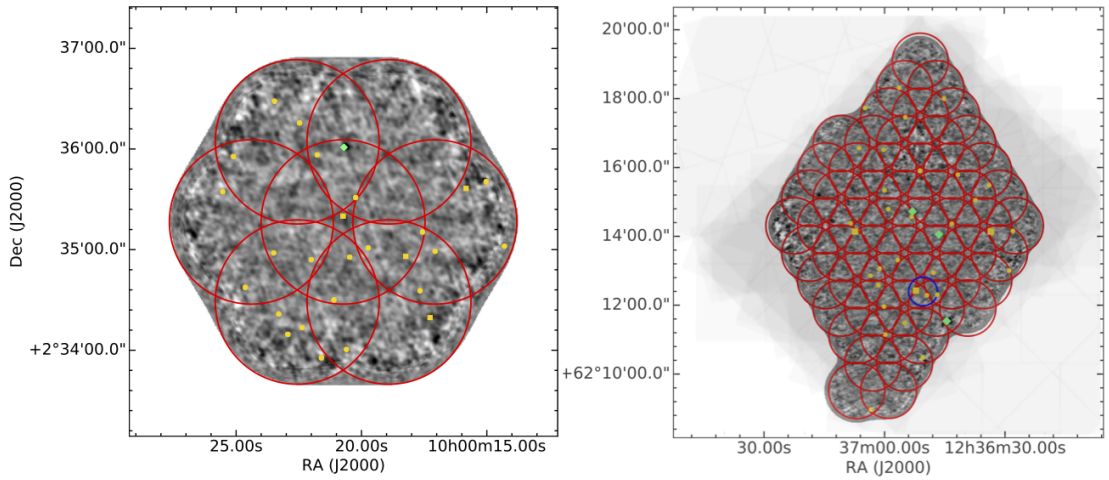

Figure 3.2: CO deep field regions covered by COLDz in the COSMOS (left) and GOODS-N/CANDELS fields (right). The mosaics are composed of 7 and 57 pointings, respectively (as shown by the red circles). The grayscale corresponds to the frequency-averaged signal data cube. The positions of our line candidates from Tables 3.4 and B.1 are marked by yellow squares and circles, respectively. Green markers indicate the position of the most significant ~ 34 GHz continuum sources. The field covered by the blind search from Decarli et al. (2014a) is shown by a blue circle. We covered the majority of the CANDELS-Deep footprint in GOODS-N, shown as the background grayscale the *HST*/WFC3 F160W exposure map (Grogin et al., 2011) for comparison.

3.4.3 Data Processing

Data calibration was performed in CASA version 4.1, using the VLA data reduction pipeline (v.1.2.0). CASA version 4.5 was used to re-calculate visibility weights using the improved version of `statwt` that excludes flagged channels when calculating weights, and for imaging and mosaicking (McMullin et al., 2007). The pipeline radio-frequency interference (RFI) flagging, which uses CASA `rflag` to identify transient lines, was switched off, as recommended by the developers, since it can potentially remove narrow spectral lines and because there is little RFI in the Ka-band (with the exception of the 31.487–31.489 GHz range, which we flag prior to running the CASA pipeline). The pipeline was further modified to only flag the first and last channel of each spectral win-

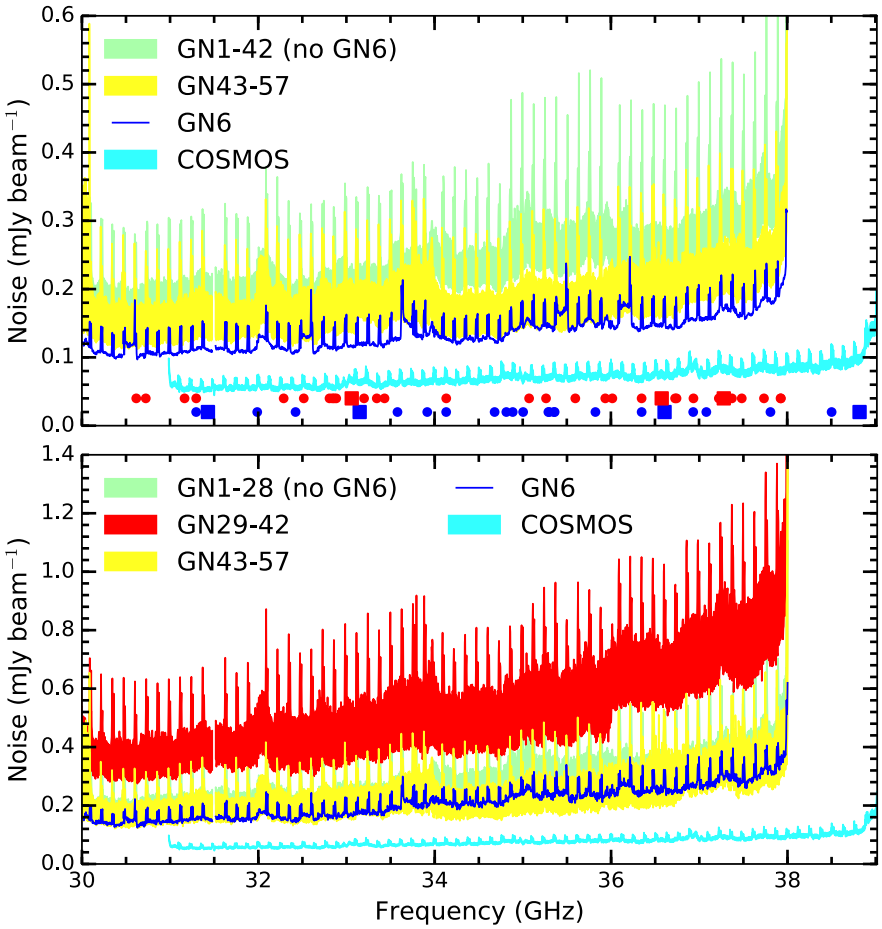

Figure 3.3: Measured *rms* noise, per pointing, in 4 MHz channels as a function of frequency, at the native spatial resolution (top), and after smoothing to a common beam size (bottom). The bands are for groups of pointings that were observed in similar conditions and thus have similar noise characteristics. The GOODS-N pointings GN29–GN42, which were observed at higher resolution (predominantly in DnC configuration), suffer a significant noise increase in the bottom panel due to spatial smoothing. The frequencies of our line candidates (blue in COSMOS, red in GOODS-N) from Tables 3.4 and B.1 are marked by squares and circles, respectively in the top panel.

dow (instead of 3 channels), regardless of proximity to baseband edges, to minimize the gap between sub-bands. We find that the bandpass is sufficiently flat that this choice gives the best trade-off between sensitivity in the end channels and additional noise, although some noise increase at the band edges is visible in Figure 3.3. After executing the pipeline, we visually inspected the visibil-

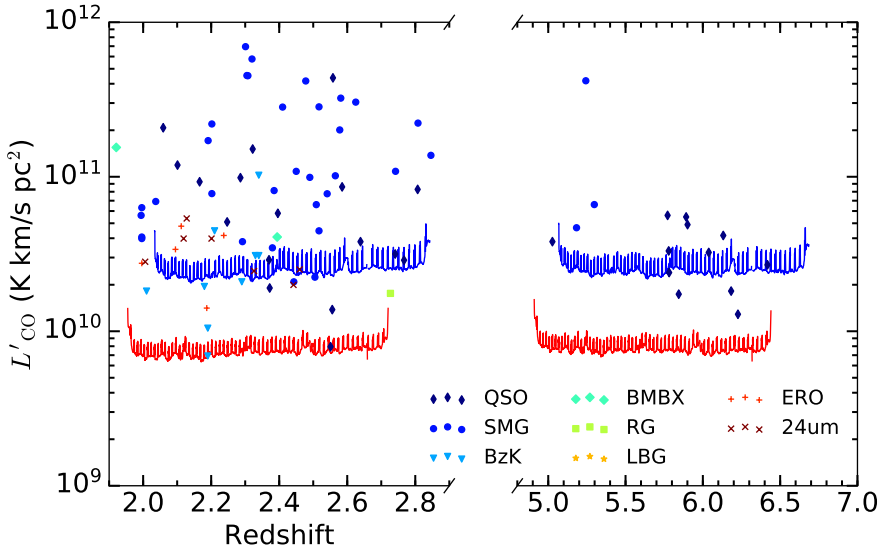

Figure 3.4: Line detection sensitivity limit reached by our observations (GOODS-N in blue, COSMOS in red). We assume a line FWHM of 200 km s^{-1}, and a 5σ limit on the average pre-smoothing noise limit for direct comparison to Decarli et al. (2016a). For comparison, we overplot all $z > 1$ CO detections to date from the compilation by Carilli & Walter (2013), as updated by Sharon et al. (2016). Colors mark different source types (quasars, submillimeter galaxies, 24 μm-selected galaxies, Lyman-break galaxies, color-selected galaxies, radio galaxies). At the sensitivity in the COSMOS field, we would be able to detect all previously detected CO emitters at high redshift in this compilation.

ities in the calibrator fields to identify any necessary additional flagging. We then re-executed the pipeline to obtain a final calibration. In addition, for most GOODS-N observations we modify the pipeline to flux-calibrate in reference to the gain calibrator (whenever a primary flux calibrator was not observed).

We identified a small number of noisy spectral channels in our observations that are not removed by the calibration pipeline. The noisy channels were initially discovered as narrow spikes of a small number of channels in amplitude vs. frequency plots of visibilities from the science target fields, and they are mostly associated with single antennas. Being very narrow in frequency (one or two 2-MHz channels), the noise spikes are not significantly reduced by the statistical weights obtained from `statwt`, which minimizes the effects of all other

noise features, since the weights are computed per spectral window. Including one of these noisy channels for the affected antenna during the imaging of a single pointing of the mosaic from a single observation track increases the rms noise by $\sim$ 20% in that frequency channel. Selecting channels whose standard deviation exceeds the mean standard deviation in that spectral window for that antenna by 3σ is a sufficient criterion to exclude most of the problematic noise spikes (these are only of order $\sim$ 0.2% of all channel-antenna combinations). This method is partially redundant to the algorithms in `rflag` (which we did not execute as part of the pipeline), but it reduces the risk of removing real spectral lines since the noisy channels are selected for individual antennas. We also found that many noisy channels in the same antenna repeat over time during an observation, and would therefore be more problematic if left in the data cube. We find a concentration of noise spikes in roughly four peaks over the frequency range, which correlate with peaks in the weighted calibrated amplitudes as a function of frequency. We consider this to be indicative of random electronic problems that manifest as increased noise and thus are more prevalent in certain hardware components of the correlator than others. The presence of four peaks is likely associated with the underlying basebands, since there appears to be one peak in each baseband, but no precise correlation of the noise peak frequencies to the baseband edges could be identified. The feature is stochastic and does not appear to preferentially affect any particular subset of antennae. These noise spikes are at least twice as narrow as the narrowest blindly selected line candidates (which are rare among all candidates) and therefore residual anomalous noise spikes are believed not to measurably affect our line search.

Calibrated data from each pointing were imaged separately without any `CLEAN` cycles, because the fields do not contain strong continuum or line sources

(see Section 4). We imaged the total intensity (sum of the two polarizations) using natural weighting and choosing a pixel size of 0.5″ consistently in the two fields. The smallest adopted channel width is 4 MHz, equivalent to 35 km s^{-1} mid-band, which is less than the typical line width from galaxies. With this choice, our data cubes have ~2000 channels after averaging polarizations. A crucial aspect of the imaging procedure, necessary for blind line searches, is to avoid any frequency regridding by interpolation, therefore we image using the nearest channel, rather than interpolating. Interpolation would introduce correlations between the noise of adjacent channels, undermining the statistical basis of the search for spectral lines, and producing a significant number of spurious noise lines. Disabling frequency interpolation when imaging visibilities may introduce a very small, less than half a channel, frequency error that we consider negligible because 4 MHz channels (35 km s^{-1}) are smaller than the typical linewidth.

The geometric average synthesized beam size for COSMOS ranges between 2.2″ and 2.8″ as a function of frequency and the beam axes ratio is in the range of 0.8–1, while for GOODS-N the synthesized beam size differs more significantly from pointing to pointing. In particular, the main difference is between the subset of "high resolution pointings" (GN20–GN42) and the rest (GN1–GN19 and GN43–GN57). The geometric average beam size ranges between approximately 1.3″ to 2.0″ for the high resolution pointings, and between 2.1″ and 3.1″ for the rest. The beam axes ratio is in the range of 0.6–0.9. The individual pointing cubes are subsequently smoothed to a common beam size of 3.38″× 2.91″ for COSMOS and 4.1″× 3.2″ for GOODS-N, using the CASA task `imsmooth`. This compromise in resolution and signal-to-noise is necessary in order to mosaic all pointings together, and to search for line emission in a uniform manner. This

is called the Smoothed-mosaic. Separately, we have also mosaicked the pointings with their native resolution (after removing the beam information from the headers), and this Natural-mosaic (where the resolution is set by natural weighting) was used to exclusively search for spatially un-resolved sources, for which the spatial size information is not important. Fig. 3.2 shows the spatial coverage provided by the individual pointings in our two mosaicked fields.

The CASA function `linearmosaic` was used to mosaic the images of our COSMOS data together. We wrote a custom script to optimally mosaic the images of the GOODS-N data, using Equation. 3.1, which takes into account the different noise levels in different pointings, per channel, in order to compute optimal weights for mosaicking:

$$I = \frac{\sum_p I_p A(\mathbf{x} - \mathbf{x_p})/\sigma_p^2}{\sum_p A(\mathbf{x} - \mathbf{x_p})^2/\sigma_p^2}, \tag{3.1}$$

where A is the primary beam function, $\mathbf{x_p}$ are the pointing center positions, I_p represents the specific intensity data from pointing p and σ_p is the noise level in pointing p (computed on a per channel basis).

All COSMOS pointings were always observed in every execution, and for comparable amounts of time. The GOODS-N pointings were observed in blocks of 7, over the course of several months due to scheduling constraints. Therefore, they have slightly different noise levels, partly due to the upgraded 3-bit samplers in the later (2014) observations. Furthermore, some GOODS-N data were not taken in the D configuration but rather in a combination of the DnC configuration, in transition between the D and the DnC and in transition between the DnC and the C configuration. Therefore, when smoothed to a common beam, these pointings have higher noise, because the information on the the longest baselines is effectively discarded. For these reasons, the noise is significantly

spatially varying in the smoothed version of the GOODS-N mosaic, which we take into account when analyzing the data (Fig. 3.3 shows the noise before and after smoothing). All pointings suffer a noise increase due to smoothing, because the targeted beam for the smoothing process has to be larger than every beam in any pointing, at any frequency, and also includes those beams that have different position angles. In the case of the COSMOS mosaic, the CASA function `linearmosaic` produces the mosaic edge at the 30% of peak level sensitivity (per-channel). For consistency, we therefore apply the same criterion in our GOODS-N mosaics. In order to do this, we define a mask which produces the mosaic edge at 30% of peak sensitivity in the Natural-mosaic, and utilize the same mask for the Smoothed-mosaic for consistency.

3.4.4 Accounting for the beam inhomogeneity in our GOODS-N mosaic

In order to mosaic pointings together, it is preferable to smooth all pointings to a common beam. This is not straightforward for the wide-area part of this survey (in the GOODS-N field), due to the large number of pointings observed over the course of several months, which caused a range of array configurations to be utilized.

For the pointings in the COSMOS field, each pointing was observed in every track. Therefore, the mosaic has uniform beam size properties. In the GOODS-N field, on the other hand, the beam differences potentially cause non-uniformity in the mosaic. This is most significant for pointings GN29 to GN42, which were mostly observed in the DnC configuration. In preparation for mosaicking the

individual pointings are all smoothed in the image plane to a common beam size with `CASA imsmooth`, but pointings for which a larger amount of smoothing was required end up with slightly larger beams than the target beam size.

The reason why smoothing DnC data seems to necessarily produce slightly different beams than D-configuration data can be appreciated from a look at the Fourier Transform of a typical image from these pointings, effectively their *uv* coverage, in Fig. 3.5. Smoothing multiplies the *uv*-plane by a tapering Gaussian of the appropriate size, calculated from the size of the starting beam size and the target beam size. However, the D-configuration *uv* coverage, does not look the same as a Gaussian-tapered DnC-configuration *uv* coverage, hence the final beam is always going to be an imperfect match (unless both datasets are smoothed to a very large beam, at which point the initial shape of either *uv*-coverage does not matter).

While the slight spatial inhomogeneity of the beam size is inconsequential in producing the Signal-to-Noise ratio cube (as the noise in the mosaic can be calculated analytically and accounted for by Eqn. 3.5), the beam size difference causes spatially varying noise in the Matched-Filtered cubes. The main difference is between the set of 14 pointings (GN29–GN42) and the rest, so we also mosaic and Match-Filter them separately, in addition to working with mosaics with and without this set. Exploiting the improved uniformity within these sub-mosaics, we can measure the noise post-Matched-Filtering. The objective is using the noise in the Matched-Filtered sub-mosaics to calculate the noise in the Matched-Filtered full GOODS-N mosaic. The Signal-to-Noise ratio in the full mosaic is related to the sub-mosaics by:

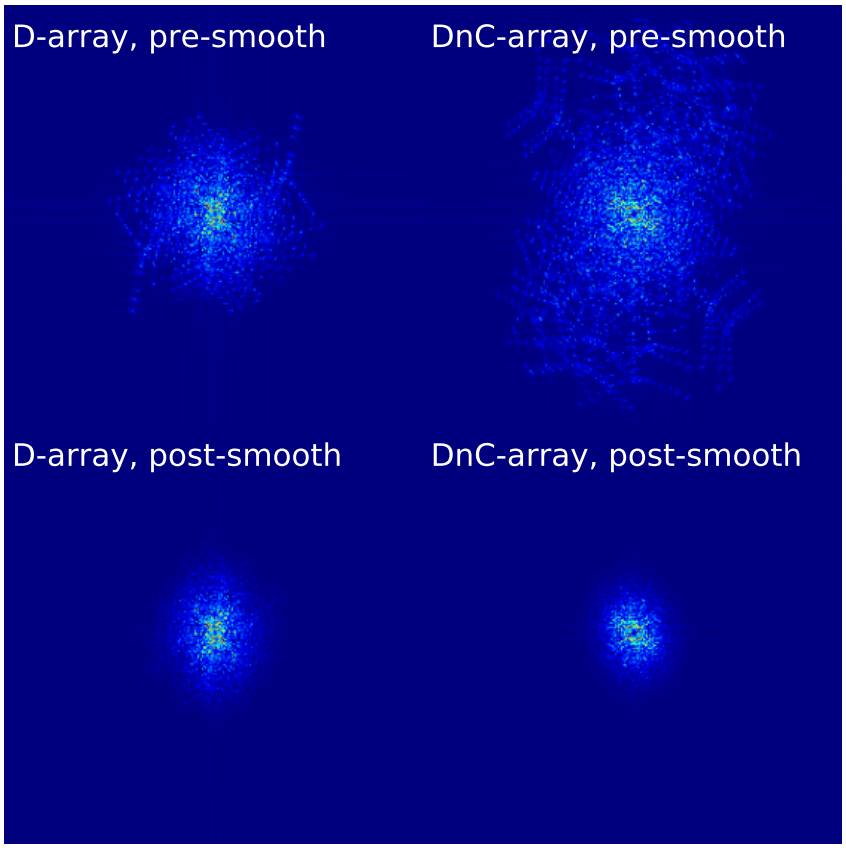

Figure 3.5: Absolute value of the Fourier transform of channel maps (in this example, channel 100), of individual pointings (in this example, pointing GN3, which has D-array data only, and GN34, which has mostly DnC array data), before and after smoothing. The post-smoothing image shows that, although the smoothing is supposed to bring the two pointings to a common beam, instead it makes the resolution of the DnC array pointings coarser, i.e. it produces a larger beam than in the pointings with D-array data only.

$$SNR_{TOT} = \frac{\sqrt{\sum_A A_i^2/\sigma_i^2}}{\sqrt{\sum_{TOT} A_i^2/\sigma_i^2}} SNR_A + \frac{\sqrt{\sum_B A_i^2/\sigma_i^2}}{\sqrt{\sum_{TOT} A_i^2/\sigma_i^2}} SNR_B \doteq f_A SNR_A + f_B SNR_B, \tag{3.2}$$

where $TOT = A \bigcup B$ represent the set of GN29–GN42 pointings and the set of the remaining pointings. Match-Filtering then corresponds to convolving with

template h. This can be expressed as:

$$(f \cdot SNR) * h = \int f(x) SNR(x) h(y-x) dx \simeq f(y) \int SNR(x) h(y-x), \tag{3.3}$$

with $f(x) \simeq f(y) + O(f' \cdot FWHM_h)$. To zeroth order, we can take f as constant over the scale of template h, which allows to pull it out of the integral. This approximation is appropriate, because the fraction functions f change slowly over the size of a template. Therefore, the noise after convolving with the template is:

$$std[(f_A(x) SNR_A) * h] \simeq f_A \cdot std[SNR_A * h], \tag{3.4}$$

and we can calculate the noise in the Matched-Filtered mosaic by summing the standard deviations from the two terms in Eqn. 3.2 in quadrature. This method only requires measuring the noise in the Matched-Filtered sub-mosaics, in which the noise is uniform, and the fraction functions: f_A and f_B, which can be calculated. Therefore, this process allows us to calculate noise maps of the Matched-Filtered cubes in GOODS-N, thereby accounting for the noise inhomogeneity due to spatially varying beam sizes.

3.4.5 Constructing the Signal-to-Noise cubes

In order to search for emission lines in our data, we produce a signal-to-noise ratio (SNR) cube by calculating a noise value for each pixel and in each frequency channel of the mosaics. Spatial variations in the noise are introduced by mosaicking pointings with different noise levels and primary beam corrections. The noise in the resulting mosaic can be calculated assuming statistical

independence of the noise in different pointings, and can therefore be calculated by summing their standard deviations in quadrature, with weights given by Eqn. 3.1:

$$\sigma(x) = \frac{1}{\sqrt{\sum_p A(\mathbf{x} - \mathbf{x_p})^2/\sigma_p^2}}, \tag{3.5}$$

where σ_p is the measured noise in the individual pointing images, A is the primary beam function and $\mathbf{x_p}$ are the pointing center positions. In the special case of pointings with approximately equal noise (as in our COSMOS data) we can use a simplified expression, where the denominator is simply the square root of the sensitivity map, output from CASA's `linearmosaic` function:

$$\sigma(x) = \frac{\sigma}{\sqrt{\sum_p A(\mathbf{x} - \mathbf{x_p})^2}}. \tag{3.6}$$

The frequency variation of the noise is accounted for by measuring the noise in each frequency channel, in the individual pointings. In COSMOS, where the noise variations from pointing to pointing can be neglected, we calculate the signal-to-noise ratio by multiplying the signal cube by the square root of the sensitivity map (which gives spatially uniform noise), and then dividing each channel map by its standard deviation to normalize the pixel value distribution. In GOODS-N, we measure the noise in each pointing and apply Eqn. 3.5 to compute noise and signal-to-noise ratio cubes.

3.5 Line search methods

The main objective of this survey is to carry out a blind search for CO(1–0) and CO(2–1) emission lines in the COLDz dataset. No other bright lines are expected

to contaminate the 30–39 GHz frequency range (Fig. 3.1). The line brightness sensitivity is approximately equal for the low and high redshift bins (corresponding to CO(1–0) and CO(2–1), respectively; Figure 3.4). We therefore expect a higher source density in the low redshift bin due to the expected evolution of the cosmic gas density (Popping et al., 2014b, 2016). Hence, we will assume that all detected features correspond to CO(1–0) unless data at other wavelengths suggest that they belong to the higher redshift bin. In order to detect emission lines in our data cubes, we have implemented a previously published method (SPREAD, Decarli et al. 2014a), and developed three new methods to explore the differences between different detection algorithms.

The objective of a line search algorithm is to systematically assess the significance (expressed as Signal-to-Noise ratio, SNR) of candidate emission lines in the data. The relevant information available to us is the strength of the signal, the number of independent samples that make up the line, and the spatial and frequency structure (for which we have priors based on previous samples of CO detections at high redshift). In particular, we expect most CO sources to be either unresolved or resolved over a few beams at most at the $\sim 3''$ resolution of our mosaics (which corresponds to ~25 kpc at $z \sim 2.5$ and ~ 17 kpc at $z \sim 6$), and we expect the line FWHM to be in the range of 50 to 1000 km s^{-1} (Carilli & Walter, 2013).

Our line search method of choice, Matched Filtering in 3D (MF3D), expands on the commonly used spectral Matched Filtering (MF1D; e.g, AIPS `serch`). Matched Filtering corresponds to convolving the data with a filter, or template, which is "matched" to the sources of interest in order to attenuate the noise and concentrate the full signal-to-noise of the source in the peak pixel. A detailed

description of the MF3D method is presented in the next section.

We also implement and test some of the previously used methods on our data, in particular SPREAD and Matched Filtering in the spectral domain, i.e., in 1D. The main limitation of SPREAD is that it does not employ the full spatial information available, but only utilizes signal strength. While Matched Filtering in 1D is arguably the optimal search method for completely unresolved sources (for which the spectrum at the peak spatial pixel contains the full information), it still requires a prescription for identifying pixels belonging to the same source, and it needs to be generalized to account for the possibility that some sources may be slightly extended. Besides accounting for extended sources, the 3D Matched Filtering also captures the spreading of the signal-to-noise over different spatial positions in different frequency channels, which is at least in part a consequence of moderate SNR. For this reason, it is natural to use the spatial information by using templates that include a spatial profile. Therefore we extended the method to Matched Filtering with 3D templates.

3.5.1 Additional details on the line search methods

In this section we provide additional details of our line search methods in interferometric data cubes, which were used to carry out the blind line search. We first provide a more complete description of our method of choice, Matched Filtering in 3D[7] (MF3D, which extends Matched Filtering in the spectral dimension; i.e., MF1D), and then we compare its performance to three alternative methods that we have also investigated.

[7]We provide a Python implementation for this algorithm at https://github.com/pavesiriccardo/MF3D

Matched filtering in 3-D interferometric data cubes

Since we do not expect the CO line emission in z = 2–3 galaxies to be resolved over more than a few beams at most, we expect our sources to be spatially well described by a family of 2-D Gaussian templates. Therefore, under the prior of source shape, Matched Filtering is theoretically an optimal detection method.

The Matched Filtering method can be thought of as concentrating all of the extended (spatially and in frequency) signal to a peak pixel that captures both the overall strength of the original signal and how closely this matches the template shape. At the same time, the smoothing of the noise in regions without signal allows us to reliably measure the noise level on the scale probed by the template size. In this way, the problem of finding emission lines with structure is effectively reduced to the problem of just examining peak heights to assess their significance.

We compute templates that are Gaussians in frequency and circular 2D Gaussians spatially (sizes given in Table 3.3). We then convolve the signal-to-noise cube with these templates by multiplication in Fourier space to produce multiple Matched-Filtered cubes, one for each template.

The main difference between the traditional application of Matched Filtering in astronomical images and our application to interferometric data comes from the spatially correlated nature of the noise in interferometric images. In the case of un-correlated (i.e., white) noise, the matched filter simply corresponds to the expected source shape and size, but correlated noise introduces deviations from this matching, as described in the following.

The frequency width of a template approximately matches the line width

that it selects, because the noise in different channels is uncorrelated. On the other hand, spatially the noise has a non-zero correlation length, as determined by the synthesized beam. Therefore, the "matching" to a template is not the intuitive relation for which spatial template size matches the size that it selects. As an example, for un-resolved sources, i.e. sources whose image is beam-sized, the maximal SNR is realized at the peak pixel rather than over an extended area. To calculate the relationship between template size and selected size, we therefore considered the idealized problem of circular Gaussian beams and Gaussian sources, which can be treated analytically. We calculate the correspondence between template size which maximizes the SNR and source size. To carry out the calculation, we have to make the approximation of source positions being known a priori, evaluating the signal-to-noise at this position. This is not what is done in practice, since positions are unknown. The pixel with the locally highest SNR is utilized instead. We briefly discuss the effects of this approximation on the recovered SNR in the next sections.

The results of this calculation show that template "matching" (i.e. providing the maximum SNR) takes place approximately when:

$$\sigma_A^2 = \sigma_h^2 + 2\sigma_b^2 \tag{3.7}$$

where σ_A is the size (radial standard deviation) of the source in the image (which is given by the sum in quadrature of the real source size and the beam), σ_h is the size of the template Gaussian, and σ_b is the beam size. For source sizes smaller than $\sqrt{2}\sigma_b$, the template size that maximizes the SNR is an infinitely narrow source template. Therefore, we include a single-pixel template (we call this "0-size", being the limit where the radius of the spatial Gaussian tends to 0), which implements a single-pixel search (i.e., MF1D as a subset of MF3D) and therefore selects un-resolved and very slightly resolved sources. The analytical expres-

sion above only provides an indication of the matching dependence, but we do not make use of it in the following. The main simplification comes from measuring the SNR at the (in practice unknown) real position of the source rather than at the local maximum. In the next chapter, we explore the analysis of simulated artificial sources through our MF3D algorithm, and we use those simulations to numerically estimate a probabilistic connection between template sizes and injected source sizes.

The detailed steps of the blind search are summarized by the flowchart in Fig. 3.6, and in the following. As described above, in order to correctly mosaic different fields together we smooth every pointing to a common, larger, beam. This procedure reduces the SNR for point sources (see Fig. 3.3). We therefore also run a single-pixel Matched Filtering search on the Natural-mosaic, which was obtained without any smoothing. While the lack of a common beam in the Natural-mosaic would, strictly speaking, imply that the spatial structure may not be accurately calculated, this effect is negligible in the COSMOS data, where the different pointings have roughly equal resolution. Furthermore, the Natural-mosaic is sufficient for a search for un-resolved sources, where the flux at the peak pixel represents the total flux, and is therefore correctly recorded in the Natural-mosaic. We treat the result of this Natural-mosaic Matched Filtering step as an additional "spatial template", one for which less smoothing was done than even the single-pixel search in the Smoothed-mosaic. We therefore refer to it as the "-1 pixel" template. In the end, we combine the results from this search with those of the other templates, as detailed in the following.

The signal-to-noise ratio of a detection corresponds to the ratio of the height of the peak in the Matched-Filtered cube to the standard deviation of empty re-

gions. We initially normalize our templates such that the sum of the squares of the template values equals one. For independent pixel noise (which applies to the frequency channels, but not to the spatial pixels), this normalization choice would imply that the noise after convolving would be the same as the noise before. This implies that the peak height corresponds to the total SNR of the candidate. For the 3D case, in particular for spatially extended templates, we need to account for the fact that the synthesized beam size results in small scale spatial noise correlations. While the calculation for the noise in the smoothed cube is close to the measured values, we decide to measure the noise in the convolved cubes directly from the standard deviation of pixel values. Since our dataset is mostly free of signal, we estimate the noise in each Matched-Filtered cube in the COSMOS field simply by taking the standard deviation of the whole cube, and normalize by dividing each pixel by this value. In the case of the GOODS-N mosaic though, the beam size is not uniform across the mosaic, even after smoothing. In particular, the beam size in the pointings that had higher native resolution, ends up being larger after smoothing than in the other pointings due to the particular nature of the *uv* coverage. The main consequence of this slightly spatially varying beam, affecting the Smoothed-mosaic for the GOODS-N field, is that during Matched Filtering, the noise in the Matched-Filtered cubes is not uniform. This is expected, as the noise change during convolution is a function of the ratio of the pre- and post-convolution beam size. We therefore measure the noise in the Matched-Filtered cubes, separately for two sets of pointings (GN29–GN42; and all the others), and use these sets to construct an approximate noise map for the Matched-Filtered mosaics in GOODS-N, for each template.

Table 3.3: Template Sizes for MF3D Line Search Technique

	Spatial FWHM (arcsec)	Frequency FWHM (4 MHz-channels)
COSMOS	0, 1, 2, 3, 4	4, 8, 12, 16, 20
GOODS-N	0, 1, 2, 3, 4	4, 8, 12, 16, 20

Note Gaussian template sizes utilized in our Matched Filtering in 3D. A spatial size of 0 stands for a single-pixel spatial extent, and implements the single-pixel search that is optimal for un-resolved sources. These sizes represent a uniform sampling of the parameter space that we conservatively expect to represent CO sources. 4 MHz correspond to ~35 km s^{-1}, mid-band.

In order to blindly identify line features in our data and evaluate their significance using the Matched-Filtered cubes (one for each template), we need to locate the peaks and determine the template which provides the highest SNR to each candidate, thereby identifying the template that best matches the feature shape. The first stage is to identify, in each Matched-Filtered cube, the peaks, i.e. the local maxima above some significance threshold. In order to find the significance and position of a peak, we select all voxels (i.e., volume pixels) in the data cube above a fixed threshold, and then retain those voxels that are local maxima by comparing to the values in a small surrounding box of 12 channels by 8 pixels by 8 pixels.

Next, we cross-match objects identified in the different Match-Filtered cubes (obtained from the different templates) in order to remove repeat identifications of the same object. We form a master list of all objects selected from all templates, sorted by SNR. We then parse through each entry, from highest to lowest SNR, and form clusters characterized by their SNR-weighted average positions and the template with the highest SNR. We add a candidate object to a cluster if it resides within a 5.3 voxel radius of the cluster center (this threshold was found to be appropriate for our pixel size and channel width; more gener-

ally the frequency and spatial separation thresholds may need to be different) and only if the template under consideration differs from the other templates in the cluster (to avoid clustering features identified in the same template since they are most likely independent objects). By moving down the SNR-sorted list, we guarantee that clusters are built from their highest significance members to their lowest. This method ensures that spatially extended/broad objects that are also identified at lower significance in smaller templates are included in the appropriate cluster as members. For neighboring point-like sources (with high significance in the smallest templates), this method maintains both objects as separate clusters, and allows their corresponding low-significance/extended template candidate to be associated with both clusters. In this way, we avoid grouping separate objects into the same cluster, and we avoid splitting single objects into multiples. Each cluster then corresponds to a single galaxy candidate in our final catalog.

In order to choose the clustering thresholds, and to asses the independence of the result from their precise values, we test how well the algorithms performs in not clumping too much or too little by computing distances to closest neighbors. We test this both for the first stage of clump-finding in the Matched-Filtered cubes to check the method to identify clump peaks works, and for the second stage of matching features across different templates. We inspect the distribution of the neighbor distances, and check that they behave as expected, without splitting clumps into different components (which would show up as many objects having a very close neighbor that would look like part of the same clump to visual inspection), and without including different clumps (by changing the clustering thresholds and looking for any significant changes). We do not find significant issues in either phase of clustering. This technique was

therefore used to refine our choice of clustering thresholds. A few objects are objectively difficult to distinguish as one or more parts and so the algorithm performance is at a comparable level to what could be achieved through manual inspection. Overall, the method does very well in finding local peaks, appropriately splitting separate objects even when they are close together. The second stage of associating entries across different templates, while more challenging to evaluate, appears to be largely insensitive to the precise value of the thresholds within a few voxels range.

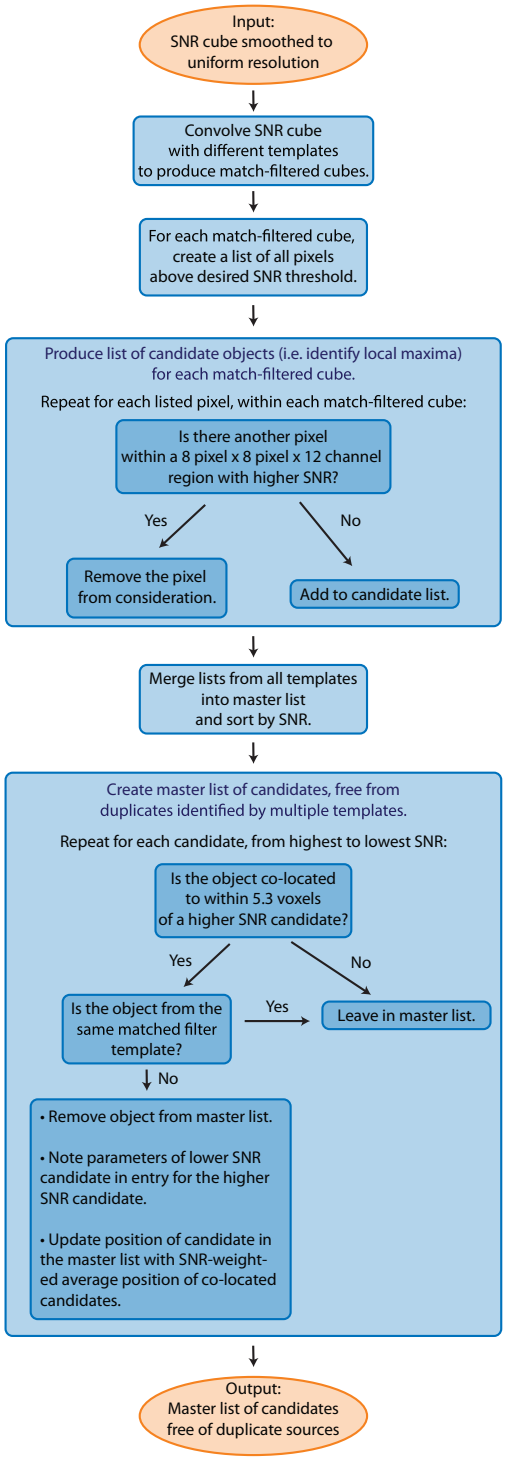

Figure 3.6: Flowchart describing the detailed procedure of our line search algorithm, utilizing Matched Filtering in 3D. The input is a signal-to-noise ratio cube and the output is a list of line features, characterized by a feature signal-to-noise ratio, which accounts for the total signal-to-noise evaluated through the template that gives the highest value.

Comparison to Matched Filtering in 1D

A simpler version of our line search algorithm, which we call Matched Filtering in 1D (MF1D), corresponds to extracting a spectrum at each spatial pixel and running a spectral line search on each spectrum with 1D Gaussian templates. As emission lines at high-z are typically approximated as Gaussians, we note that assumptions of square profile templates are less optimal matches in the frequency dimension and therefore do not maximize the SNR for candidate emission lines, although we find the difference to be small.

We have investigated the MF1D approach, which is frequently used in the case of single-dish data, in order to provide a check on the results of our line search and to evaluate its performance. Walter et al. (2016) utilized a version of this method, which is effectively matched filtering in 1D with square line templates. The main difference between the method utilized there and our implementation consists in our estimating the noise through the standard deviation of the full SNR cube, rather than individual binned channel maps. This is not expected to cause a significant difference. This method, like MF3D, also requires some prescription for recognizing clusters of significant voxels as belonging to the same candidate when they are close together. We achieved this by building lists of clumps with running average positions, and clustering up to a radius of 9 voxels. In the case of unresolved sources, where the peak pixel contains the maximum signal-to-noise, this method performs just as well as our more general method, since the set of templates used in this technique is a subset of those in MF3D ("0-size" templates). However, it will miss a large fraction of the extended sources by underestimating their true SNR. Although we do not expect a large fraction of resolved sources, a blind search should be as agnostic as pos-

sible with regards to the properties of the galaxies that may be selected. Indeed, since CO(1–0) traces the total cold, dense gas mass, it is precisely the tracer that may reveal extended gas reservoirs. One of our top candidates, COLDz.COS.3, harbors a very extended gas reservoir, with SNR peaking in the 2″ template. A single-pixel search assigns this line a SNR=8.2 rather than 9.2, which would imply a discrepancy of -10%. While this error would not significantly affect the significance of this candidate, such an error would be enough to move a moderate significance candidate with SNR=5.5 , to 4.9, and therefore would effectively be missed by our search. Another advantage of the MF3D method over the 1D is that it allows to capture a larger fraction of the signal, for broader lines, because in that case the peak signal may be substantially spread over several spatial pixels, in different frequency channels, due to noise. While this spreading of the signal over different pixels, in different channels, causes an ambiguity between spectral-SNR and moment-map-SNR for single-pixel methods, this ambiguity is resolved when the full 3D information is taken into account through MF3D. Therefore, we conclude that this method can be absorbed into our more general, improved MF3D framework and that it can be considered a subset of that technique.

Comparison to the `Source Extractor` method

We also considered modifications of existing source finding software, such as `Source Extractor`, which can effectively capture the spatial information of a line candidate while avoiding merging adjacent independent peaks (Bertin & Arnouts, 1996). We used the spatial source detection part of SExtractor on individual channel maps with varying frequency binnings. We combined the

detections across different binnings and at different frequencies and then established prescriptions to identify lines and their aperture-integrated SNR. These prescriptions made the results very dependent on the precise criteria used to evaluate the significance of a line. The principle is somewhat similar to Matched Filtering. It requires binning data cubes to multiple different velocity widths, and these binnings correspond to templates of different frequency width. Then the method relies on SExtractor for the spatial source extraction (recognizing clusters of high pixels as one unique object). It also requires finding the correct binning that maximizes the signal-to-noise ratio. A challenge for this method is the choice of an aperture size for the flux extraction in the channel maps, to be used in separately evaluating signal and noise. Combining different aperture sizes, which imitates the range of spatial templates in MF3D, introduces additional difficulties with precisely evaluating aperture flux noise. This hybrid technique is sub-optimal in the frequency dimension, because binning is equivalent to filtering with a rectangular function, which is a worse match to the expected spectral line profile than a Gaussian shape, although the difference is small. Our tests show that this line search method, can have similar outcomes in selecting lines to Matched Filtering in 3D for our data. In particular, $> 85\%$ of the top ~ 100 candidates are matched between both methods. Comparing lists of candidates, we find that objects that were assigned a high SNR by the SExtractor method but were less significant in MF3D appeared to be less plausible candidates to visual inspection because of improbable line shapes.

The SExtractor method provides a valuable check for our use of extended templates in MF3D. In particular, the extended templates in MF3D allow finding those sources that would be missed by MF1D. The SExtractor method, which is sensitive to extended structure, confirms our extended candidate selection.

Therefore, we conclude that our MF3D method coherently combines the results from single-pixel methods and other methods which are biased towards extended sources, like the use of SExtractor with fixed aperture sizes.

Comparison to the SPREAD technique

We have also explored SPREAD, an algorithm developed by Decarli et al. (2014a) for the PdBI blind field line search, to find emission lines in our VLA observations. This method corresponds to binning the data set in frequency, and identifying channel maps with an excess of signal compared to the Gaussian noise pixel intensity distribution. This method does not take advantage of the spatial information (neither spatial extent nor position), but only of the total flux. The excess signal in a channel map does not need to come from a single source, because the SPREAD statistic is a global value that characterizes the whole channel map. This method did not perform reliably on our data set, since it relies on the small number pixel statistics on the tails of the noise distribution, which are necessarily subject to large fluctuations. The SPREAD statistic was able to isolate the same top candidate sources as our other methods, but it loses discriminating power below a SNR of ~ 8, since the SPREAD statistic does not track SNR and loses the ability to locate moderate significance features. We conclude that MF3D captures any useful information obtained from SPREAD.

Comparison to Duchamp

We also compare our method to the sophisticated line-searching tool *Duchamp*, which was developed for SKA-precursor data cubes (Whiting, 2012). *Duchamp*

was extensively tested by (Westmeier et al., 2012; Popping et al., 2012), and found to provide a good blind search algorithm for both unresolved and extended emission. Because our survey is only expected to detect unresolved or slightly resolved CO emission, much of the power of *Duchamp* (e.g., "a trous" wavelet reconstruction) is not optimized for our targets of interest. The smoothing (convolution) pre-processing offered by *Duchamp* is equivalent to Matched Filtering with Gaussian templates in the spatial dimension and Hanning templates in the frequency dimension, although *Duchamp* only allows specifying one template size at a time, and not combining results from different templates. We find that smoothing along the frequency axis is necessary in order to recover even the most significant line emitters in our cubes, as expected due to the wide line-widths relative to channel widths. On the other hand, *Duchamp* does not allow to smooth in the frequency and spatial dimensions simultaneously, thereby preventing optimal recovery of the full signal-to-noise for slightly extended sources. While the "a trous" wavelet reconstruction is designed to perform well on extended structure of a general shape, it is not optimal for recovering only slightly extended spatial structure, and hence does not yield the same signal-to-noise recovery as Matched Filtering in this specific case of interest. *Duchamp* offers two choices for peak identification algorithms leading to candidate identification, with pixel clustering being predominantly carried out spatially rather than spectrally. While both of these algorithms perform equally well in recovering all of our top line candidates, the simple 3D peak identification algorithm implemented in MF3D simultaneously utilizes the full 3D information.

Based on all these considerations, we find that the best use of *Duchamp* in our data is achieved by manually adopting different frequency-width smoothing templates and combining the resulting signal-to-noise ratios, to select un-

resolved line candidates of different velocity widths. This procedure directly mimics our MF3D method, and therefore we do not adopt *Duchamp* for the COLDz survey data.

3.5.2 Matched-Filtering interferometric images

We here discuss the analytical results of our investigation of Matched Filtering in 3D, in the specific case when it is adapted to interferometric images. We study idealized noise and source conditions, in order to derive an approximate relationship between the template spatial size and the "matched" size of a feature that would display the highest SNR for that template. The purpose is to demonstrate the effect of correlated interferometric noise on the sizes that are selected through this technique.

If for simplicity we assume the synthesized beam to be a circular Gaussian, with standard deviation σ_b, then the noise correlation function can be shown to be $\langle n(\mathbf{x})n(\mathbf{x}')\rangle = \sigma_0^2 e^{-|\mathbf{x}-\mathbf{x}'|^2/4\sigma_b^2}$, where σ_0 is the noise of the image. Let us define our idealized data as containing a Gaussian source of peak intensity s and convolved size σ_A, in addition to additive, zero-mean Gaussian noise in the image. We also assume the spatial template to be a circular Gaussian of size σ_h, i.e. $h(\mathbf{x}) = \frac{1}{2\pi\sigma_h^2} e^{-x^2/2\sigma_h^2}$. The expectation value of the template-convolved image at the (assumed known) position of the source is then given by: $\frac{s\sigma_A^2}{\sigma_A^2+\sigma_h^2}$. Furthermore, the standard deviation of the convolved image is given by $\frac{\sigma_0\sigma_b}{\sqrt{\sigma_b^2+\sigma_h^2}}$. Therefore, the signal-to-noise ratio measured in the Matched-Filtered image is given by $SNR = \frac{s}{\sigma_0}\frac{\sigma_A^2\sqrt{\sigma_b^2+\sigma_h^2}}{\sigma_b(\sigma_A^2+\sigma_h^2)}$. For a fixed source size σ_A, this SNR has a maximum at $\sigma_h^2 = \sigma_A^2 - 2\sigma_b^2$ or $\sigma_h = 0$ (i.e. the delta function limit of a Gaussian, correspond-

ing to a single-pixel template) in case $\sigma_A^2 < 2\sigma_b^2$, i.e, if the intrinsic deconvolved source size is smaller than the beam size.

We have run simulations to compare these analytical results to the discretized case of pixels, and did not find significant differences. We also explored the effect of the realistic implementation of Matched Filtering, i.e. where the source position is not known a-priori but the peak of the convolved image is taken instead. The main result appears to be that for σ_A^2 up to $2\sigma_b^2$ the signal-to-noise is almost flat as a function of template size. Therefore, a single-pixel template and slightly extended templates maximize the signal-to-noise with a smooth and slow transition, as the source size becomes more important relative to the beam size. For the purpose of our measurement, a precise formula for the match between template size and source size is not needed, and a probabilistic assignment based on artificial source recovery suffices. In particular, the results from our artificial sources show that in the full 3D case the matching may be complex and it depends on signal-to-noise as well as on line velocity width. The extra dependence on the line width can be understood as due to the use of the peak value, rather than the value at the known source position, because a wider-velocity line allows for a larger area over which the peak may be found (due to the combination to positive noise and real signal). To conclude, the matching of sources and templates at the basis of Matched Filtering can be approximately estimated from the previous calculation. For unresolved or slightly resolved sources, the SNR is a weak function of templates size. As the $\sigma_A^2 \sim 2\sigma_b^2$ threshold is approached and crossed, the SNR becomes a rapidly increasing function of template size, with a clear peak for extended templates. Therefore, in order to avoid missing extended sources in blind line searches in interferometric data, we recommend the inclusion of extended (hence 3D) templates, as described in

this work.

3.6 Results of The Line Search

The 3D Matched-Filtering procedure provides an output including the maximal SNR for each line candidate, the position in the cube where that maximal SNR is achieved, the number of templates for which the candidate has $> 4\sigma$ significance, and the template size (spatial and frequency width) where the highest SNR is achieved. We run the line search down to a low SNR threshold of 4σ. The number of identified features is very large, due to the large number of statistical elements in our data cubes. Specifically, we estimate approximately 2.8×10^6 and 1.7×10^7 independent elements for the COSMOS and GOODS-N fields, respectively, by dividing the mosaic area by the beam area and dividing by a line FWHM of 200 km s^{-1}. However, we caution that naively estimating the extent of the noise tails from these numbers does not provide a good estimate, as previously described by Vio & Andreani (2016); Vio et al. (2017).

We mask radio continuum sources in our fields, which contaminate the line candidates: one in the COSMOS field at 10:00:20.67 +02:36:01.5 with a flux of 0.024 mJy beam^{-1}, and three in the GOODS-N field at 12:36:44.42 +62:11:33.5 with a flux of 0.3 mJy beam^{-1}, 12:36:52.92 +62:14:44.5 with a flux of 0.17 mJy beam^{-1} and 12:36:46.34 +62:14:04.46 with a flux of 0.07 mJy beam^{-1} (Hodge et al., in prep.). Even though the continuum fluxes of these sources only have low significance in the individual channels ($< 0.3\sigma$ and $< 2\sigma$ per 4 MHz channel for the brightest source in COSMOS and GOODS-N, respectively), we remove any candidate within 2.5″ of the spatial positions of these sources, because they

are likely spurious and caused by noise superposed to the continuum signal. Specifically, once we remove the continuum flux from their spectra, the significance of those line candidates becomes lower than $\sim 4.5\sigma$, indicating that they likely correspond to noise peaks.

In Table 3.4, we present the list of the secure line emitters in COSMOS and in GOODS-N which were independently, spectroscopically confirmed. While we are confident that our highest SNR ($> 6.4\sigma$) candidates correspond to real CO emission lines because they all have identified multi-wavelength counterparts, we also define a longer lists of line candidates which have significantly lower purity (~5%-40%) as a statistical sample in Table B.1 in Appendix B, as described below. Although only a fraction of those tabulated sources are real emission lines, they provide statistical information once we account for their fractional purity, and therefore they may be used to constrain the CO luminosity function. While a fraction of these lower significance candidates may be expected to correspond to real CO emission, we advise caution in interpreting these lower significance candidates on a per-source basis until they are independently confirmed.

In order to determine the reliability of the line candidates presented in Table B.1, we compare the SNR distribution to that for "negative" line candidates, following the standard practice (e.g., Decarli et al. 2014a; Walter et al. 2016) which relies on the symmetry of interferometric noise. We provide a detailed description of our candidate purity estimation in Appendix B, but we point out that an excess of positive candidates over the negatives, for signal-to-noise ratios above a threshold is an indication that at least a fraction of those positive candidates may correspond to real sources, rather than due to noise. By adopt-

ing this criterion, we determined the SNR thresholds for our candidate lists consistently for both fields by cutting at the SNR level that includes as many negative line candidates as unconfirmed positive candidates. Thus, we exclude from the count the high signal-to-noise, confirmed sources (4 in COSMOS and 2 in GOODS-N, Table 3.4), and we require that the number of unconfirmed sources is greater than the number of negative lines down to the same SNR threshold, thereby constituting an excess. This procedure determines SNR thresholds on the candidates catalog of 5.25σ for the smaller COSMOS field and 5.5σ for the wider GOODS-N field (Table B.1). The threshold is chosen to be higher in the wide, GOODS-N mosaic because the larger number of statistical elements produces more pronounced noise tails.

3.6.1 Measuring line candidate properties

After selecting the blind search line candidates, we separately measure their line properties using a standard method described in the following. The statistical corrections were computed adopting identical methods in the artificial source analysis (Chapter 4).

In order to extract the spectrum of the line candidates, we fit a 2D-Gaussian to the velocity-integrated line maps and extract the flux in elliptical apertures with sizes equal to the FWHM of the fitted Gaussians. For the integrated line maps, we use a velocity range equal to the FWHM of the template that maximizes the SNR. This procedure is expected to provide the highest SNR of the extracted flux. In the infinite SNR case, this aperture choice includes half of the total flux, and we therefore correct the extracted flux scale of the spectrum by

Table 3.4: Catalog of the secure line candidates identified in our analysis, which have been independently confirmed (see Table B.1 for the remainder of the full statistical sample). Columns are: (1) Line ID. (2-3) Right ascension and Declination (J2000). (4) Central line frequency and uncertainty, based on Gaussian fitting. (5) CO(1–0) redshift and uncertainity, unless otherwise noted. (6) Velocity integrated line flux and uncertainty. (7) Line Full Width at Half Maximum (FWHM), as derived from a Gaussian fit. (8) SNR measured by MF3D. (9) Presence of a spatially coincident optical/NIR counterpart (10) Comments.

ID	RA (J2000.0)	Dec (J2000.0)	Frequency [GHz]	Redshift	Flux [Jy km s^{-1}]	FWHM [km s^{-1}]	S/N	Opt/NIR c.part?	Comments
(1)	(2)	(3)	(4)	(5)	(6)	(7)	(8)	(9)	(10)
COSMOS									
COLDz.COS.0	10:00:20.70	+02:35:20.5	36.609 ± 0.002	5.2974 ± 0.0003[a]	0.17 ± 0.02	390 ± 40	14.7	Y	AzTEC-3
COLDz.COS.1	10:00:15.80	+02:35:37.0	31.430 ± 0.003	2.6675 ± 0.0004	0.11 ± 0.03	430 ± 80	10.6	Y	
COLDz.COS.2	10:00:18.20	+02:34:56.5	33.151 ± 0.006	2.4771 ± 0.0006	0.13 ± 0.03	830 ± 130	9.6	Y	source reported by Lentati et al. (2015)
COLDz.COS.3	10:00:17.23	+02:34:19.5	38.822 ± 0.003	1.9692 ± 0.0002	0.37 ± 0.10	240 ± 50	9.2	Y	extended
GOODS-N									
COLDz.GN.0	12:36:33.45	+62:14:08.85	36.578 ± 0.005	5.3026 ± 0.0009[a]	0.344 ± 0.074	610 ± 100	8.56	Y	GN10
COLDz.GN.3	12:37:07.37	+62:14:08.98	33.051 ± 0.006	2.4877 ± 0.0006	0.34 ± 0.12	580 ± 120	6.14	Y	GN19
COLDz.GN.31[b]	12:36:52.07	+62:12:26.49	37.283 ± 0.007	5.1833 ± 0.0008[a]	0.148 ± 0.057	490 ± 140	5.33	Y	HDF850.1

Notes: [a] CO(2–1) redshift. [b] Source is below the formal catalog threshold adopted here, and therefore, not part of the statistical sample.

a factor of two. We then fit a Gaussian line profile to the aperture spectrum and measure its peak flux and velocity width, from which we derive the integrated fluxes reported in Tables 3.4 and B.1. We also measure peak fluxes for the candidates, which are expected to best represent the correct flux for unresolved sources. For the peak fluxes, we extract the spectrum at the highest pixel in the integrated line map. We find that the peak fluxes are compatible with aperture fluxes for point-like sources, and so we choose to adopt the aperture fluxes because they measure the full flux of extended sources at the expense of slightly larger uncertainties. We calculate the positional and size uncertainty of the 2D Gaussian fitting using the CASA task `imfit`, applied to the same integrated line maps described above. The positional uncertainty is relevant when establishing counterpart associations (as detailed in Appendix B for the full candidate list). It is dominated by the detection SNR and the spatial size of the synthesized beam or extended emission.

In the COSMOS field, we can measure aperture fluxes in the Natural-mosaic, to make full use of the highest SNR (the fluxes are typically within 20% of the values measured in the Smoothed-mosaic). Specifically, the 7 pointings of the mosaic have an approximately equal beam size. This allows us to calculate an average beam size for each channel and hence, to correctly measure aperture fluxes. These are the fluxes we report in Tables 3.4 and B.1 for the most significant candidates, which we also use for the luminosity function.

In the GOODS-N field, on the other hand, we are limited to measuring aperture fluxes for resolved objects in the Smoothed-mosaic, because of the strong beam size variations across the mosaic which make it impossible to precisely define a beam in the Natural-mosaic. Nonetheless, since most of the candidates

are unresolved in the original data (show highest SNR in the Natural-mosaic), in those cases we report the peak fluxes, measured in the Natural-mosaic, without concern for missing any flux, and without being affected by the beam size variations.

In the GOODS-N field, there is another beam size effect that needs to be taken into account even in the Smoothed-mosaic. The measured beam size is actually larger than the formal $4.1'' \times 3.2''$ size which was targeted with the CASA task `imsmooth`, and is slightly pointing-dependent. The measured beam area is ~ 1.4 times larger in the D-array only pointings, and ~ 1.7 times larger in the higher resolution pointings than the target size for the smoothing procedure, because of the precise *uv*-plane coverage and the effect of tapering. Therefore, we measure the correct beam size after smoothing, by Gaussian-fitting to the smoothed dirty beam, in each pointing, for each channel. We correct the aperture flux for each candidate line detection in the Smoothed-mosaic by calculating an effective beam area given by a weighted average of the beams of the overlapping pointings, weighted by the square of the primary beams (the same weighted average that determines the flux in the mosaic). We calculate aperture fluxes in this way in the Smoothed-mosaic, and confirmed that the peak pixel flux in unresolved sources matches this corrected aperture flux, within the uncertainties.

The measured CO line fluxes are affected by the effect of a warmer cosmic microwave background (CMB) at the redshift of our sources, which is a uniform background (hence invisible to an interferometer) at the small scales of galaxy sizes (da Cunha et al., 2013a). While we do not expect corrections for our $z = 2$–3 sources to be significant ($\sim 20 - 25\%$) a larger correction (up to a factor ~ 2)

may be required if the gas kinetic temperature were lower than expected. On the other hand, the CO(2–1) line luminosity from the $z > 5$ sources may be underestimated by up to a factor of $\sim 2 - 5$ (da Cunha et al., 2013a). We do not apply any of these corrections to the measured line flux values reported here. These effects will be further discussed in Chapter 4, in the context of the CO luminosity function.

3.6.2 Individual candidates

We have identified 26 line candidates in the COSMOS field down to a SNR threshold of 5.25, and 31 candidates in the GOODS-N field down to a SNR threshold of 5.5 (Tables 3.4 and B.1). The top four sources in COSMOS and two among the highest SNR sources in GOODS-N have been independently confirmed through additional CO transitions (Daddi et al. 2009a; Riechers et al. 2010b, 2011c; and in prep.; Ivison et al. 2011; Pavesi et al., in prep.). Furthermore, we include COLDz.GN.31 in this set of independently confirmed sources (Table 3.4), although it is slightly below the formal 5.5σ cutoff, because it corresponds to CO(2–1) line emission from HDF850.1 (Walter et al., 2012). This line source does not contribute to our evaluation of the CO(2–1) luminosity function because it does not satisfy the significance threshold to be included in the statistical sample (Chapter 4). For reference, we here briefly describe these individual secure candidates and we show their CO line maps and spectra in Figs. 3.7 and 3.8. Line maps and spectra of the complete statistical sample are presented in Appendix B for reference.

We detect four previously known dust-obscured massive starbursting galax-

ies, and three secure sources in the COSMOS field that lie within the scatter of the high-mass end of the Main Sequence at $z \sim 2$ (Lentati et al. 2015; Pavesi et al., in prep.) These galaxies may be representative of a galaxy population that has not been well studied to date, due to our novel selection technique.

COLDz.COS.0: We identify the brightest candidate in the COSMOS field with CO(2–1) from the z=5.3 sub-millimeter galaxy AzTEC-3, detected at a SNR of 15, and which was chosen to be near the center of our survey region. This galaxy is known to reside in a massive proto-cluster (Riechers et al., 2010b, 2014a; Capak et al., 2011). The line flux is compatible with the previously measured value of 0.23 ± 0.03 Jy km s^{-1} (Riechers et al., 2010b) within the relative flux calibration uncertainty. This source is also detected at 3 GHz, with a flux of 20 ± 3 μJy (Smolčić et al., 2017a), and by SCUBA-2 at 850μm as part of the S2COSMOS survey with a significance of 9.3σ and a flux of $8.1^{+1.1}_{-1.3}$ mJy (J.M. Simpson, et al. in prep).

COLDz.COS.1: This high signal-to-noise detection is matched in position (offset 0.3″ ± 0.3″) and CO(1–0) redshift to a source with photometric redshift (z_{phot}=2.6–2.9) in the COSMOS2015 catalog (Laigle et al., 2016). We have confirmed its redshift with ALMA through a detection of the CO(3–2) line (Pavesi et al., in prep.). This source is also detected at 3 GHz, with a flux of 15 ± 2 μJy (Smolčić et al., 2017a), and at 850μm with a significance of 6.0σ and a flux of $4.9^{+1.1}_{-1.2}$ mJy (J.M. Simpson, et al. in prep).

COLDz.COS.2: This high signal-to-noise detection is matched in position (offset 0.3″ ± 0.3″) to a source in the COSMOS2015 catalog (Laigle et al., 2016). We have confirmed its redshift with ALMA through a detection of the CO(3–2) line (Pavesi et al., in prep.), and some of its properties were previously presented

in (Lentati et al., 2015). The photometric redshift in the COSMOS2015 catalog is highly uncertain, and not compatible with the CO redshift of 2.477 within 1σ (z_{phot}=2.9–4.4). This source is also detected at 3 GHz, with a flux of $19 \pm 3\,\mu$Jy (Smolčić et al., 2017a), and at 850μm with a significance of 5.9σ and a flux of $4.0^{+0.9}_{-1.0}$ mJy (J.M. Simpson, et al. in prep).

COLDz.COS.3: This high signal-to-noise detection, is a significantly spatially extended CO source with a deconvolved size of $(4.0'' \pm 1.1'') \times (1.8'' \pm 1.2'')$. It is matched in position to two galaxies in the COSMOS2015 catalog (Laigle et al. 2016; offsets of $0.14'' \pm 0.3''$ and $1.8'' \pm 0.3''$). We have confirmed its CO(1–0) redshift with ALMA through a detection of the CO(4–3) line (Pavesi et al., in prep.). The cataloged photo-z for both galaxies (z_{phot}=1.8–1.9) is not compatible with the CO redshift of 1.97 within 1σ. This source is also detected at 3 GHz, with a flux of $27 \pm 3\,\mu$Jy (Smolčić et al., 2017a). The S2COSMOS survey shows a weak signal at 850μm with a significance of 3.7σ. The formal 4σ limit on the deboosted flux is < 4.0 mJy, and the tentative detection suggests a potential source at a flux level of $\sim 2 - 3$ mJy (J.M. Simpson, et al. in prep).

COLDz.GN.0: We identify the brightest candidate in the GOODS-N field with CO(2–1) line emission from GN10, a massive, bright dust-obscured starbursting galaxy (Pope et al., 2006; Dannerbauer et al., 2008; Daddi et al., 2009a). We find a CO redshift of z =5.3, showing that the previous redshift determination (z=4.04) was incorrect. Its properties are described in Riechers et al., in prep. This source is also detected at 1.4 GHz with a flux of $36 \pm 4\,\mu$Jy (Morrison et al., 2010), and by SCUBA-2 at 850μm in the SCUBA-2 Cosmology Legacy Survey (S2CLS) with a significance of 9.2σ and a flux of 7.5 ± 1.5 mJy (Geach et al., 2017).

COLDz.GN.3: We identify this source with CO(1–0) line emission from GN19, a merger of two massive, bright dust-obscured starbursting galaxies at z=2.49 found by Pope et al. (2006) and characterized in detail by Tacconi et al. (2006, 2008), Riechers et al. (2011c), and Ivison et al. (2011). It is detected by the 5.5 GHz eMERGE survey, with a flux of 9.6 ± 1.7 μJy (Guidetti et al., 2017). Its line flux is compatible with the previously measured total flux of 0.33 ± 0.04 Jy km s^{-1} from Riechers et al. (2011c). This source is also detected at 1.4 GHz, with a flux of 28 ± 4 μJy and 33 ± 4 μJy for the W and E components, respectively (Morrison et al., 2010), and at 850μm with a significance of 7.9σ and a flux of 6.5 ± 1.1 mJy (Geach et al., 2017).

COLDz.GN.31: We also detect CO(2–1) line emission from the bright, dust-obscured starbursting galaxy HDF850.1 (z=5.183), with a moderate significance of SNR=5.3. We include this line detection here given the known match, but we do not include it in the statistical analysis because it does not reach the significance threshold for detection by the blind line search. The measured flux is compatible with the previously reported flux of 0.17 ± 0.04 Jy km s^{-1} (Walter et al., 2012). It is detected by the 5.5 GHz eMERGE survey, with a flux of 14 ± 3 μJy (Guidetti et al., 2017), but is not detected at 1.4 GHz (Morrison et al., 2010). This source is also detected at 850μm with a significance of 7.1σ and a flux of 5.9 ± 1.3 mJy (Geach et al., 2017).

The other line candidates identified by our blind line search with moderate significance are to date not independently confirmed (Table B.1). Thus, we only use their properties in a statistical sense in the following, to place more detailed constraints on the CO luminosity function. We point out that three out of the seven secure, confirmed sources in our blind search belong to the high

redshift bin, and therefore suggest caution in interpreting the indicated CO(1–0) redshift, especially for those line candidates without strong counterparts. We describe the complete candidate sample in Appendix B, where we also discuss potential counterpart associations. In Chapter 4, we develop novel statistical techniques to evaluate the purity and completeness of this statistical sample, which yield the best constraints to the CO(1–0) luminosity function at z ~2–3 to date (Chapter 4).

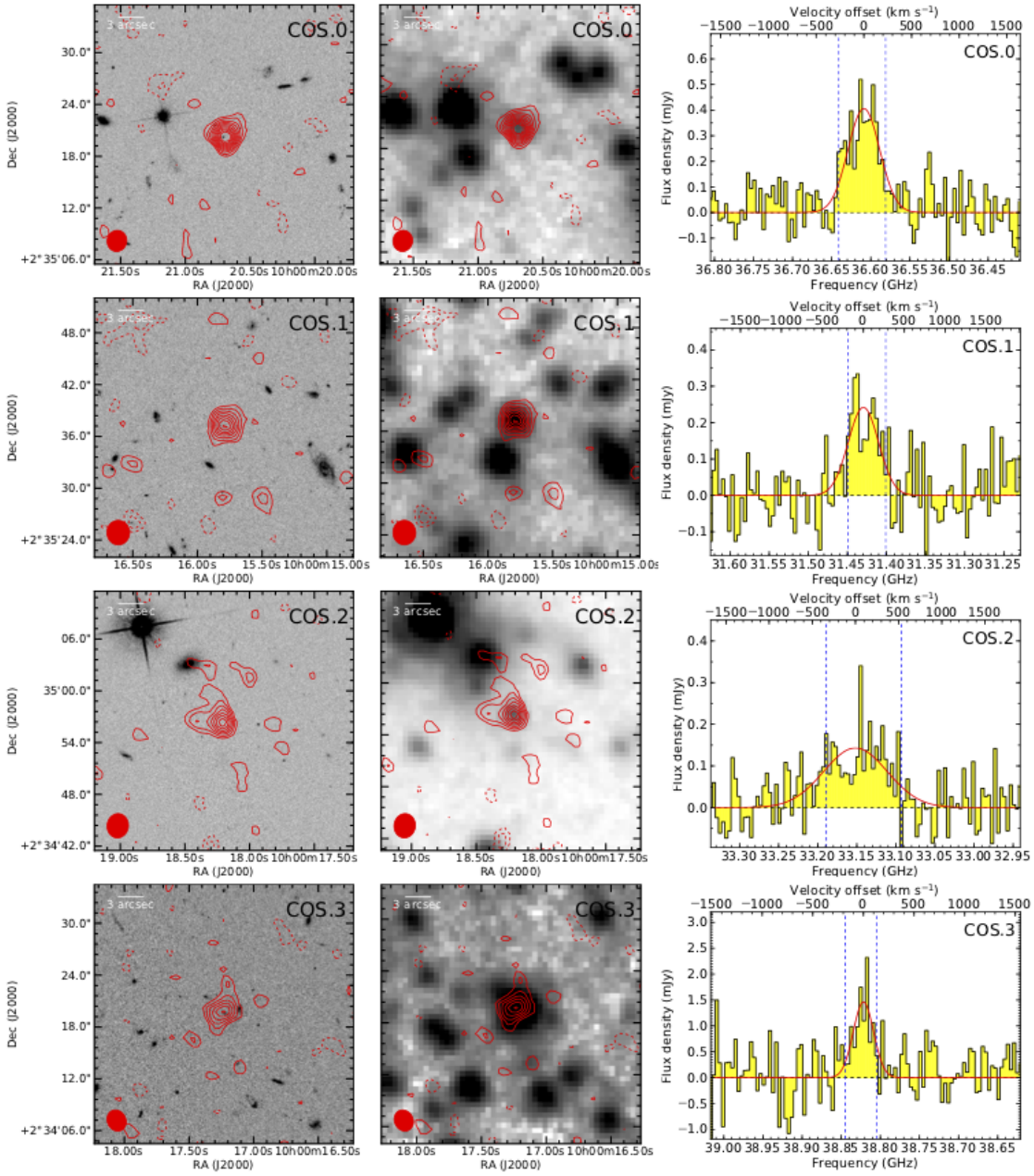

Figure 3.7: Independently confirmed candidates from our blind line search in the COSMOS field. CLEANed integrated line emission (contours) is shown overlaid on *HST* I-band (left) and IRAC 3.6 μm images (middle) from SPLASH (grayscale; Steinhardt et al. 2014). Contours are shown in steps of 1σ, starting at $\pm 2\sigma$. COS.0 corresponds to CO(2–1) emission from AzTEC-3. Right: Extracted line candidate aperture spectra ("histograms") and Gaussian fits (red curves) to the line features. The observer-frame frequency resolution of 4 MHz corresponds to $\sim$ 35 km s^{-1} mid-band. The velocity range that was used for the overlays is indicated by the dashed blue lines.

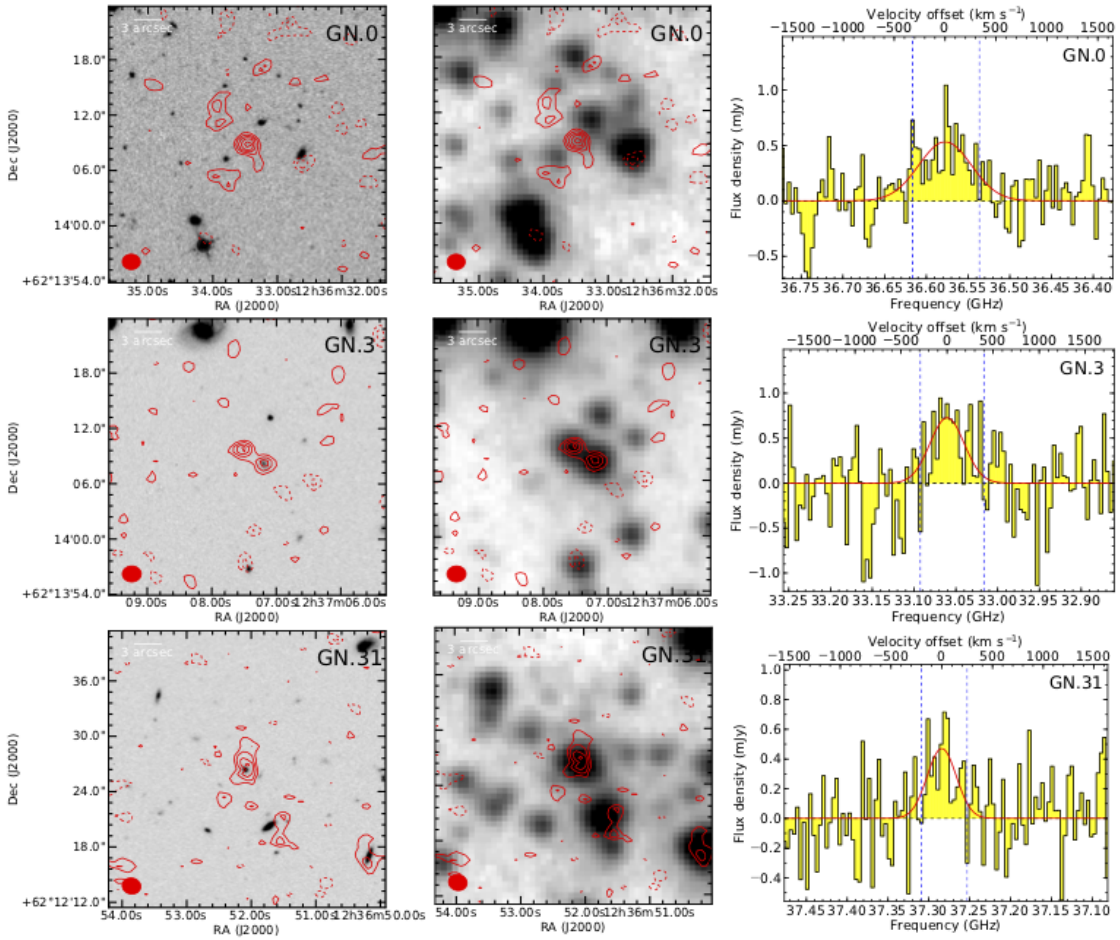

Figure 3.8: Independently confirmed candidates from our blind line search in the GOODS-N field. Integrated line emission (contours) is shown overlaid on *HST* H-band (left) and IRAC 3.6 μm images (middle; grayscale). The *HST* and *Spitzer* images were obtained from the CANDELS database. The contours are shown in steps of 1σ, starting at $\pm 2\sigma$. COLDz.GN.0 (GN10), and COLDz.GN.3 (GN19) were separately CLEANed because the high SNR allows to meaningfully deconvolve the emission. GN.31 corresponds to CO(2–1) emission from HDF850.1. Right: Extracted line candidate single-pixel/aperture spectra ("histograms"; for unresolved/resolved emission) and Gaussian fits to the line features (red curves). The observer-frame frequency resolution of 4 MHz corresponds to $\sim$ 35 km s^{-1} mid-band. The velocity range used for the overlays is indicated by the dashed blue lines.

3.6.3 Statistical counterpart matching

All SNR>6.4 candidates in COSMOS and GOODS-N have optical, NIR and/or radio/(sub)-mm counterparts (in addition to GN19 and HDF850.1). At lower SNR, it becomes more difficult to establish definitive counterparts due to the modest precision of photometric redshifts and potential (apparent or real) spatial offsets of the emission. Our purity analysis (Chapter 4) suggests that the contamination from noise is considerable. As an example, for the candidates shown below SNR=6, we may expect only 1 or 2 out of 10 to be real CO line emitters due to the large sizes of the data cubes. Therefore, we consider the lack of counterparts as a possible indication that a line candidate may be due to noise. On the other hand, the very objective of a blind search for CO emitting galaxies is to address a potential bias against optical/NIR-faint galaxies. Possible explanations for the lack of counterparts are: 1) the stellar light could be too dust-obscured to be visible in the rest-frame optical/NIR; 2) the CO line may correspond to the J=2–1 transition; placing the galaxy at $z > 5$, such that counterparts may only exist below the detection limit; 3) a CO-bright emitter may be gas-rich but have low star formation rate and/or stellar mass, which would make it optically "dark".

Optical-NIR counterparts

We here consider the uncertain line candidates near and below the SNR threshold only. If we match all $5 < SNR < 6$ candidates in COSMOS (60 in total) to the COSMOS2015 photometric catalog (Laigle et al., 2016), by requiring a spatial separation of $< 2''$ and a $z_{\rm CO10}$ or $z_{\rm CO21}$ within the 68th percentile range of the photometric redshifts, we find 10 matches. This is $\sim 2.7\sigma$ higher than

the number of matches found for random displacements of the positions of our candidates (randomly expecting $\sim 4.7 \pm 2.0$ associations). We therefore conclude that some ($\sim$ 3 – 7) of the 10 associations (out of these top 60 candidates) are likely to be real physical counterparts to real CO line emitters, in agreement with our typical purity estimate of order $\sim$ 10% for the statistical sample in this SNR interval (Chapter 4). Consistently, we also find a 1.8σ excess of positional matches within $< 2''$ for this extended candidates sample, 20 matches with a 13.8 ± 3.4 false positive rate, by spatially associating to the *Spitzer*/IRAC-based catalog by the deep SEDS survey (Ashby et al., 2013). This confirms that at least a fraction of our line candidates in the COSMOS field at these lower SNR levels may have real counterpart associations, to be confirmed by future spectroscopic observations.

We repeat the same procedure in GOODS-N, for the candidates with SNR>5.4, excluding the independently confirmed ones (51 in total). We employ the best redshifts available from Skelton et al. (2014) and Momcheva et al. (2016), using the same selection criteria with a separation requirement of $< 2''$. The grism spectroscopy does not significantly impact our matched counts, as almost all of the potential counterparts are too faint and only have photometric redshifts. We only find a slight excess relative to chance associations ($\sim 1.1\sigma$), by finding 9 associations at an expected chance rate of 6.3 ± 2.5. The latest "super-deblended" GOODS-N catalog from Liu et al. (2017) does not yield any additional associations besides the secure sources corresponding to GN10 and GN19. In addition, we search for positional matches within $< 2''$ for this extended candidate sample by searching for spatial associations in the Ashby et al. (2013) *Spitzer*/IRAC-based catalog from the deep SEDS survey. We do not find any excess of matches over the expected false positive rate .

The counterpart association signal in GOODS-N does not constitute a significant excess, perhaps due to contamination by chance associations with low redshift galaxies. However, at least approximately $\sim 6-10$ line candidates out of the top ~ 200 have a very close *Spitzer*/IRAC counterpart ($< 1''$) and a photometric redshift estimate which is compatible with the CO(1–0) line candidate, as would be expected for real counterpart matches.

In the following, we evaluate the implications of a lack of $3.6\,\mu$m counterparts for some of our lower SNR CO line candidates. The deep *Spitzer*/IRAC images in Fig. 3.7 and Appendix B are derived from the SPLASH observations (Steinhardt et al., 2014), while the *Spitzer*/IRAC images in GOODS-N were obtained as part of the legacy GOODS program (Giavalisco et al., 2004). Due to the moderate resolution of *Spitzer* observations, these images are sometimes contaminated by lower redshift galaxies or stars, reducing our ability to detect counterparts at higher redshift and hence, in those cases the following limits may not apply. In order to asses the implications of a counterpart non-detection in the IRAC 3.6μm images, we use template spectral energy distributions (SEDs) for star forming galaxies from Bruzual & Charlot (2003), redshift them to $z \sim 2.3$ and convolve them with the IRAC 3.6μm filter curve, using MAGPHYS to estimate the stellar mass limits placed by a lack of detection in COSMOS or GOODS-N (da Cunha et al., 2008, 2015a). The expected mass-to-light ratio at this wavelength depends on the stellar population ages and star formation histories, as well as on the degree of dust extinction. The following estimates are thus only indicative. We estimate that the lack of IRAC $3.6\,\mu$m counterparts at the $\sim 0.2\,\mu$Jy and $\sim 0.06\,\mu$Jy limits ($\sim 3\sigma$; Ashby et al. 2013) of the COSMOS and GOODS-N data correspond to approximate stellar mass upper limits of $\sim 6\times10^9$

and $\sim 2\times10^9\,M_\odot$ respectively at $z\sim2.3$ for a representative $A_V\sim2.5$[8]. These limits suggest that a lack of infrared counterparts implies either a very low stellar mass, or a high degree of dust obscuration. The stellar mass limits would be significantly higher for a line candidate associated with CO(2–1) emission at $z>5$. Indeed, repeating the same calculations for $z\sim5.8$ we obtain significantly less constraining stellar mass limits of $\sim1.3\times10^{11}$ and $\sim4\times10^{10}\,M_\odot$ for a representative $A_V\sim2.5$, in COSMOS and GOODS-N, respectively.

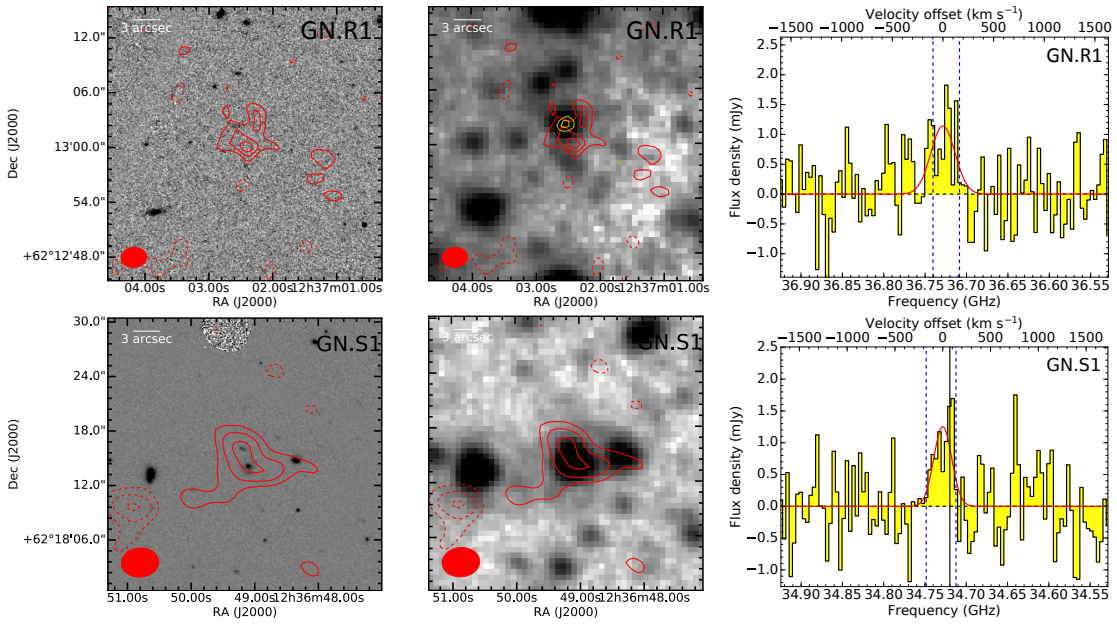

Figure 3.9: Candidates with radio continuum counterpart, and with optical spectroscopic redshift below the catalog threshold (i.e., not part of our statistical sample). Left: Line map overlays (red contours) over *HST* H-band (left) and IRAC 3.6 μm images (middle; grayscale). Red line contours show the CO line in steps of 1σ, starting at $\pm2\sigma$. Yellow contours show the radio continuum emission in steps of 2σ, starting at $\pm3\sigma$ (Morrison et al., 2010). Right: Extracted line candidate aperture spectra ("histograms") and Gaussian fits (red curves) to the line features. The frequency resolution is the same as in Fig. 3.7. The velocity range used for the overlays is indicated by the dashed blue lines. The solid black line shows the CO(1–0) frequency corresponding to the optical spectroscopic redshift of $z_{\rm spec}=2.320$.

[8]For reference, the limits would be $\sim1.6\times10^9$ and $5\times10^8\,M_\odot$ for $A_V<0.5$, and $\sim2\times10^{10}$ and $7\times10^9\,M_\odot$ at $A_V\sim5$

Radio counterparts

We also searched for counterpart matches in the deep COSMOS 3 GHz continuum catalog (Smolčić et al., 2017a), only finding associations for COLDz.COS0, COS1, COS2 and COS3 by using a 3″ search radius. Of the 18 sources from the Smolčić et al. (2017a) catalog located within the boundaries of our mosaic, our secure sources represent the only ones with a redshift estimate (photometric or spectroscopic when available) falling within our survey volume. All the remaining sources from the Smolčić et al. (2017a) catalog within our survey area lie in the range z =0.1–1.6. We performed an equivalent search in the catalog from the eMERGE 5.5 GHz survey of the GOODS-N field (Guidetti et al., 2017), finding a single association for GN19 by using a 3″ search radius. We also searched the VLA 1.4 GHz catalog of the GOODS-N field from Morrison et al. (2010) with the same criteria, finding two matches for GN19 and a radio counterpart for GN10. We also used these radio catalogs to search for counterpart associations with CO candidates to a lower significance of 5σ. We found one candidate at a SNR=5.13 which satisfies the requirement of close association with a radio source (within 3″), and with a CO redshift which is compatible with the 1σ interval for the photometric redshift listed by the optical-NIR photometric catalogs. This candidate, named COLDz.GN.R1 in the following, is at J2000 12:37:02.53 +62:13:02.1, and has an offset of 1″.7 ± 0″.6 from the radio source. We show this candidate in Fig. 3.9. The photometric redshift estimate is 4.73–5.30, which is compatible with the CO(2–1) redshift of $z_{21} = 5.277 \pm 0.001$ implied by the COLDz data. We measure a CO(2–1) line luminosity of $(8 \pm 3) \times 10^{10}$ K km s^{-1}pc^2, which implies a gas mass of $(2.9 \pm 1.1) \times 10^{11}$ M$_\odot$ for a standard $\alpha_{\rm CO}$=3.6 M$_\odot$ (K km s^{-1} pc^2)$^{-1}$ and $r_{21} = 1$. The Skelton et al. (2014) catalog reports a stellar mass of 2.8×10^{11} M$_\odot$, which suggests a molecular gas mass fraction of ~ 1. The radio

continuum fluxes are $S_{1.4\,\mathrm{GHz}} = (26 \pm 4)\,\mu$Jy and $S_{5.5\,\mathrm{GHz}} = (20 \pm 4)\,\mu$Jy (Morrison et al. 2010; Guidetti et al. 2017, respectively). This suggests a star formation rate of $\sim 200 - 400\,\mathrm{M}_\odot\,\mathrm{yr}^{-1}$ when applying the radio-FIR correlation (Delhaize et al., 2017). Although this line candidate has a higher probability of corresponding to real emission than implied by its SNR, we do not include it in the statistical analysis to preserve the un-biased (i.e., CO SNR-limited) nature of our selection.

The deep radio catalogs by Smolčić et al. (2017a) in COSMOS and by Morrison et al. (2010) in GOODS-N have a 5σ sensitivity limit of $\sim 11\,\mu$Jy at 3 GHz and 20 μJy at 1.4 GHz, respectively which can be converted to upper limits on the L_{FIR} for radio counterparts to our line candidates through the radio-IR correlation. By adopting the relationship from Delhaize et al. (2017), we deduce a detection limit of $L_{\mathrm{FIR}} < 4 - 7 \times 10^{11}\,L_\odot$ in the $z = 1.953$–2.847 redshift range. On the other hand, recent results have suggested that the radio-FIR correlation in disk-dominated star-forming galaxies may not show a redshift evolution as used by Delhaize et al. (2017) (Molnár et al., 2018). If true, this would suggest less constraining limits of $L_{\mathrm{FIR}} < 1 - 3 \times 10^{12}\,L_\odot$. The 5σ sensitivity limit of the eMERGE catalog at 5.5 GHz is approximately 15 μJy, and corresponds to limits of $L_{\mathrm{FIR}} < 8 - 14 \times 10^{11}\,L_\odot$ according to Delhaize et al. (2017), and to $L_{\mathrm{FIR}} < 2.5 - 6 \times 10^{12}\,L_\odot$ according to Molnár et al. (2018). These limits may be constraining, because our measured L'_{CO} would imply median $L_{\mathrm{FIR}} \sim 10^{12}\,L_\odot$ and $\sim 4 \times 10^{12}\,L_\odot$ based on the star-formation law (Daddi et al., 2010b; Genzel et al., 2010) for our unconfirmed line candidates in the COSMOS and GOODS-N fields, respectively. Possible reasons for the lack of radio counterparts may be due to fainter radio fluxes in our sample than expected from the radio-IR correlation, lower star formation rates than expected based on the gas masses, or that candidates may correspond to CO(2–1) emission at $z > 5$. Alternatively,

line candidates may not be real and be due to noise. The possibility of gas-rich, low star-formation rate galaxies would be particularly interesting, because surveys like the one reported here may be the only way to uncover such a hidden population.

3.7 Identification and stacking of galaxies with previous spectroscopic redshifts

Table 3.5: Low-*J* CO Counterpart Search for HDF-N PdBI Blind Mid-*J* CO Candidates.

ID	Preferred Redshift	PdBI preferred Mid-*J* line	PdBI covered Mid-*J* line	This survey Low-*J* line	Low-*J* Flux or 3σ limit (Jy km s^{-1})	$L'_{\rm CO}$ constraint
ID.01	1.88	2–1	5–4	2–1	<0.05	r_{52} >1.6
ID.02	1.81	2–1	5–4	2–1	<0.02	r_{52} >2.6
ID.03	1.78 (secure)	2–1	5–4	2–1	<0.05	r_{52} >1.8
ID.04	1.71	2–1	5–4	2–1	<0.03	r_{52} >0.9
ID.05	2.85	3–2	5–4	2–1	<0.06	r_{52} >1.2
ID.08 (HDF850.1)	5.19 (secure)	5–4	5–4*	2–1	0.17 ± 0.06	r_{52} = 0.40 ± 0.16
ID.10	2.33	3–2	3–2*/6–5	1–0/2–1	<0.03	r_{31}&r_{62} >0.7
ID.11	2.19	3–2	3–2*/6–5	1–0/2–1	<0.04	r_{31}&r_{62} >0.9
		3–2	7–6	2–1	<0.03	r_{72} >1.0
ID.12	2.19	3–2	3–2*/6–5	1–0/2–1	<0.05	r_{31}&r_{62} >0.6
		3–2	7–6	2–1	<0.03	r_{72} >0.7
ID.13	2.18	3–2	3–2*/6–5	1–0/2–1	<0.04	r_{31}&r_{62} >0.6
		3–2	7–6	2–1	<0.03	r_{72} >0.7
ID.14	2.15	3–2	3–2*/6–5	1–0/2–1	<0.04	r_{31} or r_{62} >0.8
		3–2	7–6	2–1	<0.03	r_{72} >0.7
ID.15	2.15	3–2	3–2*/6–5	1–0/2–1	<0.04	r_{31}&r_{62} >1.2
		3–2	7–6	2–1	<0.03	r_{72} >1.2
ID.17 (HDF850.1)	5.19 (secure)	6–5	6–5*	2–1	0.17 ± 0.06	r_{62} = 0.24 ± 0.10
ID.18	2.07	3–2	3–2*/6–5	1–0/2–1	<0.05	r_{31}&r_{62} >1.3
		3–2	7–6	2–1	<0.04	r_{72} >1.3
ID.19	2.05 (secure)	3–2	3–2*/6–5	1–0/2–1	<0.07	r_{31} & r_{62} >0.7
		3–2	7–6	2–1	<0.04	r_{72} >0.9
ID.20	2.05	3–2	3–2*/6–5	1–0/2–1	<0.05	r_{31}&r_{62} >0.8
		3–2	7–6	2–1	<0.03	r_{72} >1.1
ID.21	3.04	4–3	7–6	2–1	<0.04	r_{72} >0.8

Note Preferred redshifts are quoted from Decarli et al. (2014a). Although we systematically constrain every possible J line assignment that would place a CO line in our data, the asterisk marks those cases where the assignment is preferred by Decarli et al. (2014a). ID.03 has a secure redshift identification which places it outside our redshift coverage. ID.19 has a secure redshift which places it within our coverage.

3.7.1 Identification and stacking of previous mid-*J* blind CO surveys

We searched the GOODS-N dataset for low-*J* CO counterparts to the candidate mid-*J* CO detections from our previous CO blind survey in the HDF-N with the PdBI (Decarli et al., 2014a). We find a single match in our candidate list, which corresponds to CO(2–1) line emission from HDF850.1. We systematically searched for every possible mid-*J*/low-*J* CO line combination that would place a low-*J* CO line in our surveyed volume (Table 3.5). Several of these possible mid-*J*/low-*J* CO line combinations are not the preferred line identifications by Decarli et al. (2014a). Therefore, our non-detections are consistent with their preferred redshift in those cases constraining or ruling out several alternative redshift solutions allowed by the PdBI data alone. In order to search for lower significance candidate lines, we extract spectra at the mid-*J* candidate positions, and evaluate the significance of any features or place 3σ upper limits to the line fluxes. By assuming the same line FWHM as the candidate mid-*J* CO lines, we then derive limits on the line brightness temperature ratios (Table 3.5). We evaluate the signal-to-noise by spectral (1D) match-filtering of individual spectra, extracted in the central pixel and within 5 frequency channels around the expected position of the lines. We do not find any significant detections above a 3σ threshold. Some of our upper limits imply super-unity line brightness temperature ratios for the mid-*J* CO candidates. While a lower-*J* level can be less populated than a higher-*J* level, or low optical depths can cause such high line ratios, the physical conditions that give rise to such ratios are rare. In cases where super-unity line ratios are found for redshifts (i.e., mid-*J*/low-*J* CO line combinations) disfavored by Decarli et al. (2014a), our data provide support-

ing evidence for the preferred redshifts identified by Decarli et al. (2014a), under the assumption that those line candidates are real. As an example, in the case of ID.03, multiple line detections have determined a secure redshift. Since this redshift does not lie within our surveyed volume, our non-detection is consistent with the redshift identification by Decarli et al. (2014a). On the other hand, candidate ID.19 was confirmed to lie at z =2.0474 based on optical grism spectroscopy (Decarli et al., 2014a). Therefore, the candidates lies in our survey volume and our line ratio limit ($r_{31} > 0.7$) is significant. This suggests moderately elevated CO excitation compared to the average ratio found for a sample of Main Sequence galaxies at z =1.5 (r_{31} = 0.42, Daddi et al. 2015), and even compared to the average ratio ($r_{31} = 0.52 \pm 0.09$) found for a sample of sub-millimeter galaxies (Bothwell et al., 2013).

For the mid-J line candidates ID.15 and ID.18, our constraints on the line ratios are higher than unity. This suggests that an alternative lower redshift mid-J line assignment of CO(2–1) in the PdBI data may be more likely (since it would imply a redshift outside our survey volume), if the line candidate were confirmed to correspond to real emission.

We also stack the extracted spectra to obtain more sensitive limits. In particular, we select random subsets of candidates for stacking, to take into account a possible mis-identification of the correct J value for some CO lines. To search for lines in the stacked spectra, we match-filter using the same set of spectral templates as the main line search (Table 3.3). We find no line signal in the stacks above 3σ significance. Assuming an average line FWHM of 300 km s^{-1}, we therefore obtain a sensitive 3σ upper limit of 0.014 ± 0.002 Jy km s^{-1} to the line fluxes, where the quoted uncertainties on the limit depend on the number of

stacked spectra. From the same sample, we also separately stack the nine candidates for which the lines were identified as likely CO(3–2) emission by Decarli et al. (2014a), and whose redshift would place their CO(1–0) line in our data cube. We obtain a 3σ limit of ~ 0.019 Jy km s^{-1}, which implies a constraining limit of $r_{31} > 2.0$ when using the mean CO(3–2) flux in the limit (0.34 Jy km s^{-1}, using the same weights as in our stack). We estimate how many of these stacked spectra need to be removed in order for the line luminosity ratio to become smaller than unity. We find that at least six of them may not correspond to real emission, subject to the stated assumptions. In summary, we find some tentative evidence suggesting that mid-*J* blind CO searches may preferentially select galaxies with relatively high CO excitation. An alternative interpretation may be that some of the candidate mid-*J* CO emitters considered here, may be spurious and do not correspond to real CO emission. In order to more strongly differentiate between these possibilities, more sensitive 3 mm observations need to be carried out.

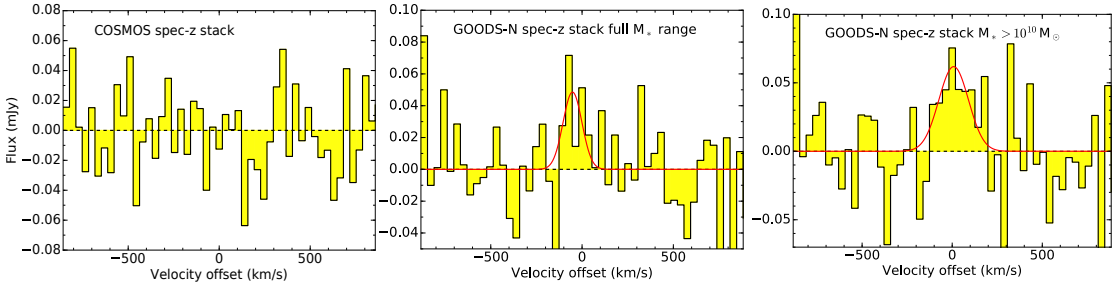

Figure 3.10: Spectral stacks of sets of galaxies with spectroscopic redshifts. Stack of galaxies with spectroscopic redshifts in COSMOS (left, 7 galaxies) and GOODS-N (right). The GOODS-N spec-z stack including the full stellar mass range (78 galaxies) displays a tentative 3.4σ detection while the stack of massive galaxies ($M_* > 10^{10}\,M_\odot$, 34 galaxies) shows a 3.5σ detection. The best-fitting Gaussian line profiles are shown in red. The spectral resolution is the same as in Fig. 3.7.

3.7.2 Identification and stacking of galaxies with optical redshifts

In order to obtain additional constraints on the CO luminosity of galaxies that remain individually undetected in the volume covered by our survey, we utilize the available optical/NIR spectroscopic redshift information for galaxies in our well studied target fields for stacking. We extract single pixel spectra of the sources described in the following, and we stack them with a weighted average. As weights, we used the inverse of the variance of the local noise following Decarli et al. (2016a). We present additional, less constraining, stacks of galaxies in the following sections, where we consider galaxies with grism redshifts and galaxies at higher redshifts, for which CO(2–1) may lie within our data.

Spectroscopic redshifts in the COSMOS field

Only seven galaxies have known ground-based optical spectroscopic redshifts that place them within our COSMOS data cube, all of which were obtained as part of the zCOSMOS-deep survey (Lilly et al., in prep.). These galaxies have relatively low stellar masses ($\lesssim 10^{10}\,M_{\odot}$). Therefore, we do not expect to detect their CO emission individually. We also do not detect their averaged CO line emission down to a deep 3σ limit of <0.008 Jy km s^{-1} (assuming a line FWHM of 300 km s^{-1}), after stacking spectra extracted at their positions (stacked spectrum shown in Fig. 3.10). This limit implies $L'_{\rm CO} < 1.7 - 2.7 \times 10^9$ K km s^{-1} pc^2 for different redshifts within our surveyed range. In order to determine the implications of this limit, we perform SED fitting of the same galaxies with MAGPHYS (da Cunha et al., 2008, 2015a) to estimate their stellar masses, finding that they

are compatible with the tabulated values in COSMOS2015 whenever the photo-z is similar to the spectroscopic redshift (only 3/7 cases). These stellar masses are in the range $10^9\,M_\odot - 10^{10}\,M_\odot$. Assuming that these galaxies lie on the Main Sequence, we use the fitting functions from Speagle et al. (2014a) to determine star formation rates (SFR) $\sim 2 - 25\,M_\odot\,yr^{-1}$. These values are consistent with the lack of detections by the 3 GHz survey by Smolčić et al. (2017a), which implies SFR$< 40 - 70\,M_\odot\,yr^{-1}$ based on the radio-FIR correlation[9] estimated by Delhaize et al. (2017). The SFRs estimated by MAGPHYS for these galaxies (with great uncertainty due to the lack of FIR detections) span the 6–150 $M_\odot\,yr^{-1}$ range, with a mean of $55\,M_\odot\,yr^{-1}$. Assuming the star formation law found for Main Sequence galaxies at high redshift[10] (Daddi et al., 2010b; Genzel et al., 2010), we can use the star-formation rate estimates to infer an expected $L'_{CO} \sim 8 \times 10^9$ K km s^{-1} pc^2, which is higher than our measured limit, and therefore not fully consistent. The adopted chain of scaling relations, including SED fitting and the star formation law have large scatter, and therefore introduce large uncertainties in the L'_{CO} estimate. The apparent tension with our upper limit would disappear if the average SFR were $\sim 10 - 15\,M_\odot\,yr^{-1}$. The non-detection of the stacked CO(1–0) emission therefore provides a valuable constraint on the CO luminosity of faint, modestly massive z = 2–3 galaxies, as our best estimates for their SFR appear to be in tension with the expectated L'_{CO} based on the star formation law by Daddi et al. (2010b); Genzel et al. (2010).

[9] Recent work by Molnár et al. (2018) suggests that radio-FIR correlation for disk-dominated galaxies may not show redshift evolution, and would imply a less constraing limit of SFR$< 100 - 300\,M_\odot\,yr^{-1}$

[10] These star formation law estimates were mostly based on CO(3–2) observations, therefore variations in the r_{31} line ratio may contribute additional uncertainty.

Spectroscopic redshifts in the GOODS-N field

The 3D-*HST* catalog (Skelton et al., 2014; Momcheva et al., 2016) provides 67 galaxies in the region in GOODS-N covered in our survey area with ground-based optical spectroscopic redshift, whose CO(1–0) line is covered by our data. We also include 13 more galaxies with more recent spectroscopic redshifts from the catalog by Liu et al. (2017) in our analysis. One of the galaxies in this combined sample corresponds to GN19 and is individually detected. Therefore, we exclude it from further investigation here.

One more galaxy with a spectroscopic redshift of $z_{\rm spec} = 2.320$ is perfectly matched, in position and redshift with a SNR=4.6 CO line candidate at coordinates J2000 12:36:49.10 +62:18:14.0 and $z_{10} = 2.3192 \pm 0.0003$, which we name COLDz.GN.S1 (Figure 3.9). This CO line candidate is significantly extended (FWHM of $\sim 9.0'' \pm 0.5'' \sim 74 \pm 4$ kpc) and appears to be associated with two, potentially interacting, galaxies with a projected separation of ~ 20 kpc. The galaxy to the south is associated with the spectroscopic redshift measurement, while the galaxy to the North has a compatible photometric redshift estimate. The total aperture CO flux of GN.S1 is (0.22 ± 0.11) Jy km s^{-1}, corresponding to $L'_{\rm CO} = (5 \pm 3) \times 10^{10}$ K km s^{-1} pc^2. We find a molecular gas mass of $(2.0 \pm 1.1) \times 10^{11}\,{\rm M}_\odot$ when assuming $\alpha_{\rm CO} = 3.6\,{\rm M}_\odot$ (K km s^{-1} pc^2)$^{-1}$. The stellar mass of the southern (brightest) component is $\sim 1.2 \times 10^{11}\,{\rm M}_\odot$, and that of the northern component $\sim 3 \times 10^9\,{\rm M}_\odot$, suggesting a high gas mass fraction ~ 1.7. This gas fraction may be elevated due to the galaxy interaction, although the star formation rate reported by Liu et al. (2017) of ~ 160 M$_\odot$ yr^{-1} is approximately $\sim 2-3\times$ lower than what may be expected from the total CO luminosity based on the star formation law (Daddi et al., 2010b; Genzel et al., 2010). There-

fore, we may be witnessing a gas-rich early phase of the merger, which may precede a starburst. This source is also tentatively detected in the S2CLS map, with a significance of $\sim 3.3\sigma$ and a 850 μm flux of 3.2 ± 1.0 mJy (Geach et al., 2017), which is compatible with the moderate star formation rate estimate.

Allowing for an offset of $< 2''$ and $< 500\,\mathrm{km\ s^{-1}}$ results in four more potential candidate association, but they are not likely to be real due to apparent offsets in the emission and because they are not associated with the most massive, or most star-forming galaxies in the sample. In the set of galaxies with spectroscopic redshifts covered by our data, nine galaxies have stellar mass estimates of $> 5\times10^{10}\,\mathrm{M_\odot}$, corresponding to a gas fraction $\mathrm{M_{gas}/M_*} \sim 1$ at our approximate 3σ sensitivity limit of $L'_{\mathrm{CO}} \sim 1.5\times10^{10}$ K km s^{-1} pc^2. These galaxies may therefore be expected to be individually detectable. Excluding GN19 and GN.S1, the remaining seven galaxies remain undetected, implying $\mathrm{M_{gas}/M_*} < 1$. Previous samples of Main Sequence galaxies at $z = 2-3$ have shown typical molecular gas mass fractions of order $\mathrm{M_{gas}/M_*} \sim 1-1.5$ in this stellar mass range (Genzel et al., 2015; Scoville et al., 2017a), i.e., higher than those limits. We note that adopting the same CO conversion factor as utilized by Genzel et al. (2015), including the correction for a stellar-mass dependent metallicity, would result in approximately 50% higher molecular gas mass estimates. Overall, the observed limits may be consistent with previous observations of the molecular gas fractions in Main Sequence galaxies, although they appear to be at the low end of the expected scatter of the relation.

Stacking all 78 spectra, i.e, excluding GN19 and COLDz.GN.S1, yields a tentative ($\sim 3.4\sigma$) CO line detection in the deep stack ($6\pm3\times10^{-3}$ Jy km s^{-1}; Fig. 3.10). The noise in this stacked spectrum is $\sim 23\,\mu$Jy beam^{-1} in 35 km s^{-1}-wide chan-

nels. The stacked galaxies in this sample have a wide range of stellar masses, and are therefore expected to show a range of CO luminosities. While constraining the average CO luminosity for this sample, we note that such an average does not represent common properties of the stacked galaxies. The measured flux in the stacked spectrum corresponds to an average CO luminosity for this galaxy sample of $L'_{\rm CO} = (1.5 \pm 0.8) \times 10^9$ K km s^{-1} pc^2 at an average $z \sim 2.4$. These 78 galaxies have a mean stellar mass of $2.1 \times 10^{10}\,M_\odot$ and an average star formation rate of $\sim 45\,{\rm M}_\odot$ yr^{-1} (with quartiles of 3.6, 22 and 66 M$_\odot$ yr^{-1}, respectively), according to Liu et al. (2017) when available, and to Skelton et al. (2014) otherwise. We also stack the subset of 34 spectra corresponding to the most massive galaxies with ${\rm M}_* > 10^{10}\,{\rm M}_\odot$, expecting them to contribute the strongest CO signal. We detect emission in this sub-stack with a significance of 3.5σ, corresponding to a line flux of $1.2 \pm 0.7 \times 10^{-2}$ Jy km s^{-1} and a line FWHM of 200 ± 80 km s^{-1} (Fig. 3.10). The line flux in the stacked spectrum corresponds to $L'_{\rm CO} = (3.2 \pm 1.8) \times 10^9$ K km s^{-1} pc^2 at an average $z \sim 2.4$, which corresponds to a molecular gas mass of ${\rm M}_{\rm gas} = (1.2 \pm 0.6) \times 10^{10}\,{\rm M}_\odot$ according to our earlier choice of $\alpha_{\rm CO}$. This gas mass should be compared to the mean stellar mass $\sim 3.6 \times 10^{10}\,{\rm M}_\odot$ of this sub-sample (with a median of $\sim 2.8 \times 10^{10}\,{\rm M}_\odot$) and the average star formation rate of $\sim 66\,{\rm M}_\odot$ yr^{-1} (median of $\sim 52\,{\rm M}_\odot$ yr^{-1}) (Liu et al., 2017). To further investigate these star formation rate estimates, we also stack SCUBA-2 S2CLS 850 μm images and derive a 3σ upper limit of < 0.7 mJy at the positions of the sample galaxies (Geach et al., 2017). Utilizing the average FIR SED from the ALESS sample, at approximately the same redshift as these galaxies, the sub-mm flux upper limit implies a star formation rate constraint of $\lesssim 60 - 100\,{\rm M}_\odot$ yr^{-1} (da Cunha et al., 2015b). A modified black body model with a dust temperature of $T_d = 35$K also implies comparable limits. We find that

the star formation rate of this set of galaxies is compatible with random scatter around the star-forming Main Sequence reported by Speagle et al. (2014a). The average expected CO luminosity based on the star formation law (Daddi et al., 2010b; Genzel et al., 2010) may be higher than our measurement by about a factor of 3 ($L'_{\rm CO} \sim 9.6 \times 10^9$ K km s^{-1} pc^2).

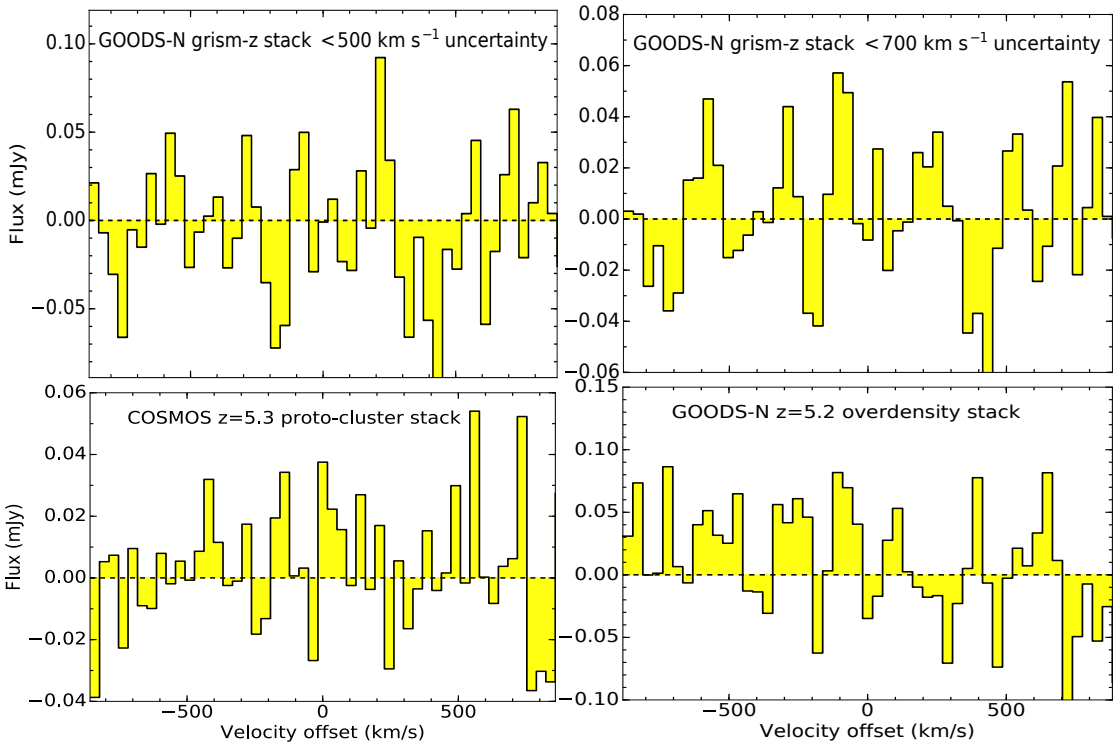

Figure 3.11: Additional spectral stacks of sets of galaxies with spectroscopic or grism redshifts. Top: CO(1–0) stacks of subsets of galaxies with the highest quality grism spectra, with redshift uncertainty <500 (left) and <700 km s^{-1} (right), respectively. Bottom: CO(2–1) stacks for samples of potential $z > 5$ galaxies belonging to previously identified over-densities in our fields, i.e. the AzTEC-3 proto-cluster at z =5.3 (left) and the overdensity around HDF850.1 (right; Capak et al. 2011; Walter et al. 2012). The spectral resolution is the same as in Fig. 3.7.

COSMOS proto-cluster at $z = 5.3$

We search for CO(2–1) from nine member galaxies of the AzTEC-3 proto-cluster, as identified through the Lyman Break (LBG) technique and color selection by Capak et al. (2011). While two of them show a hint of a CO emission line signal ($\sim 2.5\sigma$), all others (including LBG-1, the one with the strongest [CII] emission; Riechers et al. 2014a and in prep., Capak et al. 2015), are consistent with noise. The positions of the LBGs with tentative CO detections are J2000 10:00:21.96 +02:36:08.5; and 10:00:20.13 +02:35:53.9. Assuming a line FWHM of 250 km s^{-1} (i.e., the width of the [CII] line in LBG-1) we derive CO line fluxes of approximately 0.03 ± 0.012 Jy km s^{-1}, corresponding to $L'_{\rm CO21} = 7 \pm 3 \times 10^9$ K km s^{-1} pc^2. We do not claim any detections due to the low significance and only quote these as approximate limits for reference. We also stack all spectra at the positions of LBGs (limited to the seven galaxies that are not contaminated by emission from the bright CO(2–1) line in AzTEC-3 at the resolution of our survey), and do not detect a significant signal (Fig. 3.11). We therefore place a 3σ limit of <0.012 Jy km s^{-1} on their average CO(2–1) emission, corresponding to $L'_{\rm CO21} < 3 \times 10^9$ K km s^{-1} pc^2. The average stellar mass for the stacked LBGs, as reported by the COSMOS2015 catalog, is $4 \times 10^9\,{\rm M}_\odot$. If we assume an $\alpha_{\rm CO} = 3.6\,{\rm M}_\odot$ (K km s^{-1} pc^2)$^{-1}$, we obtain a gas mass upper limit of $< 1.1 \times 10^{10}\,{\rm M}_\odot$, and therefore a gas fraction of ${\rm M_{gas}/M_*} < 3$ which is not strongly constraining. None of the LBGs are detected in 3 GHz radio continuum emission (Smolčić et al., 2017a). This would place a limit of $< 165\,{\rm M}_\odot\,{\rm yr}^{-1}$ on their star formation rate if we adopted the redshift evolution of the radio-FIR correlation measured by Delhaize et al. (2017). This may be converted to an expected limit of $L'_{\rm CO} < 2.2 \times 10^{10}$ K km s^{-1} pc^2 by assuming the star formation law (Daddi et al., 2010b; Genzel et al., 2010). This limit is higher than what we derive from our CO non-detection, implying

that our deep observations provides strong constraints on the CO luminosity of $z > 5$ LBGs.

Grism redshifts in the GOODS-N field

The 3D-*HST* catalog (Momcheva et al., 2016) contains 694 galaxies in GOODS-N with grism redshifts, for which the CO(1–0) line is covered by our data. Nevertheless, the majority of these grism spectra do not significantly improve the redshift determination over the photometric redshift, and are therefore not usable for stacking. We search for matches to our line search candidates (down to 4σ) within a radius of 2″ and $\sim$ 500 km s^{-1}. We find 16 potential matches and assess the contamination by chance association by also matching our blind detection catalog to 694 random positions within the signal data cube. We find that the distribution due to random associations is well described by a Gaussian with mean 8 associations and a standard deviation of 3.5 associations. Therefore, the majority of our line associations are likely to be random, but some may be expected to be real. The measured line fluxes of these candidate counterparts would imply gas masses that are sometimes larger than the stellar masses. This is possible, but we consider it more likely that those cases may be random noise associations.

We also stack the spectra extracted at the positions of the galaxies with high quality grism redshift (Fig. 3.11). 37 of them have redshift uncertainties less than 500 km s^{-1} (based on the 95th percentile of the redshift probability distribution reported by Momcheva et al. 2016), and 35 more have redshift uncertainties less than 700 km s^{-1}. At this level of uncertainty, it would be likely that a fraction of the line signal contributes to the stacked spectrum. Both of these stacks show no

detection. Assuming a line FWHM of 300 km s^{-1}, this implies 3σ upper limits of <0.011 and <0.008 Jy km s^{-1} ; corresponding to $\lesssim$3 and 2 $\times$10^9 K km s^{-1} pc^2, respectively.

HDF850.1 z = 5.2 galaxy overdensity in GOODS-N

We also search for potential CO(2–1) emission from galaxies in the $z \sim 5.2$ overdensity around the sub-millimeter galaxy HDF850.1 (Walter et al., 2012), taking advantage of the abundance of available spectroscopic redshifts in this region. 24 of the 105 galaxies with spectroscopic redshifts presented in that work fall within our data, but none of them are individually detected. We stack the spectra to obtain an average spectrum (Fig. 3.11). No significant emission is found after stacking. Assuming a line FWHM of 300 km s^{-1} implies a 3σ upper limit of <0.015 Jy km s^{-1}, and $L'_{\rm CO21} < 3.5\times10^9$ K km s^{-1} pc^2 at $z \sim 5.2$. We match these 105 galaxies to galaxies within 1'' in the photometric catalog by Skelton et al. (2014), finding 83 matches, but we do not adopt their stellar mass estimates because the redshifts of these galaxies were often greatly under-estimated.

Implications

Figure 6.4 summarizes our constraints on the molecular gas mass fraction in the analyzed samples of galaxies. In order to convert CO luminosity to molecular gas mass, we consider two different assumptions for $\alpha_{\rm CO}$. First, we assume a constant value of $\alpha_{\rm CO}$ = 3.6 M$_\odot$ (K km s^{-1} pc^2)$^{-1}$ adopted by some previous studies (e.g., Daddi et al. 2010b; Decarli et al. 2014a; Walter et al. 2016). We then also consider a metallicity-dependent conversion factor, evaluated by assuming

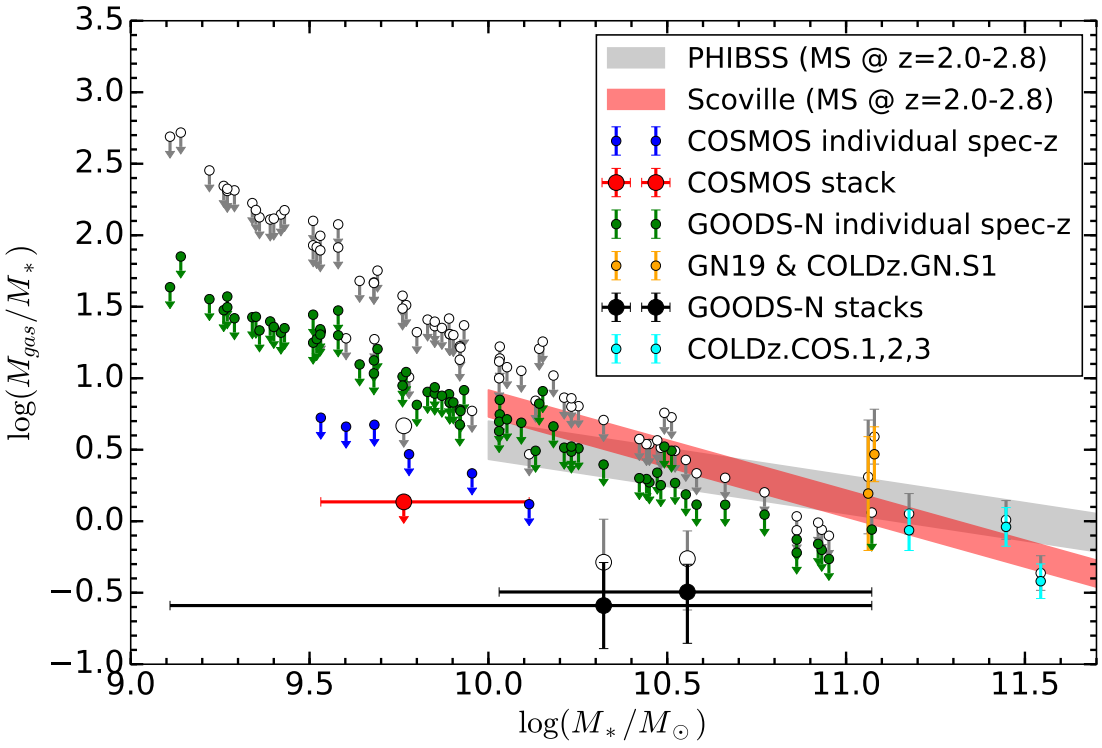

Figure 3.12: Molecular gas mass fraction constraints for galaxies with known spectroscopic redshifts for which the CO(1–0) emission can be constrained by the COLDz data. The points in color assume α_{CO}=3.6 $M_\odot$ (K km s^{-1} $pc^2)^{-1}$, while the gray points correspond to adopting the metallicity-dependent α_{CO} from Genzel et al. (2015). All upper limits correspond to 3σ limits, and assume a line FWHM of 300 km s^{-1}. The sets of individual galaxies, the origin of their stellar masses and the constraints from stacking are described in Section 6. The grey and red shaded regions correspond to the reported average expected gas mass fraction in the range $z \sim 2.0 - 2.8$ for Main Sequence galaxies according to Genzel et al. (2015) and Scoville et al. (2017a), respectively. These regions do not show the expected scatter, but rather represent the evolution within the covered redshift range. The shown scaling relations were measured over the stellar mass range $M_* \gtrsim 10^{10} M_\odot$.

a redshift and stellar mass-metallicity relation (Genzel et al., 2015). Previous studies investigating optically and FIR-selected galaxy samples have estimated the relationship between gas mass fraction, stellar mass, redshift and SFR-offset from the Main Sequence (e.g., Genzel et al. 2015; Scoville et al. 2017a). While the PHIBSS project estimated molecular gas masses by measuring the CO(3–2) line

emission (Tacconi et al., 2013; Genzel et al., 2015), Scoville et al. (2016, 2017a) have used the flux on the Rayleigh-Jeans tail of the dust continuum emission to estimate the total gas masses. We here assume that the samples of galaxies plotted, although not complete to any degree due to their pre-selection for having a spectroscopic redshift, may be somewhat representative of the star-forming Main Sequence (Figure 6.4). Their star formation rates are consistent with scatter around the Main Sequence and appear to include as many galaxies above and below the Main Sequence estimated by Speagle et al. (2014a). Although our CO detections (both blind and with previous spectroscopic redshifts) are indicative of gas fractions compatible with or above (GN19) expectations for Main Sequence galaxies, the individual CO non-detections and the stacked signal appear to be systematically lower than the predicted averages, suggesting lower gas mass fractions than might be expected (Figure 6.4). We can quantify the apparent deficit in stacked signal relative to expectations for the $M_* \gtrsim 10^{10}\,M_\odot$ sample, by calculating expected gas masses for the individual stacked galaxies, predicted as a function of their redshift, stellar masses and star formation rates. The expected sample average molecular gas mass is $5.8 \times 10^{10}\,M_\odot$ adopting the best fit relation by Genzel et al. (2015) and $7.5 \times 10^{10}\,M_\odot$ according to the relation by Scoville et al. (2017a). The constant CO luminosity conversion factor above would imply a ratio between expected and observed stacked CO luminosity of 4.8 ± 2.4 and 6.3 ± 3.1 according to the relations by Genzel et al. (2015) and by Scoville et al. (2017a), respectively. Applying instead the metallicity dependent CO conversion factor suggested by Genzel et al. (2015) to individual galaxies would somewhat reduce the tension, implying ratios of 3.0 ± 1.7 and 3.8 ± 2.1 according to the relations by Genzel et al. (2015) and by Scoville et al. (2017a), respectively. While the constraints for low stellar mass galaxies may be com-

patible with an evolving CO conversion factor due to low metallicity, this is unlikely to resolve the apparent conflict at the high mass end, and may point to lower than expected gas masses.

3.8 Total CO line brightness at 34 GHz

One additional key measurement that becomes possible with the COLDz survey is to determine the total CO line brightness at 30–39 GHz in the survey volume. We follow the simple procedure outlined by Carilli et al. (2016), and as a first conservative estimate, include only the independently confirmed line candidates, for each field in order to derive secure lower bounds. We derive lower brightness temperature limits (since we only include the securely detected sources, without any completeness correction) at the average frequency of 34 GHz of $T_B \gtrsim 0.4 \pm 0.2\,\mu$K for the COSMOS field and $T_B \gtrsim 0.05 \pm 0.04\,\mu$K for the GOODS-N field, respectively. The uncertainties are dominated by Poisson relative uncertainties, due to the limited number of sources considered. Sources near the knee of the CO luminosity function (Chapter 4) dominate the total surface brightness, as expected. Since the two measurements are sensitive to different parts of the CO luminosity function, we add the two values to obtain our best estimate for a lower limit on the average surface brightness of $T_B \sim 0.45 \pm 0.2\,\mu$K. Next, we attempt to include a longer list of candidates, down-weighted by their purities (evaluated in Chapter 4), to estimate a plausible uncertainty range. In the COSMOS field, also including all moderate SNR candidates presented in Table B.1, we obtain $T_B \sim 0.48\,\mu$K and $T_B \sim 0.57\,\mu$K without and with the completeness corrections evaluated in Chapter 4, respectively. In the GOODS-N field, also including all candidates in Table B.1, we obtain

$T_B \sim 0.18\,\mu$K and $T_B \sim 0.3\,\mu$K without and with the completeness corrections, respectively. Because the complete candidate list in GOODS-N overlaps in flux ranges with the candidates in COSMOS, it is not clear that the best estimate for this case may simply be derived by adding the two contributions; the plausible range of values from our data should therefore be considered to be the full range $T_B \sim 0.2 - 0.6\,\mu$K, with a likely lower limit of $T_B \sim 0.45 \pm 0.2\,\mu$K. These measurements are consistent with that of $T_B \sim 0.94 \pm 0.09\,\mu$K at 99 GHz by Carilli et al. (2016) within the expectation that the total (all CO lines) average surface brightness may slightly increase between 34 GHz and 99 GHz due to adding more CO transitions together (e.g., Righi et al. 2008). Our measurement of the average surface brightness is in agreement with theoretical predictions (e.g, Righi et al. 2008; Pullen et al. 2013) which suggest a range of $T_B = 0.3 - 1\,\mu$K. Our constraints on the total CO brightness at 34 GHz suggest that the CO signal will be an important contribution to CMB spectral distortion at these frequencies, which is relevant for upcoming experimental efforts. In particular, as shown in Figure 2 by Carilli et al. (2016), our constraints at 34 GHz are already higher than the PIXIE sensitivity limit (Kogut et al., 2011, 2014) and, while lower than the low-redshift Compton distortion component, it is higher than the relativistic correction to the low-redshift signal, the primordial Silk damping distortion, and the imprint of primordial hydrogen and helium recombination radiation contributions. A measurement of these important cosmological probes will therefore necessarily require a subtraction scheme that will remove the CO line signal (also see Carilli et al. 2016).

3.9 Discussion and Conclusions

In this work, we have carried out the first blind search deep field targeting CO(1–0) line emission at the peak epoch of cosmic star formation at $z = 2$–3. This allowed us to provide the least biased measurement of the molecular gas content in a representative sample of galaxies at this epoch. One of our main findings is the absence of a population of massive, gas-rich galaxies with suppressed star formation in our high signal-to-noise sample, which would have been missed by previous selection techniques. The lower signal-to-noise, and hence lower purity, CO line candidate sample includes several candidates without clear multi-wavelength counterparts, which are therefore possible candidates for such a population of "dark", gas-rich galaxies. Nonetheless, the low purity of such candidate lines requires further, independent confirmation as the absence of a counterpart is more likely to indicate that the line feature may be spurious.

Interestingly, the CO line sources detected with confidence in this study include a mix of different galaxy populations. In particular, our sub-sample of independently confirmed CO emitters contains previously known starbursts like AzTEC-3 (by design), GN10, GN19, and HDF850.1 but also COLDz.COS.1, 2 and 3 and COLDz.GN.S1 which belong to the massive end of the Main Sequence at $z \sim 2$ (Pavesi et al., in prep.). This highlights the CO(1–0)-based selection, which does not preferentially select outliers in star formation such as starbursts as preferentially selected by sub-millimeter continuum selected samples. Also, the total gas mass is accurately traced by these measurements, without the extinction biases that affect optical/NIR selected samples.

Most studies of molecular gas in galaxies at high redshift to-date have targeted mid-*J* CO lines. Although these lines have higher fluxes than the ground state, *J*=1–0 transition, and therefore are typically easier to detect, their higher critical densities and level energies imply that they do not always faithfully trace the bulk of the gas mass, but that they can be biased towards the dense and warm fraction of the gas reservoir. Therefore, in order to derive gas masses from those mid-*J* CO lines, an excitation correction needs to be assumed (i.e. a ratio of those lines to the CO(1–0) line brightness), which introduces a source of uncertainty. Previous blind CO searches have targeted mid-*J* CO lines (Decarli et al., 2014a; Walter et al., 2016), and therefore relied on similar excitation correction assumptions in order to derive constraints to the total molecular gas mass. In this study, we have shown that blind CO(1–0) searches, selecting galaxies uniquely through their total gas masses, find a varied sample of galaxies belonging to a mix of different populations, which may be characterized by significant differences in CO excitation (e.g., starbursting and Main Sequence galaxies; Daddi et al. 2010b; Carilli & Walter 2013; Riechers et al. 2006a, 2011a,b; Ivison et al. 2011; Bothwell et al. 2013). We also find significant excitation differences among the individual sources (to be described in detail by Pavesi et al., in prep.). Furthermore, our limits on the CO(1–0) line luminosities in the candidates previously selected by Decarli et al. (2014a) indicate that the corresponding galaxies either have substantially elevated CO excitation, or that a large fraction of them may not correspond to real line emission.

The so called "wedding cake" design of the COLDz survey, targeting a shallow wide field and a deep narrower field, allows us to provide valuable, independent constraints to different parts of the CO luminosity function (Chapter 4) which would not have been possible with a single field due to the limited ac-

cessible volume and depth. While the sensitivity of our deeper field (in COSMOS) is within a factor of two of the sensitivity that was previously achieved by ASPECS through ALMA in a comparable redshift bin (after correcting for CO excitation), the volume that we could sample in that field is six times larger. Furthermore, the volume covered in both fields combined is >50 times as large as that covered by ASPECS-Pilot and > 60 times as large as that carried out in the HDF-N with the PdBI, given the > 60 times larger survey area (~60 vs ~1 arcmin^2).

In this study, we have also significantly further developed the methods utilized to carry out blind searches for emission lines in interferometric datasets. In particular, we have generalized the Matched Filtering technique that is commonly used in the spectral dimension to identify spectral lines, to the regime of interferometric data cubes where sources may be spatially extended. By taking advantage of this new source selection method, we have blindly detected significantly extended CO(1–0) line sources like COLDz.COS.3, which hosts a very large cold gas reservoir ($\sim$ 30 – 40 kpc). Furthermore, one of our highest SNR line emitters in the GOODS-N field (GN19) and a galaxy with optical spectroscopic redshift (COLDz.GN.S1), also appear extended ($\sim$ 40 – 70 kpc) in CO observations due to a major gas-rich merger in this galaxy (see also Riechers et al. 2011c; Ivison et al. 2011). The high incidence, two out of the eight most significant CO(1–0) sources, suggests that extended CO(1–0) sources may in fact be prevalent, in agreement with previous findings (Riechers et al., 2011c; Ivison et al., 2011). Indeed, through the blind search we have selected other CO candidates which may be significantly extended, some of which might have been missed by previous blind line search techniques searching only for unresolved sources (Decarli et al., 2014a; Walter et al., 2016; Decarli et al., 2016a).

The candidate CO lines span a large range in line FWHM, from ~ 60 km s^{-1} to ~ 800 km s^{-1}, although the narrowest ones have not yet been independently confirmed. This demonstrates the need for the inclusion of a broad range in line width templates in order not to miss a significant fraction of the signal. The spread and distribution in the line FWHM we find is comparable to those previously measured (e.g., Tacconi et al. 2013), although the occurrence of a particularly broad line (in COLDz.COS.2) in our limited, highest quality sample, suggest that there may be a larger incidence of broad lines in blindly selected CO sources, compared to optical/NIR selections. Nonetheless, due to the limited number of sources, this finding requires further, independent study.

Although the molecular gas fraction estimates for the CO detections are comparable to expectations, the lack of CO detections for a number of massive galaxies with good quality spectroscopic redshifts and the detection of their stacked CO signal suggests that molecular gas mass fractions for typical Main Sequence galaxies may be somewhat lower than expected (Figure 6.4; Genzel et al. 2015; Scoville et al. 2017a). A possible caveat to this interpretations may come from higher systematic uncertainty than expected of the optical spectroscopic redshifts used in the stacking, which may lead to missing a fraction of the CO flux in the stack. While this analysis could only be carried out on samples of galaxies with previous spectroscopic redshift measurements, its conclusion is in agreement with the finding from the blind search. In particular, if the gas mass fraction and hence the CO luminosity of the known galaxies (in addition to all other galaxies in the observed cosmic volume without spectroscopic redshifts) were closer to expectations, the number of blind CO detections would have been higher. Empirical predictions based on SED fitting and scaling relations suggest an expected number of CO emitters in the range 10–20 for our

field in COSMOS and 5–15 for our field in GOODS-N (da Cunha et al., 2013b). In addition, the high mass end of the galaxy distribution in our cosmic volume provides the strongest result for lower than expected gas masses, but also the full sample over the shown stellar mass range provides important constraints, compatible with a metallicity evolution in the CO conversion factor (Figure 6.4). The significant detection of CO emission from galaxies in the stack suggests that our dataset is rich in additional signal, that is too faint to be reliably blindly identified at the current depth, but which can be mined through spectroscopic observations at other wavelengths. We have therefore demonstrated the power of stacking the CO signal from galaxies with spectroscopic redshifts, in order to fully take advantage of the information in CO deep field data.

We have also developed statistical methods (presented in Chapter 4) to evaluate the purity, completeness and recovered candidate properties with higher accuracy than previous techniques. This enables us to infer the best constraints to date on the CO(1–0) luminosity function at z ~2–3 (Chapter 4).

With this CO deep field study, we also further demonstrate that blind CO searches are sensitive to "optically dark", dust-obscured galaxies at very high redshift, such as GN10 and HDF850.1. In particular, the massive molecular gas reservoirs of these galaxies are among the largest in our field (Riechers et al., in prep.). Our sample of new, high-SNR CO(1–0) spectra for COLDz.COS1, 2 and 3 and for GN.S1 provides a significant contribution to the state of current CO(1–0) measurements of Main Sequence galaxies at $z > 2$[11].

Finally, the Next Generation VLA (ngVLA) is necessary to significantly im-

[11]The number of high SNR CO(1–0) detections in non-quasar hosts or sub-millimeter selected galaxies is very limited to-date (Riechers et al., 2010a; Aravena et al., 2010a, 2012, 2014; Bolatto et al., 2015; Spilker et al., 2016).

prove the constraints presented here (e.g., Casey et al. 2015; Carilli et al. 2015; McKinnon et al. 2016; Selina et al. 2018a). In particular, an equivalent survey in the 30–38 GHz range with five to ten-fold sensitivity improvement for point-source detection as provided by the ngVLA will allow reaching the depth of these observations in a small fraction of the time ($\sim$ 1/50), therefore routinely reaching depths of $\log(L'_{\rm CO}/L_\odot) \sim 9.5$ in one to two hours of observation. The high survey speed of the ngVLA will uniquely enable the deep, wide area surveys which are necessary to build large statistical samples, currently inaccessible to the VLA. These future surveys will constrain the luminosity function to well below the knee, with percent precision, for a comparable observing effort as the present survey. A significant benefit of the ngVLA will also come from the planned smaller antennas, which increase the field of view for a fixed total collecting area, therefore enhancing the survey speed. In addition, the vast bandwidth of the ngVLA will allow us to simultaneously cover CO(1–0) emission over a large fraction of the age of the Universe, and will therefore allow us to probe CO(1–0) over the almost complete redshift range up to $z \sim$10.

CHAPTER 4

COLDZ: SHAPE OF THE CO LUMINOSITY FUNCTION AT HIGH-Z AND THE COLD GAS HISTORY OF THE UNIVERSE

4.1 Context

Some of the best constraints to galaxy evolution to date have been derived from the measurement of the stellar mass functions (distributions) and star formation rate functions, at various redshifts. These have been achieved by converting the observable luminosity functions at wavelengths from optical to radio. These luminosity functions describe different "views" into the galaxy population overall and, together with correlations such as the star-forming MS, provide the main constraints to cosmological models. One of the most sought after missing pieces of the galaxy evolution puzzle is characterizing the star forming gas, especially the mass of the cold molecular phase which fuels star formation. In this chapter, we achieve the main goal of the COLDz survey by providing the best constraints to date on the CO(1–0) luminosity function and the first constraints to CO(2–1). These are a proxy for the molecular gas mass distribution in galaxies at $z = 2 - 2.8$ and $z \sim 5 - 7$, respectively. In order to accomplish this goal, we use the line search and the CO line candidates described in the previous chapter and we develop new methods to estimate the reliability of our line candidates. We also characterize the completeness of our search by studying the fraction of recovered line sources which were artificially injected into our data. In the end we use a statistical method called Approximate Bayesian Computation (ABC) in order to derive statistically robust estimates of the constraints on the CO luminosity function based on our observations. By integrating these CO luminosity

functions we derive estimates of the cosmic gas density history, which is then compared to the cosmic star formation history to provide a global average on the star formation efficiency for the overall galaxy population over cosmic time.

This chapter was previously published in the *Astrophysical Journal* partly as: Pavesi, R., et al., 2018, ApJ, 864, 49. And partly as: Riechers, D., Pavesi, R., et al., 2019, ApJ, 872, 7. In collaboration with Dominik Riechers, Chelsea Sharon, Jacqueline Hodge, Roberto Decarli, Fabian Walter, Chris Carilli, Emanuele Daddi, Ian Smail, Mark Dickinson, Rob Ivison, Mark Sargent, Elisabete da Cunha, Manuel Aravena, Jeremy Darling, Vernesa Smolčić, Nick Scoville, Peter Capak and Jeff Wagg.

4.2 Abstract

We report the first detailed measurement of the shape of the CO luminosity function at high redshift, based on >320 hr of Karl G. Jansky Very Large Array (VLA) observations over an area of ~60 arcmin^2 taken as part of the CO Luminosity Density at High Redshift (COLDz) survey. COLDz "blindly" selects galaxies based on their cold gas content through CO(J=1→0) emission at z ~2–3 and CO(J=2→1) at z ~5–7 down to a CO luminosity limit of $\log(L'_{\rm CO}/{\rm K\ km\ s^{-1}\ pc^2})\simeq 9.5$. We find that the characteristic luminosity and bright end of the CO luminosity function are substantially higher than predicted by semi-analytical models, but consistent with empirical estimates based on the infrared luminosity function at z ~2. We also present the currently most reliable measurement of the cosmic density of cold gas in galaxies at early epochs, i.e., the cold gas history of the universe, as determined over a large cosmic volume

of ~375,000 Mpc^3. Our measurements are in agreement with an increase of the cold gas density from z ~0 to z ~2–3, followed by a possible decline towards z ~5–7. These findings are consistent with recent surveys based on higher-J CO line measurements, upon which COLDz improves in terms of statistical uncertainties by probing ~50–100 times larger areas and in the reliability of total gas mass estimates by probing the low-J CO lines accessible to the VLA. Our results thus appear to suggest that the cosmic star-formation rate density follows an increased cold molecular gas content in galaxies towards its peak about 10 billion years ago, and that its decline towards the earliest epochs is likely related to a lower overall amount of cold molecular gas (as traced by CO) bound in galaxies towards the first billion years after the Big Bang.

4.3 Introduction

Our basic understanding of galaxy evolution and the build-up of stellar mass in galaxies throughout the history of the universe is founded in detailed measurements of the star-formation rate density[1] as a function of cosmic time (or redshift), the "star-formation history of the universe", and measurements of the stellar mass density in galaxies at different cosmic epochs (see Madau & Dickinson 2014 for a review). In-depth studies of significant samples of high-redshift galaxies appear to indicate that changes in this growth history at different epochs are largely driven by the cold molecular gas properties of galaxies (e.g., Daddi et al. 2010a; Tacconi et al. 2013, 2018; Genzel et al. 2015; Scoville et al. 2016), and the growth rate of dark matter halos (e.g., Genel et al. 2010; Bouché

[1]Throughout this work, densities in star formation rate, stellar mass, or gas mass refer to cosmic densities (i.e., the amount of material in galaxies per unit co-moving cosmic volume) unless stated otherwise.

et al. 2010; Faucher-Giguère et al. 2011). The cold gas constitutes the fuel for star formation (see Carilli & Walter 2013 for a review), such that a higher gas content (e.g., driven by high gas accretion rates) or a higher efficiency of converting gas into stars (e.g., driven by galaxy mergers, or by ubiquitous shocks due to high gas flow rates) can lead to increased star-formation activity, and thus, to a more rapid growth of galaxies (e.g., Davé et al. 2012b).

To better understand how the gas supply in galaxies moderates the star-formation rate density in galaxies at early epochs, it is desirable to complement targeted studies with an integrated measurement of the cold molecular gas density in galaxies at the same epochs, i.e., the "cold gas history of the universe". Surveys of cold gas ideally target rotational lines of CO, the most common tracer of the molecular gas mass in galaxies, to measure the CO luminosity function at different cosmic epochs in a "molecular deep field" study. The distribution mean of the CO luminosity function then provides a reliable measurement of the cold molecular gas density at a given redshift (Carilli & Walter 2013; see, e.g., Scoville et al. 2017a for an alternative approach). The first such efforts have recently been carried out in the *Hubble* Deep Field North (HDF-N) and the *Hubble* Ultra Deep Field (H-UDF) with the IRAM Plateau de Bure Interferometer (PdBI) and the Atacama Large Millimeter/submillimeter Array (ALMA; the ASPECS-Pilot program) at 3 mm and 1 mm wavelengths, covering fields ~0.5 and ~1 arcmin^2 in size, respectively (see Decarli et al. 2014a; Walter et al. 2016, and references therein). At z ~2–3, near the peak of the cosmic star-formation rate density ~10 billion years ago, these studies cover CO(J=3→2) and higher-J lines. At z=5–7, i.e., in the first billion years after the Big Bang, these surveys cover CO(J=5→4) and higher-J lines.

The most faithful tracer of total cold gas mass are low-J CO lines, in particular, CO(J=1→0) (see, e.g., Riechers et al. 2006b, 2011a,c; Ivison et al. 2011; Aravena et al. 2012, 2014; Daddi et al. 2015; Bolatto et al. 2015; Sharon et al. 2016; Saintonge et al. 2017; Harrington et al. 2018), for which the $\alpha_{\rm CO}$=$M_{\rm H_2}$/$L'_{\rm CO}$ conversion factor from CO luminosity ($L'_{\rm CO}$, in units of K km s^{-1} pc^2) to H_2 gas mass ($M_{\rm H_2}$, in units of $M_\odot$) has been calibrated locally (see Bolatto et al. 2013 for a review), and for which no assumptions about gas excitation are required to derive the total CO luminosity. To complement the initial "molecular deep field" studies through improved statistical uncertainties measured over larger cosmic volumes and reduced calibration uncertainties due to gas excitation, we have carried out the VLA COLDz survey,[2] "blindly" selecting galaxies through their cold gas content in the CO(J=1→0) line at z ~2–3, and in CO(J=2→1) at z ~5–7, over a ~60 arcmin^2 region.

The detailed survey parameters, line search and statistical techniques, a catalog of line candidates, and an overview of accompanying papers are presented in the COLDz survey reference paper (Pavesi et al. 2018b; Chapter 3). This work focuses on the CO luminosity function measurements to result from the survey data, and the implied constraints on the evolution of the cosmic cold gas density in galaxies as a function of redshift.

Section 4 provides a brief description of the data. Section 5 summarizes the selection of CO line candidates and the statistical methods used to characterize the survey parameters, before describing the CO luminosity function and cold gas density measurements. Section 6 provides a discussion of the results in the context of previous surveys and model predictions. Section 7 provides the main conclusions based on our measurements and analysis.

[2]See `coldz.astro.cornell.edu` for additional information.

4.4 Data

The VLA was used to "blindly" observe redshifted CO(J=1→0) and CO(J=2→1) line emission (rest-frame frequencies: $\nu_{\rm rest}$=115.2712 and 230.5380 GHz) at z ~2.0–2.8 and z=4.9–6.7, respectively (VLA program IDs 13A-398 and 14A-214; PI: Riechers), covering a region corresponding to a total co-moving survey volume of ~375,000 Mpc^3 in both lines combined (see Table 4.1 for details). Observations covered a 7-pointing mosaic in the COSMOS field (center position: J2000 10:00:20.7; +02:35:17.0), and a 57-pointing mosaic in the GOODS-North field (center position: J2000 12:36:59.0; +62:13:43.5), providing total survey areas of 8.9 and 50.9 arcmin^2 at 31 and 30 GHz, respectively.[3]

Observations in COSMOS and GOODS-North covered the 30.969 to 39.033 and 29.981 to 38.001 GHz frequency ranges in a single tuning with ~8 GHz bandwidth (dual polarization) each, respectively, using the Ka band receivers and the 3-bit samplers at a spectral resolution of 2 MHz (17 km s^{-1} at 35 GHz). Observations were carried out for a total of 324 hr between 2013 January 26 and 2015 December 18 under good to excellent weather conditions in the D and DnC array configurations, and in the D→DnC and DnC→C re-configurations, yielding approximately 93 and 122 hr on source across all configurations and pointings in COSMOS and GOODS-North, respectively. This yields characteristic synthesized beam sizes of ~3″ when imaging the data with natural baseline weighting after data calibration using the CASA package, and approximately 3 times better point source sensitivity in the smaller COSMOS mosaic. The corresponding CO luminosity limits across the redshift range are shown in Fig. 4.1. More details on the observations and data reduction are given in the previous chapter.

[3]The mosaicked images made from individual pointings were trimmed at the outer edges at the 30% level of the peak sensitivity in each spectral channel.

Table 4.1: Lines, redshift ranges, and volumes covered by the COLDz survey (see Fig. 4.1 for luminosity limits across the survey volume).

Transition	$\nu_{\rm rest}$ [GHz]	$z_{\rm min}$	$z_{\rm max}$	$\langle z \rangle$	Volume [Mpc^3]
COSMOS "Deep" Field (~9 arcmin^2; ~31–39 GHz)					
CO(J=1→0)	115.271	1.953	2.723	2.354	20,189
CO(J=2→1)	230.538	4.906	6.445	5.684	30,398
GOODS-North "Wide" Field (~51 arcmin^2; ~30–38 GHz)					
CO(J=1→0)	115.271	2.032	2.847	2.443	131,042
CO(J=2→1)	230.538	5.064	6.695	5.861	193,286

Note The co-moving volume is calculated to the edges of the mosaics, and does not account for varying sensitivity across the mosaics, which is accounted for by the completeness correction.

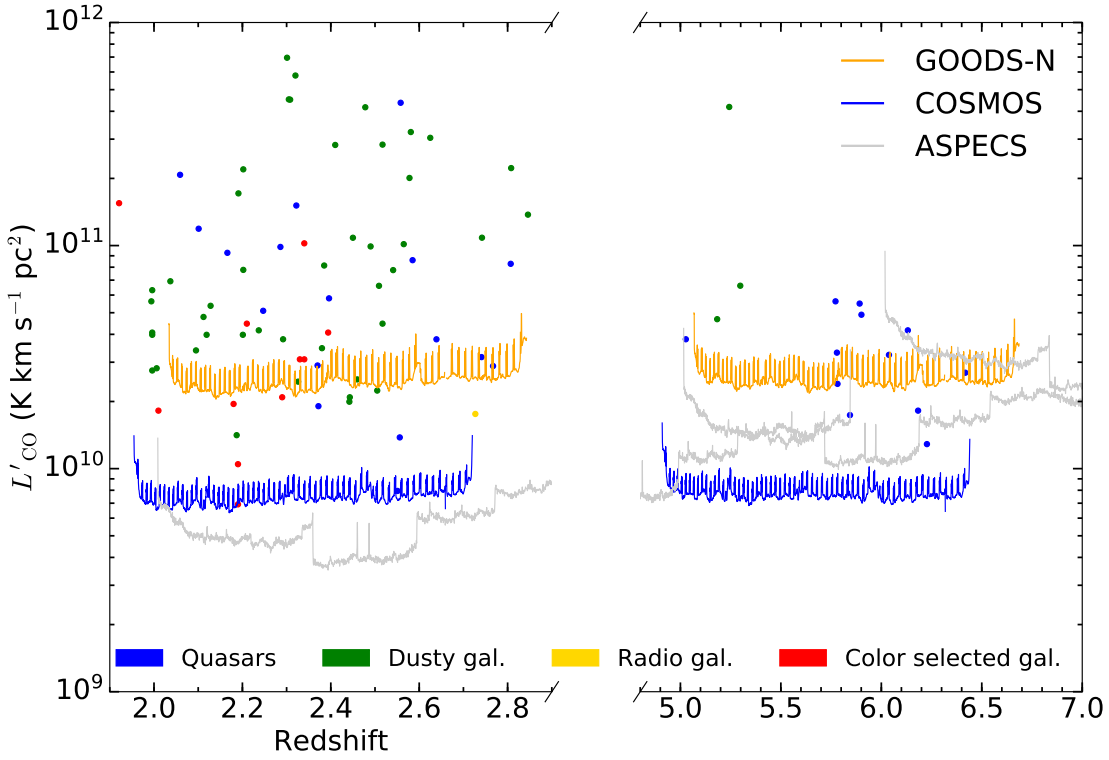

Figure 4.1: Representative line luminosity detection sensitivity limits as a function of redshift reached by our observations in the COSMOS and GOODS-North fields, when adopting 5 times the rms noise at a line FHWM of 200 km s^{-1} (see Chapter 3 for variations between individual pointings). The corresponding sensitivity limits of the ALMA ASPECS-Pilot survey in the CO J=3→2 to 7→6 lines in the same redshift ranges are shown for comparison (Walter et al. 2016). ASPECS limits are scaled to CO(J=1→0) line luminosity limits using the same, representative line excitation correction factors adopted by Decarli et al. (2016a) based on Daddi et al. (2015) up to CO(J=5→4). For the higher-J lines, we assume an intermediate excitation based on Fig. 10 of Daddi et al. (2015), corresponding to brightness temperature ratios of r_{65} ≃0.66 and r_{75} ≃0.29 relative to the CO J=5→4 line, respectively. For reference, colored points show all previous z >1 CO detections as compiled by Carilli & Walter (2013), incorporating updates by Sharon et al. (2016). Colors indicate different galaxy types ("dusty galaxies" includes submillimeter galaxies, extremely red objects, and 24 μm-selected galaxies, and "color-selected galaxies" includes Lyman-break, BzK, and BMBX galaxies, respectively).

4.5 Results and Analysis

4.5.1 CO Line Candidates

Based on our matched filtering algorithm using three-dimensional spatial/spectral templates, we find 57 candidate CO(J=1→0) and CO(J=2→1) line emitters in our survey volume down to signal-to-noise ratio (SNR) limits of 5.25 and 5.50 in the COSMOS (26 candidates) and GOODS-North (31 candidates) fields, respectively (Chapter 3). These SNR limits are chosen to provide comparable ratios of line candidates with positive fluxes over noise spikes with negative fluxes at matching SNR between both fields. This misses at least one independently confirmed CO(J=2→1) emitter, HDF 850.1 at z=5.18 in the GOODS-North field (Walter et al. 2012), which has a SNR of 5.33. Including this source, 7 out of the 58 candidates are presently independently confirmed to be real CO(J=1→0) (three sources in COSMOS, one in GOODS-North)[4] or CO(J=2→1) line emitters (one in COSMOS, two in GOODS-North)[5] through the detection of additional CO lines (see, e.g., Chapter 3; Riechers et al. 2010b, 2011c, 2014a; Walter et al. 2012). To remain robust against individual, potentially spurious candidates, all other line candidates are used only in the statistical analysis of the survey data in a probabilistic manner until independent confirmation is obtained. All candidates except the three independently-confirmed CO(J=2→1) emitters are considered to be CO(J=1→0) emitters unless stated otherwise.[6]

[4]Sources are COLDz.COS.1 to 3 and COLDz.GN.3 (GN19) in Chapter 3.

[5]Sources are COLDz.COS.0 (AzTEC-3), and COLDz.GN.0 (GN10) and 31 (HDF 850.1) in Chapter 3.

[6]This initial assumption is based on the expectation of a significantly lower space density of bright CO-emitting galaxies at $z \gtrsim 5$ compared to $z < 3$ in our current understanding. Alternative scenarios are also discussed below.

4.5.2 Statistical properties of the candidate CO emitter sample

In order to extract as much statistical information as possible from our CO candidate list, we have to evaluate: 1) the probability of each line candidate to be real, 2) the line luminosity probability function and, 3) for each luminosity bin, the completeness of our line search, i.e. the probability that a galaxy would in fact be detected by our line search, as a function of the line emission luminosity, spatial size and velocity width.

In the following sub-sections, we will describe the methods we have developed to evaluate each of these separate components, which enter the luminosity function calculation.

Reliability analysis

The purpose of a reliability (also called purity or fidelity) analysis is to consistently assign probability estimates to each line candidate to represent a real line source. In this section, we attempt to provide a general solution to the problem of evaluating purities in the case of blind interferometric line searches, which builds the foundation for our analysis.

The most accurate way to tackle this problem is to utilize the symmetry around zero of the noise distribution provided by interferometric data. This is subject to the caveat of imperfect calibration and of sidelobes of bright sources which, however, should be negligible in our case, because the continuum sources in our field are not very bright ($< 0.3\sigma$ and $< 2\sigma$ per 4 MHz channel for the brightest source in COSMOS and GOODS-N, respectively). An alternative approach would be to try and reproduce many instances of the noise dis-

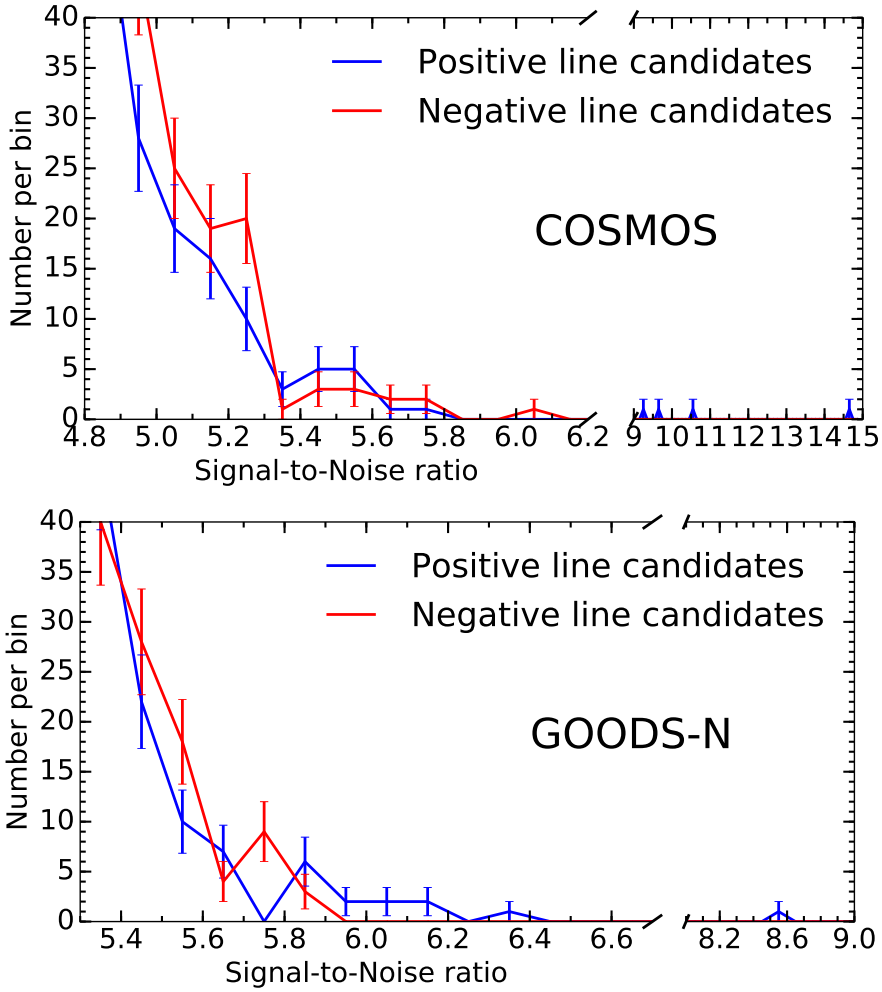

Figure 4.2: Signal-to-noise ratio distributions of our line search candidates. The blue line shows the histogram of positive line features and the red shows negative line features. Poisson errors per bin are shown. The statistical evaluation of the "excess" of positive over negative line features at a given SNR provides a measure of how many candidates may be expected to be real sources.

tribution by a well defined, simplified noise model, and to evaluate the rate of false positive detections as a function of SNR. However, this procedure may be strongly dependent on precisely capturing the statistical correlation properties of the noise (e.g., González-López et al., 2017). We therefore run an equivalent blind line search for negative line features in our data, in order to estimate the contamination due to noise. We show the comparison of the distributions of

SNR for positive and negative lines in Fig. 4.2, which were used in the following to estimate the reliability for each positive line candidate. In the following, we apply Bayesian techniques to obtain estimates of the purities that are subject to well controlled assumptions.

The basic idea is to estimate the significance of the excess of positive over negative features at a given SNR. Any excess can be considered indication that a fraction of the positive features may correspond to real line signal. Some previous studies have taken a "cumulative" approach to this problem, and used the ratio of the number of positive and negative features with SNR greater than the SNR of the line under consideration, utilizing this ratio to estimate purities (e.g., Walter et al. 2016). This may cause a substantial bias for purities that refer to individual candidates. In particular, the presence of high SNR real candidates would raise the purity of moderate SNR positive features. We therefore choose a "differential" approach, but we also choose not to use bins in SNR. This choice is motivated by the small number of candidates in the bins of interest, which would make the results highly dependent on the precise binning of the SNR axis. We therefore model the occurrence rate of lines as an inhomogeneous Poisson process along the SNR axis, with a parametrized mean occurrence rate per unit SNR interval (see Section 14.5 of Gregory 2010, for an introduction). We can then use the machinery of Bayesian inference to study the posterior probability distribution for the rate of real sources and noise spikes, and therefore infer purities for each line candidate.

In order to derive our final likelihood function, we first consider a case where we group line candidates in bins of SNR. While the result of this calculation already has wide applicability and offers certain benefits (e.g., by avoiding any

parametric assumptions for the source and noise distributions), binning introduces an unnecessary dependence on bin choice, and does not allow to capture the intrinsic continuity of the source and noise rates as a function of SNR. Therefore, we will follow the standard procedure and take the limit in which the bins are small, such that each bin contains at most one detection, thereby eliminating the bias introduced by binning (e.g., Gregory & Loredo 1992). In each SNR bin, the task at hand is to determine the probability distribution for the fraction of line detections that are real sources rather than noise.

As a starting point, we infer a model for the noise distribution by fitting a Poisson process to the distribution of negative line features. Complex modeling for the noise feature occurrence rate is not necessary for estimating purities because in the moderate SNR regime of interest, the uncertainty will be dominated by shot noise due to the small number of candidate features. We therefore assume the Poisson rate (i.e., the expected number of negative lines per bin) to be well described by the tail of a Gaussian as a function of SNR, centered at zero. We fit for the normalization and width, of this Gaussian and thereby obtain a probabilistic description of the noise. The adopted two-parameter Gaussian tail model provides an excellent fit to the distribution of negative features. We stress that this method does not rely on the assumption of a Gaussian noise distribution, but it rather represents a convenient fitting function which takes advantage of the smoothness of the underlying noise distribution as a function of SNR. This method avoids using discontinuous bins or discontinuous cumulative functions, and allows us to exploit the symmetry between positive and negative noise features to generalize the noise realization provided by the negative features, and to estimate the probability of any positive line candidate to also be due to noise.

In the following, we derive purities using SNR bins. We then consider the continuum limit, as explained above. The quantity of interest is the probability of having $N_{s,i}$ real sources in the i-th SNR bin, given that we observed $N_{o,i}$ lines, $p(N_{s,i}|N_{o,i}, \mu_{b,i})$. Here, $\mu_{b,i}$ is the mean number of noise lines expected in the i-th bin. By explicitly introducing the dependence on the real source rate (for the Poisson process), $\mu_{s,i}$, we can calculate this probability as follows:

$$p(N_{s,i}|N_{o,i}, \mu_{b,i}) = \int \mathrm{d}\mu_{s,i}\, p(N_{s,i}|N_{o,i}, \mu_{b,i}, \mu_{s,i})\, p(\mu_{s,i}|N_{o,i}, \mu_{b,i}). \tag{4.1}$$

The first term, i.e. the probability of $N_{s,i}$ real sources once we assume a source rate, is the same as the product probability for $N_{s,i}$ sources given a source rate $\mu_{s,i}$ times $N_{o,i} - N_{s,i}$ noise features, given a noise rate of $\mu_{b,i}$:

$$p(N_{s,i}|N_{o,i}, \mu_{b,i}, \mu_{s,i}) = \frac{Pois(N_{s,i}, \mu_{s,i}) \cdot Pois(N_{o,i} - N_{s,i}, \mu_{b,i})}{\sum_{k=0}^{N_{o,i}} [Pois(k, \mu_{s,i})\, Pois(N_{o,i} - k, \mu_{b,i})]}. \tag{4.2}$$

Here, $Pois(N, \mu)$ stands for the Poisson probability for N events, given a mean μ, and the denominator in the previous expression is a normalization factor. The second term in Eqn. 4.1 is the probability for the source rate, given the observed number and noise rate, and it is therefore given by

$$p(\mu_{s,i}|N_{o,i}, \mu_{b,i}) \propto p(N_{o,i}|\mu_{s,i}, \mu_{b,i})\, p(\mu_{s,i}) = Pois(N_{o,i}, \mu_{s,i} + \mu_{b,i})\, p(\mu_{s,i}) \tag{4.3}$$

by a straightforward application of Bayes theorem.

We then follow the standard prescription for inhomogeneous Poisson processes, considering it as the case where the equally-distributed bins are so small that each bin either contains a single line or not. In this section, we use the term rate of the Poisson process to indicate the number of line feature occurrences

per unit SNR interval. In the limit of small bins, containing at most one line detection, the probability for a Poisson rate μ, (which can be assumed to take the form of a parametric function of SNR) given the list of detection SNR, is calculated by the standard formula for the likelihood of an inhomogeneous Poisson process:

$$\log p(\{SNR_i\}|\mu) = \sum_i \log \mu(SNR_i) - \int_a^b \mathrm{d}(SNR')\,\mu(SNR'). \tag{4.4}$$

Here, $\{SNR_i\}$ refers to the list of line detection signal-to-noise ratios, the a and b integration limits reflect the range of SNR that is considered for fitting, and μ is our parametric model function for the rate of lines as a function of SNR.

In the next steps, we use the occurrence rate of background, noise lines, measured from the negatives by maximizing the likelihood for the noise model. A more complex approach would include the full probability distributions for the noise model parameters in the purity evaluation. We have tested this approach and confirmed that it does not affect our purity results. In particular, using MCMC samples from the probability distribution for the noise model parameters, we have evaluated the purity of one of our moderate SNR candidates. We found that the median purity coincides with the purity evaluated with our simpler method, and that the relative scatter in the purity introduced by this uncertainty on the noise model is $\lesssim 10\%$. This is much smaller than our conservative estimate of the systematic uncertainty, which we adopt in the following. Therefore, we maximize the probability for the complete set of negative lines (range of the integral $SNR \in [4, \infty)$), while assuming a Gaussian tail model for the rate function $\mu_b = N\ \exp(-\frac{SNR^2}{2\sigma_b^2})$, in order to determine the parameters N and σ_b. To determine the purity/reliability of each object, we calculate the proba-

bility that its "small bin" contains one real source and zero noise lines. Eqn. 4.2 therefore gives

$$p(N_s = 1|N_o = 1, \mu_b, \mu_s) = \frac{\mu_s}{\mu_s + \mu_b}, \tag{4.5}$$

and hence Eqn. 4.1 becomes

$$\begin{aligned} \text{purity}_\text{k} &= p(SNR_k \text{ is real}|\{SNR_i\}, \mu_b) = \\ &\int \mathrm{d}\mu_s(SNR_k) \frac{\mu_s(SNR_k)}{\mu_s(SNR_k) + \mu_b(SNR_k)} p(\mu_s|\{SNR_i\}, \mu_b). \end{aligned} \tag{4.6}$$

The last term is important, and represents the probability distribution for the source rate parameters (replacing Eqn. 4.3). It can be written as the product of the probability in Eqn. 4.4 (for a rate equal to $\mu_b + \mu_s$) multiplied by priors on the source rate parameters (i.e., the last term above).

In order to compute these purities, we therefore implement a posterior probability function for the source rate μ_s, computed by Eqn. 4.4, as a function of the model parameters. We sample it using an MCMC technique, making use of the python package `emcee` (Foreman-Mackey et al., 2013). The integral in Eqn. 4.6, which corresponds to the purity of the k-th detection, is equivalent to averaging the ratio

$$\frac{\mu_s(SNR_k)}{\mu_s(SNR_k) + \mu_b(SNR_k)} \tag{4.7}$$

over these MCMC samples of source rate parameters. It may be seen as a weighted average of this ratio, weighted by the posterior probability for μ_s.

The simple parametrization adopted for $\mu_s(SNR)$ is $\mu_{s0}(\frac{SNR}{6})^{-\alpha}$. Thus, we normalize the occurrence rate of real sources at a SNR=6 and allow for a shallow power-law increase of the rate toward lower SNR values, as we expect that there may be more real faint sources than bright sources. We impose uniform, unconstraining priors on μ_{s0} and α. This parametrization is intended to only accu-

rately describe the source rate over a small range of SNR, because the line candidates of dominant interest for the purity estimation are those with 5 <SNR< 6.5.

By applying this procedure, we face a choice of the SNR range to be fitted. In the COSMOS field, we start by including all the line candidates with $SNR > 5$. This results in purities of 100% for the top candidates (with secure counterparts) and < 7% for the next objects down the list. This is caused by the large gap between SNR=5.7 and 9, where no candidates were found, and which favors a low source rate, for our assumed model for the source distribution. Our simplified Poisson model, with slowly varying source rates as a function of SNR, may only be assumed to be an accurate description of the data over a limited range in SNR. We therefore also attempt to exclude the brightest sources, and the large SNR gap without detections in the model fitting. Therefore, to obtain an upper limit on the purities, we exclude the brightest candidates and only fit the range $5 < SNR < 5.8$. This yields an upper limit on the purities of up to $\sim 10\% - 20\%$ of the top few remaining objects to be real (Fig. 4.3). In the GOODS-N field, there is no gap in the SNR distribution of the line candidates (the highest SNR source is GN10 at z>5). Therefore we include all candidates in the range $5 < SNR < 6.4$.

The procedure we have described would attribute a purity of 70% for the candidate COLDz.GN.1, of 50% to GN19 (which we manually correct to be 100% because we know it to be a real line) and in the 30%–50% range for the other SNR~6 candidates, subsequently decreasing to about 7% at SNR=5.5 (Fig. 4.3).

When utilizing these purities to assemble the CO luminosity function, we consider two possible alternative strategies which allow to estimate the effects of the systematic uncertainties introduced by our purity computation. In the first approach, we treat these purities as having 100% uncertainty, i.e. we will

draw purities (for the Monte Carlo sampling used to estimate the allowed range of the luminosity function) as independent random numbers, normally distributed around the estimated values with standard deviation equal to the purity estimate themselves and truncating at zero. The alternative approach is to implement these purities as upper limits, and to draw purities from a uniform distribution between zero and the calculated values. The latter provides a more conservative purity estimation. Therefore, the luminosity function constraints are somewhat lower in this method, although compatible between the two methods. This conservative approach attempts to implement the additional information coming from the lack of clear multi-wavelength counterparts to our moderate SNR candidates. We will present the detailed results of both approaches in the following.

The SNR thresholds adopted in Section 6 of Chapter 3 and Table 3.4 correspond to approximate purities of ~4% and ~7% for COSMOS and GOODS-N, respectively. We emphasize that previously employed definitions of purity have differed significantly. In particular, we attempt to assess the fidelity defined by Walter et al. (2016) for our candidate selection. The comparison is not straightforward, because the definition of fidelity used in that work relies on the details of their line search algorithm, but an approximate implementation of their method indicates an equivalent fidelity of approximately 80%–90% for COSMOS and 50%–60% for GOODS-N in their method.

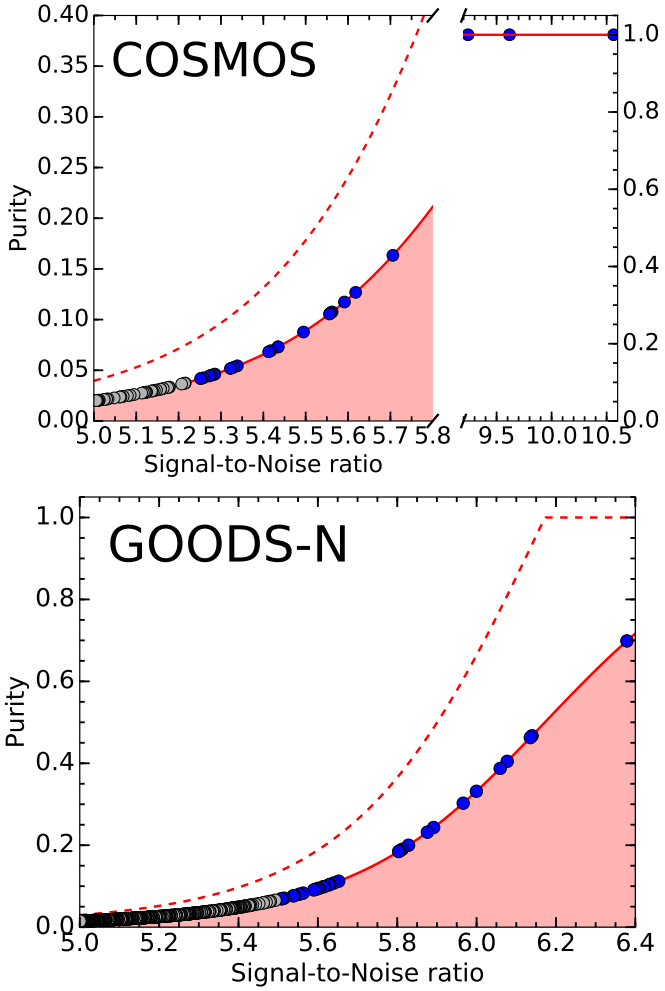

Figure 4.3: Estimated purity as a function of candidate SNR. The blue points indicate the higher significance candidates reported in this work. The purity estimation utilizes an extended candidate list down to a SNR of 5. The red shaded area indicates the SNR range that we consider for calculating purities. We also show the more conservative prescription adopted in applying purity corrections, i.e. assuming a uniform distribution for the purity, treating the calculated value as an upper limit. Our alternative prescription instead uses the calculated purities as having a Gaussian uncertainty of 100% (the upper 1σ limit is indicated by the dashed line). We do not show the highest SNR line detections corresponding to AzTEC-3 and GN10, because they correspond to CO(2–1) line emission, and they were not included in the purity estimation because of their high SNR (see text for details).

Estimating noise tail extent from data cube sizes

Due to the short-scale noise correlation intrinsic to interferometric noise (over the synthesized beam length-scale), the calculation of the highest expected SNR due to noise (both positive and negative) is not straightforward as the counting of "independent elements" is non-trivial. Vio & Andreani (2016) and Vio et al. (2017) have independently discussed a similar analysis of this case. We have reached the same conclusions, although we take a slightly different approach as we describe below. A detailed analysis of extreme value statistics in the case of smooth Gaussian random fields (which is a good approximation for interferometric noise) was developed by Bardeen et al. (1986) and Bond & Efstathiou (1987), among others, and was expanded upon by Colombi et al. (2011). Here we only summarize the main results as relevant to our data, and discuss the implications. The objective is a description of the probability distribution function for the highest SNR in a data cube which is uniquely due to noise, and how this varies as a function of cube "size". If we consider the original data cube, then noise is not correlated across different channels and a noise realization is equivalent to a 2D case, with spatial correlation only, and an area equivalent to the total area across the full cube (i.e., the sum of the areas over the independent channels). In this case, the approximate cumulative distribution function for the highest SNR (ν) to be expected from such a noise realization is given by:

$$P(\nu_{max} < \nu) \simeq \exp(-\frac{1}{4\sqrt{2\pi}} N_n \nu e^{-\nu^2/2}), \tag{4.8}$$

where N_n is the "naive" counting given by the total area divided by the "beam area" (defined by a radius equal to the beam standard deviation). The second case regards the case where correlation of the noise across channels has been introduced (for example by convolution with a spectral template in order to

Matched-Filter) and is also relevant to line searches in the form of the noise properties of Matched Filtered cubes. In this case the correlation takes place in 3D and a slightly different approximate formula describes the cumulative distribution function for the highest SNR (ν) to be expected:

$$P(\nu_{max} < \nu) \simeq \exp(-\frac{1}{6\pi\sqrt{2}} N_n \nu^2 e^{-\nu^2/2}), \tag{4.9}$$

where N_n is the "naive" counting given by the total cube volume divided by the "effective beam volume" (an ellipsoid with a radius equal to the beam standard deviation in the spatial dimension and the standard deviation of the template used in the spectral dimension). We have verified that the highest significance noise peaks measured as negative features in our data are compatible with these probabilistic predictions. We note that these distribution functions are quite broad, and only predict the highest SNR expected due to noise to be approximately in the SNR=5.5–6 range for our deeper mosaic and SNR=5.7–6.4 for our wider mosaic. This is a manifestation of the strong intrinsic stochasticity of the noise tails. We also note that the "effective number of independent elements" implied by these estimates is $\sim$ 10 and $\sim$ 20 times higher than the naive counting in the 2D and 3D cases, respectively, and that these ratios are themselves increasing functions of data cube size. The naive counting of independent elements would therefore lead to a significant underestimation of the extent of the noise tails. This conclusion is compatible with the results of Vio & Andreani (2016) and Vio et al. (2017). However, we here report equations that explicitly describe the distribution of the maximum SNR to be expected from noise rather than implicitly, through the probability distribution function of local maxima. The analysis above is only approximately equivalent to the analysis presented in Vio et al. (2017), because they express the distribution function of interest as a function of N_p, i.e., the number of local maxima in the noise realization, which

Table 4.2: Artificial sources injected sizes

	COSMOS	GOODS-N
Intrinsic spatial size (arcsec)	~0.5, ~3.0, ~4.7	1.0, 2.5, 4.5
Convolved spatial size (arcsec)	2.6, 4.0, 5.3	2–3, 3–4,4.8–5.4
Frequency width (MHz)	23.2, 46.8, 70	23.2, 46.8, 70
Velocity width (km s^{-1})	~200, ~400, ~600	~200, ~400, ~600

Note: Gaussian sizes utilized for the injected artificial sources. All sizes refer to the Gaussian FWHM. The convolved sizes are the injected sizes in the Natural-mosaic. These are fixed in COSMOS while in GOODS-N, because of the larger beam differences across the mosaic, we injected sources of fixed intrinsic sizes and convolved them to the local beam size, appropriate for each mosaic position.

is itself a random variable with its own probability distribution.

Artificial source analysis

In order to estimate the completeness and biases introduced by our line search and flux extraction methods, we perform an extensive probabilistic analysis of artificially injected sources into our maps. The main goals of this analysis is to establish a probabilistic connection between recovered candidate properties and intrinsic properties such as spatial size, velocity width and line flux. This will provide some control over the uncertainties that affect the analysis of the CO luminosity function. We also develop a method to correct the luminosity function by the completeness of our line search, which avoids a purely "per-source" completeness estimation as far as possible (due to the bias of "per-source" corrections), while avoiding assumptions that would significantly affect the result.

Since the large majority of the data cube contains very little signal, we use

the data themselves as our model for the noise, and inject artificial sources of varying size, velocity width and fluxes at random positions in the data cube (Table 4.2). We inject sources in each cube (500 in COSMOS and 2500 in GOODS-N), estimating that this will not cause crowding of the field, therefore not causing overlaps between different sources, during the line search and effectively simulating the recovery of each injected source individually. We then analyze each injected cube following the same steps of Matched Filtering in 3D that we applied to the real data, and in the end, we search for the injected sources to determine the recovered SNR, and the line parameters that would have been measured. We define the "flux-factor" as the ratio of the measured line flux to the injected flux. Therefore, the distribution of flux-factors captures both flux corrections, and uncertainties on our flux estimations. The purpose of the flux-factor analysis is not just to correct for potential biases in our flux extraction procedure, but also to estimate the uncertainty of the flux recovery. We subsequently utilize these flux probability distributions to inform our luminosity function estimates. We ignore dependencies on frequency or position of the injected sources flux-factors (determined as function of local SNR) and completeness, thereby obtaining average values that correctly sample the data for an approximately uniform distribution of real sources in our cube.

Both the completeness and the flux-factors are dependent on the source size and line FWHM. Since we only inject sources of three spatial sizes and three frequency widths, we develop a probabilistic framework to relate each line candidate to the different injected sizes (Table 4.2). For each detected candidate, based on the template size and velocity width where their signal-to-noise peaks, we determine a probability distribution of belonging to each category of "injected" spatial size and line width, therefore matching in a continuous and probabilistic

way the measured sizes to a discrete grid of intrinsic properties, as explained in detail in the following.

Flux-factors based on artificial sources

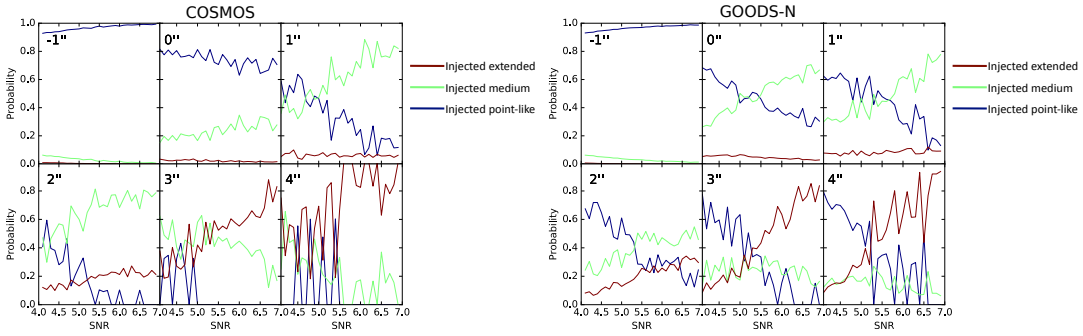

Figure 4.4: Probability of injected spatial size (proxy for "real" size) as a function of SNR, for different measured sizes (injected sizes are color-coded: smallest in blue; intermediate size in green; significantly extended in red; sizes of the artificial sources listed in Table 4.2). Measured sizes are indicated by the spatial size of the peak template (see Table 3.3). Left: Results for the COSMOS field. Right: Results for the GOODS-N field. A measured (peak-template) size of -1″ corresponds to a source which achieves its peak SNR in the Natural-mosaic, i.e. before any smoothing, at the native resolution, while the 0″ template is to a point-source template applied to the Smoothed-mosaic.

The artificial source analysis allows us to estimate how well our measured fluxes correspond to the injected flux, for candidates of different SNR, spatial size and velocity width. The objective of the flux-factor analysis is to characterize the uncertainty and bias of our flux estimates, in order to correctly estimate the uncertainty of our luminosity function measurement.

We confirm that aperture fluxes have a slight bias toward higher fluxes, because positive noise adjacent to a candidate source tend to enlarge the fitted sizes, and therefore to contribute spurious flux to the candidate (Condon, 1997). We thus need to estimate the magnitude of this bias, at the SNR range of interest ($\sim$ 5–6), to correct the measured fluxes accordingly. A correction factor

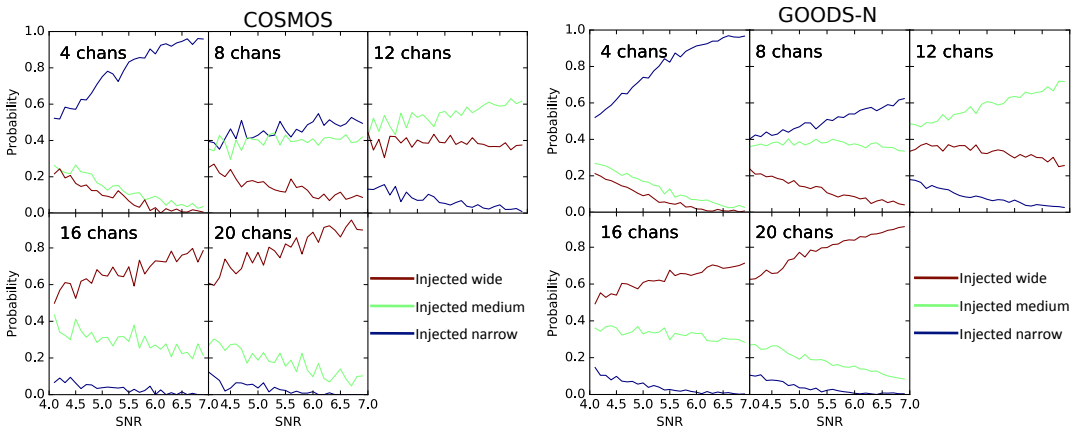

Figure 4.5: Probability of injected velocity width (proxy for "real" width) as a function of SNR, for different measured widths (injected sizes are color-coded: narrowest in blue; intermediate size in green; wide in red; FWHM of the artificial sources are listed in Table 4.2) in the COSMOS (left) and GOODS-N (right) fields. The measured FWHM are indicated by the frequency size of the peak template (see Table 3.3).

relies on an estimate of how likely a measured extended source is to be due to noise rather than real extended structure. In order to determine this bias, we need to assume an expected approximate size distribution for our sources, to be combined with information from the artificial sources, regarding how the flux is affected by the interplay of real and measured sizes.

We use the artificial sources to determine the probabilities of spatial extension (probability of being like spatial bin 0, 1 or 2 of the injected sources, Table 4.2) given the measured size, as traced by the size of the spatial template which gives the highest SNR. This probability is used in the following to relate the measured properties of each line candidate to the flux-factor and completeness, which are computed for the bins of injected properties. We use Bayes theorem to relate the probability of a given real size, conditional to a measured size: p(real-injected size | measured size) to the probability distribution that we can measure from the artificial sources, which is the probability of measuring a

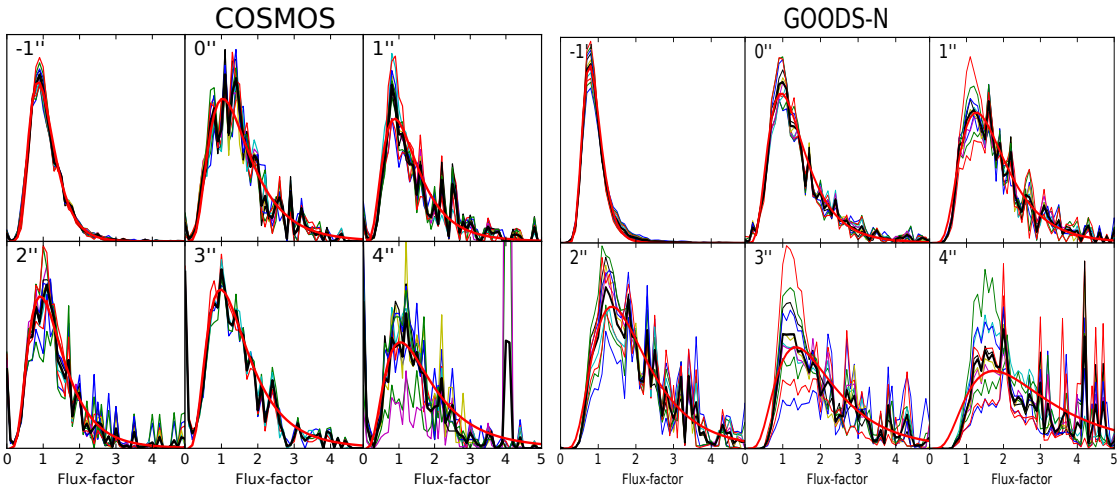

Figure 4.6: Probability distribution functions of the "flux-factor" (i.e., the ratio of measured-to-injected line flux) for the range 5<SNR<6 (in steps of 0.1σ), conditional to the measured spatial size, as indicated by the spatial size of the peak template. We also show in thick, black the mean distribution taken over the full SNR range, to obtain a more representative estimate. We fit this probability distribution by a log-normal distribution, and show the best fit model in red. On the left, we show the results for the COSMOS field and on the right for the GOODS-N field. A measured (peak-template) size of -1'' corresponds to a source which achieves its peak SNR in the Natural-mosaic, i.e. before any smoothing, at the native resolution, while the 0'' template is to a point-source template applied to the Smoothed-mosaic.

given size, conditional to a certain injected size p(measured size | injected size), by employing a prior on the expected real size distribution[7]. We must employ a prior for the probabilities of the real sizes that captures our expectation that most sources would be unresolved, while allowing for a fraction of resolved sources coming from extended gas reservoirs, merging and/or blended objects. We adopt 88%, 10% and 2% for the size bins in Table 4.2, respectively. We stress that although these relative fractions are uncertain, their precise choice does not significantly affect any of the results, because their effect is simply to modulate our assignment between line candidates and injected sources. The main

[7]Note that the artificial sources can only be used to estimate distributions conditional to a given injected size, because the relative frequency of injected sizes that was utilized (uniform) is not representative of the expected distribution of real sizes.

effect of this assignment is in the estimation of completeness corrections, where the uncertainty introduced by these priors is small compared to the systematic uncertainty introduced by choosing a weighting based on the detected size distribution.

We estimate p(measured size | injected size), by measuring the fraction of injected sources of a given size, recovered at different match-filter spatial template sizes. In this way, we compute the final posterior probability for a given measured size, to originate from an unknown "injected" size, by combining this with the prior (Fig. 4.4):

$$\begin{aligned} &p(\text{real/injected size}|\text{measured size, SNR}) \propto \\ &\quad p(\text{real size}) \times p(\text{measured size}|\text{injected size, SNR}). \end{aligned} \tag{4.10}$$

We follow the same procedure for relating the measured velocity width (from the peak template) to the injected line widths, by assuming a flat prior for the line width over the three injected bins (Table 4.2). These are required to compute the completeness of line candidates by relating their measured properties to the injected sources. The derived probability distribution functions are shown in Fig. 4.5.

In order to calculate flux-factors from the artificial sources, we employ an analogous technique. We calculate probability distributions of the flux-factors, given source spatial template size and SNR, by weighing the distribution of flux-factors found for given measured sizes, by the probability that the given measured size originates from the different possible injected sizes. Specifically, the correction ratio depends both on the injected and the measured size, as a

larger ratio is needed to correct for a compact source that appears extended: [8]

$$p(\text{flux ratio}|\text{measured size, SNR}) = \sum_{injected} p(\text{flux ratio}|\text{measured, injected, SNR}) \times \times p(\text{injected}|\text{measured, SNR}). \quad (4.11)$$

These flux-factor distributions (Fig. 4.6) can be approximated by log-normal distributions, peaking near a factor of one, but with a tail to larger ratios to correct for the bias towards larger spatial size, which is introduced by including positive noise as part of the candidate source. We stress that this is just a convenient parametrization of the measured distributions. We calculate the probability distribution of flux ratios for each measured spatial size in bins of SNR. Since the distributions are noisy due to the limited number of artificial sources, and since they do not strongly depend on SNR in the narrow 5–6 range of interest for our candidates, we consider the mean distribution over the 5 <SNR< 6 range (Fig. 4.6). The fitted log-normal curves to these mean distributions, which provide a good interpolation to the noisy distribution estimates, will be utilized in the construction of the luminosity function. We can understand the general trend seen in these shapes as follows: the smallest template selects point sources. Therefore, the distribution peaks near one. Slightly extended sources have a larger mean flux correction, reflecting the finding that they are most likely noise-smeared point sources and so their flux needs to be reduced. Slightly larger (intermediate-size) sources then require less correction, because it becomes more likely that they are somewhat extended in reality. Even larger sources show a long tail of larger flux-factors, because it is extremely un-

[8]The only distribution which can be directly estimated through counting artificial sources is conditional to injected size. We cannot marginalize over those sizes without specifying a distribution of expected source sizes first.

likely that the real source is very extended. Therefore their fluxes need to be significantly corrected (or rather, there is significant uncertainty as to their real flux, and we need to account for this in constructing the luminosity function).

Completeness

In order to estimate the completeness of our detection process, we utilize the artificial sources to measure the fraction of the injected sources that are detected. The objective of the completeness correction is to account for the fraction of the mosaic volume where a given line candidate would be detectable, and to account for the fraction of objects of given intrinsic line luminosity that would be missed by a fixed SNR threshold.

We assume that the fraction of detected lines (a proxy for the probability of detection) only depends on the integrated line flux, on the spatial size, and on the velocity width. By injecting artificial sources that uniformly sample random positions within the edges of the mosaic, we derive completeness corrections that account for the effects of the spatial and frequency variation of the sensitivity, as previously adopted by Walter et al. (2016).

While completeness is a property of the overall number counts in a luminosity bin, we partially adopt the spirit of the $1/V_{max}$ method of calculating a "per source" completeness only in so far as this depends on the line velocity width and especially spatial size of the detection. While this may potentially introduce a bias[9] (see e.g., Hogg et al. 2010), it saves us from additional assumptions about the size distribution. We therefore point out the important

[9]Regions of parameter space that have very low completeness tend to be poorly sampled and hence cannot properly be accounted for in a completeness calculation that is weighted by the detected candidates

caveat that our luminosity function estimate does not correct for missed objects due to poor sampling of the size distribution. The effect can be seen by noticing, for example, that the completeness for extended objects at low flux values drops very quickly. This is reflected in the fact that all of our low-flux objects are point sources (therefore, the completeness correction in the lowest line luminosity bins misses the potential contribution from undetected extended sources).

The completeness is measured from the artificial sources as a function of "injected" properties, i.e. injected integrated flux, and spatial size and frequency width (in three bins each, see Table 4.2), as the ratio of injected sources recovered with SNR above a threshold value of 5σ to the total number of injected sources (the precise choice of a threshold does not change the result appreciably). These measured completeness values are shown in Figure 4.7, together with the interpolating functions that we use in deriving the luminosity function: the two-parameter (I_0 and I_1) family of functions $1 - e^{-I/I_0}/(I + I_1)$, where I is the integrated line flux. While this chosen family of interpolating functions has no specific significance, we found it to provide an appropriate description of the measured completeness.

The optimal way to correct for the completeness of a luminosity function bin would require calculating the mean completeness within the bin, over the full "internal" parameter space (in our case these are spatial and velocity line sizes, frequency, and precise luminosity within the bin), weighted by the model expectation for the distribution of sources within this space. We adopt an intermediate approach between this "mean completeness" approach and a purely "per-candidate" approach. We assume that the distribution of line luminosity within a bin and the frequency distribution are uniform and average over this

subset of the internal space by randomly sampling it. On the other hand, we do not assume an intrinsic spatial size and velocity width distribution, in order to avoid biasing our result. We therefore adopt the sizes and line widths of the candidates to calculate the appropriate completeness, thereby letting the data determine the size and velocity width distributions.

In summary, for each detected line candidate, the size properties (i.e. the spatial size and frequency width) of the "real" underlying source are estimated probabilistically based on the measured size and width (from the peak template). Then, probability-weighted completenesses are the factors that enter the evaluation of the luminosity function. The dependence of these completenesses on the line flux are mean values evaluated for the full luminosity function bin, rather than depending on the candidate line flux measurement. This hybrid approach helps us mitigate the bias which would derive from a purely "per-source" correction (e.g., Hogg et al. 2010).

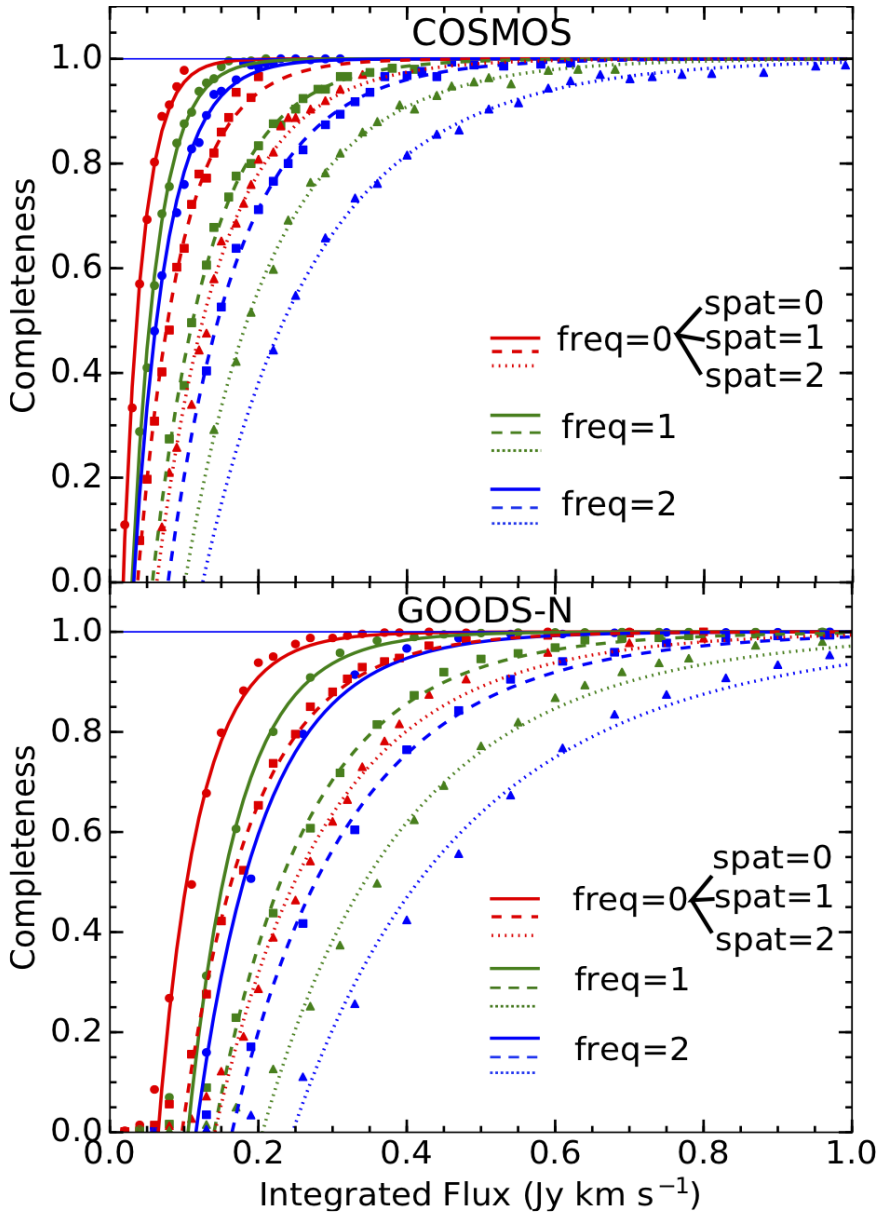

Figure 4.7: Completeness corrections calculated as a function of injected flux of the artificial sources. Top: Completeness in the COSMOS field. Bottom: Completeness in the shallower GOODS-N field. Colors distinguish the three different velocity widths of the artificial sources, and the line (marker) style distinguishes different spatial sizes. Markers represent the measured completeness, in bins of line flux, and lines represent the best-fitting interpolating functions.

Implementation of the statistical corrections

In order to assemble the luminosity function, we use a variation on the method used by Decarli et al. (2014a, 2016a). We weigh the contribution of each line candidate to the luminosity bin by its purity and inversely by its completeness, and use the total cosmic comoving volume covered within the edges of the mosaic. The completeness correction converts this volume to an effective V_{max}, for each galaxy, also accounting for the spatial variation in sensitivity. In order to estimate the systematic uncertainty introduced by our assumptions, we evaluate the luminosity function with many random realizations of flux-factor, purity assignment and luminosity bin widths and boundaries. One of the differences between our approach and the approach employed by Decarli et al. (2014a, 2016a) consists in including a larger number of candidates. We have also calculated the luminosity function using the same method employed by Decarli et al. (2016a), and the result is consistent with our more extensive method. The advantage of our approach consists in relying less heavily on the properties of the few moderate SNR, individual candidates that happen to be located near the top of the SNR list, but that still have a limited probability of being real. Although a fraction of the moderate SNR candidates are expected to be real, it is not clear that those near the top (of the set of uncertain candidates) of the SNR list have a significantly greater likelihood of being real given the limited range in SNR considered ($\sim 5-6$). By utilizing a larger sample of candidates in deriving constraints to the luminosity function, down-weighted by appropriate purities, we do not introduce additional bias, but rather better explore the implications of the systematic uncertainties. In particular, the statistical justification for a "per-source" purity and completeness correction (which we cannot fully avoid) only holds for large enough samples. By better sampling the "internal" space of possible candidate

sizes and line widths, and by adopting average per-bin completenesses (i.e., not using the uncertain, measured fluxes), we aim to achieve a more accurate completeness correction and, evaluation of the systematic uncertainties introduced by these factors.

In detail, for each $L'_{\rm CO}$ bin we calculate a completeness factor appropriate for each of the nine bins in the spatial size-frequency width grid, by averaging over 1000 random realizations of values of $L'_{\rm CO}$ in each bin, using random redshifts to calculate the corresponding integrated flux, and hence the appropriate completeness correction for each. We average over this frequency distribution and precise $L'_{\rm CO}$ within each bin. We therefore enforce a uniform prior, and maintain the dependence on the spatial-frequency size information separate. We subsequently apply them, for each line candidate, as weighted by the candidate probability distribution for its spatial-frequency size assignment. In this way, we use the measured relative occurrence of different spatial and velocity sizes as weights for the appropriate completeness, for each luminosity function bin.

In order to explore the range of luminosity function values allowed by our systematic uncertainty, we use 10,000 Monte Carlo realizations of the luminosity function calculation, for each bin width and shift, where we vary the purity assignment independently for each candidate, and the flux-factor to be applied. We therefore "move candidates around" among adjacent luminosity bins, simulating the effect of the uncertainty in their intrinsic fluxes. We separately implement the purity in one of the two ways that we previously described, either as normally or uniformly distributed. We also implement the flux correction as taking a random value drawn from the appropriate log-normal distribution, which was derived for each spatial size in the previous section. We also add a

Table 4.3: Schechter function fit parameter constraints to the CO(J=1→0) luminosity function at z=1.95–2.85 from COLDz.

Parameter	5$^{\rm th}$ percentile	50$^{\rm th}$ percentile	95$^{\rm th}$ percentile
$\log L'^{*}_{\rm CO}$	10.22	10.70	11.33
$\log \Phi^{*}_{\rm CO}$	–4.66	–3.87	–3.20
α	–0.78	0.08	0.99

Note The CO luminosity function is defined as $\log \Phi_{\rm CO} = \log \Phi^{*}_{\rm CO} + \alpha\,(\log L'_{\rm CO} - \log L'^{*}_{\rm CO}) - L'_{\rm CO}/(L'^{*}_{\rm CO} \ln 10) + \log(\ln 10)$. L' is given in units of K km s^{-1} pc^{2}. Φ is given in units of Mpc^{-3} dex^{-1}.

normal uncertainty of 20% to the measured flux, to reproduce the uncertainty in our flux calibration.

Finally, in order to describe the range of values for the luminosity function (in log comoving volume density space) spanned by our 10,000 Monte Carlo realizations, we calculate the median value for each bin and a measure of the scatter around the median. We evaluate the scatter conservatively by quoting luminosity function ranges that include 90% of the probability. We also evaluate the statistical Poisson uncertainty as appropriate for each bin as a relative uncertainty of $1/\sqrt{N}$, where N corresponds to the number of candidates in a $L'_{\rm CO}$ bin.

Given the limited survey statistics due to the moderate number of line candidates, luminosity function constraints are displayed in bins that are not statistically independent throughout, but which instead sample the luminosity function in luminosity bins of 0.5 dex width, in steps of 0.1 dex. Independent bins thus are recovered by only considering every fifth bin (see Table 4.4). Since candidates are primarily taken into account in a probabilistic manner instead of on a per-candidate basis, this choice of partially redundant sampling does reveal additional information on the shape of the luminosity function, and shows trends more clearly than broader, more sparsely sampled bins.

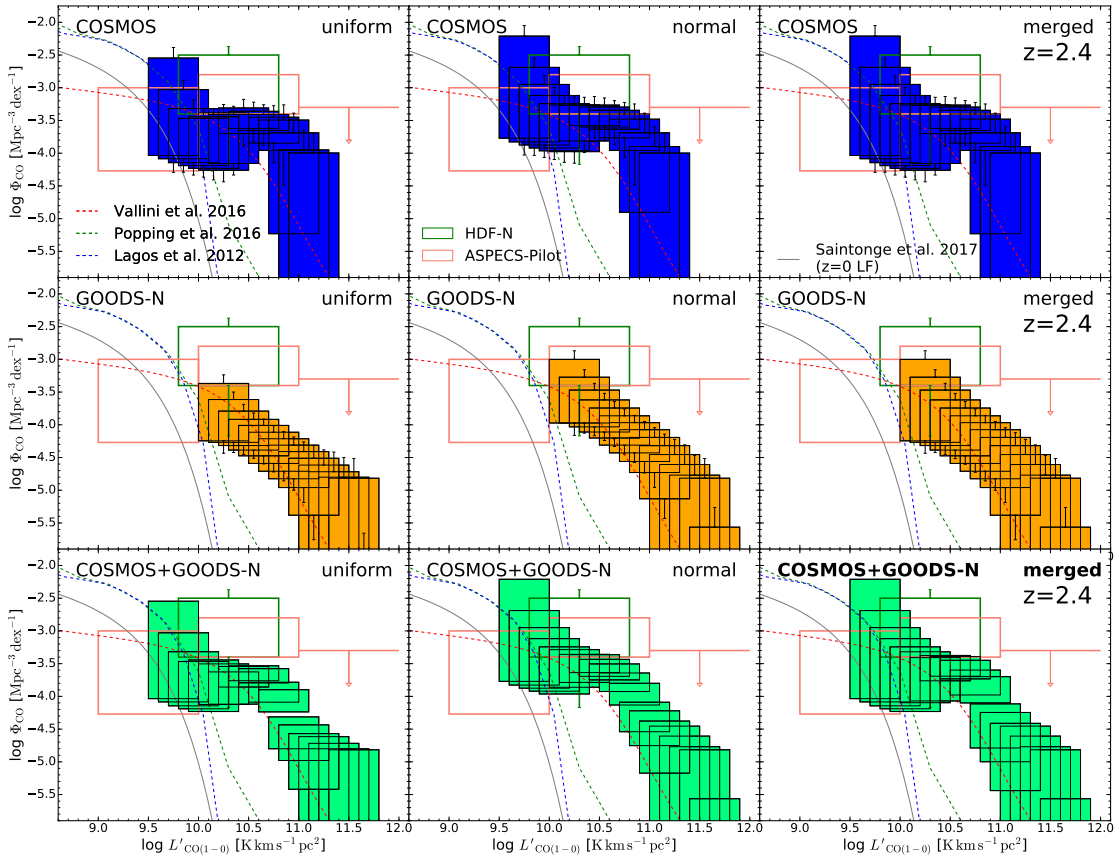

Figure 4.8: VLA COLDz CO(J=1→0) luminosity function at $\langle z \rangle$=2.35 and 2.44 in the COSMOS (*top*) and GOODS-North (*middle*) fields (shaded boxes), respectively, and the combination of both fields, weighted by the statistical uncertainties in each field (*bottom*), showing the consistency between methods and fields. The *left* panels show the constraints obtained when conservatively assuming a uniform distribution between zero and the most likely values for the purities. The *middle column* panels show the constraints when assuming the most likely values for the purities and assigning 100% uncertainty to these values, truncated at zero and 100%. The *right* panels show the composite uncertainties merged from both methods, obtained by assuming the lowest and highest values covered by their respective uncertainty ranges in each bin. Bins have a width of 0.5 dex in $L'_{\rm CO}$, and step through the covered luminosity range in steps of 0.1 dex. As such, individual bins are not statistically independent. Error bars on the boxes indicate Poissonian uncertainties in each bin. Empty green boxes are the constraints on the CO(J=3→2) luminosity function at $\langle z \rangle$=2.75 from the PdBI HDF-N survey (Walter et al. 2014). Empty orange boxes are the CO(J=3→2) constraints at $\langle z \rangle$=2.61 from the ALMA ASPECS-Pilot survey (Decarli et al. 2016a). A constant CO(J=3→2)/CO(J=1→0) brightness temperature ratio of r_{31}=0.42 has been applied to correct the CO(J=3→2) luminosities to CO(J=1→0) luminosities for both these surveys. The gray line shows the z=0 luminosity function for comparison (updated from Saintonge et al. 2017; A. Saintonge, private communication). Dashed lines are semi-analytical and empirical model predictions (Lagos et al. 2012; Popping et al. 2016; Vallini et al. 2016). All except the COLDz data are the same in all panels.

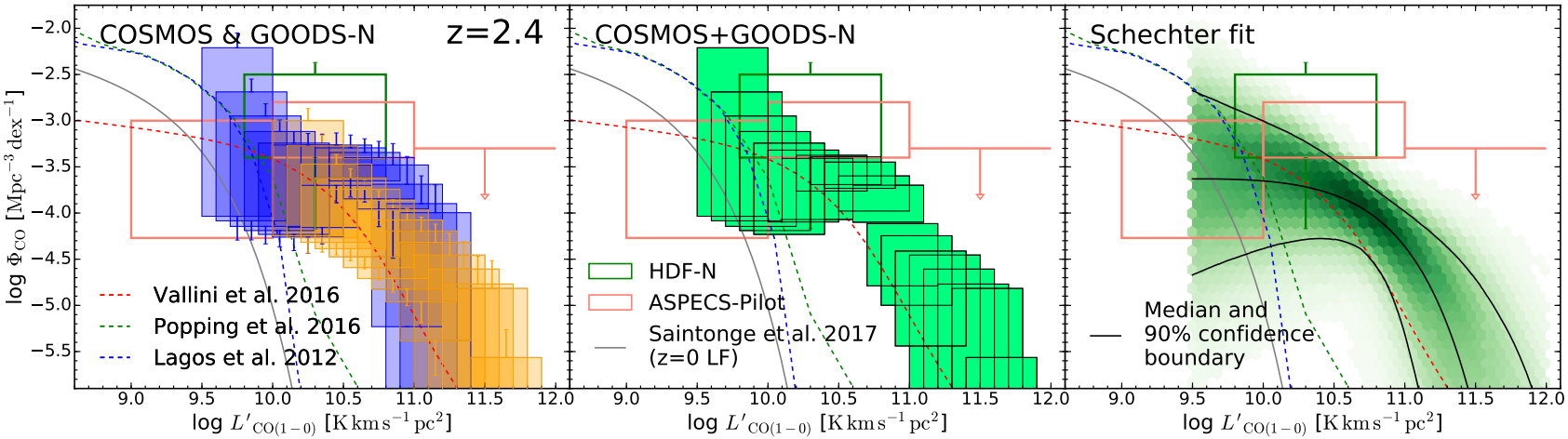

Figure 4.9: Comparison between the two COLDz survey fields and combined constraints on the CO(J=1→0) luminosity function. *Left:* Same as Fig. 4.8, top and middle right, but showing the COSMOS and GOODS-North constraints overlaid with each other. *Middle:* Same as Fig. 4.8, bottom right, combining the measurement from both fields, for comparison. *Right:* Density of Schechter function fits to the combined data, as distributed according to the fit parameter distributions as obtained with the ABC method (shaded region). Darker colors represent higher probabilities. For reference, solid black lines show the median and 90% confidence boundary of the implied luminosity function distributions (see Tab. 4.3 for corresponding Schechter parameters). All except the COLDz data are the same as in Fig. 4.8 in all panels.

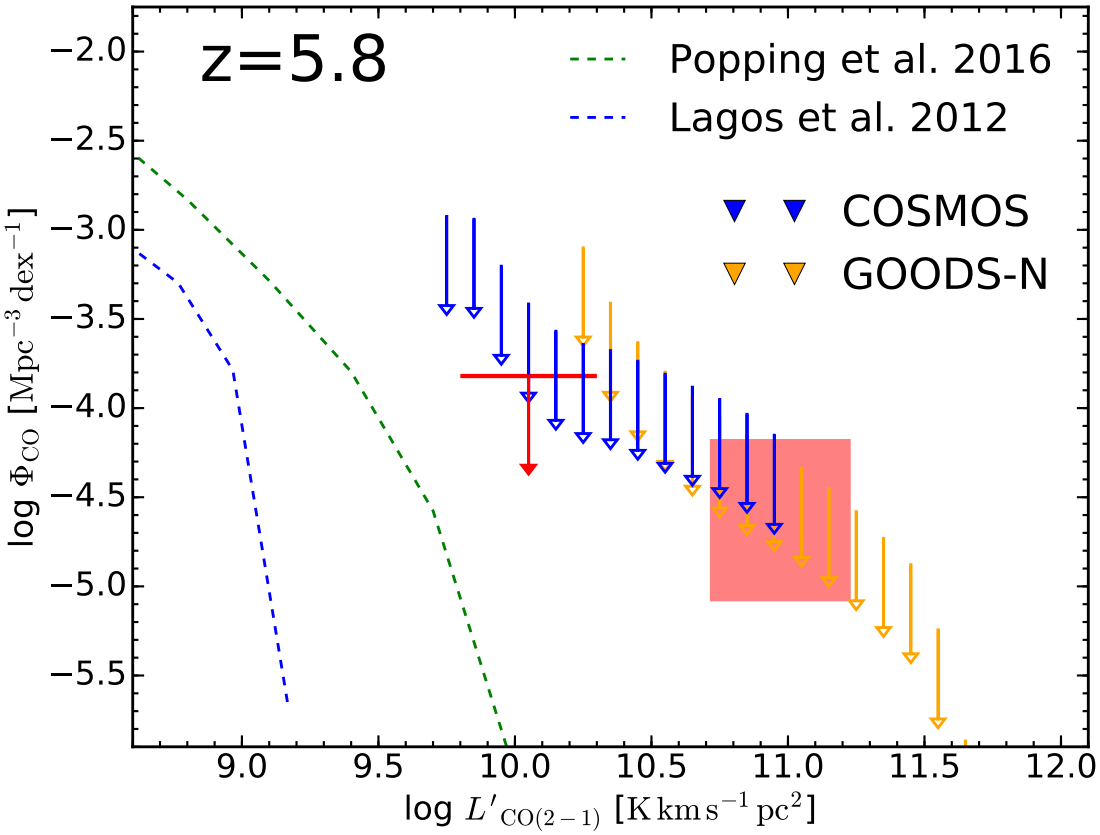

Figure 4.10: VLA COLDz CO(J=2→1) luminosity function at $\langle z \rangle$=5.68 and 5.86 in the COSMOS (blue and red arrows) and GOODS-North (orange arrows and red boxes) fields, respectively. The blue and orange arrows show upper limits under the unlikely assumption that any candidates not independently confirmed to be CO(J=1→0) emission would correspond to CO(J=2→1) emission, for the same binning in $L'_{\rm CO}$ as in Fig. 4.8. Red arrows and boxes consider only independently confirmed CO(J=2→1) candidates. The dashed lines show model predictions.

4.5.3 COLDz CO Luminosity Function

CO(*J*=1→0) Luminosity Function

The estimates of the CO(J=1→0) luminosity function, which include all candidates except independently confirmed CO(J=2→1) emitters,[10] are consistent[11] between both survey fields (Fig. 4.9, left). We thus decided to merge the constraints from both fields through a weighted average in each bin (Fig. 4.8, bottom, and Fig. 4.9, middle).

The data reveal the shape of the CO(J=1→0) luminosity function at z ~2.4, which resembles that of a Schechter function. While not a unique solution given current observational constraints, we obtain an estimate of the allowed range of Schechter parameters by fitting the characteristic parameters $L'^{*}_{\rm CO}$ and $\Phi^{*}_{\rm CO}$ and the power-law slope α to the data (Fig. 4.9, right and Table 4.3). We adopt the Approximate Bayesian Computation (ABC) method (see, e.g., Cameron & Pettitt 2012; Weyant et al. 2013; Ishida et al. 2015, and references therein) to derive posterior distributions of the Schechter parameters, in order to account for all selection effects affecting our measurement without having to specify an explicit equivalent likelihood function.

We first assume uniform, unconstraining priors on the Schechter parameters (i.e., $L'^{*}_{\rm CO}$, $\Phi^{*}_{\rm CO}$, and α) to describe the intrinsic distribution of the CO lu-

[10]The level of the CO luminosity function is dominantly determined by independently-confirmed sources, such that unconfirmed candidates mainly contribute to the size of the uncertainty ranges. For reference, in the COSMOS field, 1, 2, or 3 secure detections in a bin correspond to $\log \Phi_{\rm CO}$ [Mpc^{-3} dex^{-1}] =–4.00, –3.70, or –3.53, respectively. In the GOODS-North field, the same number of detections correspond to values of –4.82, –4.52, and –4.34, respectively.

[11]There are some apparent variations between the two fields within the uncertainties, e.g., around the $\log(L'_{\rm CO}/{\rm K\ km\,s^{-1}\,pc^2})$ =10.5–11.0 bin, which are likely a reflection of cosmic variance.

minosity density. Following the ABC method, we then iteratively sample from these priors, randomly sampling galaxies with randomly assigned line widths and spatial sizes (according to the same prior distributions as assumed before) from the assumed distributions. Here, the number of galaxies is assumed to follow a Poisson distribution around the mean. We then correct for completeness and flux recovery in our line search to determine a mock observed sample of galaxies. We then compare this mock sample to observations by only including line candidates with probability equal to their purity, where purities are a random variable determined according to the "normal" and "uniform" methods described earlier.

The decision criterion for a mock sample to provide a sufficient match to the observed sample, and thus, to retain an initial set of Schechter parameters for the posterior distribution, is to result in the same number of sources as observed, with line fluxes matching to within the 20% flux calibration uncertainty. For each of the survey fields, the process is repeated until sufficient accepted samples are generated to accurately define the posterior distribution. The same procedure is repeated for both survey fields combined, requiring that the resulting data set can be represented by a single, common CO luminosity function.[12] In a final step, we merge the results from both purity methods by giving each method equal probability. The resulting model parameter posterior distributions are shown in Fig. 4.11. The adopted prior ranges are $\log(L'_{\rm CO}/{\rm K\ km\,s^{-1}\,pc^2})$=9.5 to 11.5, $\log(\Phi_{\rm CO}/{\rm Mpc^{-3}\,dex^{-1}})$=–5 to –2.5, and α=–1 to 1.

As shown in Figs. 4.9 and 4.11, uncertainties are dominated by the faint-end

[12]For this last run, the number of mock sources was allowed to differ by one from the observed sample, which we expect to have a minor impact on the result.

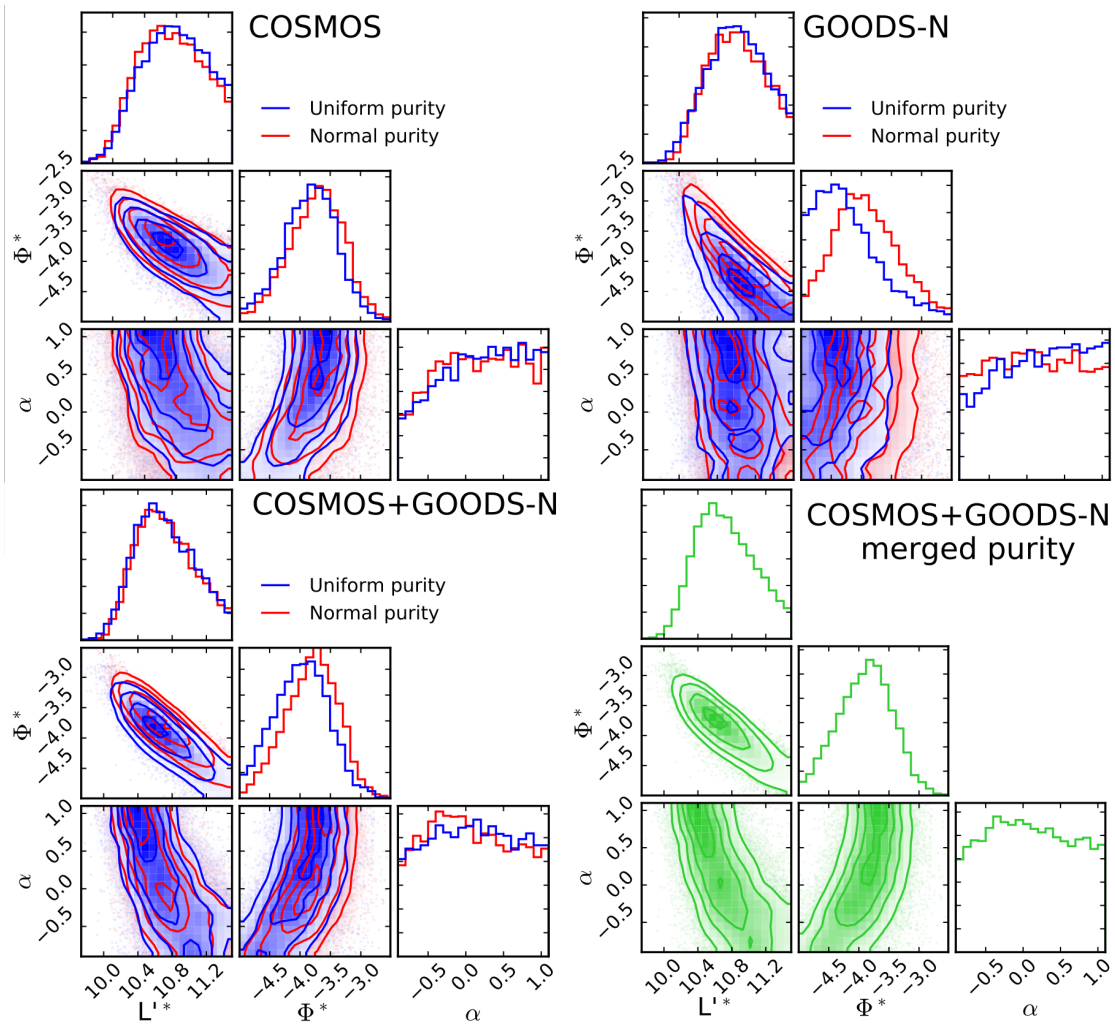

Figure 4.11: Corner plots of the Schechter model parameter posterior distribution from fitting the CO(J=1→0) luminosity function with the ABC method. Contour levels correspond to 0.5, 1.0, 1.5, and 2.0σ in two dimensions. *Top:* Parameters found when fitting results obtained with the "uniform" (blue) and "normal" (red) purity methods for the COLDz COSMOS (*left*) and GOODS-North (*right*) fields, respectively. *Bottom:* Same as found when combining the constraints from both fields, before (*left*) and after (*right*) merging the two methods used to calculate purities, respectively.

slope below the "knee", given the sensitivity of the survey. On the other hand, $L'^{*}_{\rm CO}$, $\Phi^{*}_{\rm CO}$ are constrained fairly reliably by the data, with a reasonable agreement within the uncertainties between the two survey fields.

CO(J=2→1) Luminosity Function

For estimates of the CO(J=2→1) luminosity function, we followed two approaches. The first approach excludes all candidates used to construct the CO(J=1→0) luminosity function from our search, only leaving confirmed CO(J=2→1) sources and upper limits as available constraints. We further exclude one of the CO(J=2→1) sources, AzTEC-3 in the COSMOS field (Riechers et al. 2010b, 2014a; Capak et al. 2011), because the field was chosen to include this source as a bright "calibrator" for the line search methods. Including this source thus would likely bias the measurement in its luminosity bin towards high values, under the reasonable assumption that a random ~9 arcmin^2 field would be unlikely to include a z >5 source as luminous as AzTEC-3. As lower and upper bounds on the uncertainties, the 5th and 95th percentiles of the Bayesian posterior for inferring a Poisson rate are adopted in GOODS-North (where sources are detected), and the 68th percentile is adopted as an upper limit for the COSMOS field (where no secure CO J=2→1 detections remain after the exclusion of AzTEC-3). The second approach assumes that all CO(J=1→0) candidates that are not independently confirmed could potentially be CO(J=2→1) emitters at higher redshifts. Although unlikely, this provides shallower but more detailed upper limits on the CO(J=2→1) luminosity function in smaller luminosity bins. Estimates are weighted by purities and corrected for completeness, using the "normal" purity method, adopting the upper, 90th percentile bounds as upper limits. The results from both methods are consistent with each other, and are shown together in Figure 4.10.

Luminosity Function Constraints: Tabulated Results

For reference, we here include the measured ranges of the CO luminosity function from the COLDz CO(J=1→0) data at $\langle z \rangle$=2.4 (Table 4.4) and the CO(J=2→1) data at $\langle z \rangle$=5.8 (Tables 4.5 and 4.6), as utilized in Figures 4.8 to 4.10. $\log(L'_{\rm CO})$ bins are 0.5 dex wide and given in steps of 0.1 dex, such that every 5$^{\rm th}$ bin is statistically independent.

Table 4.4: Measured ranges of the CO(J=1→0) luminosity function at z ~2.4 from the COLDz data (5th and 95th percentiles).

$\log(L'_{CO})$ bin [K km s^{-1} pc^2]	COSMOS "uniform"[a] [Mpc^{-3} dex^{-1}]	COSMOS "normal"[a] [Mpc^{-3} dex^{-1}]	GOODS-N "uniform"[a] [Mpc^{-3} dex^{-1}]	GOODS-N "normal"[a] [Mpc^{-3} dex^{-1}]	Combined Fields "merged"[a] [Mpc^{-3} dex^{-1}]
9.5 – 10.0	–4.04, –2.55	–3.77, –2.21	···	···	–4.04, –2.21
9.6 – 10.1	–4.08, –3.03	–3.83, –2.69	···	···	–4.08, –2.69
9.7 – 10.2	–4.14, –3.32	–3.87, –2.95	···	···	–4.14, –2.95
9.8 – 10.3	–4.19, –3.47	–3.92, –3.12	···	···	–4.19, –3.12
9.9 – 10.4	–4.23, –3.44	–3.96, –3.24	···	···	–4.23, –3.24
10.0 – 10.5	–4.26, –3.38	–3.98, –3.26	–4.25, –3.37	–3.97, –3.00	–4.10, –3.32
10.1 – 10.6	–4.16, –3.41	–3.81, –3.27	–4.27, –3.61	–3.97, –3.27	–4.07, –3.41
10.2 – 10.7	–3.70, –3.31	–3.58, –3.26	–4.32, –3.79	–4.03, –3.47	–3.76, –3.37
10.3 – 10.8	–3.62, –3.36	–3.60, –3.29	–4.39, –3.92	–4.11, –3.62	–3.69, –3.39
10.4 – 10.9	–3.65, –3.41	–3.63, –3.34	–4.47, –4.01	–4.20, –3.74	–3.73, –3.45
10.5 – 11.0	–3.85, –3.45	–3.77, –3.40	–4.59, –4.11	–4.31, –3.86	–3.98, –3.60
10.6 – 11.1	–3.96, –3.49	–3.96, –3.48	–4.71, –4.21	–4.43, –3.97	–4.10, –3.70
10.7 – 11.2	–5.23, –3.69	–4.90, –3.69	–4.82, –4.31	–4.56, –4.07	–4.79, –4.11
10.8 – 11.3	<(–8.00), –3.95	<(–8.00), –3.90	–4.96, –4.41	–4.73, –4.19	–5.00, –4.25
10.9 – 11.4	<(–8.00), –4.00	<(–8.00), –4.00	–5.38, –4.51	–5.13, –4.32	–5.44, –4.41
11.0 – 11.5	···	···	–6.28, –4.62	–6.23, –4.45	–6.28, –4.45
11.1 – 11.6	···	···	<(–8.00), –4.72	<(–8.00), –4.61	<(–8.00), –4.61
11.2 – 11.7	···	···	<(–8.00), –4.80	<(–8.00), –4.77	<(–8.00), –4.77
11.3 – 11.8	···	···	<(–8.00), –4.82	<(–8.00), –4.82	<(–8.00), –4.82
11.4 – 11.9	···	···	<(–8.00), –5.96	<(–8.00), –5.56	<(–8.00), –5.56

[a]Given as $\log(\Phi_{CO})$. Based on "uniform", "normal", and merged (last column) purity uncertainty estimates as described in Section 3.

Table 4.5: Measured ranges of the CO(J=2→1) luminosity function at z ~5.8 from the COLDz data (90th percentile upper limits).

$\log(L'_{CO})$ bin [K km s^{-1} pc^2]	COSMOS[a] [Mpc^{-3} dex^{-1}]	GOODS-N[a] [Mpc^{-3} dex^{-1}]
9.5 – 10.0	<(–2.92)	···
9.6 – 10.1	<(–2.94)	···
9.7 – 10.2	<(–3.20)	···
9.8 – 10.3	<(–3.42)	···
9.9 – 10.4	<(–3.57)	···
10.0 – 10.5	<(–3.64)	<(–3.10)
10.1 – 10.6	<(–3.68)	<(–3.41)
10.2 – 10.7	<(–3.74)	<(–3.63)
10.3 – 10.8	<(–3.81)	<(–3.80)
10.4 – 10.9	<(–3.88)	<(–3.94)
10.5 – 11.0	<(–3.95)	<(–4.06)
10.6 – 11.1	<(–4.03)	<(–4.16)
10.7 – 11.2	<(–4.15)	<(–4.25)
10.8 – 11.3	···	<(–4.34)
10.9 – 11.4	···	<(–4.45)
11.0 – 11.5	···	<(–4.58)
11.1 – 11.6	···	<(–4.73)
11.2 – 11.7	···	<(–4.88)
11.3 – 11.8	···	<(–5.24)
11.4 – 11.9	···	<(–5.87)

[a]Given as $\log(\Phi_{CO})$. Based on "normal" purity uncertainty estimates as described in Section 3.

Table 4.6: CO(J=2→1) luminosity function at z ~5.8 from the COLDz data based on confirmed sources only (red symbols in Fig. 4.10).

$\log(L'_{CO})$ bin [K km s^{-1} pc^2]	COSMOS[a] [Mpc^{-3} dex^{-1}]	GOODS-N[a] [Mpc^{-3} dex^{-1}]
9.8 – 10.3	<(–3.82)	···
10.7 – 11.2	···	–5.07, –4.19

[a]Given as $\log(\Phi_{CO})$. See Section 3.3.2 for details.

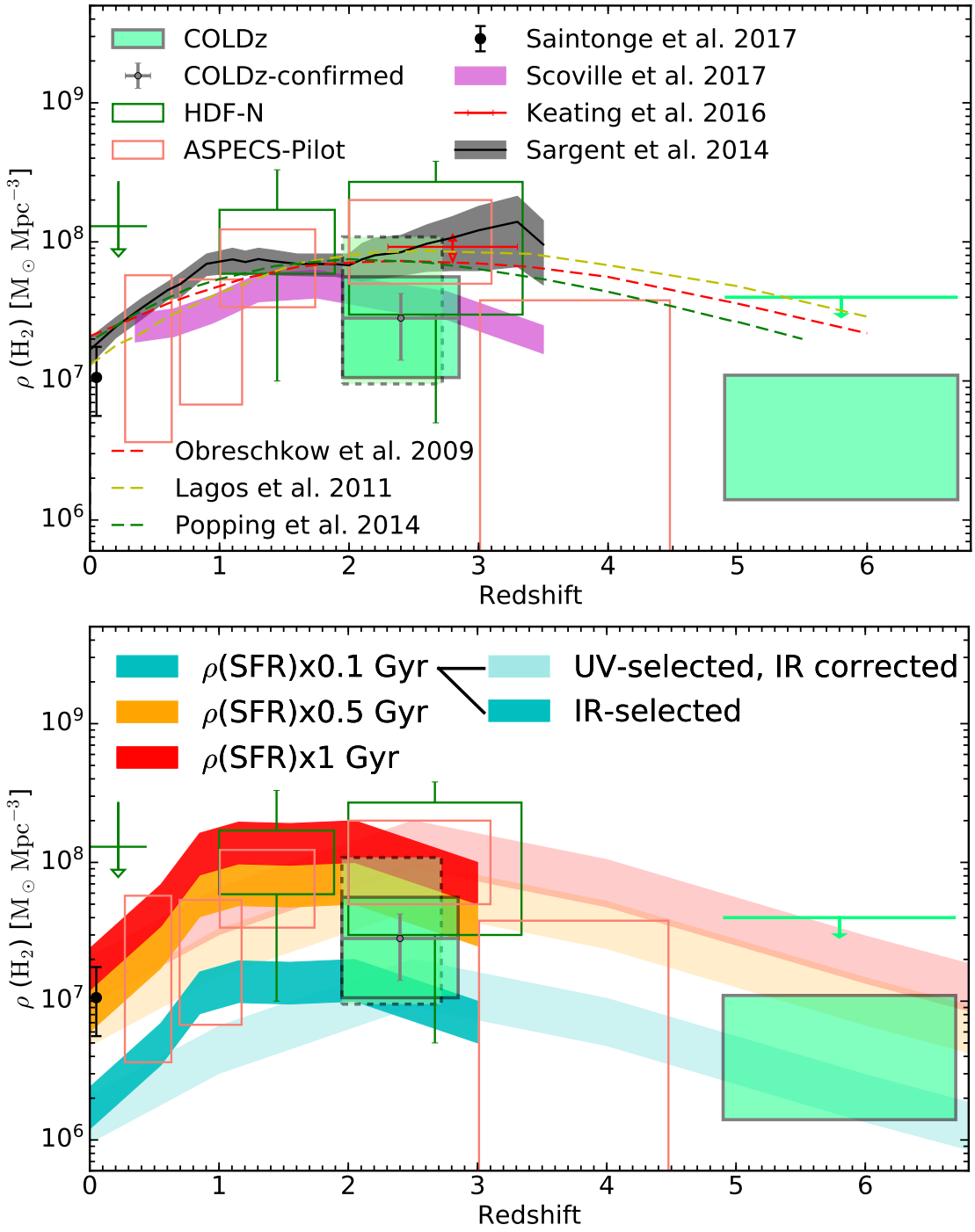

Figure 4.12: Caption on the next page.

Figure 4.12: VLA COLDz measurements of the cold gas history of the universe (green boxes), i.e., the co-moving cosmic mass density of cold molecular gas as a function of redshift, showing that the gas density evolves. Vertical sizes indicate the uncertainties in each bin. In the $z \simeq$2–3 bin, the smaller solid box shows the constraints from both fields combined, and the larger dashed box shows the constraints from the COSMOS field only (both after merging the two purity methods), as an illustration of the impact of field-to-field variations. Assumptions for the measurement and uncertainties in the z=4.90–6.70 bin are the same as in Fig. 4.10. For reference, the gray point shows the measurement obtained when only including independently confirmed candidates, which is fully consistent with the measurement obtained from the complete statistical analysis. Empty green and orange boxes show the constraints from the same surveys as in Fig. 4.8, where different boxes correspond to estimates obtained in different CO transitions (Walter et al. 2014; Decarli et al. 2016a). The black point shows constraints at z=0 (Saintonge et al. 2017). *Left:* Dashed lines show model predictions (Obreschkow et al. 2009; Lagos et al. 2011; Popping et al. 2014a,b). The gray shaded range shows empirical predictions based on an inversion of the $M_{\rm gas}$–SFR relation (e.g., Sargent et al. 2012, 2014; scaled to $\alpha_{\rm CO}$=3.6 $M_{\odot}$ (K km s^{-1} pc^2)$^{-1}$ from its original effective value of $\sim$4.4 $M_{\odot}$ (K km s^{-1} pc^2)$^{-1}$). The mangenta range shows estimates based on galaxy stellar mass functions using the dust-based interstellar medium mass scaling method as described by Scoville et al. (2017a). None of the measurements are extrapolated to account for the faint end of the molecular gas mass function that remained inaccessible to each survey. The red bar indicates the constraint obtained from intensity mapping by Keating et al. (2016). No uncertainties are shown for this measurement, since they are dominated by model assumptions rather than statistical measurement errors. *Right:* Same data, but also showing the total star-formation rate density, multiplied by equivalent gas depletion timescales of 0.1, 0.5, and 1.0 Gyr, for reference. Lighter shaded regions correspond to star-formation rate estimates based on ultraviolet stellar light measurements, with "corrections" for estimated losses due to dust extinction of the ultraviolet light applied. Darker shaded regions correspond to star-formation rate estimates based on direct measurements of the dust-obscured stellar light at infrared wavelengths (Bouwens et al. 2016, including infrared-bright sources from Magnelli et al. 2013; see, e.g., Madau & Dickinson 2014 for further details on uncertainties of the star-formation rate density measurements).

Table 4.7: Cold gas density evolution measurements from COLDz.

Redshift range	Lower limit (5^{th} percentile) $10^7\,M_\odot\,\mathrm{Mpc}^{-3}$	Median (50^{th} percentile) $10^7\,M_\odot\,\mathrm{Mpc}^{-3}$	Upper limit (95^{th} percentile) $10^7\,M_\odot\,\mathrm{Mpc}^{-3}$
1.95–2.85	1.1	2.7	5.6
1.95–2.72	0.95[a]	3.5[a]	10.9[a]
2.03–2.85	*0.30*[b]	*1.9*[b]	*7.3*[b]
4.90–6.70	0.14	0.47	1.1
			4.0[c]

[a]Measurement for the COSMOS field alone, after merging both purity methods.
[b]Measurement for the GOODS-North field alone, after merging both purity methods. These data alone do not fully sample the "knee" of the CO luminosity function.
[c]Less constraining upper limit obtained when making the (unlikely) assumption that all CO(J=1→0) candidates not yet independently confirmed could, in principle, be CO(J=2→1) emitters.

4.5.4 COLDz Cold Gas Density of the Universe

By integrating the measurements and upper limits obtained on the CO(J=1→0) and CO(J=2→1) luminosity functions across each of the full redshift intervals, we obtain estimates of the total CO luminosity density per unit volume. For the higher-redshift bin, we use the results from the two methods described above as a direct measurement and as a conservative upper limit, respectively. As done in previous work (e.g., Walter et al. 2014; Decarli et al. 2016a), we do not extrapolate the faint end of the luminosity function, but instead only include measurements down to the limit of our survey of $\log(L'_{\rm CO}/{\rm K\ km\,s^{-1}\,pc^2})\simeq 9.5$. Given the consistency of the COLDz data with a flat faint-end slope, and the moderate survey statistics, this assumption is not likely to dominate the uncertainty budget of our measurement, but more sensitive observations are required to fully assess the impact of this assumption.[13] We then convert the measurements of the CO luminosity density to a molecular gas mass density by applying a "standard" conversion factor of $\alpha_{\rm CO}$=3.6 $M_\odot$ (K km s^{-1} pc^2)$^{-1}$ (e.g., Daddi et al. 2010a). This choice is motivated by the finding that the majority of the independently-confirmed CO(J=1→0) emitters (with the exception of the major merger GN19) are consistent with the star-forming galaxy "main sequence" at z ~2–3. We do not apply a separate correction to $\alpha_{\rm CO}$ for the CO(J=2→1)-based measurement, since typical CO(J=2→1)/CO(J=1→0) line brightness temperature ratios for "normal" high-redshift galaxies are of order 90% (e.g., Carilli & Walter 2013), and since the actual CO(J=2→1) detections in our survey are all massive dust-obscured starburst galaxies. As such, the implied ~10% correc-

[13]For reference, integrating our best-fit model Schechter functions down only to $\log(L'_{\rm CO}/{\rm K\ km\,s^{-1}\,pc^2})$=10.0 would result in a 0.07 dex lower median value for the integrated CO(J=1→0) luminosity density. Integrating down further to $\log(L'_{\rm CO}/{\rm K\ km\,s^{-1}\,pc^2})$=8.0 or 9.0 would result in 0.044 dex or 0.03 dex higher values, respectively.

tion required is likely sub-dominant to the assumptions made for the choice of $\alpha_{\rm CO}$ (which also depends on other factors like metallicity; see Bolatto et al. 2013 for a review). The choice of $\alpha_{\rm CO}$ will be re-evaluated in upcoming work, once dynamical mass estimates based on spatially-resolved measurements of individual line candidates are available, but we note that the choice of a smaller, "starburst-like" $\alpha_{\rm CO}$ of order unity would result in significantly lower cold gas density estimates. The resulting measurements of the cold gas density of the universe are shown in Fig. 4.12 and summarized in Table 4.7.

4.6 Discussion

Due to improved statistics, the COLDz data provide the currently best constraints on the CO luminosity function at z ~2–3 and z ~5–7, and they allow for a measurement of the shape of the CO luminosity function in the z ~2–3 bin. This provides the to date perhaps most solid constraints on the cosmic density of cold molecular gas in galaxies at these redshifts.

4.6.1 Comparison to Previous "Blind" CO Surveys

CO Luminosity Function

The most similar measurements of the CO luminosity function to COLDz are those in the *Hubble* Deep Field North (HDF-N) and in the *Hubble* Ultra Deep Field (H-UDF; ASPECS-Pilot survey) over ~0.5 and 1 arcmin^2 size regions, covering the CO(J=3→2) line at $\langle z \rangle$=2.75 and $\langle z \rangle$=2.61, respectively (Walter et al.

2014, 2016; Decarli et al. 2014a, 2016a). We consider the differences in redshift in these previous works to the ~60 arcmin^2 COLDz CO(J=1→0) survey ($\langle z \rangle$=2.35 and 2.44 in the COSMOS and GOODS-North fields, respectively) presented here negligible compared to other sources of uncertainty, such that we directly compare these measurements in the following. The difference in line search methods and the luminosity function calculation yield perhaps more conservative uncertainty estimates for the COLDz constraints, but we have confirmed that we would obtain consistent results when adopting the same methods employed in the analysis of the ASPECS-Pilot survey (Decarli et al. 2016a). We thus adopt the measurements and uncertainties from the previous surveys without further modifications.

As shown in Figures 4.8 and 4.9, we find that the measurements of all three surveys are consistent within the relative uncertainties. There may be tentative evidence that the COLDz measurements are somewhat lower than the ASPECS-Pilot measurements in the best-constrained common luminosity range at $\log(L'_{\rm CO}/{\rm K\,km\,s^{-1}\,pc^2})\simeq$10.2–11.0 (Figs. 4.8 and 4.9). If real, this effect may be due to cosmic variance, or it could be an indication that CO(J=3→2)-based surveys preferentially select galaxies with higher gas excitation, such that CO(J=3→2)/CO(J=1→0) brightness temperature ratio of r_{31}=0.42±0.07 assumed by Decarli et al. (2016a) to correct for the average gas excitation may be too low (which could then mimick such an effect in principle, depending on the intrinsic shape of the CO luminosity function).[14] The latter would be consistent with the finding of a high line ratio limit of r_{31} >0.7 for a candidate overlapping between the HDF-N and COLDz surveys (ID19; Decarli et al. 2014a), and the

[14]For a sample of bright, observed-frame 850 μm–selected galaxies, Bothwell et al. (2013) find a median r_{31} of 0.52±0.09, but while there is source overlap, these galaxies are typically more intensely star-forming than the majority of sources found in the "blind" CO surveys. Also, the ~20%±20% difference in r_{31} is perhaps not sufficient to fully explain the observed effect.

lack of CO(J=1→0) detections for other mid-J CO candidates in the same field (see Chapter 3). Since some of these earlier candidates may be spurious, and given the limited statistics of the current surveys and the limited magnitude of the effect, additional data are required to further investigate the relevance of potential selection effects due to CO excitation. In particular, Decarli et al. (2016b) find that some confirmed sources in the ASPECS-Pilot survey appear to show comparatively low CO excitation, opposite to what would be expected in the case of a CO excitation-based selection bias. The full, extended ASPECS survey data expected from an ongoing ALMA Large Program will further constrain the contribution of cosmic variance to the observed effect.

Cold Gas Density of the Universe

The constraints on the evolution of the cold gas density with redshift resulting from the improved CO luminosity function measurements provided by COLDz are consistent with those from previous surveys within the relative uncertainties, and they extend the range of estimates to earlier cosmic epochs (Fig. 4.12; all CO surveys assume the same $\alpha_{\rm CO}$). As in the case of the CO luminosity function constraints, we adopt the measurements and uncertainties from previous works without further modifications. Due to differences in the methods used to determine and report uncertainties, caution is advised when comparing the constraints from different surveys at face value.[15] Previous surveys carried out at 3 mm and 1 mm did not provide estimates at z >4.5, since those redshifts are

[15]For the HDF-N measurements, the lower and upper limits of the boxes shown represent secure detections and all line candidates reported by Walter et al. (2014), respectively, with Poissonian uncertainties due to the number of candidates added as error bars. For the ASPECS-Pilot measurements, box sizes indicate Poissonian errors, with a minor contribution due to flux errors and potential line misidentifications added (Decarli et al. 2016a). Both surveys adopt 1σ uncertainty ranges, rather than the more conservative 90% confidence intervals adopted for the COLDz measurements.

only covered in high-J lines, where estimates of CO excitation as necessary to extrapolate the CO(J=1→0) luminosity are increasingly uncertain.

The COLDz measurements likely suggest a higher gas density at z ~2–3 ($\rho(H_2)$=0.95–10.9×10^7 $M_\odot$ Mpc^{-3}, with a preferred range of 1.1–5.6×10^7 $M_\odot$ Mpc^{-3})[16] compared to z=0 ($\rho(H_2)=1.1^{+0.7}_{-0.5}\times10^7$ $M_\odot$ Mpc^{-3}; Saintonge et al. 2017; see also Keres et al. 2003; Boselli et al. 2014)[17] by a factor of a few. This finding is consistent with what was reported by the ASPECS team within the relative uncertainties ($\rho(H_2)$=4.9–19×10^7 $M_\odot$ Mpc^{-3}; Decarli et al. 2016a). These measurements are also in agreement with estimates based on galaxy stellar mass functions in COSMOS using the dust-based interstellar medium mass scaling method as described by Scoville et al. (2017a). Averaging their data at z=2.25 and 2.75, Scoville et al. suggest ρ(ISM)=3.8×10^7 $M_\odot$ Mpc^{-3} at z=2.5.[18] The latter agrees to within ~30% with the median value of the COLDz measurement, and within <10% with the median value measured in the COSMOS field alone. The COLDz results are also consistent with the constraints obtained from CO(J=1→0) intensity mapping experiments at similar redshifts in the GOODS-North field ($\rho(H_2)=9.2^{+5.9}_{-3.3}\times10^7$ $M_\odot$ Mpc^{-3} at z=2.3–3.3; Keating et al. 2016).[19] A comparison of these results is valuable in general, since CO intensity maps in principle may

[16]For reference, the contribution from independently confirmed sources alone is $\rho(H_2)$=(2.8±1.4)×10^7 $M_\odot$ Mpc^{-3}, which is consistent with the median value of the total of 2.7×10^7 $M_\odot$ Mpc^{-3}. Chapter 3 also reports a weak CO(J=1→0) detection from stacking 34 individually-undetected z=2.0–2.8 galaxies with stellar masses of $M_\star$ >10^{10} $M_\odot$ in the GOODS-North field. As they are not detected individually, these galaxies are not part of the statistical sample used in this paper. If we were to include these sources, they would contribute an additional $\rho(H_2)\simeq0.3\times10^7$ $M_\odot$ Mpc^{-3} in aggregate.

[17]We here and in Fig. 4.12 adopt α_{CO}=3.6 $M_\odot$ (K km s^{-1} pc^2)$^{-1}$ for consistency. Adopting α_{CO}=6.5 $M_\odot$ (K km s^{-1} pc^2)$^{-1}$ as used by Keres et al. (2003) would result in a factor of 1.8 higher $\rho(H_2)$.

[18]We here and in Fig. 4.12 adopt α_{CO}=3.6 $M_\odot$ (K km s^{-1} pc^2)$^{-1}$ for consistency. Adopting α_{CO}=6.5 $M_\odot$ (K km s^{-1} pc^2)$^{-1}$ as used by Scoville et al. (2017a) would result in a factor of 1.8 higher $\rho(H_2)$.

[19]We here and in Fig. 4.12 adopt α_{CO}=3.6 $M_\odot$ (K km s^{-1} pc^2)$^{-1}$ for consistency. Adopting α_{CO}=4.3 $M_\odot$ (K km s^{-1} pc^2)$^{-1}$ as used by Keating et al. (2016) would result in a factor of 1.2 higher $\rho(H_2)$.

contain signal below the detection threshold of galaxy surveys, but we note that a quantitative comparison of the relative uncertainties is difficult. This is due to the fact that the intensity mapping constraints only measure the second raw moment of the luminosity function, and therefore cannot distinguish between contributions due to the characteristic luminosity and volume density to the measurement. Furthermore, the detailed interpretation of the nature of the intensity mapping signal in principle relies on assuming a scaling relation between dark matter halo mass and CO luminosity, which is currently not well constrained at z ~2–3. We thus do not show formal error bars for this measurement in Fig. 4.12.

The COLDz measurements are also consistent with a decrease in gas density from z ~2–3 towards z ~5–7 ($\rho(H_2)$=0.14–1.1×10^7 $M_\odot$ Mpc^{-3}), possibly to below the present-day value. The redshift evolution of the cold gas history of the universe thus appears qualitatively similar to that of the star-formation history of the universe (e.g., Madau & Dickinson 2014), which is consistent with what is expected if a universal "star-formation law" between gas mass and star-formation rate (e.g., Carilli & Walter 2013) already exists at early epochs.

Gas Depletion Times

In combination, the cold gas mass and star-formation rate density evolution entail information about the evolution of galaxy gas depletion times as a function of redshift.[20] As shown in Fig. 4.12, simply multiplying the total star-formation rate density (Bouwens et al. 2016) by a characteristic gas deple-

[20]The analysis presented here concerns the redshift evolution of gas depletion times, and thus, does not further consider the potential range of values expected for different galaxy populations that contribute to the signal.

tion timescale (which, to first order, represents the ratio between molecular gas mass and star-formation rate, M_{H_2}/SFR) of several hundred million years provides a reasonable match to the cold gas density relation at all redshifts currently probed within the uncertainties, although the data may tentatively prefer shorter depletion times towards higher redshifts. At z=0, a characteristic gas depletion timescale in the range of τ_{dep}^{ch}=0.5–1 Gyr is preferred with the adopted α_{CO} conversion factor (see also discussion by Saintonge et al. 2017). Based on the COLDz measurements of $\rho(H_2)$ at z=2.4 and adopting ρ(SFR)=0.15±0.05 $M_\odot$ yr^{-1} Mpc^{-3} (e.g., Madau & Dickinson 2014), we find a characteristic gas depletion timescale of τ_{dep}^{ch}=70–750 Myr with 90% confidence, with a median value of 200±70 Myr. Since the star-formation rate density relation includes significantly less luminous galaxies than probed by current blind CO surveys, this may either indicate that low-luminosity galaxies below our L'_{CO} detection limit do not contribute dominantly to the total cold gas density (perhaps implying that the faint-end slope of the CO luminosity function is not steeply rising towards lower L'_{CO}), or that the characteristic gas depletion timescales are longer than 200–500 Myr when averaged over the entire galaxy population. Assuming substantially shorter gas depletion timescales (or, high star-formation efficiencies) appears to be inconsistent with the data, unless the characteristic α_{CO} conversion factor is substantially lower than assumed. The COLDz measurements of $\rho(H_2)$ at z=5.8 are consistent with characteristic gas depletion timescales of τ_{dep}^{ch} >100 Myr, with a factor of a few higher values allowed by the data within the uncertainties. Although not a unique conclusion based on the COLDz data given the remaining uncertainties, a shortening in gas depletion times despite the observed increase in cold molecular gas content in star-forming galaxies towards higher redshift would be consistent with similar

findings based on targeted studies of CO(J=3→2) emission and dust-based interstellar medium mass estimates (e.g., Genzel et al. 2015; Scoville et al. 2017a), and thus, with an effective increase in star formation efficiency (i.e., SFR per unit $M_{\mathrm{H_2}}$) towards higher redshifts.

4.6.2 Comparison to Model Predictions

CO Luminosity Function

Given the consistency between the COLDz data and previous surveys, we compare the new CO luminosity function measurements to predictions based on semi-analytical models (Lagos et al. 2012; Popping et al. 2016) and empirical estimates based on the infrared luminosity function of *Herschel*-selected galaxies under the assumption of a "star-formation law" (Vallini et al. 2016; Figs. 4.8 to 4.10; see, e.g., Lagos et al. 2015; Davé et al. 2017; Xie et al. 2017 for additional model predictions).

The measurements at z ~2–3 appear to be inconsistent with the semi-analytical predictions (see Decarli et al. 2016a for a detailed comparison of both models), which place the characteristic luminosity L'^{*}_{CO} ("knee") of the luminosity function at significantly lower luminosities than observed. This is consistent with the excess of bright sources compared to the predictions seen in the ASPECS-Pilot data alone in some luminosity bins (Decarli et al. 2016a), but the trend becomes clearer at the higher statistical significance of the COLDz measurements – showing a significantly (by one to two orders of magnitude) higher characteristic luminosity than what is observed at $z \sim 0$ (e.g., Keres et al. 2003; Boselli et al. 2014; Saintonge et al. 2017). These predictions also prefer a strong

contribution from faint sources, which are not preferred by the data, but agree within the considerable uncertainties of the measurements at low luminosities. Qualitatively, the underprediction in the number of luminous CO emitters may be related to the finding that semi-analytical models tend to underpredict the star-formation rates of galaxies on the star-forming main sequence at similar redshifts (see, e.g., review by Somerville & Davé 2015).

At $z \sim 5-7$, the excess of bright sources compared to the semi-analytical predictions appears to be even more pronounced than at lower redshifts, but we caution that the most constraining measurement is based on a small number of sources only, and thus, needs to be put on a firmer statistical footing. On the other hand, the observations at $z \sim 2-3$ appear to be consistent with the empirical predictions by Vallini et al. (2016), and thus, with what is expected from estimates of dust-obscured star-formation activity at high redshift based on infrared luminosity functions.

Cold Gas Density of the Universe

The observational constraints on the evolution of the cold gas density with redshift remain in agreement with both semi-analytical (Obreschkow et al. 2009; Lagos et al. 2011, 2012; Popping et al. 2014a,b) and empirical (Sargent et al. 2012, 2014) model predictions at $z \sim 2-3$. Since most of the semi-analytical models include a varying $\alpha_{\rm CO}$ between individual galaxies, a simple interpretation of the consistency despite the disagreement in the luminosity function estimates remains challenging. In addition, the predictions do not account for the sensitivity limits of the CO surveys, or uncertainties due to cosmic variance. Given the differences in the CO luminosity functions between models

and observations at high z, this effect could lead to up to a factor of a few difference in the corresponding gas densities at high redshift in principle. However, as discussed earlier, the impact of the sensitivity limits, which would bias the measurements towards lower values, appears to be relatively minor based on the preferred model Schechter function fits to the COLDz data. On the other hand, cosmic variance due to large-scale structure in the distribution of gas-rich galaxies (which is assumed to be uniform in our analysis) could bias the measurements either low or high. To obtain an approximate estimate of systematic uncertainties introduced by cosmic variance, we follow the prescription by Driver & Robotham (2010), based on the distribution of galaxies near the characteristic stellar mass at a given redshift.[21] Including both Poisson uncertainty and cosmic variance scaled to the volume of the COLDz survey, we find a sample variance uncertainty of ~30%–40% and ~25% for the COSMOS and GOODS-North fields, respectively. Alternatively, adapting results based on models of the evolution of the most massive galaxies (i.e., $M_\star$ >10^{11} $M_\odot$) by Moster et al. (2011)[22] yields an estimated uncertainty of ~40%–50% based on cosmic variance alone for the smaller COSMOS field. These estimates are consistent with what is found from more detailed calculations based on the *IllustrisTNG* simulations (of order ~30%–50% in the z ~2–3 bin for both fields combined; G. Popping 2018, private communication). All estimates appear to suggest that uncertainties due to cosmic variance are subdominant to other sources of uncertainty, given the large volume of the COLDz survey due to the broad range in redshift covered

[21]This method is based on a generalized expression (their equation 4) calibrated through an examination of galaxies within ±1 mag of the characteristic optical magnitude out to $z \sim 0.1$ in the Sloan Digital Sky Survey (SDSS), which represent the most common galaxies at a given redshift. See `cosmocalc.icrar.org` for additional details. The field sizes and CO(J=1→0) redshift ranges in Table 4.1 are used for all calculations.

[22]For our estimate, we have made use of the predictions provided for the H-UDF, since this field has a similar area as the COLDz COSMOS field. We have assumed $\langle z \rangle$=2.35 and Δz=0.8 in our calculations, and we adopt the values found for the $M_\star$=$10^{11.0}$–$10^{11.5}$ $M_\odot$ bin.

and the comparatively large field size. This is also consistent with the broad distribution in redshift of the confirmed CO emitters and candidates in the COLDz survey volume (see, e.g., Chapter 3, Fig. 3).[23] In any case, if we were to conservatively correct down the model predictions by factors of $\sim 1.5-2$ to account for the combined effects of sensitivity limits and cosmic variance, they would in fact move close to the median $\rho(H_2)$ implied by the COLDz measurements. Taken at face value, the apparent agreement between the model predictions and COLDz data could indicate that there is no significant, or at least, no dominant contribution from sources far below the COLDz detection limit, such that steeply-rising faint-end slopes of the CO luminosity function towards lower L'_{CO} may be disfavored. This would also be consistent with the agreement between the COLDz measurement and intensity mapping constraints.

If true, this could be related to lower metallicities towards fainter, low-mass galaxies, leading to disproportionally low CO luminosity per unit molecular gas mass (e.g., Genzel et al. 2012; Bolatto et al. 2013). Although not a unique explanation, this would be consistent with the finding of a lower median redshift of galaxies with low submillimeter continuum fluxes compared to brighter ones (implying low dust masses, and thus, likely low gas masses; Aravena et al. 2016), and with the apparent finding of a low dust content in lower stellar mass galaxies at z >2 (Bouwens et al. 2016). This would also be consistent with the finding that we do not detect CO(J=2→1) emission from several known, modestly massive and star-forming Lyman-break galaxies at $z \sim 5.2-5.3$ in our survey area (Chapter 3; see also Capak et al. 2011; Walter et al. 2012; Riechers et al. 2014a), which is compatible with a perhaps elevated α_{CO} due to lower metallic-

[23]The COSMOS field contains the AzTEC-3 protocluster region at z=5.3 (e.g., Capak et al. 2011; Riechers et al. 2010b, 2014a), and thus, is biased in principle. However, only upper limits are reported in this field for the corresponding redshift bin, such that this does not impact the reported measurements.

ity. All confirmed z >5 COLDz detections are massive, dust-obscured starburst galaxies with likely high metallicity.

The observational constraints at $z \sim 5-7$ are also in agreement with the model predictions, albeit lower than the Obreschkow et al. and Lagos et al. models unless some unconfirmed sources (which are taken into consideration for the upper limit shown) contribute to the signal. They are less secure than in the lower-redshift bin due to more limited statistics and because it is currently not possible to measure the characteristic CO luminosity at these redshifts, such that the fraction of the total cold gas density recovered down to the sensitivity limit of the survey is less certain than at lower redshifts. Nonetheless, this finding appears to be consistent with the assumption of an evolving $\alpha_{\rm CO}$ due to lower metallicity in fainter galaxies and towards higher redshifts, resulting in a steep drop in the gas volume density as traced by CO emission. Further observations are required to investigate if the drop in H_2 density towards very high redshift is as steep as observed in CO, or if the effect is enhanced due to metallicity affecting the strength of the CO signal.[24]

4.7 Conclusions

We have used the "blind" molecular line scans over ~60 arcmin^2 in the COSMOS and GOODS-North survey fields taken as part of the VLA COLDz survey (Chapter 3) to measure the shape of the CO luminosity function at z ~2–3 and to constrain it at $z \sim 5-7$, utilizing CO(J=1→0) and CO(J=2→1) emission line

[24]The strength of the CO signal may also be reduced at the highest redshifts due to the increased temperature of the cosmic microwave background, relative to which the cold gas emission is detected. The importance of this effect strongly depends on the excitation of the gas traced by CO, in particular the kinetic gas temperature (e.g., da Cunha et al. 2013c).

galaxy candidates. We also provide constraints on the evolution of the cosmic molecular gas density out to $z \sim 7$. We compare our findings to previous ~0.5 and 1 arcmin^2 surveys in the HDF-N and the H-UDF (ASPECS-Pilot) in higher-J CO lines (Decarli et al. 2014a; Walter et al. 2016), estimates based on galaxy stellar mass functions in COSMOS scaled using dust-based interstellar medium mass estimates (Scoville et al. 2017a), and a CO intensity mapping study in GOODS-North (Keating et al. 2016), finding broad agreement within the relative uncertainties. The COLDz data provide the first solid measurement of the shape of the CO luminosity function at $z \sim 2-3$, reaching below its "knee", and the first significant constraints at $z \sim 5-7$. The characteristic CO luminosity at $z \sim 2-3$ appears to be one to two orders of magnitude higher than at z=0 (Keres et al. 2003; Saintonge et al. 2017), which is consistent with the idea that the dominant star-forming galaxy populations ~10 billion years ago were significantly more gas-rich compared to present day. We also independently confirm an observed apparent excess of the space density of bright CO-emitting sources at high redshift compared to semi-analytical predictions, but our findings are consistent with empirical predictions based on the infrared luminosity function and observed star-formation rates of distant galaxies.

Integrating the CO luminosity functions down to the sensitivity limit of our survey, we obtain robust estimates of the volume density of cold gas in galaxies at high redshift. Our measurement is consistent with a factor of a few increase from $z \sim 0$ to $z \sim 2-3$, and a decrease towards $z \sim 5-7$ by about an order of magnitude (which may be less steep in practice if metallicity has an increasing effect on CO-based measurements towards the highest redshifts). This is consistent with semi-analytical and empirical model predictions and previous constraints from the ASPECS-Pilot survey (Decarli et al. 2016a), and with previous findings

of increased gas fractions at $z > 1-2$ (e.g., Daddi et al. 2010a; Tacconi et al. 2013, 2018; Scoville et al. 2017a). The overall shape of the cosmic gas density evolution resembles that of the star-formation history of the universe, consistent with an underlying "star-formation law" relation out to the highest measured redshifts. This suggests that the star-formation history, to first order, follows the evolution of the molecular gas supply in galaxies, as regulated by the gas accretion efficiency and feedback processes. A more direct comparison of the star-formation rate and cold gas density relations as a function of cosmic time holds critical information about the true gas depletion timescales, and thus, the gas accretion rates required to maintain the ongoing build-up of stellar mass. The data appear broadly consistent with a characteristic gas depletion timescale of several hundred million years, but there may be tentative evidence for a shortening in gas depletion times despite the observed increase in cold molecular gas content in star-forming galaxies towards higher redshift. This finding would be consistent with previous, targeted investigations based on CO(J=3→2) and dust-based interstellar medium mass estimates (e.g., Genzel et al. 2015; Scoville et al. 2017a), and thus, with an effective increase in star formation efficiency in the dominant star-forming galaxy populations towards higher redshifts.

While COLDz is the currently largest survey of its kind, the size of the volume probed and the number of line candidates found implies that larger areas need to be surveyed to greater depth in the future to more clearly address effects of cosmic variance and to reduce the error budget due to Poissonian fluctuations. Such studies will be possible with large investments of observing time at the VLA and ALMA in the coming years, until the next large leap in capabilities will become available with the construction of the Next Generation Very Large Array (ngVLA; e.g., Bolatto et al. 2017; Selina et al. 2018b).

CHAPTER 5

ALMA REVEALS WEAK [NII] EMISSION IN "TYPICAL" GALAXIES AND INTENSE STARBURSTS AT $Z = 5 - 6$

5.1 Context

As the previous chapter showed, the efficiency of star formation does not appear to change substantially up to $z \sim 3$, at least based on global average quantities for the overall galaxy population. Our study also showed a highly significant evolution in the gas mass content of galaxies, with many more gas-rich galaxies at the cosmic "noon" rather than at $z \sim 0$. However, at even higher redshift, we expect that the ISM physical properties in normal galaxies should change because of approaching the time of formation for the observed galaxies. Indeed, optical studies of the ionized gas properties in lower mass galaxies already at $z \sim 2$ have shown the characteristic signs of a more intense radiation field, which appears to indicate lower metallicity gas and, especially, lower metallicity stars (e.g., Steidel et al. 2016). The expectation is that in order to observe the early stages of formation, and therefore detect an evolution in the ISM composition of more massive galaxies, even higher redshifts need to be probed (e.g., Bouwens et al. 2016; Faisst et al. 2016b,a). Better understanding the changes in ISM properties as a function of redshift, in the early Universe, is crucial in order to constrain the mechanisms leading to the formation of present day galaxies, and to understand the cosmological impact of galaxies on the largest scales (e.g., reionization, cluster formation) . As we saw in Chapter 1, Capak et al. (2015) used ALMA to show that moderately massive, "normal" galaxies at $z = 5 - 6$ appear to show significant evolution in their ISM properties. In particular, they found

lower dust continuum emission relative to their [CII] luminosity which indicates a change in the conditions of the star forming gas. Furthermore, Barišić et al. (2017); Faisst et al. (2017) have shown that the dust in these galaxies is likely to be significantly warmer, and confirmed that the dust properties appear to show an evolution relative to lower redshift. In order to investigate these changes in the ISM with redshift, we used ALMA to further explore the well characterized sample of "normal" galaxies from Capak et al. (2015), by measuring the [NII] fine-structure line at 205 μm, one of the best probes of the ionized gas immediately surrounding recent star formation. While the [CII] line has become a workhorse of ISM studies at high redshift due to its high luminosity, this line is emitted by neutral as well as ionized gas. This widespread origin makes it an excellent tracer of the gas dynamics but it makes interpreting the line luminosity in terms of physical gas conditions more difficult because we first need to assess the fraction of [CII] coming from atomic rather than ionized gas. Measuring this fraction is the main return of the [NII] 205 μm line, although not the only goal. Crucially, *Herschel* observations of fine-structure line emission from local dwarf galaxies have found fainter [NII] and brighter [NIII] and [OIII], relative to massive galaxies (Cormier et al., 2015). These measurements indicate a strong metallicity effect, producing a higher intensity and harder radiation field which causes the ionized gas to be in a higher ionization state. This important change in the ISM may affect star formation and is likely to affect reionization in the early Universe.

This chapter was previously published in the *Astrophysical Journal* as Pavesi, R., et al., 2016, ApJ, 832, 151; in collaboration with Dominik Riechers, Peter Capak, Christopher Carilli, Chelsea Sharon, Gordon Stacey, Alexander Karim, Nick Scoville, Vernesa Smolčić.

5.2 Abstract

We report interferometric measurements of [NII] 205 μm fine-structure line emission from a representative sample of three galaxies at z = 5–6 using the Atacama Large (sub)Millimeter Array (ALMA). These galaxies were previously detected in [CII] and far-infrared continuum emission and span almost two orders of magnitude in star formation rate (SFR). Our results show at least two different regimes of ionized inter-stellar medium properties for galaxies in the first billion years of cosmic time, separated by their $L_{[CII]}/L_{[NII]}$ ratio. We find extremely low [NII] emission compared to [CII] ($L_{[CII]}/L_{[NII]} = 68^{+200}_{-28}$) from a "typical" $\sim L^{*}_{UV}$ star-forming galaxy, likely directly or indirectly (by its effect on the radiation field) related to low dust abundance and low metallicity. The infrared-luminous modestly star-forming Lyman Break Galaxy (LBG) in our sample is characterized by an ionized-gas fraction ($L_{[CII]}/L_{[NII]} \lesssim 20$) typical of local star-forming galaxies and shows evidence for spatial variations in its ionized-gas fraction across an extended gas reservoir. The extreme SFR, warm and compact dusty starburst AzTEC-3 shows an ionized fraction lower than expected given its star-formation rate surface density ($L_{[CII]}/L_{[NII]} = 22 \pm 8$) suggesting that [NII] dominantly traces a diffuse ionized medium rather than star-forming HII regions in this type of galaxy. This highest redshift sample of [NII] detections provides some of the first constraints on ionized and neutral gas modeling attempts and on the structure of the inter-stellar medium at z = 5–6 in "normal" galaxies and starbursts.

5.3 Introduction

The first billion years after the Big Bang is a crucial epoch for understanding galaxy evolution because we can directly witness the initial stages of galaxy assembly. In contrast to present day, most galaxies at these epochs are thought to have only formed a small fraction of their final stellar mass, to be accreting pristine gas very actively from the cosmic web, to have low metal abundances, and to have been affected in their star formation properties by the pristine quality of the inter-stellar medium (ISM; e.g., Bolton & Haehnelt 2007; Pawlik et al. 2009; Lacey et al. 2010; Choi & Nagamine 2010; Ryan-Weber et al. 2009; Becker et al. 2009; Simcoe 2006). Investigating the ISM and its relationship to star formation during the first billion year of cosmic time is a promising test bed for galaxy formation models (e.g., Dekel et al. 2009b,a; Dekel & Krumholz 2013), complementing studies of the peak epoch of galaxy assembly ($z \sim 2$–3; e.g., Shapley 2011; Carilli & Walter 2013; Casey et al. 2014a).

To faithfully model the interplay of the physical processes at the root of galaxy assembly and evolution we need observations of accurate diagnostics of the different physical phases of the gas. While luminous starbursting galaxies like submillimeter galaxies (SMGs) and quasar hosts have been targeted for more than a decade at $z > 5$ (e.g., Maiolino et al. 2005; Walter et al. 2009; Riechers et al. 2013; see Carilli & Walter 2013 for a review), we are only now reaching the capability of investigating the ISM in "normal" star-forming galaxies that are more representative of the general galaxy population at these epochs, in particular Lyman-break galaxies (LBGs; Riechers et al. 2014a, hereafter R14; Capak et al. 2015, hereafter C15; Willott et al. 2015). CO excitation ladders have become a routine tool to investigate the physical conditions in molecular gas for

starbursts (e.g., Riechers et al., 2010b, 2011a, 2013; Weiß et al., 2005; Scott et al., 2011); however, the prospects for detection in normal galaxies at $z > 5$ are not clear due to metallicity effects (Tan et al., 2013, R14). In fact CO detections of LBGs to-date, even exploiting strong lensing, have been limited to $z \lesssim 3$ (e.g., Baker et al., 2004; Coppin et al., 2007; Riechers et al., 2010a; Saintonge et al., 2013).

Sub-millimeter fine-structure lines of the most abundant atomic metal species (mainly C, N, O) and their ions offer a unique angle and an unobscured view of the ISM properties and conditions for star formation that is accessible to ALMA at high redshift. The far-infrared (FIR) cooling lines, less affected by dust attenuation than optical lines, are powerful probes of the star formation activity, linking them directly to the surrounding medium from which stars are born. Different lines, better in combination, can be used as diagnostics of the far-ultraviolet (FUV) flux, gas density, temperature, and filling factor of the photon-dominated regions (PDRs) and ionized regions (e.g., Tielens & Hollenbach, 1985; Wolfire et al., 1990; Kaufman et al., 1999). Recent surveys with the *Herschel Space Observatory* provide the context for high redshift studies by giving benchmark sets of local galaxies, for which almost complete suites of FIR lines yield solid constraints and allow detailed ISM modeling (e.g., Rosenberg et al., 2015; Cormier et al., 2015; De Looze et al., 2014; Spinoglio et al., 2015; Kamenetzky et al., 2016).

The ionization potential of nitrogen (14.5 eV) is greater than that of hydrogen, therefore the singly ionized nitrogen lines, [NII], probe the effect of UV photons emitted by massive young stars. Since N^+ is only present in the ionized medium it is a tracer of the extended low density envelope of HII regions, the

ionized surfaces of dense atomic and molecular clouds and the warm ionized medium (WIM). Goldsmith et al. (2015) find that the dominant source of [NII] emission in the Milky Way is not the WIM, because the electron density they measure from [NII] fine-structure line ratios is two orders of magnitude higher than what is expected in the Galactic diffuse medium, but it is expected that different types of galaxies, at different ages, will differ significantly in their ISM phase structure.

The high brightness of the [CII] 158 μm line makes it an ideal target at high redshift, where it allows dynamical studies and a probe into the ISM properties and star formation. However, [CII] can originate from a range of gas phases and the line luminosity alone gives no direct information on its origin. In fact, low-z observations have shown that while most of the [CII] luminosity comes from the atomic photon-dominated regions (PDR) and diffuse cold neutral medium (CNM), significant fractions also come from ionized gas regions and CO-dark molecular clouds (Pineda et al., 2013). Oberst et al. (2006, 2011) suggested that the [NII] 205 μm line could be used in conjunction with [CII] 158 μm to separate the ionized from neutral fraction of the ISM, because the latter is emitted by both weakly ionized and atomic gas. The transition critical densities of these two lines in ionized gas are very similar, implying that the line ratio for the ionized medium is nearly constant ($\sim$ 3–4, Oberst et al. 2006) and set by the relative carbon to nitrogen abundance, making [NII] a tracer of the ionized fraction of [CII]-emitting gas.

Langer et al. (2016) combined [NII] and [CII] Galactic observations to determine the fraction of ionized gas contributing to the [CII] emission in the Milky Way for many lines of sight, finding this to vary mostly between 0.5 and 0.8 (cor-

responding to [CII]/[NII] ratios ~4–10), where the Galactic center line of sights have the smallest ionized fraction, probably due to higher gas densities.

The [NII] 205 μm line is the tool of choice to characterize the low-density ionized ISM at high redshift. Thus, we here use ALMA to measure the [NII] properties of a sample spanning the variety of star-forming activity known at z = 5–6: a hyper-luminous nuclear starburst (AzTEC-3; SFR $\sim 1100\,M_\odot\,yr^{-1}$), a dusty, high star formation rate LBG (HZ10; SFR $\sim 170\,M_\odot\,yr^{-1}$) and a typical, less star-forming LBG (LBG-1; SFR $\sim 10-30\,M_\odot\,yr^{-1}$). These last two galaxies are near L^*_{UV} for LBGs at z = 5–6, and can be considered "typical" because they are consistent with the current constraints on the star-forming main sequence of galaxies at these redshifts (e.g., Speagle et al., 2014a). All galaxies were previously detected in [CII] with ALMA (R14; C15).

The structure of this paper is as follows. In Section 5.4 we describe the ALMA observations of the [NII] and [CII] lines utilized in this study. Our results are presented in Section 5.5, and in Section 5.6 we describe the HII and PDR models we have utilized to assist our interpretation. In Section 5.7, we present our interpretation for each galaxy in our sample. We close with a discussion of the impact of our findings and of this kind of FIR line studies in the first giga-year of cosmic time in Section 5.8. In this work we assume a flat ΛCDM cosmology with H_0=70 km s^{-1} Mpc^{-1}, Ω_m=0.3 and Ω_Λ=0.7.

5.4 Observations

5.4.1 ALMA Cycle-3 observations of [NII]

We observed the [NII] 205 μm ($^3P_1 \rightarrow {}^3P_0$) transition line ($\nu_{\rm rest}$=1461.131 GHz, redshifted to ~220–230 GHz at $z \sim 5.3$–5.7), using ALMA in Band 6 (see Table 7.1 for details). Observations were carried out in Cycle 3, with 32–47 usable 12 m antennae under good weather conditions at 1.3 mm (precipitable water vapor columns of 2.8 mm for AzTEC-3, 1.1 mm for HZ10 and 1.6–1.8 mm for LBG-1) for 4 tracks between 2015 December 16 and 2016 January 14, using 3 tracks in a compact configuration (max. baseline ~ 300 m) and one track on LBG-1 in transition from an extended to a compact configuration (min. baseline 15 m, max. baseline 6 km; two additional tracks were discarded due to poor data quality because of weather). These observations resulted in total on-source times of 25 min for AzTEC-3, 50 min for HZ10 and 64 min for LBG-1, with standard calibration overheads.

The nearby radio quasar J0948+0022 was observed regularly for amplitude and phase gain calibration, J1058+0133 and J0854+2006 were observed for bandpass and flux calibration, and Ganymede was also used for flux calibration of two tracks. We estimate the overall accuracy of the flux calibration to be within ~ 10%.

For each target the correlator was set up to cover two spectral windows of 1.875 GHz bandwidth each at 3.9 MHz (~ 5 km s^{-1}) resolution (dual polarization) in each sideband. The [NII] line was centered in one of the spectral windows, in the upper sideband for AzTEC-3 and LBG-1 (also covering the

CO(J=12→11) line in the lower sideband) and in the lower sideband for HZ10, and the other three spectral windows were placed to provide contiguous coverage of the continuum emission within the available bandwidth.

The Common Astronomy Software Application (CASA) version 4.5 was used for data reduction and analysis. All images and mosaics were produced with the CLEAN algorithm, using natural weighting for maximal sensitivity. We also apply an outer taper of 300 kλ to the LBG-1 observations that included unwanted long baselines (> 300 m).

AzTEC-3 and LBG-1 are separated by only 15″, so their individual pointings were imaged both separately and together in a mosaic. This significantly improves our sensitivity for AzTEC-3 (primary beam correction factor of ~0.7 in the mosaic), due to the longer on-source time of the LBG-1 pointing. We therefore extracted the AzTEC-3 line and continuum fluxes from the mosaic, while LBG-1 was analyzed in the single pointing, after confirming that the results are equivalent in both cases.

The mosaic has a synthesized beam size of 1.4″ × 1.2″ and the rms noise is ~ 0.34 mJy beam^{-1} at the position of AzTEC-3 in 41 km s^{-1} wide channels and ~ 0.21 mJy beam^{-1} at the position of LBG-1. The rms noise in the continuum maps are ~ 20 μJy beam^{-1} and ~ 15 μJy beam^{-1} at the positions of AzTEC-3 and LBG-1 in the mosaic, respectively. The LBG-1 pointing has a synthesized beam of 1.3″ × 1.1″ and the rms noise is also ~ 0.21 mJy beam^{-1} in the middle of the field in 41 km s^{-1} channels, and the continuum rms noise is ~ 16 μJy beam^{-1} .

For HZ10, the imaging results in a synthesized beam size of 1.7″ × 1.2″ at the redshifted [NII] frequency and in the continuum map. The rms noise in the

phase center is ~ 0.2 mJy beam^{-1} in a 44 km s^{-1} wide channel and the final rms noise when averaging over all spectral windows (i.e. over a total 7.5 GHz of bandwidth) is $\sim 35\,\mu$Jy beam^{-1}.

5.4.2 Archival ALMA Cycles 0 & 1 observations of [CII]

The ALMA data targeting the [CII] lines for our sample galaxies have previously been presented by R14 for the Cycle-0 observations of AzTEC-3 and LBG-1, and by C15 for the Cycle-1 observations of HZ10 and LBG-1 (referred to as HZ6 by C15). The Cycle-1 observations were taken on 2013 November 15-16 in band 7 as part of a larger project; we here provide a brief description of the data that we have re-analyzed from C15. The HZ10 pointing resulted in 56 min on source with 25 usable antennae. Ganymede was observed as flux calibrator, J0538–4405 was observed as bandpass calibrator, and J1058+0133 was observed as amplitude/phase gain calibrator. The LBG-1 (HZ6) data taken in Cycle-1 resulted in 42 min on source with 29 antennae. Pallas was observed as flux calibrator, and the bandpass and gain calibrators were the same as for the HZ10 observations. In both cases the correlator was set up to target the expected frequency of the [CII] line and to provide continuous coverage of the continuum emission in adjacent spectral windows with channels of 15.6 MHz in Time Division Mode (TDM).

We have re-calibrated these archival data and the Cycle-0 data described by R14 using the scripted pipelines on the archive after appropriately modifying them to be executed with CASA 4.5 and using the updated flux calibration tables from Butler-JPL-Horizons 2012 for Solar System objects. This modification

lowers the fluxes of the Cycle-0 data compared to R14 by $\sim 15\% - 20\%$ because of a corresponding lowering of the assumed flux of Callisto compared to Butler-JPL-Horizons 2010. We have furthermore modified the default flags at the edges of the spectral windows that cover the [CII] line in HZ10, to only flag two channels per window. This is sufficient because the bandpass calibration shows a sharp drop-off, and by imaging both spectral windows we recover the full line emission.

We have produced image cubes and continuum maps using the CLEAN task with natural weighting in CASA 4.5. LBG-1 was imaged by mosaicking Cycle-0 and Cycle-1 data as part of the CLEAN process. AzTEC-3 was imaged separately using the Cycle-0 data for the single pointing close to the source, after checking that mosaicking the second pointing (centered near LBG-1) does not significantly alter the results due to the high signal-to-noise ratio of the continuum and line detection in this source.

5.5 Results

5.5.1 The massive dusty starburst AzTEC-3

We detect the [NII] line (Table 7.1) in AzTEC-3 at 5σ confidence in the mosaic of the AzTEC-3 pointing and the LBG-1 pointing (the significance is 3.5σ in the AzTEC-3 data alone). The integrated line map (Fig. 5.1) shows tentative evidence ($\sim 3\sigma$) for extended structure in the [NII] emission, over a scale of $(2.8'' \pm 1.0'') \times (0.7'' \pm 0.6'')$ P.A. 15 degrees (deconvolved).

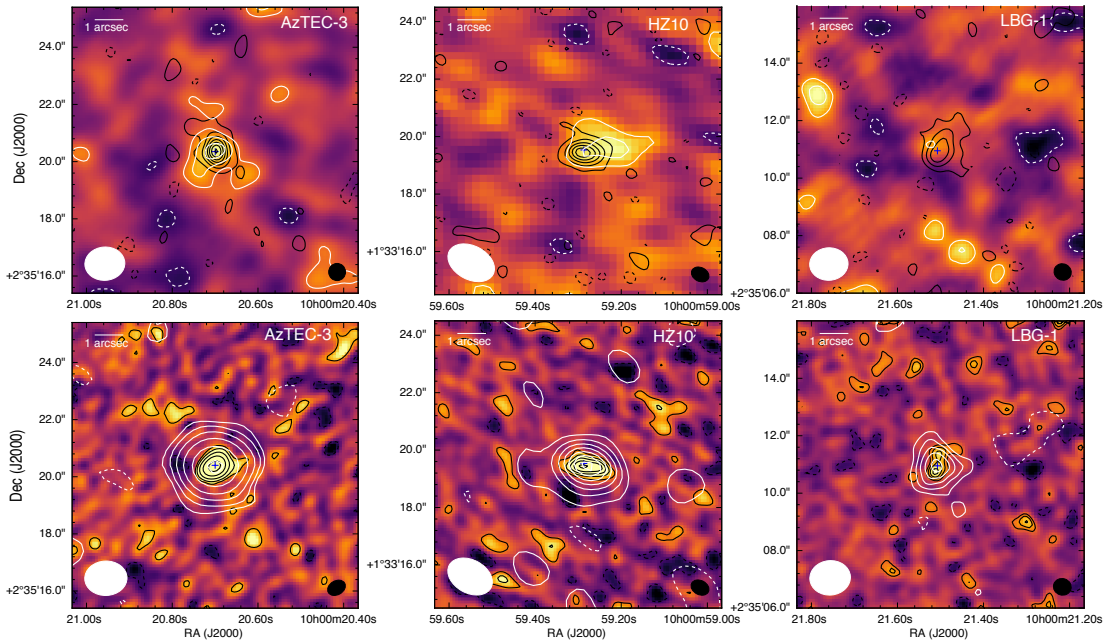

Figure 5.1: Top: Integrated line maps (over the line FWHM) showing [NII] colorscale with [NII] (white) and [CII] (black) contours. Blue crosses indicate the positions of the 205 μm continuum peak. The [NII] ([CII]) beam is shown in the bottom left (right) corner of each panel. The [NII] ([CII]) contours are multiples of 1σ (4σ), starting at $\pm 2\sigma$. The [NII] in the starburst AzTEC-3 is a 5σ detection, it is consistent with being centered at the position of the [CII] and continuum emission, and it may be resolved. In the FIR-bright LBG, HZ10, the [NII] emission (3.2σ per beam at the peak) is slightly resolved (5.3σ integrated significance) and appears to be offset with respect to the center of the [CII]-emission indicating significant variation of [CII]/[NII] across the galaxy. The significance of the tentative [NII] detection in LBG-1 is only 2σ, which constrains the [CII]/[NII] ratio to be very high (68^{+200}_{-28}). Bottom: Continuum maps showing 158 μm colorscale with 205 μm (white) and 158 μm (black) contours. Contours start at $\pm 2\sigma$ and are at powers of 2σ (i.e. $\pm 2\sigma, 4\sigma, 8\sigma$...) for AzTEC-3; in steps of 2σ for HZ10 and in steps of 1σ for LBG-1. The 205 μm (158 μm) beam is shown in the bottom left (right) corner.

Because of the moderate signal-to-noise ratio and consequently poorly constrained spatial extent of the emission we extract the [NII] line spectrum using an aperture of $1.5'' \times 1.3''$, which is fitted to the size of the [CII] emission convolved with the [NII] beam. This yields a line peak flux in the spectrum of (0.65 ± 0.14) mJy.[1] The flux measured through 2D-Gaussian fitting in the inte-

[1]Unless otherwise stated, all aperture spectra are extracted in apertures fitted to the FWHM

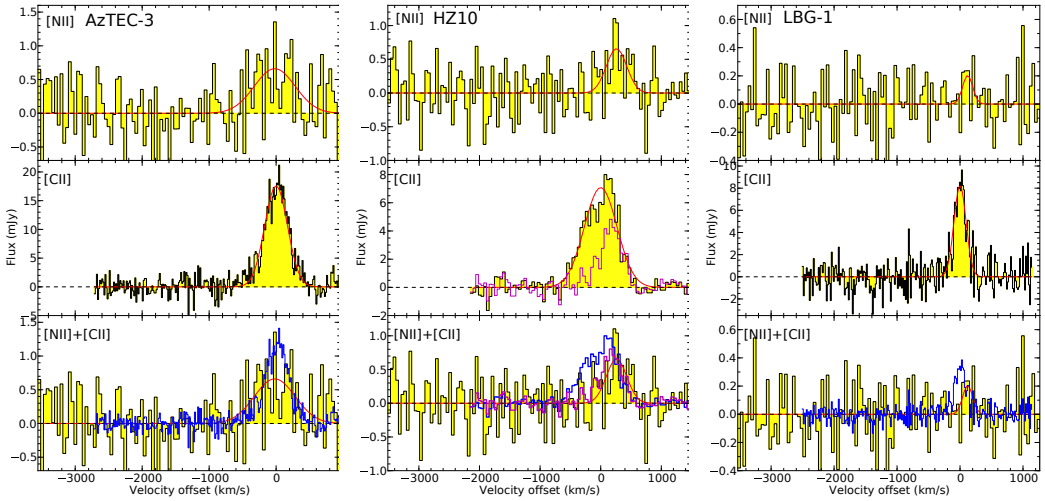

Figure 5.2: [CII] and [NII] spectra of our sample galaxies at z = 5–6, and Gaussian fits to the line emission (red curves). The channel velocity width in all [NII] spectra is $\sim 42\,\mathrm{km\,s^{-1}}$; in the [CII] spectra it is $\sim 16\,\mathrm{km\,s^{-1}}$ in AzTEC-3 and LBG-1 and $\sim 44\,\mathrm{km\,s^{-1}}$ in HZ10. [CII] is scaled arbitrarily down in flux density in the bottom panels for comparison. The [NII] line appears to be broader than [CII] in AzTEC-3. HZ10 shows a velocity shift between [CII] and [NII]. The magenta spectra in the central middle and bottom panels show a "local" [CII] spectrum extracted at the [NII] peak position (after smoothing to the [NII] resolution), suggesting a common kinematic origin with [NII].

grated line map would result in [NII] line flux which is ~25% higher, compatible with our measurement to within $\sim 1\sigma$. However, given the significance of the detection of only $\sim 5\sigma$, the spatial size of the Gaussian fit is highly uncertain. This leads us to adopt the [CII]-based aperture flux in the following.

The measured width of the [NII] line profile appears $\sim$ 60% ± 40% greater than [CII], which could be indicative of a different origin for the gas traced by [NII] and the [CII] emission, however the significance of this difference is only 1.4σ. By fitting the FWHM of the [NII] line (Fig. 5.2, $660 \pm 180\,\mathrm{km\,s^{-1}}$) we measure an integrated line flux of $(0.46 \pm 0.16)\,\mathrm{Jy\ km\ s^{-1}}$, yielding a [CII] to [NII]

of the spatial emission, and then corrected by a factor of ×2, to account for the missed flux outside the aperture, based on the assumption of Gaussian spatial profiles.

luminosity line ratio of 22±8. Due to the poorly constrained velocity width of the line it is worth considering the possibility that the real FWHM of [NII] be the same as in [CII]. Fixing the [NII] line width to the [CII] line width in the fitting would yield a ratio of 42 ± 9.

5.5.2 The FIR-luminous LBG HZ10

We detect the [NII] line in HZ10 with an integrated significance of $\sim 5.3\sigma$ (peak signal-to-noise ratio of ~3.2 per beam).

The [CII] emission is spatially resolved and shows a smooth velocity gradient suggestive of a disk, with deconvolved size of $(0.80'' \pm 0.07'') \times (0.42'' \pm 0.06'')$. The [NII] emission also appears to be extended with a marginally larger size of $(1.9'' \pm 0.9'') \times (0.6'' \pm 0.7'')$, and it appears to be associated with only one part of the [CII] emitting region (offset $\sim 0.8'' \pm 0.3''$). Figs. 5.1 and 5.2 show that both the velocity and position shift relative to the [CII] emission are compatible with the interpretation of differential emission, with [NII] coming predominantly from a location offset spatially and kinematically with respect to the center of the [CII] and FIR emission. Because the [NII] emission appears extended and not coincident with the [CII], we extract the [NII] line spectrum in an aperture of size equal to the FWHM of the 2D-Gaussian fit to the [NII] integrated line map.

The global [CII] to [NII] luminosity ratio obtained from the integrated line fluxes is 19 ± 6 for HZ10, but this does not take into account the potentially different origin of the emission. In order to correct for this effect, we also derive a "local" line ratio based upon measuring the fraction of [CII] line flux in a moment-0 map that uses the [NII] velocity range. This shifts the center of the

[CII] peak by 0.2″ in the direction of the [NII] peak and gives a line luminosity ratio of 14 ± 5. A lower bound on the [CII] to [NII] luminosity ratio can be obtained by measuring the [CII] line flux in a single pixel at the position of the [NII] peak (after convolving the [CII] data-cube to the resolution of the [NII] map), which yields a low ratio of 8 ± 3.

5.5.3 The "normal" L^* galaxy LBG-1

Our sensitive data on LBG-1 only resulted in a tentative (2σ) detection of the [NII] line at (0.2 ± 0.1) mJy peak flux. The emission appears unresolved and its position and velocity width are compatible with that of the [CII] line within the uncertainties. The single-pixel flux we extract at the peak of the integrated line map is compatible with the aperture flux, within the significant uncertainties. There is tentative evidence for a slight velocity redshift of the [NII] line with respect to the [CII] by (120 ± 40) km s^{-1}. Although the moderate signal-to-noise does not allow us to conclusively establish this offset, it appears to be reminiscent of our findings in HZ10. The extremely low value of the [NII] luminosity constrains the ratio of [CII] to [NII] line luminosities to be $\sim 68^{+200}_{-28}$, which may indicate ISM properties never seen before at high redshift.

5.5.4 Continuum measurements

We extract continuum fluxes and sizes from 2D-Gaussian fitting or aperture fluxes for each source both in the archival 158 μm and our new 205 μm data. All the sources are detected with moderate to high significance. Table 5.2 presents

the results of the flux measurements in the two separate sidebands, where the signal-to-noise ratio is sufficient.

In order to measure the far-infrared luminosity, we explore the parameter space of modified black-body models with a Markov chain Monte Carlo (MCMC) routine to fit the continuum measurements for the LBGs (HZ10 and LBG-1) whose FIR SED shapes were previously unconstrained.[2] The FIR luminosity implied by our fits is strongly dependent on the assumed dust temperature, which is poorly constrained by our measurements; since the dust emissivity index β and the dust temperature are degenerate on the Rayleigh-Jeans tail of the dust emission. We assume optically thin FIR emission and impose weak Gaussian priors on the dust temperature (30 ± 20 K) and β (1.7 ± 0.5) based on the SEDs of local dwarf galaxies (Rémy-Ruyer et al., 2013) and compatible with Milky Way values, to obtain dust temperatures of 33^{+12}_{-8} K for HZ10 and 38^{+16}_{-13} K for LBG-1. The resulting FIR luminosities (between 42.5 and 122.5 μm) implied by the fits are $6.4^{+9.5}_{-3.6} \times 10^{11}\,L_\odot$ for HZ10 and $1.9^{+3.8}_{-1.4} \times 10^{11}\,L_\odot$ for LBG-1, compatible with previous estimates (C15). If we relax the prior on the dust temperature to a uniform prior between 10–100K, we obtain 36^{+25}_{-10} K for HZ10 and 60^{+35}_{-27} K for LBG-1, respectively, showing that the dust temperature is significantly uncertain given current constraints, and potentially allowing for higher FIR luminosity, if the dust temperature were higher than expected. In fact the remaining uncertainty on the upper end of the dust temperature probability distribution, and thus the FIR luminosity, implies that "normal" systems like LBG-1 may have higher than previously estimated FIR luminosity (C15), and thus may remain consistent with the SMC IRX–$\beta_{\rm UV}$ relation between the infrared and ultraviolet luminosity ratio and the ultraviolet continuum slope discussed

[2]The FIR SED of AzTEC-3 was already constrained by numerous previous studies and is not significantly improved by the current measurement.

in C15, despite apparently falling below when "average" dust temperatures are assumed.

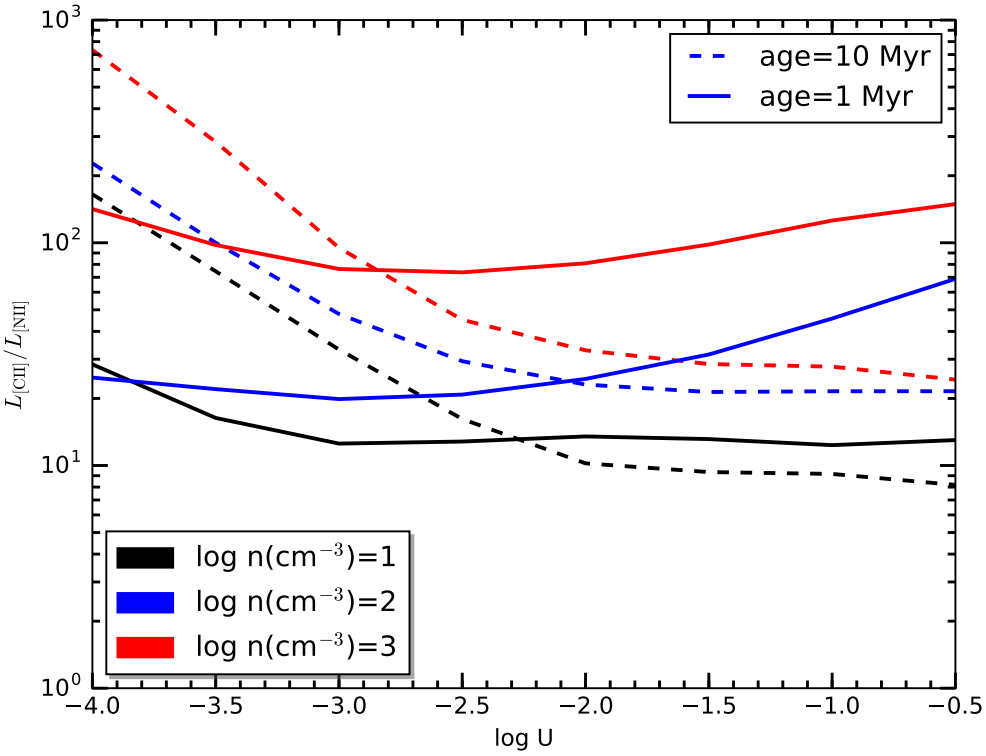

Figure 5.3: Cloudy model results for the ratio of the [CII] and [NII] line luminosities for a grid of HII region+PDR models. The age of the starburst (1 and 10 Myr, dashed and solid lines) determines the mass of the most massive Main-Sequence star still present and affecting the hardness of the radiation field. The main difference between the different age tracks is that the 1 Myr starburst produces a significant N^{++} region, while the 10 Myr starburst does not. The density range (from 10 cm^{-3} to 1000 cm^{-3}) covers diffuse ionized gas to ultra-compact HII regions. The substantial uncertainty on the intensity of the radiation field at high redshift, in very different environments, is captured by the broad range of ionization parameter (U) considered, along the abscissa. Of particular note are the strong density effect (high density implies higher line ratio) and the slight rise of the ratio for hard radiation and high intensities due to further ionization of N^+ to N^{++}.

Table 5.1: Measured [CII] and [NII] line properties of our sample galaxies

Quantity	AzTEC-3	HZ10	LBG-1
[CII] line properties			
$\nu_{\rm obs}$(GHz)	301.771 ± 0.006	285.612 ± 0.013	301.980 ± 0.007
Redshift	5.29795 ± 0.00013	5.6543 ± 0.0003	5.29359 ± 0.00015
$S_{\rm [CII]}$(mJy)	17.5 ± 0.7	7.1 ± 0.3	8.2 ± 0.5
$FWHM_{\rm [CII]}$ (km s^{-1})	410 ± 15	630 ± 30	230 ± 20
$I_{\rm [CII]}$ (Jy km s^{-1})	7.8 ± 0.4	4.5 ± 0.3	2.1 ± 0.2
$L_{\rm [CII]}$ ($10^9 L_\odot$)	6.4 ± 0.3	4.0 ± 0.3	1.71 ± 0.16
deconvolved size	(0.65″ ± 0.06″) × (0.33″ ± 0.07″)	(0.80″ ± 0.07″) × (0.42″ ± 0.06″)	(1.00″ ± 0.12″) × (0.57″ ± 0.10″)
size (kpc^2)	(4.0 ± 0.4) × (2.1 ± 0.4)	(4.8 ± 0.4) × (2.5 ± 0.4)	(6.2 ± 0.7) × (3.5 ± 0.6)
[NII] line properties			
$\nu_{\rm obs}$(GHz)	232.02 ± 0.06	219.39 ± 0.04	232.1 ± 0.3
$S_{\rm [NII]}$ (mJy)	0.65 ± 0.14	0.66 ± 0.18	0.20 ± 0.09
$FWHM_{\rm [NII]}$ (km s^{-1})	660 ± 180	400 ± 120	190 ± 90
$I_{\rm [NII]}$ (Jy km s^{-1})	0.46 ± 0.16	0.31 ± 0.11	0.04 ± 0.03
$L_{\rm [NII]}$ ($10^9 L_\odot$)	0.29 ± 0.10	0.21 ± 0.08	0.025 ± 0.019
$L_{\rm [CII]}/L_{\rm [NII]}$	22 ± 8	19 ± 6 (local: 14 ± 5)	68^{+200}_{-28}

Table 5.2: Measured continuum properties of our sample galaxies

Target	$\nu_{\rm obs}$ (GHz)	S_ν (mJy)	$\nu_{\rm obs}$ (GHz)	S_ν (mJy)
AzTEC-3	303.62	5.2 ± 0.3	233.93	3.19 ± 0.09
	289.87	4.4 ± 0.3	217.61	2.58 ± 0.09
HZ10	297.84	1.21 ± 0.24	234.50	0.87 ± 0.14
	285.81	1.05 ± 0.20	220.37	0.69 ± 0.11
LBG-1	296.79	0.22 ± 0.07	233.06	0.14 ± 0.04
			218.62	0.11 ± 0.04

5.6 Cloudy modeling of the [CII]/[NII] ratio

In order to aid the interpretation of our observations we have run a grid of Cloudy models using version 13.03 (Ferland et al., 2013). We simulate constant pressure clouds with spherical geometry (although the inner radius of 3 kpc that we adopt implies the HII region and PDR are close to the plane-parallel regime), extending up to A_V=10 to include both HII regions and PDRs. The input spectrum is taken from Starburst99 models (Leitherer et al., 1999) with Geneva stellar tracks (Meynet et al., 1994), default parameters for solar metallicity stellar atmospheres and a burst of star formation in order to use the age of the starburst as a proxy for hardness of the radiation field. We also explore the effect of low stellar metallicity tracks (Z = 0.001, i.e. $\sim 0.07\,Z_\odot$) on our results but find little difference for the main quantities of interest. We adopt all gas element abundances for solar metallicity from Nagao et al. (2011) and include Orion-like dust and magnetic fields (intensity of 10^{-5} G at the inner edge, as appropriate for the Orion nebula according to the Cloudy documentation). We fix the cloud inner edge gas density and ionization parameter (U) for starburst ages of 1 Myr and 10 Myr, and vary both parameters in a grid. Figure 5.3 shows the integrated line luminosities predicted by our Cloudy simulations from large,

single clouds illuminated by a central starburst. While the precise values are model-dependent and should not be directly compared to the measured values (and depend on the precise carbon to nitrogen abundance ratio and gas density structure) we examine the main trends to gain insight into the major factors affecting the [CII]/[NII] line luminosity ratio.

The main trend is a clear density dependence, with higher density (for a fixed ionization parameter, U) corresponding to higher $L_{[\mathrm{CII}]}/L_{[\mathrm{NII}]}$. Although this effect does not appear straightforward to interpret, we suggest some elements that are likely to play a role. The effect that we see in these models is probably partly caused by a saturation of the [NII] total emission with increasing density, i.e., a lack of substantial increase due to the low critical density ($\sim 100\,\mathrm{cm}^{-3}$) of the [NII] transition. At the same time the Cloudy models show a steady increase of the [CII] emission from the PDR with the simultaneous increase in density and radiation field (an increase in density at constant U implies a proportional increase of the input stellar flux). The gas density in the PDR is higher than in the HII region but not as high as one might expect from simple gas pressure balance; this is due to the magnetic pressure becoming important in the PDR for some of the low and intermediate density models. As a consequence the density in the PDR approaches the [CII] critical density for neutral gas from below and only crosses it for the high density models, with [CII] saturating at higher HII gas densities than naively expected. Thus, the increase of the gas density in the PDR, together with the increase in far-UV flux (G_0) due to keeping U constant, implies stronger PDR [CII] emission with approximately unchanged [NII] emission; which causes an increase in [CII]/[NII] ratio as a function of model density.

Another important effect controlling the line ratio is the conversion of [NII] to [NIII] in high ionization conditions (caused by both high U and hard radiation). Its effects can be seen in isolation from the difference between the two ages of the burst of star formation (a proxy for hardness of the incident radiation) since we find that [NIII] is very important in the 1 Myr case, while it is negligible in the 10 Myr models. Its main contribution is clear: while in the low-hardness case an increase in U favors [NII] emission over PDR tracers (like [CII]), this trends reverses for hard radiation, when the increased [NIII] implies a deficit of [NII] emission with increasing ionization parameter.

We have also run equivalent Cloudy simulations with stellar radiation input produced by the lowest available stellar metallicity Geneva tracks to investigate the approximate effect of a young stellar population, as expected at high redshift. The effects on the line ratio of interest do not significantly affect our interpretation ($\lesssim$ 50%). However it is possible that an inclusion of more realistic stellar population models, e.g., accounting for stellar binary effects which could produce higher effective stellar temperatures, may have a greater impact, which requires further investigation. We have not attempted changing the gas-phase metallicity because this would further complicate the interpretation of the model results, (e.g., given the uncertainty in the effect of metallicity on the carbon-to-nitrogen ratio). It is also possible that the structure of the ISM might be significantly altered by radically different stellar populations and star-forming conditions, which would therefore require changing the standard geometry of HII regions around recently formed stars, surrounded by atomic PDR gas, assumed here which could systematically change the model results. For example, Vallini et al. (2016) explore the effect on FIR emission lines of time-dependent cloud photo-evaporation, and suggest that equilibrium models

might be systematically incorrect.

5.7 Analysis of the individual sources

5.7.1 AzTEC-3

AzTEC-3 is one of the most intensely star-forming starbursts known at $z > 5$ (not amplified by gravitational lensing). It is centrally located in one of the earliest galaxy proto-clusters known (showing an 11-fold over-density of LBGs and color-selected galaxies within 2 Mpc, suggesting a halo mass $> 4 \times 10^{11}\, M_{\odot}$; Capak et al., 2011) and is known to be compact and dusty (Riechers et al., 2010b, 2014a). Its very compact starburst ($\lesssim 2.5$ kpc in diameter), leads to a high dust temperature (~ 50 K–90 K; R14), indicating extreme conditions even among high redshift SMGs. We have detected the [NII] line in AzTEC-3, with a measured [NII] luminosity of $2.9 \times 10^{8}\, L_{\odot}$ implying $L_{[\mathrm{NII}]}/L_{\mathrm{FIR}} = 2.5 \times 10^{-5}$, which is very low compared to local (U)LIRGs (Zhao et al., 2016). Lu et al. (2015) and Zhao et al. (2013) argue that low values of [NII] luminosity to FIR emission correlate with warm dust in local galaxy samples. This is consistent with the intense radiation field and high dust temperature already found by SED modeling of AzTEC-3 (R14).

The [NII]/FIR deficit can be interpreted as the product of two effects which can be studied in isolation: the [CII]/[NII] ratio, which is dependent on the relation between ionized and neutral gas; and the [CII]/FIR ratio, which characterizes the gas heating efficiency. The latter was discussed by R14, where it was interpreted as analogous to the deficit found in local ULIRGs (e.g., Luhman

et al. 1998, 2003). On the other hand, the [NII] line in AzTEC-3 also appears marginally fainter compared to [CII] than observed in local (U)LIRGs (Farrah et al., 2013; Kamenetzky et al., 2016; Rosenberg et al., 2015; Díaz-Santos et al., 2013; Zhao et al., 2016) and in other high redshift SMGs (Decarli et al. 2014a[3]; Béthermin et al. 2016), for which typical sample averages of $L_{[CII]}/L_{[NII]}$ are in the range $\sim 10-20$. In addition, the measured $L_{[CII]}/L_{[NII]}$ ratio of 22 ± 8 might be under-estimated due to optical depth effects. R14 found that dust extinction might significantly affect the [CII] flux (we estimate a factor of ~ 1.6 in the line ratio, based on the global SED-modeling parameters from R14) and could obstruct the view to the innermost, densest regions.

On the other hand, if we qualitatively extrapolate the correlation between star-formation rate surface density and ionized gas density and ionization parameter found by Herrera-Camus et al. (2016) in local galaxies, we are led to expect gas densities $\sim 1000\,\mathrm{cm}^{-3}$ in the HII regions in the central part of AzTEC-3, far above the [NII] 205 μm critical density of $100\,\mathrm{cm}^{-3}$. Based on our Cloudy simulations such high gas densities in the HII regions would produce a [CII]/[NII] ratio almost an order of magnitude higher than observed (Fig. 5.3). The finding of a "normal" ratio of 20–40 is therefore surprising and needs to be interpreted carefully.

Röllig et al. (2016) found a [CII]/[NII] luminosity ratio of 12 in the central regions of IC 342, a normal local star-forming galaxy, similar to our own Milky Way, suggesting that a majority of the [CII] emission originates in ionized gas. However, Lu et al. (2015) find a positive correlation between the [CII]/[NII] ratio and FIR-color in local galaxies. Based on the expectation that FIR-color cor-

[3]See Section 5.8 for updated values of [CII]/[NII] in the objects studied by Decarli et al. (2014a).

relates both with ionization parameter and with ionized gas density (Herrera-Camus et al., 2016), we interpret this trend as predominantly a density effect, reducing the importance of the ionized gas component of [CII] emission in hotter, denser starbursts.

Why does the trend to higher [CII]/[NII] ratios not extend to high redshift SMGs, and especially AzTEC-3 with its extreme density compared to local ULIRGs? It is possible that the tentatively detected low-level, extended emission, if real, might indicate a warm ionized component that is more extended and diffuse than the denser star-forming, FIR and [CII]-emitting central region. This may also indicate a gas flow either in the process of being ejected or accreting onto the central galaxy. Furthermore the tentative evidence for a broader [NII] line than [CII], (660 and 410 km s^{-1} respectively) could be indicative of higher dynamical mass enclosed within the [NII]-tracing gas versus the neutral star-forming medium or it could be associated with the systemic velocity in a potential ionized gas flow.

This tentative evidence for non-nuclear emission may suggest that, in contrast to local starbursts, the hard and intense radiation field of AzTEC-3 might ionize a dominant large diffuse component of the ISM, outside the dense, molecular star-forming core. The lower density of this component, perhaps comparable to the critical density of [NII] would imply that this gas would dominate the emission over the gas directly surrounding the current star-formation. Higher signal-to-noise observations are necessary to further investigate this possibility.

The slightly elevated [CII]/[NII] ratio in AzTEC-3, compared to other high-z SMGs is unlikely to be due to gas-phase metallicity alone since this source is very dusty ($M_{\rm d} = 2.7 \times 10^8\,M_{\odot}$; R14). The low dynamical mass also puts an

upper limit on $\alpha_{\rm CO} < 1.3\ {\rm M}_\odot({\rm K\,km\,s^{-1}\,pc^2})^{-1}$ (R14), which is incompatible with expectations for low-metallicity gas (Bolatto et al., 2013).

If the [NII] emission is indeed extended at very faint levels, perhaps over a scale up to $\sim$ 15 kpc, our results may be suggestive of ionized gas flows, either ejected from the hyper-starburst activity or funneling gas into the core of the dense proto-cluster associated with AzTEC-3, fueling the extreme star-formation. The strong OH molecular emission feature detected in R14, apparently blue-shifted, is indicative of warm, dense ouflows which could be related to the tentatively detected extended ionized gas, if confirmed by more sensitive observations.

Assuming that the [NII]-emitting ionized gas is also emitting [CII] with a predictable relative intensity we can determine the fraction of [CII] emission that comes from ionized rather than neutral gas using the measured [CII]/[NII] ratio.[4] Following Oberst et al. (2006), we assume a C^+/N^+ abundance ratio of $\sim$ 1.8 (from Savage & Sembach, 1996), to infer a line luminosity ratio $[{\rm CII}]_{\rm ionized}/[{\rm NII}]\simeq 3.5$, for ionized gas density in the range $\sim$10–1000 cm^{-3}. With these assumptions the measured fraction of [CII] emission from ionized gas in AzTEC-3 lies in the range 10–25%.

Following Faisst et al. (2016b) we can use the *Spitzer* IRAC [3.6 μm]–[4.5 μm] color to qualitatively constrain the strengths of some of the main optical emission lines. At the redshift of AzTEC-3 the Hα line falls into the 4.5 μm band,

[4]This particular inference depends on several assumptions. The line emission needs to be optically thin in order to be additive. Also, the ratio of carbon and nitrogen gas-phase abundances are not well constrained and enter the conversion of [NII] to [CII] luminosity coming from ionized gas. In addition, complete and equivalent ionization state of carbon and nitrogen in the traced ionized gas is assumed (i.e., we assume that in [NIII] regions carbon atoms are also in a higher ionization state, thus not contributing to the [CII] emission). Furthermore the inferred fraction of [CII] emission from ionized gas represents a spatial average over possibly heterogeneous regions.

and therefore the *Spitzer* [3.6 μm]–[4.5 μm] color is related to its Hα equivalent width. From the COSMOS2015 catalog (Laigle et al., 2016) we calculate a color of 0.48 mag, close to the average for the z = 5–6 galaxy population (Faisst et al., 2016b). However the optical counterpart of AzTEC-3 is shifted with respect to the (sub)millimeter continuum emission, indicative of strong dust obscuration (e.g., Riechers et al., 2010b, R14); hence it is possible that the optical emission lines may not be directly associated with the peak starburst emission, but either with a secondary component or with a less obscured part of the central galaxy.

5.7.2 HZ10

We have detected [NII] in the most IR-luminous LBG of the C15 sample, HZ10 ($z \sim 5.7$). This galaxy appears to be more dusty than average LBGs at its redshift based on our ALMA continuum measurements at $\sim 158\,\mu$m and $\sim 205\,\mu$m. It displays extended [CII] emission, showing a smooth velocity gradient possibly suggestive of coherent rotation and is characterized by a $L_{[\mathrm{CII}]}/L_{\mathrm{FIR}}$ ratio of 1.5×10^{-3} (C15). This ratio is suggestive of "normal" star-forming conditions (radiation fields and density perhaps similar to local star-forming galaxies), which is surprising for a young stellar population expected at z = 5–6. The measured [NII] luminosity of $2.1\times10^{8}\,L_{\odot}$ corresponds to $L_{[\mathrm{NII}]}/L_{\mathrm{FIR}} = 3.3\times10^{-4}$, when using our median estimate for the FIR luminosity, placing it in the regime of local star-forming galaxies (Farrah et al., 2013; Kamenetzky et al., 2016; Rosenberg et al., 2015; Díaz-Santos et al., 2013; Zhao et al., 2016).

In contrast to AzTEC-3, the extended gas reservoir in HZ10 suggests a lower density star-forming environment ($\Sigma_{\mathrm{SFR}} \sim 1/50\times$ in AzTEC-3, based on a com-

parison of continuum sizes and SFRs). This lower $\Sigma_{\rm SFR}$ is qualitatively consistent with the lower [CII]/[NII] ratio observed in HZ10, but it appears not to cause as large an effect as we might expect from our Cloudy models, which is consistent with the interpretation that a significant fraction of the [NII] emission in AzTEC-3 is probably dominantly emitted by a more diffuse medium than the actively star-bursting gas. The global [CII]/[NII] ratio of $\sim$ 20 measured for HZ10 is comparable to local galaxies with high SFRs (Zhao et al., 2016) indicating a significant contribution of ionized gas to the [CII] emission. In fact, under the same assumptions as for AzTEC-3, we find a fraction of [CII] emission from ionized gas in HZ10 in the range 10–25%; this would support the interpretation that the ISM in HZ10 is more mature than in "normal" LBGs at z = 5–6. This is also consistent with the fact that the stellar mass of HZ10 ($\sim 2 \times 10^{10}\,M_{\odot}$; C15) is higher than in most of the C15 sample, therefore it may have synthesized more metals already. Furthermore, the ionized fraction could be enhanced in parts of the galaxy; the tentative local line ratios (Fig. 5.2) suggest a [CII]/[NII] ratio as low as $\sim$ 10, perhaps caused by an ionization-dominated region of the galaxy. Such regions are consistent with what is seen in the models of Vallini et al. (2013). The tentative evidence for heterogeneity of the ionization state in the star-forming gas reservoir of HZ10 is suggestive of regions of different density (clumpiness), a recent massive starburst event, or a recent/active merger.

At the redshift of HZ10, the Hα line falls into the 4.5 μm band, and the [OIII] and Hβ lines fall into the 3.6 μm band, allowing us to use the relative equivalent widths of the two sets of lines as a diagnostic tool (Faisst et al., 2016b); the [3.6 μm]–[4.5 μm] color in this case is a measure of the strength of the [OIII] emission line relative to the hydrogen lines. In HZ10, we measure a [3.6 μm]–[4.5 μm] color of 0.41 mag, which falls towards the "red" end of the distribution

for comparable galaxies, implying that [OIII] is not as bright as observed in normal galaxies at the same redshift. This lower than average [OIII] strength is consistent with our inference of a more mature galaxy, which is less dominated by high ionization state gas than LBG-1.

Fig. 5.4 shows an optical (rest-UV) spectrum of HZ10, taken with Keck/DEIMOS as part of the COSMOS DEIMOS spectroscopic survey (PI: Capak). This spectrum shows Lyα emission and some of the main UV absorption lines commonly observed in LBGs (Shapley et al., 2003); we identify Si II, O I/Si II, C II, N V and Si IV. Assuming that the FIR [CII] emission traces the systemic velocity for the whole galaxy, several low-ionization ISM lines (Si II, O I/Si II and Lyα) are slightly blue-shifted by $(110 \pm 180)\,\mathrm{km\ s^{-1}}$ relative to the systemic velocity, likely due to outflowing winds, as commonly observed in $z \sim 3$ LBGs (Shapley et al., 2003). Interestingly, the C II absorption (usually originating from the neutral ISM) and the high-ionization Si IV lines (mostly originating from HII regions and stellar winds) are significantly redshifted with respect to the systemic velocity by $(522 \pm 200)\,\mathrm{km\ s^{-1}}$. This redshift, consistent with what is observed for the FIR [NII] line ($255 \pm 50\,\mathrm{km\ s^{-1}}$), may suggest a potential common origin for these lines, which thus may predominantly emerge from the western part of the galaxy. This would be consistent with the velocity gradient seen in the FIR [CII] emission, which shows a spatial displacement from west to east between the red- and blueshifted part of the emission. This may indicate a higher ionization fraction in the western part of HZ10 compared to the rest of the galaxy.

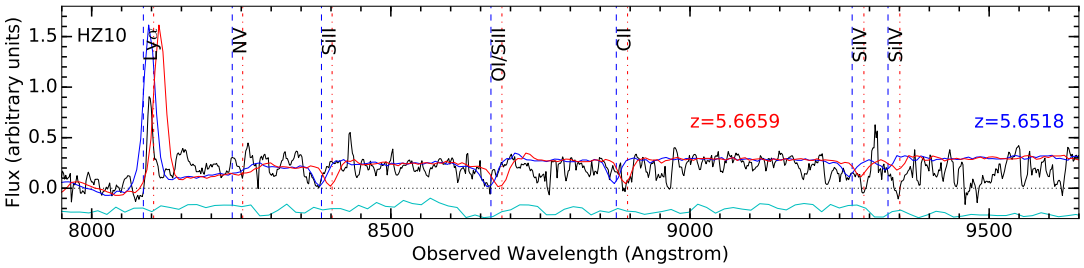

Figure 5.4: Optical Keck/DEIMOS spectrum of HZ10 shown in black with UV emission/absorption lines identified for two different redshifts (z = 5.6518 and 5.6659). Si II, O I/Si II and Lyα are slightly blue-shifted (110 ± 180 km s^{-1}) relative to the systemic redshift inferred from the FIR [CII] line, likely due to outflowing winds. The UV C II absorption and the high-ionization Si IV lines are redshifted with respect to the systemic velocity (522 ± 200 km s^{-1}) and are compatible with the FIR [NII] emission redshift, which may indicate higher ionization conditions in a part of the galaxy. The blue (red) spectrum shows the stacked $z \sim 3$ LBG template from Shapley et al. (2003) redshifted to the best fitting match to the two observed sets of lines in HZ10 and scaled to its continuum flux level. The cyan line shows the telluric transmission spectrum (arbitrarily scaled), estimated by the inverse sample variance.

5.7.3 LBG-1

We tentatively detect [NII] emission from LBG-1, a relatively quiescent star-forming galaxy in the AzTEC-3 proto-cluster that can be considered "typical" of LBGs at z = 5–6 based on its UV properties (luminosity, spectral slope) and low IR luminosity (R14). LBG-1 shows a complex, three-component morphology with velocity gradients in the ALMA [CII] data confirming the physical association of the HST sources, and suggesting either a merger or an extended clumpy star-forming gas reservoir. LBG-1 shows an extremely faint FIR continuum compared to its [CII] emission ($L_{[\mathrm{CII}]}/L_{\mathrm{FIR}} \sim 10^{-2}$), pointing towards low dust content and perhaps low gas-metallicity conditions that are suggestive of a young starburst, possibly triggered by the merging/accreting event responsible for the complex morphology. The potential absence of an older stellar popula-

tion makes this galaxy an ideal target for exploring the state of the ISM in young, forming galaxies typical in the first giga-year of cosmic time.

The measured [NII] luminosity of $2.5 \times 10^7\,L_\odot$ corresponds to a ratio of $L_{[\mathrm{NII}]}/L_{\mathrm{FIR}} = 1.3 \times 10^{-4}$, which is lower than what we find in HZ10, suggestive of different ISM properties.

In particular, the [CII]/[NII] ratio is very high (68^{+200}_{-28}) compared to local normal star-forming galaxies as well as all high redshift galaxies observed to date, indicating that only a small fraction of the bright [CII] emission is coming from ionized gas. It is unlikely that the mechanism responsible for the high ratio of [CII]/[NII] is the same as in AzTEC-3 since LBG-1 has a low star-formation rate and spatially extended [CII] emission. At least two scenarios are compatible with our observations: either the ISM is dominated by neutral PDR gas, or most of the ionized gas could be in a high ionization state (compared to Galactic HII regions) with a larger abundance of N^{++} than N^+.

A low dust-to-gas ratio could imply very extended PDRs, where the transition to molecular hydrogen is due to self-shielding instead of dust opacity. This interpretation is consistent with a large neutral-to-ionized gas fraction by increasing the proportion of the atomic regions emitting in [CII].

As suggested by $z \sim 2$–3 studies (e.g., Kewley et al., 2013) we assume a large ionization parameter to be characteristic of normal star-forming galaxies, especially at this higher redshift. The trend to harder radiation fields and low dust content could cause the ISM properties to differ dramatically in this extremely young star-forming galaxy, which suggests that we may have to turn to local dwarfs in the search for local analogs. In the case of dwarf galaxies, Cormier

et al. (2015) also find extremely elevated values for the [CII]/[NII] ratio, although this is deduced indirectly as they only measured [NII] 122 μm, which has a higher critical density. They also find evidence for strong [OIII] emission, which is indicative of higher ionization in the majority of the ionized gas; they associate the high ionization with the deficit in [NII] emission. De Looze et al. (2014) and Cormier et al. (2015) also find the [OIII] emission to be the dominant FIR line by luminosity, while local HII regions are almost never dominated by such high-ionization gas. This explanation could be applicable to LBG-1 and would support the need to invoke a low dust content, as in dwarfs, to explain the low [NII] luminosity.

At the present level, a third interpretation such as a lower nitrogen abundance in the gas phase remains possible. A reduced gas phase metallicity would not directly affect the [CII]/[NII] ratio through the ion abundances unless it were differentially reducing nitrogen relative to carbon. Local studies (e.g., Vincenzo et al., 2016) have shown a non-linear dependence of the nitrogen abundance relative to oxygen and perhaps carbon, and low metallicity gas could be expected to show reduced nitrogen abundance if it behaves as a secondary element. On the other hand, no conclusive evidence has been found so far at high redshift, with results indicating a potentially higher nitrogen abundance than expected or a N/O ratio that depends on stellar mass in tracing galaxy maturity (e.g., Masters et al., 2016; Steidel et al., 2014).

Under the same assumptions as for AzTEC-3, we find a fraction of [CII] emission from ionized gas in LBG-1 that is only about $\sim 5\%$. We do not expect the presence of significant [NIII]-emitting regions to affect this conclusion as the higher ionization-state gas is not expected to emit [CII].

We measure a *Spitzer* IRAC [3.6 μm]–[4.5 μm] color of 0.44 mag for LBG-1 which is consistent with a median value of the Hα equivalent width for LBGs, i.e., consistent with what is expected for a "typical" galaxy at this redshift (Faisst et al., 2016b). The [OIII]/Hβ lines are not redshifted into the 3.6 μm window for LBG-1.

5.8 Discussion and Conclusions

We have detected [NII] 205 μm emission towards the highest redshift sample of galaxies to date. Our sample spans almost two orders of magnitude in star formation rate and includes the compact starbursting SMG AzTEC-3 ($z = 5.3$; SFR $\sim 1100\,M_\odot\,yr^{-1}$; R14). From the combined R14 & C15 sample of [CII]-detected LBGs we also selected the relatively dusty, above average SFR galaxy, HZ10 ($z = 5.7$; SFR $\sim 170\,M_\odot\,yr^{-1}$), which lies at the upper limit, although within the scatter of the $z = 5$–6 star-forming Main Sequence, and a typical lower-SFR galaxy, LBG-1 (SFR $\sim 10 - 30\,M_\odot\,yr^{-1}$), which we consider representative of the "normal" population of star-forming galaxies at $z \sim 5.3$ because it appears to lie on the Main Sequence.

Our observations of the [CII]/[NII] luminosity ratio are summarized in Fig. 5.5, and are shown together with all other high-redshift measurements to-date, as well as some local galaxy samples. We have re-measured the [NII] line luminosity in the BR1202–0725 system members (a QSO, an SMG and two LAEs at $z = 4.7$) based on higher sensitivity archival ALMA data (project ID: 2013.1.00745.S) to update the ratios presented in Decarli et al. (2014a). The [NII] line is detected with high significance for the QSO, SMG, and LAE-2, but is not

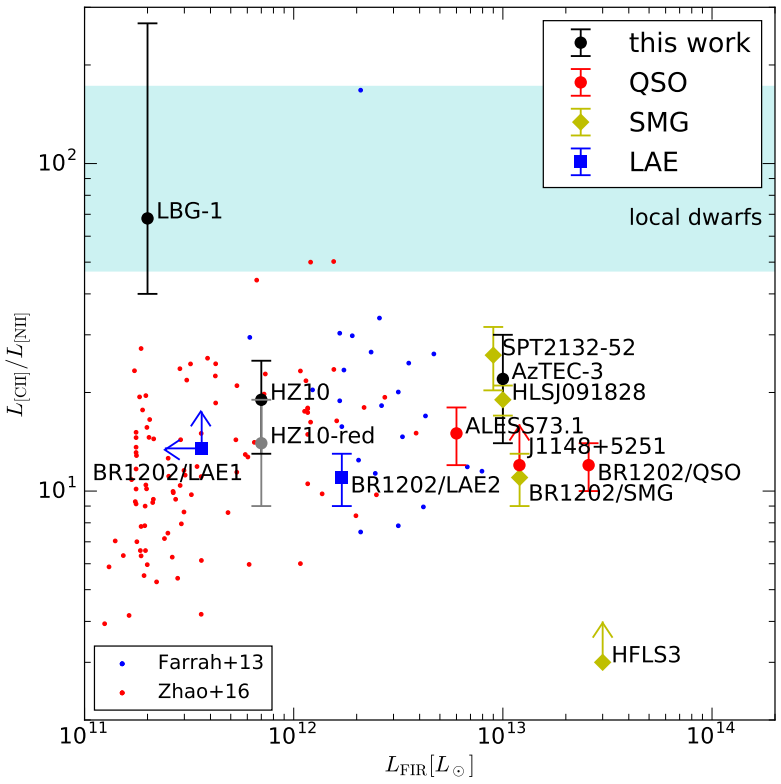

Figure 5.5: [CII]/[NII] line luminosity ratios observed in high redshift galaxies to-date as a function of their FIR luminosity (Carilli & Walter 2013; De Breuck et al. 2014; Béthermin et al. 2016; Rawle et al. 2014; Combes et al. 2012; Carilli et al. 2013; Riechers et al. 2013; R14; C15). For comparison we also show a sample of ULIRGs from Farrah et al. (2013) (using the [NII] 122 μm line) and LIRGs with [NII] (using the [NII] 205 μm line) from Zhao et al. (2016) and [CII] from Díaz-Santos et al. (2013). The range of ratios in dwarfs (Cormier et al., 2015) (using the [NII] 122 μm line) is shown as a cyan band. The [NII] 122 μm line measured in the indicated local samples was converted to a [NII] 205 μm luminosity assuming a ratio of 1/2.5, estimated from Herrera-Camus et al. (2016). The abscissa in the local samples are defined as total IR luminosity; no attempt was made to convert to a common FIR luminosity scale because it does not affect our interpretation.

detected in LAE-1.[5] The non-detection of [NII] emission in LAE-1 may not be strongly constraining if it is similar to LBG-1, with the caveat that it is likely to

[5]The [NII] line fluxes are 1.5 ± 0.2 Jy km s^{-1} for the SMG, 0.74 ± 0.07 Jy km s^{-1} for the QSO, < 0.5 mJy peak (3σ limit) for LAE-1, and 0.30 ± 0.06 Jy km s^{-1} for LAE-2.

be affected by tidal forces from the SMG-QSO merger and the intense QSO radiation. Furthermore the [NII] line in LAE-2 is very broad ($\sim 1000\,\mathrm{km\ s^{-1}}$), suggesting that the [CII] line measured in Carilli et al. (2013) is truncated due to the band edge, and thus may only cover ~30% of the full line emission.[6] The very broad [NII] line in LAE-2 is compatible with the Lyα FWHM of $1225 \pm 257\,\mathrm{km\ s^{-1}}$ in Williams et al. (2014), which may imply that the ISM in this galaxy is strongly affected by quasar winds.

Recent work (e.g., Kewley et al., 2013; Steidel et al., 2016) suggests that stellar metallicity in early galaxies might be very low compared to gas-phase metallicity (which is dominated by oxygen, nitrogen, and carbon abundances). This is due to the expected enrichment time for iron of the order of 1 Gyr; the iron abundance is responsible for the biggest contribution to stellar opacity and is not enriched in the ISM by core-collapse supernovae and is therefore expected to be low in galaxies at this epoch, hence greatly affecting massive star structure and UV radiative output. Since we expect the gas properties of the ISM under investigation to depend on the hardness and intensity of the stellar radiation field, these properties may not be directly comparable to local galaxies. It is also expected that the high gas fractions typical for galaxies at these epochs might strongly modify the gas phase structure (e.g., Vallini et al., 2013).

Figure 5.5 shows that there seems to be a relatively narrow range (0.5 dex) for [CII]/[NII] ratios in SMGs and quasar-hosts at high-redshift. Their range is similar to, although perhaps slightly higher than the ratios measured in local LIRGs and ULIRGs. This does not fit our expectations based on local trends with density and star formation rate surface density (e.g., Lu et al., 2015); these

[6] Adopting the [CII] line luminosities from Carilli et al. (2013), the [CII]/[NII] line ratios are 11 ± 2 for the SMG, 12 ± 2 for the QSO, > 13.5 for LAE-1, and, when using the velocity range corresponding to the [CII] measurement, 11 ± 2 for LAE-2.

trends would suggest a significantly higher ratio than we observe. We therefore suggest that the global measurements at high-redshift may not be observing the [NII] emission coming from the equivalent regions in local starbursts, where the HII regions at the site of recent star-formation dominate, but a more diffuse ISM component which might not be as prevalent in less gas-rich local analogs. If this were to be correct, it is possible that the ionized gas in the nuclear regions, all of which is surrounding the recently formed massive stars may be in a state of higher ionization. In this case both nitrogen and oxygen may predominantly be in their doubly ionized state as perhaps observed in LBG-1.

It is likely that in order to unravel the physical origin of the line ratio under consideration, spatially resolved line studies are needed; spatial global averages might give a very biased view of the physical gas conditions if the neutral and the ionized gas are not co-spatial. HZ10 is the first high redshift galaxy where this type of study seems possible. In fact we find tentative evidence for the [NII] emission originating from only part of the [CII]-emitting region, which is reminiscent of clumpy star-forming gas disks observed in other tracers of ionized gas like Hα (e.g., Genzel et al., 2011; Wisnioski et al., 2015). Since rest-frame optical wavelength tracers like Hα are presently not accessible in the first giga-year of cosmic time, FIR fine-structure lines like [NII] may become the tracer of choice for this kind of resolved clump/disk dynamic studies in the earliest galaxies. Due to the lower density and dust content relative to a compact starburst like AzTEC-3, regions of different ionization might be more easily accessible in less extreme $z > 5$ galaxies, like HZ10. Future studies are necessary to determine if the regions with lower [NII] emission are dominated by neutral gas, perhaps at higher density than the [NII]-emitting fraction (as potentially observed in AzTEC-3), or whether [NIII] dominates the nitrogen emission in these regions,

suggesting LBG-1-like conditions.

A different effect may become dominant for "normal" galaxies at z = 5–6, like LBG-1, where the low dust content of the ISM and the very young stellar population perhaps start affecting the phase structure of the low-metallicity gas. In fact our data constrain the [CII]/[NII] ratio to be larger than $\sim$ 40 and probably in the 60–100 range, indicative of a minor contribution from ionized gas to [CII], compared to that in local normal star-forming galaxies for which the measured ratio is typically 10–25 (Zhao et al., 2016; Díaz-Santos et al., 2013). Understanding the [CII] emission line in such galaxies appears crucial as the low FIR and CO emission (R14, C15) suggest that [CII] might be an essential neutral gas coolant in low dust environments at $z > 5$, which is necessary to achieve dense gas formation and hence star-formation. Our measurement is compatible with the recent findings of high ratios in local dwarfs (Cormier et al., 2015), strengthening the case that these might be appropriate analogs for the ISM in early galaxies, in some respects. Cormier et al. (2015) find [OIII] to be the brightest FIR line in these galaxies, suggesting abundant ionized gas, in a higher ionization state than what is traced by [NII]. Measuring either [OIII] or [NIII] will be necessary to determine the relative importance of the ionized ISM component in normal z = 5–6 galaxies, and it could become an important tool due to its brightness, possibly comparable to [CII] or brighter (Inoue et al., 2016). The extremely low [NII] value measured in LBG-1 holds further evidence in favor of hard and intense radiation in early star-forming galaxies, with possibly much higher escape fraction of hard ionizing photons (dominating the ISM throughout the galaxy) due to low dust abundances, and therefore could potentially help to shed light on the mechanisms of cosmic re-ionization.

CHAPTER 6

LOW STAR FORMATION EFFICIENCY IN TYPICAL GALAXIES AT $Z = 5 - 6$

6.1 Context

As we saw in the last chapter, we have tentatively confirmed an evolution toward low metallicity conditions in at least one of the "normal", massive galaxies studied in the first billion years of cosmic time. In this chapter, we further explore this finding by extending our [NII] measurements to a larger sample. Using the [CII]/[NII] FIR line ratio we have developed a dust unobscured tracer of the ISM phase structure, and its variation may be interpreted as suggesting a strong evolution in the star-forming ISM properties, likely driven by metallicity evolution. The level of enrichment of the ISM in forming galaxies is important because it traces the balance between accretion of pristine gas from the IGM and enrichment from previous stellar generations. In addition, the metallicity and dust abundance may affect the ISM phase structure and the star formation process as evidenced by local dwarf galaxies. Measuring metallicity, especially at $z > 3$, is particularly difficult as the strong line optical tracers shift into the mid-IR and are not accessible without *JWST*. In order to better characterize the conditions for star formation it is also crucial to constrain the dense gas supply. As we saw in previous chapters, the best tracer for this cold molecular phase is low-J CO line emission. Although CO observations from "normal" galaxies have been attempted to date (e.g., Tan et al. 2014) they have usually resulted in non-detections which have suggested CO may not be a useful tracer at the highest redshifts. Metallicity variations are expected to shrink the size

of the CO emission, relative to the bulk of the molecular gas cloud as seen in local dwarfs (e.g., Rubio et al. 2015) due to the reduced dust shielding against the strong FUV field. In this chapter, we observe CO(2–1) from two galaxies from the Capak et al. (2015) sample, and find a range of different conditions, in relatively similar galaxies. We find that faint [NII] (relative to [CII]) is accompanied by faint CO(2–1) in these galaxies, which might be expected if both were caused by lower metallicity gas conditions. Furthermore, we find that the more mature, metal enriched galaxy of the sample has very bright CO emission indicating a massive molecular gas reservoir dominating the total baryonic mass in this galaxy. This is the first measurement of the cold gas content in a "normal" galaxy at $z > 3.5$ and allows us to place the first constraints on the physics of star formation in the first galaxies.

This chapter will be published in the *Astrophysical Journal* as Pavesi, R., et al., submitted to ApJ, arXiv: 1812.00006. In collaboration with Dominik Riechers, Andreas Faisst, Gordon Stacey, Peter Capak.

6.2 Abstract

We report the detection of CO(2–1) line emission from a Lyman Break Galaxy at $z \sim 5.7$ with the VLA. The CO line luminosity implies a massive molecular gas reservoir of $(1.3 \pm 0.3)(\alpha_{\rm CO}/4.5\,M_\odot\,({\rm K\,km\,s^{-1}\,pc^2})^{-1}) \times 10^{11}\,M_\odot$, suggesting low star formation efficiency, with a gas depletion timescale of order ~1 Gyr. This efficiency is much lower than traditionally observed in $z \gtrsim 5$ starbursts, indicating that star forming conditions in Main Sequence galaxies at $z \sim 6$ may be comparable to those of normal galaxies probed up to $z \sim 3$ to-date, but with

rising gas fractions across the entire redshift range. We also obtain a deep CO upper limit for a Main Sequence galaxy at $z \sim 5.3$ with ~ 3 times lower SFR, perhaps implying a high $\alpha_{\rm CO}$ conversion factor, as typically found in low metallicity galaxies. Using ALMA, we find faint [NII] 205μm emission relative to [CII] in all but the most IR-luminous "normal" galaxies at $z = 5 - 6$ for a sample including both CO targets, suggesting more intense or harder radiation fields in the ionized gas relative to lower redshift. These radiation properties indicate low metallicity may be common in typical $\sim 10^{10}\,M_{\odot}$ galaxies at $z = 5 - 6$, consistent with our CO measurements. Our sample shows evidence for high dust temperatures, and a young starburst producing high radiation intensity and hardness even with substantial dust obscuration. While a fraction of Main Sequence star formation in the first billion years may take place in conditions not dissimilar to lower redshift, lower metallicity may affect the remainder of the population.

6.3 Introduction

Massive galaxies started forming during the epoch of reionization at $z > 6$ and may have experienced their fastest growth toward the end of the first billion years of cosmic time ($z \sim 4 - 6$), doubling their stellar mass content on timescales of order a hundred million years (e.g., Bouwens et al. 2015; Faisst et al. 2016b). While the high redshift universe offers the promise of strong new constraints to dark matter physics through the early halo growth (e.g., Buckley & Peter 2017), they have, so far, been limited to coarse stellar mass-halo mass relationships which do not capture the variety in galaxy formation history hinted at by observations (e.g., Behroozi et al. 2018; Moster et al. 2018; Tacchella et al. 2018). The details of such an early growth epoch may also carry the imprint

of re-ionization, therefore shining light on the physics of the dark ages (e.g., Ferrara 2016; Castellano et al. 2018; Ma et al. 2018).

Crucially, while abundant optical and near infrared (NIR) observations have revealed the end product of early galaxy formation (e.g., Bouwens et al. 2015), the drivers of such evolution are the gas processes of intense gas inflows, outflows, and cooling which lead to primordial star formation, galaxy growth, and dynamical assembly (e.g., Davé et al. 2011; Hopkins et al. 2014). Such gas flows are difficult to observe directly, but measurements of the gas conditions provide the most direct constraints on the physics of early galaxy evolution. For example, the observable gas phase metallicity probes the balance between gas inflows, outflows and metal enrichment due to star formation (e.g., Tremonti et al. 2004; Davé et al. 2012b; Lilly et al. 2013). On the other hand, the relationship between local gas properties and star formation rate (the "star formation law") in early, forming galaxies provides the critical link between observable stellar properties and the more fundamental properties of the interstellar gas (e.g., Sharda et al. 2018; Krumholz et al. 2018). Since the "star formation law" may emerge from the complex effects of stellar feedback and local gas dynamics, it is of great interest to explore its redshift evolution and any variations across galaxy types and gas conditions (e.g., Daddi et al. 2010b; Genzel et al. 2015; Scoville et al. 2016, 2017a; Tacconi et al. 2018; Orr et al. 2018).

The CO rotational transitions and the atomic fine structure lines in the far infrared (FIR) provide some of the most accurate tracers of the properties of the star-forming interstellar medium (ISM) in galaxies because they are bright, unaffected by dust extinction and probe all the main gas phases (e.g., Stacey et al. 1991; Hollenbach & Tielens 1997; Kaufman et al. 1999; Carilli & Walter 2013). In

order to constrain the star formation law we need to trace the cold, molecular gas mass because it is found to be most causally connected to star formation in local galaxies (Schruba et al., 2011; Bigiel et al., 2011; Leroy et al., 2013; Carilli & Walter, 2013). The best characterized tracers of such molecular gas are low-J rotational emission lines of the CO molecule, which have been calibrated within the Milky Way and in local galaxies, and achieve a high degree of consistency (e.g., Leroy et al. 2011; Sandstrom et al. 2013b; Bolatto et al. 2013). These measurements may depend on metallicity estimates, since metallicity appears to strongly affect the fraction of molecular gas emitting CO lines and therefore, the gas mass-to-light ratio $\alpha_{\rm CO}$ (e.g., Maloney & Black 1988; Madden et al. 1997; Kaufman et al. 1999; Bolatto et al. 2013). However, it is difficult to measure metallicity directly in the cold molecular medium because no hydrogen lines are directly accessible. Indirect tracers of metallicity typically involve either probes of the nitrogen abundance ratio to other metals or probes of the hardness and intensity of the radiation field (e.g., Masters et al. 2016; Vincenzo et al. 2016). The latter technique rests on observations of local dwarf galaxies, which have shown that lower metallicity environments may produce harder and more intense ultraviolet radiation, producing stronger lines from higher ionization states (e.g., Cormier et al. 2015).

Few observations of the ISM in galaxies at $z > 5$ are available, and the most luminous galaxies have preferentially been targeted to date, e.g., quasar hosts and the brightest dusty star forming galaxies (DSFGs, Maiolino et al. 2005, 2009; Walter et al. 2009, 2012; Riechers et al. 2013, 2014a; Gullberg et al. 2015; Strandet et al. 2017). Although such brightness allows a great level of detail (e.g., Riechers et al. 2013), it is unlikely that the conditions in the most extreme outliers are representative of typical galaxies. For example, although the fraction of dust

obscured star formation in extreme starbursts is close to unity, and the metallicity may be close to solar (e.g., Magdis et al. 2011a), the first ALMA sample study of [CII] at 158μm and dust emission from normal galaxies at $z > 5$ found lower dust emission than expected from low redshift extrapolations (Riechers et al., 2014a; Capak et al., 2015; Barišić et al., 2017; Faisst et al., 2017). The sample described by Capak et al. (2015) includes representative, massive galaxies ($M_* \sim 10^{10}\,M_\odot$) with optical spectra selected as Lyman Break Galaxies (LBGs) or Lyman Alpha Emitters (LAEs), two of the most common selection techniques at $z > 5$. While the ultraviolet luminosity and stellar mass of all sample galaxies is approximately equal, one of the main results of the ALMA observations was the wide range of [CII] and dust continuum luminosity observed. This wide range of FIR properties already in this small sample may suggest an evolutionary sequence, spanning the range from younger galaxies during their first major starburst to more "mature" and dust-rich galaxies bridging the gap to, traditionally sub-mm selected, DSFGs. This interpretation was confirmed by the analysis of the IRX/$\beta_{\rm UV}$ relation (Faisst et al., 2017), which found similar conditions as observed in massive galaxies at lower redshift in some while suggesting different dust properties (such as those observed in low metallicity dwarfs) for the others.

In order to constrain the conditions for star formation, low-J CO transitions provide the best probe and the most direct comparison to lower redshift surveys (e.g., Tacconi et al. 2013, 2018). The cold molecular gas properties in "normal" star-forming galaxies are poorly constrained beyond $z \sim 3$. Even at $z \sim 3-4$ few significant detections have been achieved, mostly afforded by strong gravitational lensing (Coppin et al., 2007; Riechers et al., 2010a; Dessauges-Zavadsky et al., 2015, 2017), a serendipitous detection at $z \sim 3.22$ (Gowardhan et al. 2017,

Gowardhan et al. 2018, submitted), and constraining upper limits for unlensed targets (Tan et al., 2013). The low detection rate has suggested a strong evolution in $\alpha_{\rm CO}$ with redshift, possibly driven by a rapid metallicity evolution (Tan et al., 2013, 2014). However, as shown by Capak et al. (2015), standard selection techniques at $z > 5$ yield a wide range of dust obscuration, and suggest that a corresponding range of CO enrichment may also be present. We here present observations of the CO(2–1) transition from the FIR-brightest "normal" galaxy of the sample to obtain the first solid constraints at $z \sim 6$.

[CII] at 158μm is now commonly observed at high redshift due its high luminosity and it allows probing the gas dynamics in star-forming galaxies due to its widespread distribution (e.g., Stacey et al. 1991; Maiolino et al. 2005, 2009; Walter et al. 2009; Stacey et al. 2010; Riechers et al. 2013, 2014a). The [CII]/IR luminosity ratio appears to trace the surface density of star formation, providing an important measure of starburstiness (e.g., Luhman et al. 1998; Malhotra et al. 2001). Furthermore, metallicity was shown to be the primary variable controlling the residual scatter in the [CII]/IR–$\Sigma_{\rm IR}$ relation (Smith et al., 2017). However, the [CII] line can originate from gas where hydrogen is ionized, neutral or molecular. Therefore observations of additional diagnostic lines that probe specific phases of the ISM are required to connect observations to physical conditions. In particular, the [NII] line at 205 μm is expected to be emitted under similar conditions of radiation intensity and gas density to [CII], but uniquely from the ionized phase (Oberst et al., 2006; Decarli et al., 2014b; Pavesi et al., 2016; Díaz-Santos et al., 2017), therefore assessing the fraction of [CII] coming from the ionized rather than neutral gas. The [CII]/[NII] line ratio has been proposed as a metallicity tracer due to its sensitivity to abundance ratios (Nagao et al., 2011, 2012) and especially due to its sensitivity to the hardness of the ra-

diation field (Pavesi et al., 2016) as traced by the ionization state of carbon and nitrogen in the ionized gas (Cormier et al., 2015). In the present work, we discuss inference from new ALMA measurements of the [NII] line luminosity in all the galaxies from the Capak et al. (2015) sample with dust continuum and [CII] detections.

In Section 4, we describe new spectroscopic observations of the CO(2–1) line transition from HZ10 (Capak et al., 2015), and we summarize analogous observations targeting LBG-1 (also named HZ6; Riechers et al. 2014a; Capak et al. 2015) obtained as part of the CO Luminosity Density at High-z (COLDz) survey (Pavesi et al., 2018b). We also present new ALMA observations targeting the [NII] transition at 205 μm from the dust-detected sub-sample presented by Capak et al. (2015), composed of HZ4, LBG-1, HZ9 and HZ10, expanding our previous sample study (Pavesi et al., 2016). in Section 5 we present the results of the analysis of our CO and [NII] measurements. In Section 6 we discuss the implications of our measurements for the metallicity, the state of maturity of the star-forming ISM and the "star formation law" in this sample of "normal" galaxies at $z > 5$. Finally, we present our conclusions in Section 7. In this work, we adopt a Chabrier IMF and a flat, ΛCDM cosmology with $H_0 = 70\,\mathrm{km\ s^{-1}\ Mpc^{-1}}$ and $\Omega_\mathrm{M} = 0.3$.

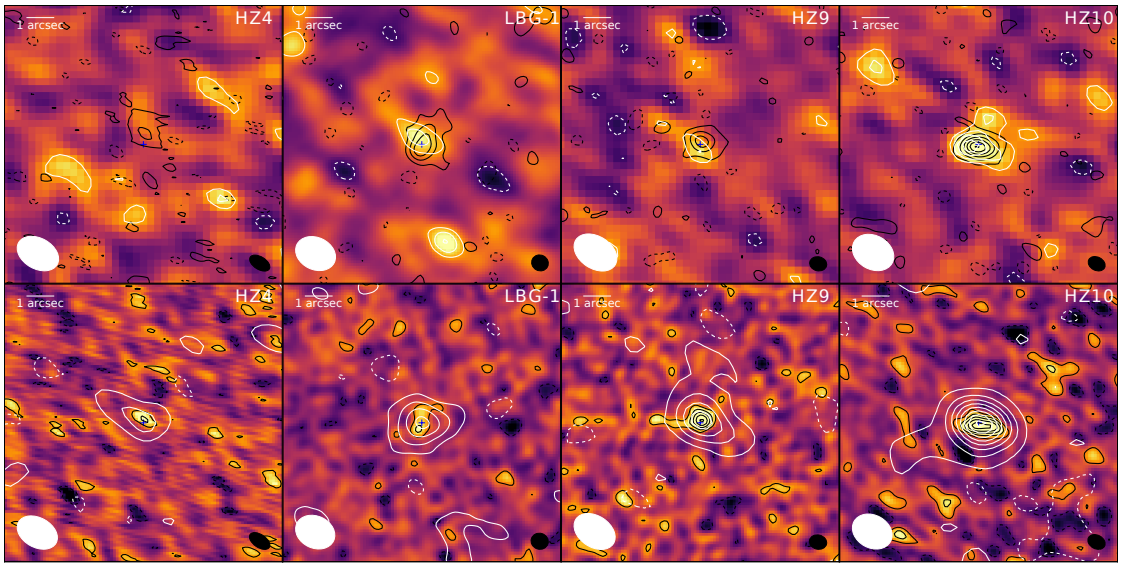

Figure 6.1: Top: Integrated line maps (over the line FWHM) showing [NII] color-scale with [NII] (white) and [CII] (black) contours overlaid. Blue crosses indicate the positions of the 205 μm continuum peak. The [NII] ([CII]) beam is shown in the bottom left (right) corner of each panel. The [NII] ([CII]) contours are multiples of 1σ (4σ), starting at $\pm 2\sigma$. The noise levels in the [CII] line maps are 0.07, 0.04, 0.11, 0.09 Jy km s^{-1} beam^{-1}, and in the [NII] line maps are 0.019, 0.016, 0.016, 0.04 Jy km s^{-1} beam^{-1}, respectively. Bottom: Continuum maps showing 158 μm color-scale with 205 μm (white) and 158 μm (black) contours overlaid. Contours start at $\pm 2\sigma$ and are in steps of 2σ (with the exception of the 205 μm contours in HZ9 and HZ10, in steps of 4σ). The 205 μm (158 μm) beam is shown in the bottom left (right) corner.

6.4 Observations

6.4.1 VLA observations of CO(2–1)

We observed the CO(2–1) transition in HZ10 using NSF's Karl G. Jansky Very Large Array (VLA) in Ka band (project ID: 17A-011, PI: Pavesi). A complete description of these observations may be found in Pavesi et al. (2018a), which describes the properties of CRLE, an hyper-luminous DSFG at the same redshift as HZ10 and located within the same field view, with a separation of only 13″.

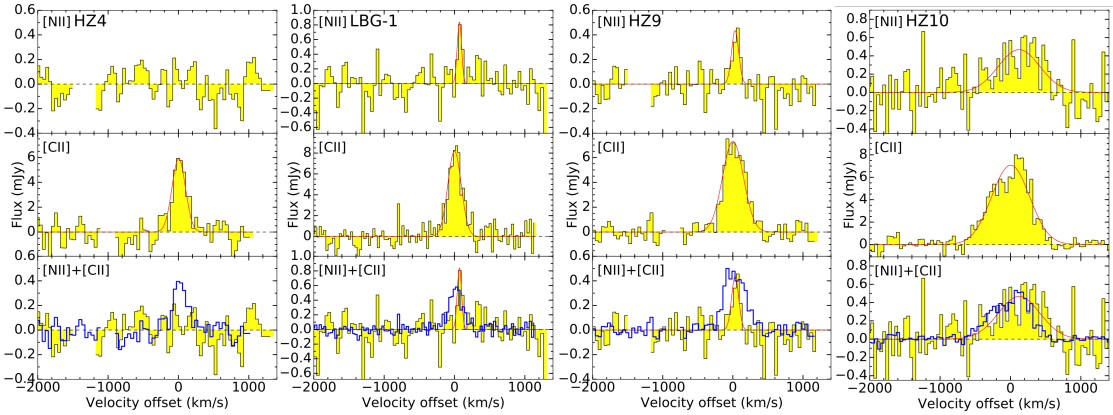

Figure 6.2: [CII] and [NII] spectra of our sample galaxies, and Gaussian fits to the line emission (red curves). The channel velocity width in all spectra is $\sim 42\,\mathrm{km\ s^{-1}}$ (except in the LBG-1 [CII] spectra it is $\sim 32\,\mathrm{km\ s^{-1}}$). [CII] is scaled down by a factor 15 in flux density in the bottom panels for comparison (in blue).

In three of the eight observing sessions the two intermediate frequencies (IFs) were tuned to the central frequency of the CO(2–1) line in HZ10, and to the adjacent frequency range to maximize continuum sensitivity. However, in the remaining five sessions the second IF was moved in order to provide uninterrupted coverage of the CO(2–1) line in CRLE, by partially overlapping the first IF (Pavesi et al., 2018a). The total observing time was 19.8 hrs, on source. We image the data with the CLEAN algorithm in the Common Astronomy Software Application (CASA version 4.7, using natural weighting for maximal sensitivity. The imaging of the CO line data results in a synthesized beam size of $3.0'' \times 2.3''$ at the redshifted CO(2–1) frequency and $2.7'' \times 2.3''$ in the continuum map. The rms noise at the position of HZ10 (i.e., at the phase center) is $\sim 45\,\mu\mathrm{Jy\ beam^{-1}}$ in a 35 km s^{-1} wide channel. The final rms noise when averaging over the line-free 2.0 GHz of bandwidth is $\sim 2.7\,\mu\mathrm{Jy\ beam^{-1}}$. The CO(2–1) transition in LBG-1 was observed as part of the COLDz survey (Pavesi et al., 2018b; Riechers et al., 2018) and a preliminary version was shown by Riechers et al. (2014a). A complete de-

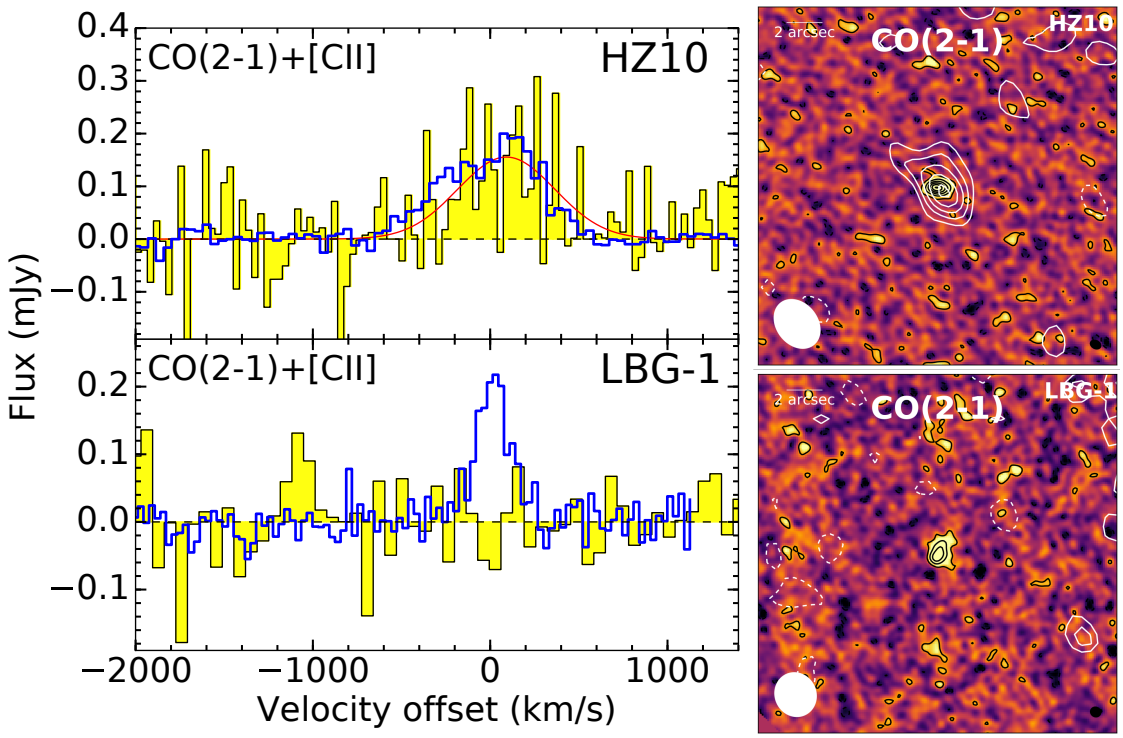

Figure 6.3: Left: CO(2–1) spectra of HZ10 and LBG-1, and Gaussian fit to the detected line emission (red curves). [CII] is shown scaled down by a factor 40 in flux density for comparison (in blue). The channel velocity width is ~ 40 km s^{-1} for HZ10 in both spectra, ~ 32 km s^{-1} and ~ 64 km s^{-1} for LBG-1 for [CII] and CO, respectively. Right: Integrated line maps (over the line FWHM) showing [CII] color-scale with CO(2–1) (white) and [CII] (black) contours. The CO(2–1) ([CII]) beam is shown in the bottom left (right) corner of each panel. The CO(2–1) ([CII]) contours are multiples of 1σ (4σ), starting at $\pm 2\sigma$. The noise levels in the [CII] line maps are 0.04, 0.09 Jy km s^{-1} beam^{-1} for LBG-1 and HZ10, respectively, and in the CO(2–1) line maps are 0.006, 0.010 Jy km s^{-1} beam^{-1} for LBG-1 and HZ10, respectively.

scription of these observations and of the imaging may be found in Pavesi et al. (2018b). The equivalent time on-source in the mosaic is 14 hours at the position of LBG-1. The imaging of the CO line data results in a synthesized beam size of 2.5″ × 2.3″ at the redshifted CO(2–1) frequency and 2.7″ × 2.4″ in the continuum map. The rms noise at the position of LBG-1 is ~ 67 μJy beam^{-1} in a 35 km s^{-1} wide channel. The final rms noise when averaging over the full 8 GHz of bandwidth is ~ 1.3 μJy beam^{-1}.

6.4.2 ALMA observations of [CII] and [NII]

Our observations of the [CII] line, data reduction and imaging for LBG-1 and HZ10 were previously described by Riechers et al. (2014a); Capak et al. (2015); Pavesi et al. (2016). The ALMA Cycle-1 observations targeting the [CII] lines for HZ4 and HZ9, have previously been presented by Capak et al. (2015) and here we provide a brief description of the data that we have re-processed and re-analyzed. These observations were taken on 2013 November 4-16 in band 7 as part of a larger project (ID: 2012.1.00523.S, PI: Capak). The HZ4 pointing resulted in 20 min on source with 28 usable antennae. Ganymede was observed as flux calibrator, J0522−3627 was observed as bandpass calibrator, and J1008+0621 was observed as amplitude/phase gain calibrator. The HZ9 data resulted in 38 min on source with 27 antennae. Ganymede was observed as flux calibrator, J1037−2934 was observed as bandpass calibrator, and J1058+0133 was observed as amplitude/phase gain calibrator. In both cases the correlator was set up to target the expected frequency of the [CII] line and to provide continuous coverage of the continuum emission in adjacent spectral windows with channels of 15.6 MHz in Time Division Mode (TDM). The CASA version 4.5 was used for data reduction and analysis. All images and mosaics were produced with the CLEAN algorithm, using natural weighting for maximal sensitivity. For HZ4, the imaging results in a synthesized beam size of $0.8'' \times 0.5''$ at the redshifted [CII] frequency and in the continuum map. The rms noise in the phase center is ~ 0.5 mJy beam^{-1} in a 44 km s^{-1} wide channel and the final rms noise when averaging over all spectral windows (i.e. over a total 7.5 GHz of bandwidth) is $\sim 54\,\mu$Jy beam^{-1}. For HZ9, the imaging results in a synthesized beam size of $0.6'' \times 0.5''$ at the redshifted [CII] frequency and in the continuum map. The rms noise in the phase center is ~ 0.4 mJy beam^{-1} in a 43 km s^{-1} wide channel and

the final rms noise when averaging over all spectral windows (i.e. over a total 7.5 GHz of bandwidth) is $\sim 47\,\mu$Jy beam^{-1}.

Cycle-3 observations of [NII] 205 μm targeting our sample galaxies were taken on 2016 January 1 and 5 in band 6, as part of two separate programs (2015.1.00928.S and 2015.1.00388.S, PIs: Pavesi and Lu, respectively) with one track from each program for HZ10 and LBG-1 and one track for HZ4 and HZ9 from the second program, taken in a compact configuration (max. baseline $\sim$ 300 m). Observations from the first program were previously described in Pavesi et al. (2016), and the HZ10 observations for both programs were previously used in the analysis of CRLE in the field of view, presented by Pavesi et al. (2018a). We here present the remaining observations for LBG-1, HZ4 and HZ9. The two sets of observations for LBG-1 resulted in 64 min, and 18 min on source respectively, with ~41–45 usable 12 m antennae under good weather conditions at 1.3 mm. The first set of observations was previously described by Pavesi et al. (2016). For the second set of observations of LBG-1, the nearby radio quasar J0948+0022 was observed regularly for amplitude and phase gain calibration, and J0854+2006 was observed for bandpass and flux calibration. The observations of HZ4 and HZ9 resulted in 30 and 47 min on source, with 45 and 47 usable 12 m antennae, respectively. The same radio quasar was observed for amplitude and phase calibration as for LBG-1, and J1058+0133 was observed for bandpass and flux calibration. The correlator was set up in identical configuration for these observations, to cover two spectral windows of 1.875 GHz bandwidth each at 15.6 MHz (~ 20 km s^{-1}) resolution (dual polarization) in Time Division Mode (TDM), in each sideband. We estimate the overall accuracy of the flux calibration to be within $\sim$ 10%. We used the Common Astronomy Software Application (CASA) version 4.5 for data reduction and analysis. We

combined data from all observations, and produced all images with the CLEAN algorithm, using natural weighting for maximal point source sensitivity. Imaging the [NII] data for HZ4 results in a synthesized beam size of $1.6'' \times 1.1''$ at the redshifted [NII] frequency of HZ4 and in the continuum map. The rms noise in the phase center is $\sim 0.14\,\mathrm{mJy\ beam^{-1}}$ in a $44\,\mathrm{km\ s^{-1}}$ wide channel. The final rms noise when averaging over the line free spectral windows (i.e. over a total 7.5 GHz of bandwidth) is $\sim 13\,\mu\mathrm{Jy\ beam^{-1}}$. Imaging the [NII] data for LBG-1 results in a synthesized beam size of $1.5'' \times 1.2''$ at the redshifted [NII] frequency of LBG-1 and in the continuum map. The rms noise in the phase center is $\sim 0.16\,\mathrm{mJy\ beam^{-1}}$ in a $40\,\mathrm{km\ s^{-1}}$ wide channel. The final rms noise when averaging over the line free spectral windows (i.e. over a total 7.5 GHz of bandwidth) is $\sim 15\,\mu\mathrm{Jy\ beam^{-1}}$. Imaging the [NII] data for HZ9 results in a synthesized beam size of $1.7'' \times 1.2''$ at the redshifted [NII] frequency of HZ9 and in the continuum map. The rms noise in the phase center is $\sim 0.15\,\mathrm{mJy\ beam^{-1}}$ in a $44\,\mathrm{km\ s^{-1}}$ wide channel. The final rms noise when averaging over the line free spectral windows (i.e. over a total 7.5 GHz of bandwidth) is $\sim 14\,\mu\mathrm{Jy\ beam^{-1}}$. Imaging the [NII] data for HZ10 results in a synthesized beam size of $1.6'' \times 1.2''$ at the redshifted [NII] frequency of HZ10 and in the continuum map. The rms noise in the phase center is $\sim 0.14\,\mathrm{mJy\ beam^{-1}}$ in a $44\,\mathrm{km\ s^{-1}}$ wide channel. The final rms noise when averaging over the line free spectral windows (i.e. over a total 7.5 GHz of bandwidth) is $\sim 19\,\mu\mathrm{Jy\ beam^{-1}}$ (Figures 7.1 & 7.2).

Table 6.1: a

nd [NII] line properties of our sample galaxies.]Measured CO, [CII] and [NII] line properties of our sample galaxies

Quantity	HZ4	LBG-1	HZ9	HZ10
[CII] line properties				
$\nu_{\rm obs}$(GHz)	290.400 ± 0.013	301.980 ± 0.007	290.545 ± 0.019	285.612 ± 0.013
Redshift	5.5445 ± 0.0003	5.29359 ± 0.00015	5.5413 ± 0.0004	5.6543 ± 0.0003
$S_{\rm [CII]}$(mJy)	5.9 ± 0.7	8.2 ± 0.5	7.3 ± 0.9	7.1 ± 0.3
$FWHM_{\rm [CII]}$ (km s^{-1})	230 ± 30	230 ± 20	350 ± 50	630 ± 30
$I_{\rm [CII]}$ (Jy km s^{-1})	1.3 ± 0.3	2.1 ± 0.2	2.7 ± 0.3	4.5 ± 0.3
$L_{\rm [CII]}$ ($10^9 L_\odot$)	1.1 ± 0.3	1.71 ± 0.16	2.2 ± 0.2	4.0 ± 0.3
deconvolved size	(1″.1 ± 0″.3) × (0″.6 ± 0″.3)	(1″.00 ± 0″.12) × (0″.57 ± 0″.10)	(0″.68 ± 0″.12) × (0″.48 ± 0″.11)	(0″.80 ± 0″.07) × (0″.42 ± 0″.06)
size (kpc^2)	(6.6 ± 1.8) × (3.6 ± 1.8)	(6.2 ± 0.7) × (3.5 ± 0.6)	(4.1 ± 0.7) × (2.9 ± 0.7)	(4.8 ± 0.4) × (2.5 ± 0.4)
$S_{158\mu\rm m}$ (mJy)	0.24 ± 0.05	0.26 ± 0.07	0.60 ± 0.09	1.18 ± 0.16
[NII] line properties				
$\nu_{\rm obs}$(GHz)	—	232.114 ± 0.007	223.348 ± 0.009	219.49 ± 0.04
$S_{\rm [NII]}$ (mJy)	—	0.8 ± 0.2	0.4 ± 0.1	4.7 ± 0.8
$FWHM_{\rm [NII]}$ (km s^{-1})	—[a]	73 ± 19	120 ± 30	700 ± 130
$I_{\rm [NII]}$ (Jy km s^{-1})	< 0.06	0.06 ± 0.02	0.05 ± 0.02	0.34 ± 0.10
$L_{\rm [NII]}$ ($10^9 L_\odot$)	< 0.04	0.036 ± 0.012	0.032 ± 0.013	0.22 ± 0.07
$S_{205\mu\rm m}$ (mJy)	0.10 ± 0.02	0.20 ± 0.03	0.33 ± 0.04	0.83 ± 0.05
$L_{\rm [CII]}/L_{\rm [NII]}$	> 24	41^{+20}_{-10}	61^{+40}_{-17}	17^{+7}_{-4}
CO(2–1) line properties				
$\nu_{\rm obs}$(GHz)	—	—	—	33.157 ± 0.006
$S_{\rm CO}$ (mJy)	—	—	—	0.16 ± 0.03
$FWHM_{\rm CO}$ (km s^{-1})	—	—[a]	—	650 ± 140
$I_{\rm CO}$ (Jy km s^{-1})	—	< 0.018	—	0.10 ± 0.02
$L'_{\rm CO}$ (10^{10} K km s^{-1} pc^2)	—	< 0.44	—	2.9 ± 0.6
$S_{\rm 34GHz}$ (μJy)	—	< 4	—	< 7.8

Notes: All quoted uncertainties correspond to 1σ statistical uncertainty intervals and all limits correspond to 3σ. [a]: We assume FWHM equal to that of the [CII] line in order to derive upper limits on the line flux.

Table 6.2: Derived properties of our sample galaxies

Quantity	HZ4	LBG-1	HZ9	HZ10
$L_{\rm FIR}$ $(10^{11}\,L_\odot)$	$5.2^{+4.6}_{-2.6}$	$4.9^{+4.4}_{-2.6}$	12^{+10}_{-6}	13^{+11}_{-7}
SFR $(M_\odot\ {\rm yr}^{-1})$	52^{+46}_{-26}	49^{+44}_{-26}	120^{+100}_{-60}	130^{+110}_{-70}
M_* $(10^9\,M_\odot)^a$	$4.7^{+2.9}_{-1.8}$	15^{+6}_{-5}	$7.2^{+5.0}_{-2.9}$	25^{+12}_{-8}
$M_{\rm gas}$ $(10^{10}\,M_\odot)^b$	—	< 2	—	13 ± 3
$M_{\rm dyn}(< R_{1/2})$ $(10^{10}\,M_\odot)$	$1.8^{+1.3}_{-1.0}$	$1.9^{+0.6}_{-0.4}$	$3.5^{+3.1}_{-1.6}$	10 ± 3

Notes: All quoted uncertainties correspond to 1σ intervals and all limits correspond to 3σ. ^{a}: Stellar masses reported by Capak et al. (2015). ^{b}: Gas masses are derived from the CO luminosity assuming a Galactic $\alpha_{\rm CO} \sim 4.5$ conversion factor.

6.5 Analysis

6.5.1 Results from the dust continuum measurements

We detect dust continuum emission from the full galaxy sample at 158 μm and 205 μm (Figure 7.1, Table 7.1). No continuum signal is detected in the VLA observations targeting HZ10 and LBG-1 at ~34 GHz (corresponding to rest-frame $\sim$ 1.3 mm), yielding deep 3σ upper limits (Table 7.1). We measure the continuum flux at 158 μm and 205 μm by imaging all line-free channels using natural baseline weighting, and using the CASA task IMFIT to fit a 2D Gaussian model to the emission.

We fit these continuum fluxes with a modified black-body smoothly connected to a mid-IR power law (Pavesi et al., 2016). We adopt high dust temperature priors, as suggested by Faisst et al. (2017) for these galaxies. We employ Gaussian priors for the dust emissivity β parameter (1.7 ± 0.5), for the dust temperature (60 ± 15 K), for the mid-IR power law index (2.0 ± 0.5) and for the transition rest-frame wavelength to the optically thick regime ($60 \pm 20\,\mu$m). We note that the relative fluxes at 158 μm and 205 μm across our sample suggest a diversity of dust SED shapes, hinting to possible lower dust temperatures in LBG-1 and HZ10 relative to the rest of the sample, which may be consistent with the higher stellar masses in these two galaxies. However, the available constraints are not sufficient to resolve the degeneracy between dust temperature and emissivity index variations. We derive Far-IR (FIR) luminosities by integrating between 42.5 and 122.5 μm (Table 6.2). Because the dust spectral energy distributions (SEDs) are not constrained in the mid-IR, we follow the standard practice of adopting the FIR luminosities as an estimate of total IR, without ex-

trapolating to shorter IR wavelengths (e.g., Riechers et al. 2014a; Pavesi et al. 2018a). We caution, however, that this is likely to be an under-estimate, and that the total IR luminosity may be ~1.5-2× higher than the FIR.

We can use the available dynamical mass and Rayleigh-Jeans dust continuum emission estimates to provide constraints to the gas masses in these galaxies, independently from the CO measurements. Dust mass estimates based on the full SED fitting may be unreliable because they are strongly dependent on the model dust temperature distribution, which is poorly constrained for our sample galaxies. Alternatively, the Rayleigh-Jeans dust continuum emission may be used to estimate dust and gas masses, assuming an average emissivity and dust temperature for the dominant cold dust component, and a constant dust-to-gas ratio (Hildebrand 1983; Eales et al. 2012; Scoville 2013; Scoville et al. 2013, 2016, 2017a; Bourne et al. 2013; Groves et al. 2015). The dependence on cold dust temperature and dust-to-gas ratio may make the Rayleigh-Jeans method less reliable than at lower redshifts (e.g., Pavesi et al. 2018a). On the other hand, the opposing effects of increasing dust temperatures, and decreasing dust-to-gas ratios that may occur in "normal" galaxies at high redshift may partially compensate each other. The 34 GHz upper limits imply 3σ gas mass limits of $< 2.8 \times 10^{11}\,M_{\odot}$ for HZ10 and $< 1.6 \times 10^{11}\,M_{\odot}$ for LBG-1, adopting the relation derived by Scoville et al. (2016, 2017a). We also use the ~230 GHz continuum fluxes to derive approximate estimates, although these measurements may not lie on the Rayleigh-Jeans tail, and therefore may not accurately trace the cold dust component. These continuum measurements would imply gas masses of $\sim 1.3 \times 10^{10}\,M_{\odot}$ for HZ4, $\sim 2.5 \times 10^{10}\,M_{\odot}$ for LBG-1, $\sim 4.4 \times 10^{10}\,M_{\odot}$ for HZ9, and $\sim 1.1 \times 10^{11}\,M_{\odot}$ for HZ10, with large systematic uncertainties.

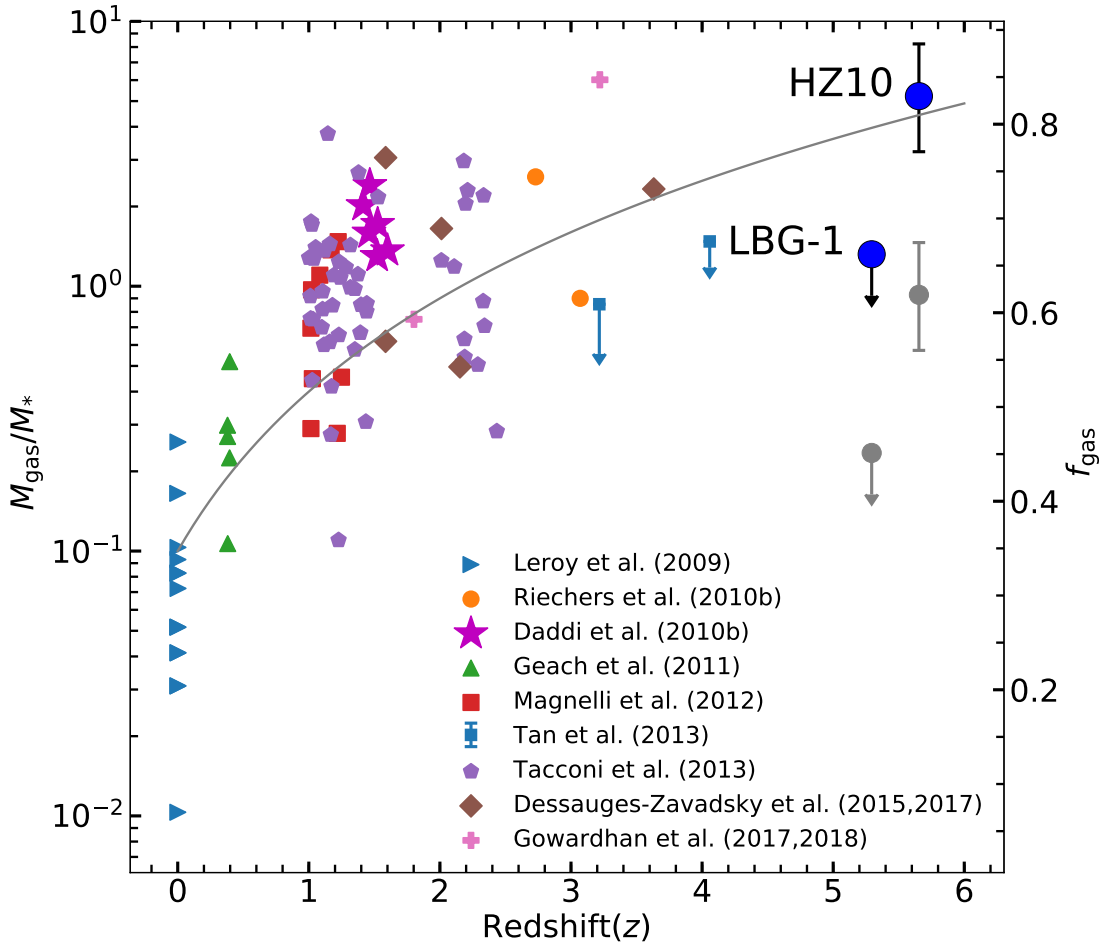

Figure 6.4: The ratio of molecular gas mass to stellar mass (calculated using an $\alpha_{\rm CO}$=4.5 $M_\odot$ (K km s^{-1} pc^2)$^{-1}$ for all sources) adapted from Carilli & Walter (2013); Leroy et al. (2009); Riechers et al. (2010a); Daddi et al. (2010a); Geach et al. (2011); Magnelli et al. (2012); Tan et al. (2013); Tacconi et al. (2013); Dessauges-Zavadsky et al. (2015, 2017); Gowardhan et al. (2017) The grey line shows $M_{\rm gas}/M_* \propto (1+z)^2$ (Geach et al., 2011). An alternative choice of $\alpha_{\rm CO}$=0.8 for HZ10 and LBG-1 is also shown in light grey.

6.5.2 Results from the CO measurements

We detect CO(2–1) line emission from HZ10 with a significance of $\gtrsim 8\sigma$, and provide a constraining upper limit to the CO(2–1) emission toward LBG-1 (Fig-

ure 6.3). We extract an aperture spectrum for HZ10[1] and a single pixel spectrum at the peak position of the [CII] emission toward LBG-1, in order to measure or constrain the CO(2–1) line properties (Table 7.1). The CO(2–1) emission toward HZ10 appears slightly resolved, although the coarse resolution of compact array configuration observations does not allow a precise size determination. We use CASA UVMODELFIT to fit a circular Gaussian model to the line visibilities in HZ10 and derive a deconvolved FWHM size of $1''.2 \pm 0''.4$ for the CO(2–1) emission, corresponding to 7 ± 2 kpc, which is compatible with the [CII] and [NII] size estimates.

While the CO(2–1) line luminosity is expected to provide a reliable estimate of the molecular gas mass, several factors affect the proportionality factor such as heating from, and contrast against, the cosmic microwave background (CMB; e.g., da Cunha et al. 2013c) and the strong metallicity dependence of the CO luminosity per unit molecular gas mass (e.g., Bolatto et al. 2013). Here, we further assume a brightness temperature ratio of $R_{21} = 1$ between the CO J=2–1 and 1–0 transitions.[2] Contrast against the warmer CMB, and the additional gas heating this provides at $z > 5$ is only weakly constrained without additional CO excitation measurements. da Cunha et al. (2013c) suggest that we may expect the observed CO line flux to be suppressed by a factor $\sim 1.25 - 2$ at this redshift. We do not attempt to estimate this effect independently, but simply absorb it into the definition of $\alpha_{\rm CO}$.

Our constraints indicate that CO(2–1) line emission from LBG-1 is unexpectedly weak, relative to low redshift trends. This may be a consequence of

[1]We adopt elliptical apertures of sizes equal to the FWHM of the best fit 2D Gaussian to the integrated line emission.

[2]Current samples of high redshift dusty star-forming galaxies, and main-sequence galaxies show nearly thermalized gas excitation up to the J=2–1 transition, justifying this assumption ($R_{21} \sim 0.80 - 0.95$; e.g., Carilli & Walter 2013; Daddi et al. 2015).

low metallicity and relatively low dust abundance (Bolatto et al., 2013). LBG-1 shows an unusually high inferred [CII]/CO(1–0) luminosity ratio ($\gtrsim$ 9000, Figure 6.3), relative to the value in HZ10 ($\sim$ 3000) and to the values commonly measured in local starbursts ($\sim$ 4400; e.g., Wolfire et al. 1989; Stacey et al. 1991, 2010) and high redshift dusty star forming galaxies (5200 ± 1800; e.g., Gullberg et al. 2015). The high ratios observed in LBG-1 are difficult to explain within standard PDR models, but naturally arise as a consequence of lower metallicity (e.g., Maloney & Black 1988; Stacey et al. 1991; Madden et al. 1997). In particular, low metallicity dwarfs typically show similar ratios of $\sim$ 7000 – 10^5 (e.g., Cormier et al. 2014; Jameson et al. 2018). On the other hand, the ratio observed in HZ10 points to star-forming gas conditions which are typical of "normal" lower redshift Main Sequence galaxies.

We can use the gas mass estimates based on the Rayleigh-Jeans dust continuum emission to constrain the $\alpha_{\rm CO}$ conversion factor by assuming that the gas mass is dominated by molecular gas. The main uncertainties inherent in the Rayleigh-Jeans dust method are a dependence on the gas-to-dust ratio and on dust properties affecting the dust SED. These estimates would imply constraints to $\alpha_{\rm CO}$[3] of $\lesssim$ 10 ($\sim$ 4 based on the 220 GHz flux) for HZ10 and $\gtrsim$ 5.7[4] based on the 230 GHz flux for LBG-1. These are in agreement with our inference of "normal" star-forming conditions for HZ10 and of lower metallicity gas in LBG-1.

[3]Units of $M_\odot$ (K km s^{-1} pc^2)$^{-1}$ assumed throughout the following

[4]In order to deal with relative uncertainties of order unity throughout this work, we adopt the convention of quoting Gaussian-equivalent percentiles. Therefore, uncertainty ranges correspond to 16th, 50th and 84th percentiles and 3σ limits are defined to imply a 99.7% probability. Propagation of these uncertainties to derived quantities was carried out by numerical sampling and evaluation of posterior distribution percentiles. Lognormal distributions were used to sample skewed distributions described by asymmetric 1σ ranges. Upper limits from non-detections are treated as positive-truncated (enforcing a uniform prior), 0-centered Gaussians with specified standard deviation as determined by the noise level.

6.5.3 Dynamical Modeling

We carry out dynamical modeling of the [CII] line emission from HZ10 and HZ9 using a rotating disk model generated by `KinMS` (Davis et al., 2013), fitted to the visibility data using `GALARIO` Tazzari et al. (2018) and `Multinest` (Feroz et al., 2009), using the method[5] previously described by Pavesi et al. (2018a). We model the continuum as two and one Gaussian components for HZ10 and HZ9, respectively. We model the line emission intensity as a Gaussian profile and the rotation curve as a "tangent" function parametrised by the maximum velocity and the half-maximum radius (Table 7.4). We fit a total of 18 parameters for HZ10 (also including line flux, disk center along each coordinate and continuum sizes, fluxes and position for both components) and 12 parameters for HZ9 (also including line flux, disk center along each coordinate and continuum size and flux) as afforded by the available signal-to-noise ratio. The data, median parameter model (indistinguishable from the best-fit model) and residuals are shown in Figures 6.5 and 6.6, together with the derived probabilistic constraints to the rotation curves and the implied dynamical masses.

Table 6.3: Results of dynamical modeling for our sample galaxies.

	HZ10			HZ9		
Parameter (Units)	16th perc.	50th perc.	84th perc.	16th perc.	50th perc.	84th perc.
Gas dispersion (km s^{-1})	210	218	226	80	89	100
Emission FWHM (arcsec)	0.84	0.88	0.91	0.47	0.51	0.55
Maximum velocity (km s^{-1})	380	430	510	300	445	750
Velocity scale length (arcsec)	0.12	0.18	0.28	0.014	0.03	0.08
Inclination (degrees)	59	61	63	13	21	31
Position angle (degrees)	−7	−5	−3	71	77	83

[5]Python code available at https://github.com/pavesiriccardo/UVmodeldisk

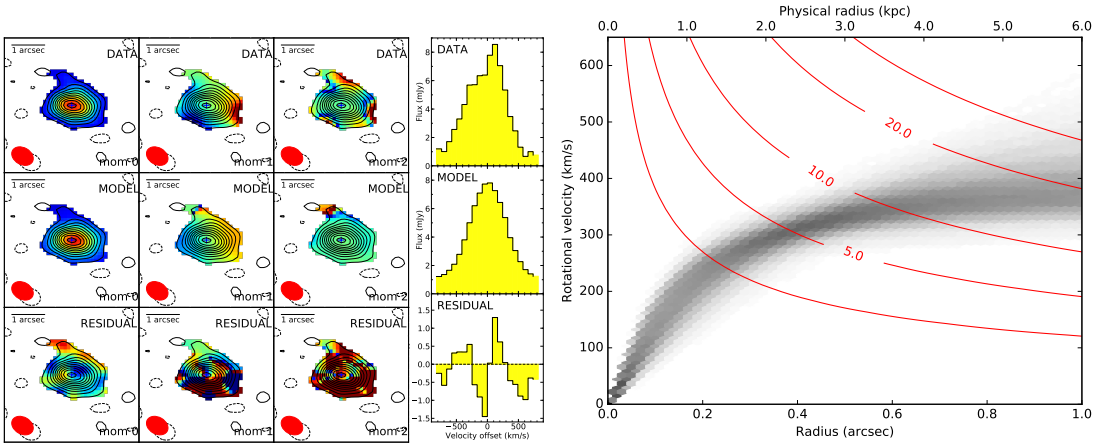

Figure 6.5: Left: Visibility space dynamical modeling results for the [CII] line emission in HZ10. We show the "natural" weighting line moment 0 (intensity), 1 (velocity) and 2 (dispersion) maps and spectra for the data, the single-disk model corresponding to posterior median parameters, and the visibility residuals. Two-Gaussian components were adopted as model for the continuum. Right: Probabilistic constraints to the rotation curve for a "tan" model with two disk modeling parameters (maximum velocity and half-velocity radius). The darker shading corresponds to higher probability density, as determined by the MCMC samples. We also show the enclosed dynamical mass in units of $10^{10}\,M_{\odot}$ (red curves).

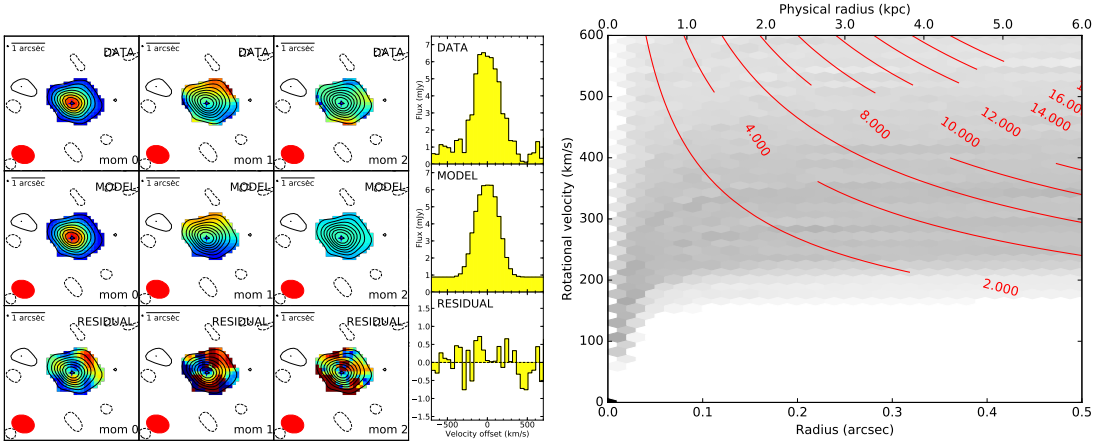

Figure 6.6: Dynamical modeling results for HZ9. A single Gaussian component was adopted as continuum model. See Figure 6.5 for further details.

6.5.4 Dynamical mass analysis and gas masses constraints

We have carried out a dynamical modeling analysis directly on the visibilities for the [CII] observations in HZ9 and HZ10, following the method previously described by Pavesi et al. (2018a). We simultaneously fit a rotating disk model generated by KinMS (Davis et al., 2013) to the line emission and a simple continuum model (one and two Gaussian components for HZ9 and HZ10, respectively). While the [CII] line in HZ9 and HZ10 shows a smooth velocity gradient, the line in LBG-1 shows a more complex morphology and dynamics, with three components, and two separate velocity gradients (Riechers et al., 2014a). Therefore we do not attempt modeling the emission from LBG-1, as the data are not sufficient to properly constrain such a high-complexity model. Although the [CII] line in HZ10 shows a smooth velocity gradient, the *HST* NIR and dust continuum images from ALMA suggest the presence of two separate morphological components. These may be associated with either a galaxy merger, or with clumpy gas and stellar distributions, embedded in a rotating disk. The somewhat asymmetric [CII] line profile may also be caused by massive gas clumps, as shown by the simulations of Daddi et al. (2010a); Bournaud et al. (2014, 2015). Because of the limitation of assuming a single disk model, we note that substantial uncertainties regarding the detailed dynamics of HZ10 affect our inference as evidenced by the non-negligible residual structure after model fitting.

We use the disk model scale-length and rotation curve to derive dynamical mass estimates within the half-light radius, by adopting the measured rotational velocity. We do not apply corrections for velocity dispersion because the physical origin of the apparent dispersion is uncertain (particularly in the case of HZ10, for which two distinct components may be partly responsible for the line

broadening). We estimate that these systematic corrections may be as large as $\sim$ 50%, toward increasing the dynamical masses inferred by fitting a rotating disk, based on the measured gas dispersion ($\sigma \sim 90 \pm 10$ km s^{-1} and 220 ± 10 km s^{-1} for HZ9 and HZ10, respectively). We obtain $\sim (6.1 \pm 0.7) \times 10^{10}\, M_{\odot}$ for HZ10 and only an approximate estimate of $5^{+5}_{-3} \times 10^{10}\, M_{\odot}$ for HZ9, within the half light radius of the [CII] emission. Our results agree within the uncertainties with previous estimates based on tilted-ring modeling in the image plane by Jones et al. (2017), although our uncertainty estimates are significantly more conservative due to the larger number of fitted parameters. We also use the dynamical mass estimation method by Daddi et al. (2010a), which was calibrated on disk galaxy simulations, to derive dynamical mass estimates for our full sample, based on the measured [CII] size. We apply this technique by using the line FWHM, the fitted size of the [CII] emission and the disk inclination from the ratio of minor to major axes (the latter is compatible with our results from UV-space dynamical modeling). We derive dynamical masses within the half light radius for the full galaxy sample using the method by Daddi et al. (2010a) and list them in Table 6.2. These are in agreement with our previous gas estimates, within the large uncertainties of both methods utilized. The inferred dynamical mass for LBG-1 is $\sim$ 2.5 times lower than previous estimates, although within the original uncertainties, due to a revised [CII] size and due to differences in the method employed (Riechers et al., 2014a). However, dynamical mass estimates for LBG-1 may be affected by potential multiplicity. In the following, we adopt these dynamical mass estimates based on the Daddi et al. (2010a) method for HZ9 and HZ10 as well, because they are compatible with our estimates based on UV-space dynamical modeling, and because they are based on a simulation-based calibration that includes the expected turbulent pressure contribution to

the inferred circular velocity.

We can use these dynamical masses to provide coarse estimates of the total gas mass, by accounting for the contribution of stellar and dark matter masses (25%) according to Daddi et al. (2010a). These dynamical mass estimates would imply total gas masses of $(1.4 \pm 0.9) \times 10^{10}\ M_\odot$ for LBG-1, $4.5^{+4.5}_{-2.5} \times 10^{10}\ M_\odot$ for HZ9 and $(1.2 \pm 0.5) \times 10^{11}\ M_\odot$ for HZ10. If we assume this gas mass to be dominated by molecular gas, these estimates imply $\alpha_{\rm CO}$ (in units of $M_\odot\,(\mathrm{K\,km\,s^{-1}\,pc^2})^{-1}$) $4.2^{+2}_{-1.7}$ for HZ10, but do not provide a significant constraint for LBG-1[6]. The derived $\alpha_{\rm CO}$ factor for HZ10 is compatible with the Milky Way value (~ 4.5, in the same units) which may also apply to $z \sim 1-2$ main-sequence disk galaxies (Daddi et al., 2010a; Carilli & Walter, 2013; Tacconi et al., 2013; Genzel et al., 2015). In the following, we assume a fixed value of $\alpha_{\rm CO} = 4.5$ for definiteness, in order to derive and constrain gas masses in HZ10 and LBG-1 (Table 6.2, Figure 6.4), with the caveat that this value may only be a lower limit in the case of LBG-1, due to metallicity effects.

6.5.5 Constraints to high redshift star formation

To study the star formation efficiency in HZ10 and LBG-1, first we directly compare the FIR to CO luminosity (Figure 6.7) relative to expectations based on previous determinations of the star formation law in the local and high redshift Universe (Carilli & Walter, 2013). The Main Sequence star formation law by Daddi et al. (2010b) allows converting our CO luminosity measurements to total IR luminosities of $(2.3 \pm 0.5) \times 10^{12}\ L_\odot$ for HZ10 and $< 2.7 \times 10^{11}\ L_\odot$ for LBG-1,

[6]Due to the large uncertainty in the gas mass estimate, the 3σ CO limit only implies a 3σ limit of $\alpha_{\rm CO} > 0.2$ when appropriately propagated through posterior sampling. See footnote 4

respectively, which are compatible with our FIR luminosity estimates. The best fit relation for starburst galaxies by Carilli & Walter (2013) would, on the other hand, over-predict the IR luminosity in HZ10 ($(3.9 \pm 0.8) \times 10^{12}\ L_{\odot}$) relative to our independent estimates. Adopting our best estimate of the gas mass and the star formation rate in HZ10 (Table 6.2) yields a gas depletion timescale (the inverse of the star formation efficiency) of 960^{+1200}_{-470} Myr, which is significantly longer than what is commonly measured in starburst galaxies and is instead compatible with typical star-forming galaxies. HZ10 therefore appears to be very rich in molecular gas, and the efficiency of star formation appears compatible with what is commonly observed in lower redshift, disk-like, main-sequence galaxies (e.g., Leroy et al. 2013).

The IR luminosity constraints implied by the CO upper limit in LBG-1 when adopting the main-sequence and starburst relations are approximately equal. Although the derived IR luminosity constraint is compatible with our uncertain, independent estimate within 1σ, our best estimates for the IR luminosity of LBG-1 are at least a factor of 2 higher, further suggesting that the CO luminosity in LBG-1 may be lower than in lower redshift galaxies with comparable SFR (Figure 6.7). If we adopt our best estimates for the SFR in LBG-1 based on the inferred IR luminosity, we can derive estimates of the gas depletion timescale for the gas masses derived from the long-wavelength dust method ($\sim 500^{+500}_{-250}$ Myr) and from the dynamical mass constraints ($\sim 280^{+420}_{-180}$ Myr). Assuming $\alpha_{\rm CO} = 4.5$, the CO upper limit corresponds to an upper limit on the gas depletion timescale of $\lesssim 2.8$ Gyr with 3σ confidence (i.e., with 99.7% probability).

In a second step, we also use our estimates for the gas reservoir physical sizes derived from the [CII] line to compare the gas surface density to the star

formation rate density probed by the dust continuum flux and size (Figure 6.8), probing the physical drivers of star formation more directly, i.e., the Kennicutt-Schmidt law (Kennicutt, 1998b; Leroy et al., 2008; Bigiel et al., 2008; Daddi et al., 2010b; Bigiel et al., 2011; Schruba et al., 2011; Kennicutt & Evans, 2012; Leroy et al., 2013). Specifically, we include in this comparison both Main Sequence galaxies at $z \sim 1-3$ (Tacconi et al., 2013; Daddi et al., 2010b) and very intensely star forming sub-millimeter galaxies (SMGs, Bouché et al. 2007; Bothwell et al. 2010). In particular, we focus our comparison on CRLE and AzTEC-3, two hyper-luminous DSFGs at $z > 5$ which are located in proximity of HZ10 and LBG-1, respectively. Based on their global gas masses and SFR, the gas depletion timescales for CRLE and AzTEC-3 are $\sim 45-50$ Myr (Riechers et al., 2010b, 2014a; Pavesi et al., 2018a), i.e., an order of magnitude shorter than we observe in HZ10 and LBG-1. Due to the extreme compactness of the star formation in AzTEC-3 and CRLE, the local depletion timescale characterizing the ratio of gas and SFR surface densities are as short as $\sim 10-30$ Myr, while our estimates for HZ10 and LBG-1 are ~ 1 Gyr and $\lesssim 300$ Myr, respectively (Figure 6.8). Therefore, the physical efficiency, in terms of surface densities, may potentially differ by up to two orders of magnitude already among these galaxies at $z > 5$. This comparison shows that, while AzTEC-3 and CRLE have high star formation efficiency, compatible with other high redshift starbursts, HZ10 (and to a smaller degree LBG-1) appear to exhibit the lower efficiencies, longer depletion times typically observed in Main Sequence disks. Although the depletion time measurement in HZ10 is incompatible with that in the starbursts (e.g., Silverman et al. 2015, 2018), the significant systematic uncertainty implies compatibility with both the efficiency in $z \sim 0$ disk galaxies (e.g., Leroy et al. 2013) but also the potentially higher efficiency suggested for Main Sequence galaxies by Tacconi

et al. (2013); Genzel et al. (2015); Scoville et al. (2016, 2017a); Tacconi et al. (2018).

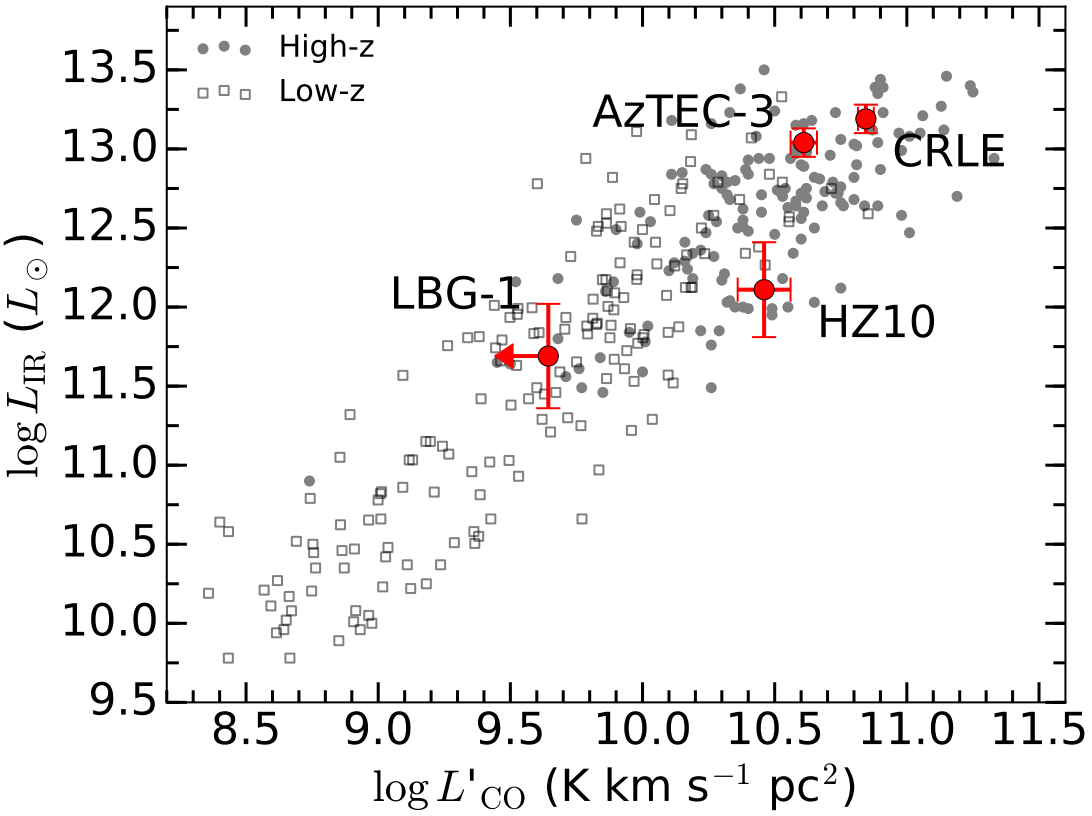

Figure 6.7: IR luminosity observed in a sample of local and high redshift galaxies as a function of their CO luminosity, for comparison to the measurements in HZ10 and LBG-1 (Carilli & Walter, 2013). We also include two $z > 5$ DSFGs for reference (AzTEC-3 and CRLE; Riechers et al. 2010b, 2014a; Pavesi et al. 2018a,b), clearly occupying a distinct part of the parameter space.

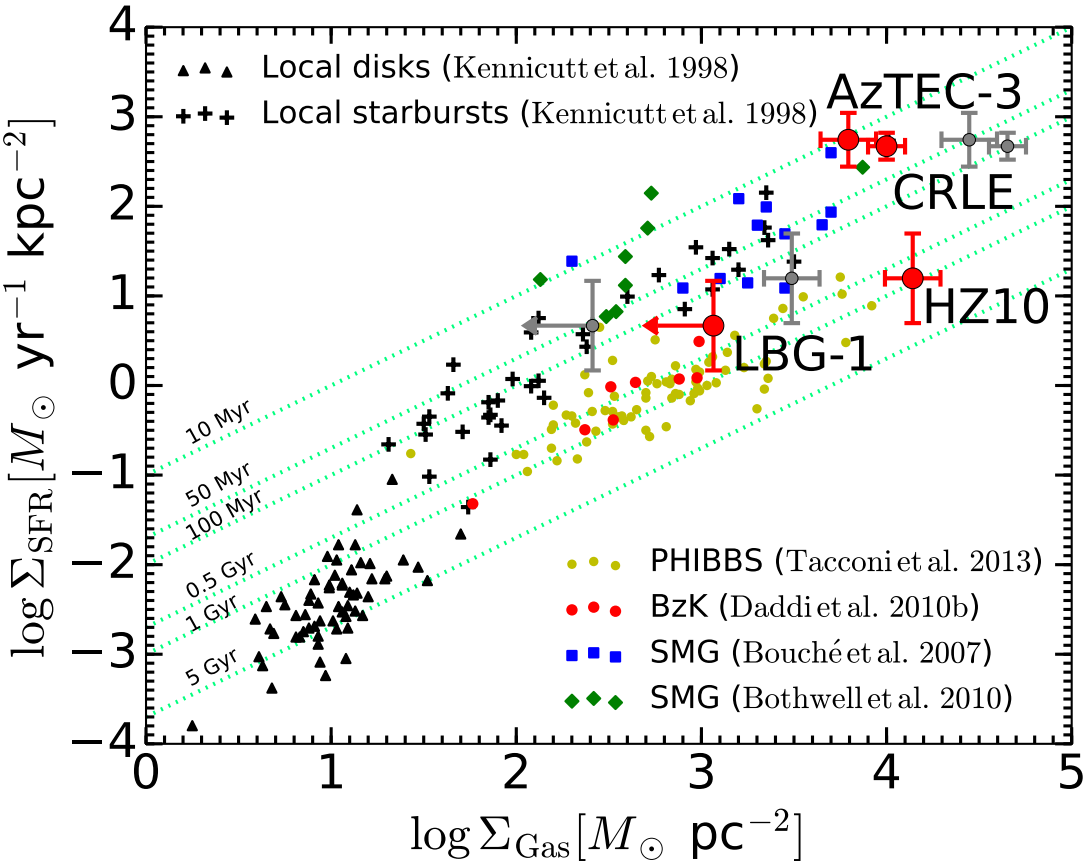

Figure 6.8: Star formation rate surface density as a function of the gas mass surface density for a sample of local and high redshift galaxies, including HZ10, LBG-1, AzTEC-3 and CRLE (adapted from Daddi et al. 2010b, updated by Tacconi et al. 2013). The star formation rate surface density was estimated for the $z > 5$ galaxies through the FIR luminosity and the dust continuum sizes. The gas surface density was estimated for these galaxies through the CO luminosity and the [CII] emission spatial size. Following Daddi et al. (2010b) we adopt $\alpha_{\rm CO} \sim 4.5$ for Main Sequence galaxies such as HZ10 and LBG-1 and the other disk galaxies, and $\alpha_{\rm CO} = 0.8$ for starbursts such as CRLE, AzTEC-3, local starbursts and high-z sub-millimeter galaxies (SMGs). Fixed gas depletion time (corresponding to fixed star formation efficiency) lines are shown for characteristic time-scales spanning from 10 Myr to 5 Gyr (green lines).

6.5.6 Results from the [NII] measurements

We tentatively detect [NII] 205 μm emission toward LBG-1 (at $\sim 3.4\sigma$), and HZ9 (at $\sim 3.1\sigma$), we confidently detect it from HZ10 (at $\gtrsim 6\sigma$), and we provide a constraining upper limit for HZ4 (Figures 7.1 & 7.2). We confirm the tentative detection toward LBG-1 and the detection toward HZ10 previously reported by Pavesi et al. (2016) achieving a higher signal-to-noise ratio. We measure [NII] and [CII] line properties using aperture spectra consistently for the whole sample (Table 7.1, see footnote 1). The [NII] emission from HZ10 appears extended, although the extended structure only has low significance ($\sim 2-3\sigma$, Figure 7.1). In order to measure the [NII] emission size we fit a circular Gaussian model to the integrated [NII] line visibilities from HZ10, using CASA UVMODELFIT. The moderate signal-to-noise ratio of the [NII] detections in LBG-1 and HZ9 does not allow measuring the [NII] emission size. We measure a deconvolved [NII] spatial FWHM size of $1''.71 \pm 0''.25$ for HZ10, corresponding to 10 ± 2 kpc. We use the same technique to measure an effective circular [CII] size of $0''.61 \pm 0''.04$, corresponding to 3.6 ± 0.2 kpc, which is compatible with our more sophisticated UV plane modeling. The [NII] line emission appears to be marginally more extended, than the [CII] emission, but higher resolution and higher signal to noise [NII] observations are necessary to confirm this finding. In particular, a manual inspection of the UV-radial profile of the [NII] line visibilities appears compatible with the size of the [CII] emission within the relative uncertainties.

We do not detect spatial offsets between the [NII] and [CII] line emission in LBG-1, HZ9 and HZ10. Although the [NII] line emission in HZ10 comes from the full [CII] velocity range, the comparison of the [NII] and [CII] spectra (Figure 7.2) suggests a possible differential intensity ratio, with stronger [NII] inten-

sity coming from the red part of the emission (as previously found by Pavesi et al. 2016). The [NII] line velocity width appears narrower than [CII] toward LBG-1 and HZ9, although the limited signal-to-noise does not allow a precise measurement of the line width.

We here update our measurement of the [CII]/[NII] line ratio for HZ10 and LBG-1 (Pavesi et al., 2016), while expanding the sample to include HZ9 and HZ4 (Table 7.1, Figure 6.9). We confirm the relatively low line ratio for HZ10, compatible with most local and high redshift active star-forming galaxies (Pavesi et al., 2016). On the other hand, we also find a substantially higher ratio for HZ9, LBG-1 and HZ4, providing further evidence for the diversity of conditions at $z > 5$ already present in this small sample (Pavesi et al., 2016). The [CII]/[NII] line ratio is sensitive to the fraction of [CII] emission coming from ionized gas, rather than PDRs, because while [CII] may originate from both PDRs and ionized gas, [NII] is expected to only come from ionized gas due to its higher formation energy. The constant [CII]/[NII] line ratio in ionized gas (weakly dependent on density and radiation field) makes it a good tracer of the fraction of [CII] coming from ionized gas rather than PDRs (e.g., Oberst et al. 2006). We assume a line ratio of 3 ± 0.5 in the ionized gas (Díaz-Santos et al., 2017), to infer fractions of [CII] coming from PDRs of $83\% \pm 6\%$ for HZ10, $96\% \pm 2\%$ for HZ9, $93\% \pm 3\%$ for LBG-1 and $> 86\%$ for HZ4.

As previously described by Pavesi et al. (2016), a high [CII]/[NII] line ratio may be expected in the case of very high gas density, or of high intensity and hardness of the radiation field. The latter explanation appears consistent with observations of a high line ratio in local dwarf galaxies by Cormier et al. (2015), which may be interpreted as the consequence of high radiation intensity and

hardness due to low metallicity conditions. A high intensity and hardness radiation field is expected to induce higher ionization conditions in the ionized gas. This implies weak [NII] and [CII] emission from ionized gas because nitrogen, carbon and oxygen are expected to be in a higher ionization state. This prediction is testable by observing strong [NIII] 57 μm and [OIII] 52 μm or 88 μm emission lines. Therefore, in analogy to the case of local dwarf galaxies, we interpret our high line ratio measurements and limits for HZ9, LBG-1 and HZ4 as indicative of low gas (and stellar) metallicity, relative to $z < 5$ galaxies of comparable masses ($\sim 10^{10}\,M_{\odot}$). On the other hand, the lower line ratio observed in HZ10 suggests higher metallicity in this galaxy, confirming the inference based on high dust and CO emission, and suggesting a particularly "mature, normal" galaxy at the same epoch (see also discussion by Faisst et al. 2017). We note that an alternative interpretation for the low [NII] luminosity may invoke lower nitrogen abundance, relative to carbon. While this abundance ratio change may also be a consequence of low metallicity conditions due to the secondary nature of nitrogen, the carbon abundance dependence on gas phase metallicity is not well constrained.

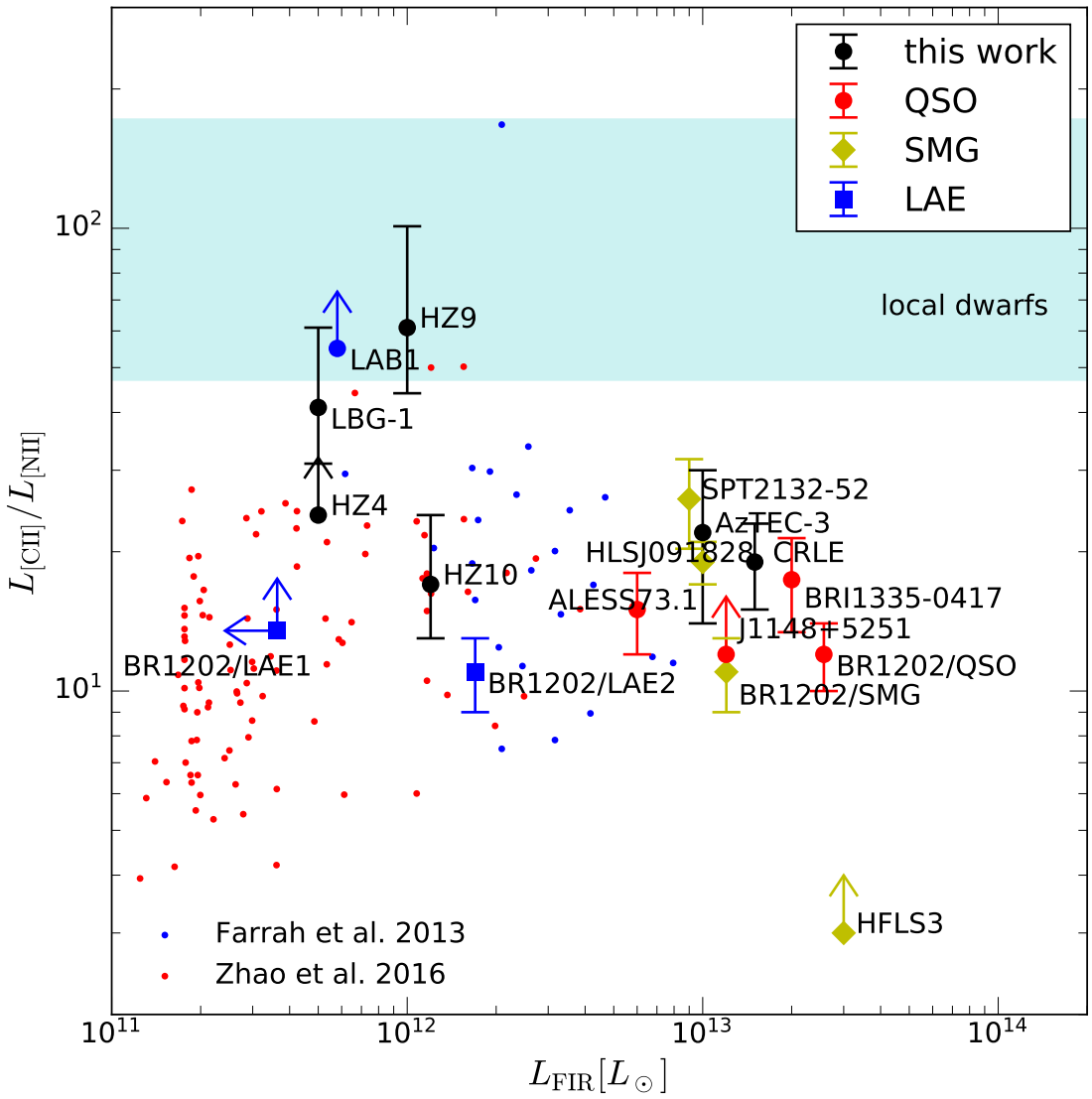

Figure 6.9: [CII]/[NII] line luminosity ratios observed in high redshift galaxies to-date as a function of their FIR luminosity (updated from Pavesi et al. 2016, with additions from Wagg et al. 2010; Umehata et al. 2017; Lu et al. 2018; Pavesi et al. 2018a). For comparison we also show a sample of local ULIRGs from Farrah et al. (2013) (using the [NII] 122 μm line) and LIRGs with [NII] (using the [NII] 205 μm line) from Zhao et al. (2016) and [CII] from Díaz-Santos et al. (2013). The range of ratios in dwarfs (Cormier et al., 2015) (using the [NII] 122 μm line) is shown as a cyan band. The [NII] 122 μm line measured in the indicated local samples was converted to a [NII] 205 μm luminosity assuming a ratio of 1/2.5, estimated by Herrera-Camus et al. (2016). The abscissa in the local samples are defined as total IR luminosity; no attempt was made to convert to a common FIR luminosity scale because it does not affect our interpretation.

6.6 Discussion

The detection of bright CO emission from HZ10 represents the highest redshift CO detection from a "normal", Main Sequence galaxy to date (the next highest redshift CO line from a Main Sequence galaxy was serendipitously detected by Gowardhan et al. 2017 at $z \sim 3.2$). We note that HZ10 appears to have a very high gas fraction based on the measured CO luminosity ($M_{\rm gas} > M_{\rm stars}$ with high confidence and likely $M_{\rm gas} \sim 4 - 5 \times M_{\rm stars}$, Figure 6.4). Such high gas fractions may be expected at $z > 5$ based on the extrapolation of observed trends (e.g., Magdis et al. 2012b; Genzel et al. 2015; Tacconi et al. 2018). A high gas fraction may also potentially be connected with the possibility of a galaxy merger in HZ10. Merging galaxies have been found to potentially show enhanced gas fractions (e.g., Pavesi et al. 2018b). Assuming $\alpha_{\rm CO} \sim 4.5$ for LBG-1 would imply a $\gtrsim 4$ times lower gas fraction, potentially suggesting significant scatter within the general population. However, the low CO luminosity in LBG-1 is likely to be due to low metallicity, as suggested by the faint [NII] emission (Pavesi et al., 2016), and the gas fraction may therefore be substantially higher.

Zavala et al. (2018) recently reported observations of CO and [CII] emission lines from the strongly lensed galaxy G09 83808 at $z \sim 6$, presenting analogies with HZ10. Although the inferred CO(1–0) luminosity of G09 83808 is approximately three times fainter than HZ10, the dust continuum emission is at least twice as bright (rest-frame 158 μm flux) indicating a significantly higher star formation efficiency than found in HZ10. Therefore, while G09 83808 appears to have a comparable star formation rate as HZ10 (within a factor of a few), its star formation resembles starbursts such as CRLE and AzTEC-3, while HZ10 is more gas rich and exhibits star forming conditions compatible with lower red-

shift Main Sequence, disk galaxies. This finding is in agreement with the ten times higher [CII]/FIR ratio in HZ10 relative to G09 83808. This ratio is a probe of the local physical density of star formation and is inversely proportional to the starburst intensity. Based on PDR models, a fixed PDR gas density implies that the far UV (FUV) field intensity (G_0) scales inversely with [CII]/FIR (to a power of $\sim 1 - 1.2$) (**?**Kaufman et al., 1999; Stacey et al., 2010). This scaling implies that the FUV intensity in G09 83808 may be $\sim 10 - 15$ times higher than in HZ10, confirming that HZ10 may be forming stars in a much less intense environment.

The finding of significant dust and, especially, CO emission from HZ10 suggests that a fraction of "normal" galaxies (not extreme starbursts) at $z > 5$ may be rich in molecular gas and significantly metal-enriched, in contrast to some previous indications (e.g., Tan et al. 2013, 2014). This finding is in agreement with the recent measurement of a high volume density of CO-selected galaxies at $z > 5$ by the CO Luminosity Density at High-z (COLDz) project (Pavesi et al., 2018b; Riechers et al., 2018). Although the galaxies selected by COLDz at $z > 5$ are bright starbursts, their volume density is significantly higher than predicted by current models (Riechers et al., 2018). However, if HZ10 had been located within the COLDz field of view it would have been selected by the blind line search based on the survey detection limit (Pavesi et al., 2018b), therefore placing an upper limit to the volume density of evolved, gas-rich "normal" galaxies at $z > 5$ with CO luminosity greater than HZ10 of $\lesssim 5 \times 10^{-5}\,\mathrm{Mpc}^{-3}$ (Riechers et al., 2018).

HZ10 is believed to reside in a galaxy overdensity at $z \sim 5.7$, potentially indicating a protocluster environment (Pavesi et al., 2018a). In particular, the

presence of the bright hyper-starburst CRLE only ~ 70 kpc away constitutes evidence for a possible physical association. This association with the massive, dusty galaxy CRLE and the protocluster may be related to the advanced evolutionary stage of HZ10. If this connection were confirmed, it would point to a more rapid evolution for galaxies in higher density environments (e.g., Chiang et al. 2017).

The PHIBBS survey has measured star formation efficiency and gas fractions for lower redshift (up to $z \sim 2-3$) Main Sequence galaxies (Tacconi et al., 2013; Genzel et al., 2015; Tacconi et al., 2018). Based on the extrapolation of the latest measured trends reported by Tacconi et al. (2018), combining the PHIBBS CO measurements with the dust-based estimates by Scoville et al. (2016, 2017a) we can derive expectations for the average gas fraction and depletion times expected for Main Sequence galaxies such as HZ10 at $z \sim 5.7$. We derive an approximate gas depletion timescale of ~ 400 Myr, which is compatible with our estimate for HZ10 within 1σ (in particular due to the uncertainty in the estimate of total IR luminosity). The molecular gas fraction predicted by the fitting formula suggested by Tacconi et al. (2018) is $M_{\rm gas} \sim M_{\rm stars}$ (the quadratic fitting formula predicts, perhaps artificially, a turnover of the trend at $z \sim 3.5$), which is lower than observed in HZ10. Our observations therefore suggest that the increase in molecular gas fraction with redshift may continue beyond $z \sim 3$, although with very limited statistical power due to the small sample size. In summary, HZ10 shows the characteristic properties of lower redshift Main Sequence galaxies, all the way back to the first billion years of cosmic time.

Vallini et al. (2018) presented some of the latest models of the CO line emission from "normal" galaxies at $z > 5$. They modeled the radiative transfer af-

fecting CO emission from a clumpy molecular medium in a $M_{\rm stars} \sim 10^{10}\,M_{\odot}$ Main Sequence galaxy at $z \sim 6$. Although their model galaxy is characterized by sub-solar ($0.5Z_{\odot}$) metallicity they predict a low effective CO conversion factor of $\alpha_{\rm CO} \sim 1.5$ due to the dominant effect of warmer gas, high turbulence and high gas surface density (Vallini et al., 2018). While this low $\alpha_{\rm CO}$ may be allowed for HZ10 (although disfavored by our dynamical mass estimates), it is ruled out for the more typical LBG-1 if the gas mass is predominantly molecular. In addition, the predicted CO luminosity for the "typical" model galaxy is ~ 20 times lower than observed in HZ10, suggesting that the molecular gas mass may be significantly underestimated. Therefore, HZ10 may be more mature and may therefore not be analogous to the model galaxy, but rather to the lower redshift Main Sequence galaxies observed at $z \sim 2-3$. Although our constraints for the CO luminosity in LBG-1 are compatible with the model prediction, the higher dynamical mass estimates suggest higher gas masses for LBG-1 than the molecular mass predicted by the models. A possible interpretation of this result may invoke a significant fraction of gas in the atomic phase, which may dominate the total gas mass in such "typical", massive galaxies. Based on the [CII] luminosity in LBG-1 we can derive an estimate of the atomic PDR mass of $\sim 2-5\times10^{9}\,M_{\odot}$ following Stacey et al. (1991), which may be comparable to the molecular gas mass for low $\alpha_{\rm CO}$, but it is unlikely to provide the total gas mass inferred from our dynamical mass estimate.

The measurement of [CII] and dust continuum emission from the first sample of "normal", rest-UV selected galaxies revealed a variety of star-forming conditions (Capak et al., 2015). The finding of bright CO line emission from HZ10 and faint emission from LBG-1 is in agreement with the interpretation of a range of metallicities and dust-to-gas ratios being the main contributors to the

variation within the sample (Capak et al., 2015). This interpretation is strongly supported by the significant difference in [CII]/[NII] ratio between HZ10 and LBG-1 already noted by Pavesi et al. (2016). Faint [NII] emission relative to [CII] directly implies (with the possible caveat of differences in the C/N abundance ratio) low contribution of the ionized gas to the [CII] emission, which may therefore be predominantly due to emission from neutral PDRs. The simplest interpretation for faint [NII] emission suggests higher ionization conditions in the ionized gas, predicting bright [NIII] and [OIII] emission, instead. This interpretation would suggest that intensity and, especially, hardness of the radiation field may be the most relevant physical parameter affecting this line ratio. Recent detections of bright [OIII] 88 μm line emission at high redshift support this interpretation and suggest that [OIII] may be even brighter than [CII] in "normal" galaxies at very high redshift (e.g., Inoue et al. 2016; Laporte et al. 2017; Carniani et al. 2017; Marrone et al. 2018; Hashimoto et al. 2018b,c,a; Tamura et al. 2018), as typically observed in local dwarfs (Cormier et al., 2015). Furthermore, recent optical studies of LBGs and LAEs have also found increasing [OIII]λ5008 brightness at high redshift together with high sSFR and low metallicity (e.g., Strom et al. 2017a,b). The metallicity dependence may also be responsible for the downturn due to reduced oxygen abundance at even lower metallicity (Harikane et al., 2018).

Faisst et al. (2017) explore the level of maturity, stellar population properties and dust attenuation in $z = 5 - 6$ "normal" galaxies through the IRX/$\beta_{\rm UV}$ diagnostic plane. While IRX, defined as the ratio $L_{\rm IR}/L_{\rm UV}$, represents the prevalence of dust-obscured star-formation, $\beta_{\rm UV}$ is the power-law slope of the UV emission, which bears the imprint of dust reddening. A correlation between these quantities was observed to hold for local starburst galaxies, and approx-

imately holding up to high redshift (e.g., Meurer et al. 1999; Reddy et al. 2006, 2010, 2018; Bouwens et al. 2016), however variations may be expected due to varying dust properties, star-formation geometry and stellar population ages (e.g., Faisst et al. 2017; Narayanan et al. 2018). These diagnostics suggest that HZ10 may resemble dusty star-forming galaxies, with elevated IR to UV luminosity ratio, intriguingly sharing similarities to lower redshift IR-selected galaxies (e.g., Casey et al. 2014c). However, HZ10 was selected through the LBG and LAE techniques at $z \sim 5.7$ and appears "typical" based on its UV emission. In particular, HZ10 lies within the scatter of the Main Sequence at this redshift (e.g., Speagle et al. 2014b; Capak et al. 2015; Barišić et al. 2017; Faisst et al. 2017). Faisst et al. (2017) also interpret the observed properties of LBG-1 as being consistent with lower dust and metal abundances, likely connected to young stellar populations. The IRX/$\beta_{\rm UV}$ diagnostic, however, would suggest that HZ4, and especially HZ9, may be more dusty than LBG-1 since they lie on or above the local Meurer et al. (1999) relation (Faisst et al., 2017). However, the measured [CII]/[NII] ratios for HZ4 and HZ9 are compatible with that in LBG-1 and significantly higher than the ratio in HZ10 (Figure 6.9). The intriguing observation of faint [NII] emission together with relatively bright dust continuum in HZ9 therefore suggests the presence of additional variables controlling the relationship between the level of dust obscuration and the metallicity (or age of the most recent stellar population) which may be critical to diagnose the interplay between gas inflows, outflows and star formation. An important next step would require measuring the CO line luminosity from HZ9 as well as achieving a detection in LBG-1. In case of relatively bright CO emission (e.g., in relation to its FIR luminosity) from HZ9, the high [CII]/[NII] line ratio would not be explained by the analogy to local dwarf galaxies and would point to unexplored

star formation conditions. However, faint CO line emission from HZ9 would either suggest variations in the dust SED shape or would intriguingly suggest the possibility of significant dust-obscured star formation even in more "typical", lower metallicity, younger high redshift galaxies. The ratio of our continuum measurements tentatively suggests higher dust temperatures in HZ9 than in HZ10. If correct, this might imply that the moderate IR luminosity in HZ9 may be due to higher temperatures, perhaps associated with higher radiation intensity, rather than a high dust content (Faisst et al., 2017). Ferrara et al. (2017) suggested that galaxies at $z > 5$ may be FIR-faint due to colder dust than "normal" due to the very high molecular gas fraction. Their prediction of bright CO emission, specifically from galaxies with low IRX, may be in conflict with our deep upper limits on the CO luminosity from LBG-1. However, this effect may link the high molecular gas mass fraction in HZ10 to the tentatively lower dust temperature we observe in this galaxy relative to the rest of the sample (Ferrara et al., 2017).

The faint [NII] emission from HZ4 and HZ9, together with significant dust-obscured star formation, may be analogous to the properties observed in the eastern component of SPT0311-58 (Marrone et al., 2018). This galaxy at $z = 6.90$ was shown to display high [OIII] 88μm luminosity ($\sim 2\times$ its [CII] luminosity) while being characterized by very high dust-obscured star formation (at the level observed in HZ9 and HZ10). Similarly, the bright [OIII] emitters studied by Hashimoto et al. (2018b) and Tamura et al. (2018) at $z > 7$ which also show significant dust emission may be somewhat analogous to the case we observe in HZ9, i.e., high intensity and hardness of the radiation causing a higher ionization state in the ionized ISM while showing significant dust-obscured star formation. Furthermore, a comparison of the [OIII]/[CII] luminosity in two

quasars at $z \sim 6$ suggests that this line ratio may strongly correlate with dust temperatures (Hashimoto et al., 2018a), supporting our interpretation of higher dust temperatures in [NII]-faint galaxies. We therefore suggest that a higher dust temperature may drive the observed FIR luminosity in such galaxies, perhaps due to a significant contribution from dust in the ionized regions (Faisst et al., 2017).

In order to assess how common the different star forming conditions observed in LBG-1, HZ9 and HZ10 are, larger samples of "normal" galaxies at $z = 5 - 6$ need to be studied. The ALMA Large Program to Investigate [CII] at Early Times (ALPINE)[7], is now observing the [CII] and dust emission from large samples of typical galaxies at $4 < z < 6$ over a wide range of stellar mass and star formation rate. While the brightness of [CII] and dust continuum, and their relation to the ultra-violet flux, provide a wealth of information (e.g., distinguishing LBG-1 from HZ10-type conditions), our analysis shows that relevant residual degrees of freedom are unconstrained unless either CO or a tracer of the ionized gas (such as [NII], [NIII] or [OIII]) is measured in addition to [CII] (to distinguish HZ10 from HZ9-type conditions) possibly due to metallicity, and/or dust temperature variations. Furthermore, resolved observations for larger samples of galaxies are necessary because accurate dynamical masses may be the best way to constrain the gas mass and, hence, to directly infer the $\alpha_{\rm CO}$ conversion factor.

[7]https://cesam.lam.fr/a2c2s/index.php

6.7 Conclusions

We have presented measurements of CO(2–1) line emission from two "normal" Lyman Break Galaxies galaxies, at the end of the "Epoch of Reionization", achieving the highest redshift low-J CO detection from a Main Sequence galaxy to date. We have found large variation in the CO line luminosity between the two targeted sources which may not be completely accounted for by SFR variation (the CO luminosity ratio is $\gtrsim$6.5 while the SFR ratio is $\sim$ 3). While this difference in CO luminosity may suggest variations in star formation efficiency, it appears consistent with our expectation of lower gas metallicity and dust abundance strongly affecting the CO abundance. We infer a large molecular gas reservoir in at least one of the sources, suggesting low efficiency star formation with gas depletion time ~1 Gyr already at $z \sim 6$, analogous to what is commonly observed in lower redshift disk galaxies. This low efficiency contrasts to what is typically observed in $z > 5$ starbursts and provides the first evidence of such "Main sequence" star-forming conditions at $z > 3$. We also find evidence for a continuously rising gas fraction up to $z \sim 6$, although our sample may suggest either significant scatter or systematic variations in the $\alpha_{\rm CO}$ conversion factor.

By observing the largest sample of "normal" galaxies at $z > 5$ in [NII] 205 μm emission to date, we find a general trend of increasing [CII]/[NII] ratios with lower IR luminosity; consistent with what was previously reported by Pavesi et al. (2016). Our findings support an interpretation where low gas and stellar metallicity raise the ionization state of carbon and nitrogen in the ionized gas. This interpretation suggest that the large majority of [CII] emission from most "normal" galaxies at $z > 5$ may emerge from the neutral gas phase. We also find a high [CII]/[NII] ratio in our sample with moderate IR luminosity, suggesting

either significant dust temperature variations affecting the IR luminosity estimate, or the possibility of a young starburst with high radiation intensity and hardness (and potentially low metallicity) together with substantial dust obscuration. Our findings imply that a significant fraction of Main Sequence star formation taking place up to $z \sim 6$ may resemble the conditions observed in "normal" galaxies at lower redshift, suggesting that the efficiency of star formation may only weakly depend on those physical properties which are affected by redshift evolution. In particular, the high inferred gas fractions and the higher merger rates do not appear to significantly affect Main Sequence star formation. Although low metallicity may be common in the Main Sequence galaxy population at $z > 5$, we do not find conclusive evidence for an effect on the star forming conditions, although larger samples and more sensitive observations are needed to study this fainter population.

CHAPTER 7

HIDDEN IN PLAIN SIGHT: A MASSIVE, DUSTY STARBURST IN A GALAXY PROTOCLUSTER AT $Z = 5.7$ IN THE COSMOS FIELD

7.1 Context

As we described in the introduction, clustering of galaxies may have an increasingly important role in early galaxy evolution relative to now. The clustering of low mass galaxies such as Lyman Break Galaxies and Lyman Alpha Emitters at high redshift has been studied for years and measurements of the correlation length-scale allowed inference on the dark matter halo connection (e.g., Giavalisco et al. 1998). On the other hand, the clustering properties of massive, dust-obscured star-forming galaxies (DSFGs) have been harder to characterize due to smaller samples, due to the apparent inhomogeneity of the selection criterion (star-forming galaxies may not be active as DSFGs for a long time, e.g., Miller et al. 2015) and because the coarse resolution of single-dish sub-mm telescopes produces numerous blends (e.g.,Amvrosiadis et al. 2018). However, recent ALMA observations, particularly at $z > 4$, seem to show a surprisingly large number of physical associations of DSFGs (e.g., Daddi et al. 2009b; Hodge et al. 2013; Bussmann et al. 2015; Riechers et al. 2017; Oteo et al. 2017b; Decarli et al. 2017; Lewis et al. 2018; Miller et al. 2018). These cases of simultaneous DSFGs, within tens of kpc, are extremely suggestive of some mechanism coordinating or stimulating the star-forming event. In this chapter, we analogously report the serendipitous discovery of a massive DSFG, a hyper-starburst at $z \sim 5.7$, selected based on ALMA observations for being in physical association with a "normal" galaxy at the same redshift studied in the previous two chapters. This DSFG is

the most luminous and most distant DSFG in the COSMOS survey field. The close physical association between these two star forming galaxies at $z \sim 5.7$ is indicative of a proto-cluster and provides a lab to investigate the star forming progenitors of a single central cluster galaxy of the local Universe. In addition, both the bright DSFG and the "normal" galaxy also appear to be in a merger phase, suggesting that mergers may be common in such early proto-clusters and may be associated with star-formation events.

This chapter was previously published in the *Astrophysical Journal* as Pavesi, R., et al., 2018, ApJ, 861, 43; in collaboration with Dominik Riechers, Chelsea Sharon, Vernesa Smolčić, Andreas Faisst, Eva Schinnerer, Christopher Carilli, Peter Capak, Nick Scoville, Gordon Stacey.

7.2 Abstract

We report the serendipitous discovery of a dusty, starbursting galaxy at $z = 5.667$ (hereafter called CRLE) in close physical association with the "normal" main-sequence galaxy HZ10 at $z = 5.654$. CRLE was identified by detection of [CII], [NII] and CO(2–1) line emission, making it the highest redshift, most luminous starburst in the COSMOS field. This massive, dusty galaxy appears to be forming stars at a rate of at least 1500 $M_\odot$ yr^{-1} in a compact region only ~ 3 kpc in diameter. The dynamical and dust emission properties of CRLE suggest an ongoing merger driving the starburst, in a potentially intermediate stage relative to other known dusty galaxies at the same epoch. The ratio of [CII] to [NII] may suggest that an important ($\sim 15\%$) contribution to the [CII] emission comes from a diffuse ionized gas component, which could be more extended than the dense,

starbursting gas. CRLE appears to be located in a significant galaxy overdensity at the same redshift, potentially associated with a large-scale cosmic structure recently identified in a Lyman Alpha Emitter survey. This overdensity suggests that CRLE and HZ10 reside in a protocluster environment, offering the tantalizing opportunity to study the effect of a massive starburst on protocluster star formation. Our findings support the interpretation that a significant fraction of the earliest galaxy formation may occur from the inside out, within the central regions of the most massive halos, while rapidly evolving into the massive galaxy clusters observed in the local Universe.

7.3 Introduction

While a significant fraction of the visible sky is covered by moderate-redshift, low-mass galaxies, the view of dust-obscured star formation in the submillimeter sky preferentially selects high-mass, dusty star-forming galaxies (DSFGs) at high redshift. This complementary view of the Universe can provide unique insights into galaxy formation processes (e.g., Blain et al. 2002a; Casey et al. 2014a). While the general population of DSFGs was found to predominantly occupy the peak epoch of cosmic star formation at $z = 2 - 3$, a significant tail of higher redshift, and often brighter, examples appears to already be in place at $z > 5$ (e.g., Riechers et al. 2010b, 2013, 2017; Walter et al. 2012; Weiß et al. 2013; Strandet et al. 2016, 2017). These submillimeter-selected galaxies in the early Universe are often extreme "hyper-starbursts", reaching infrared luminosities of $L_{\rm IR} > 10^{13}\,L_\odot$, and star formation rates (SFRs) exceeding $1000\,M_\odot\,{\rm yr}^{-1}$ within small spatial regions of a few kiloparsecs in diameter. They are likely the result of major mergers and/or extreme gas accretion events, which may only

be possible in the highest density regions of the early Universe (e.g., Riechers et al. 2011c, 2017; Ivison et al. 2011, 2013; Capak et al. 2011; Oteo et al. 2016; Marrone et al. 2018).

Recent single-dish studies of the evolution of the sub-millimeter luminosity function have suggested that, while the space density of DSFGs may significantly decrease at $z > 3$, the knee of the luminosity function appears to shift to higher infrared luminosities, perhaps capturing the high redshift tail of "titans" (e.g., Koprowski et al. 2017). While the $z > 4$ infrared luminosity function is far from accurately constrained, and the diversity of processes that may produce dusty hyper-starbursts are not completely understood (e.g., Narayanan et al. 2015), these results may not be completely surprising in the context of recent theoretical work exploring the role of protocluster star formation (e.g., Chiang et al. 2013, 2017). In particular, simulations suggest that a large fraction of early Universe star formation may have taken place in the densest regions, traced by the most massive halos, in an inside-out fashion. That is, a significant fraction of galaxy formation may have started in protocluster cores where the gas densities and the galaxy merger probability would have been highest, implying that this star formation may have been bursty and highly dust-obscured, as seen in high-redshift DSFGs. The importance of the connection between DSFGs and galaxy overdensities has been known for some time (e.g., Aravena et al. 2010b). Even the first $z > 5$ DSFG known, AzTEC-3 at $z = 5.3$, was quickly recognized to be located near the center of a rich galaxy protocluster (Capak et al., 2011; Riechers et al., 2014a). Recent studies have explored the connection between DSFGs and galaxy overdensities in detail, finding evidence for a strong relationship, potentially getting stronger with redshift toward the early Universe (e.g., Smolčić et al. 2017b; Lewis et al. 2018). Two notable case studies of clustered,

dusty galaxy formation are the extremely rich protocluster of dusty star forming galaxies identified at $z = 4$ by Oteo et al. (2017b), and the surprisingly high incidence (4/25) of very close association (<600 kpc) of dusty star forming galaxies to $z > 6$ quasars (Decarli et al., 2017). The former case shows that several protocluster members may be experiencing a dusty starburst phase simultaneously, perhaps triggered by a massive gas flow. Both cases show that active galactic nuclei (AGN) or massive starburst galaxies may be found in association and can be serendipitously discovered in sensitive Atacama Large (sub-)Millimeter Array (ALMA) observations.

Here we describe the serendipitous discovery of the brightest and highest redshift dusty starburst in COSMOS (Scoville et al., 2007) at J2000 $10^h0^m59^s.2$, 1°33′6.6″, which we identified in ALMA observations of atomic fine-structure lines in a close-by galaxy, HZ10. This new DSFG is located only 13″ (∼ 77 kpc) away from HZ10, which is an above average dusty but "normal" (i.e., $\sim L^*_{\rm UV}$) galaxy at $z = 5.654$ (Capak et al., 2015; Pavesi et al., 2016). HZ10 is a Lyman Alpha Emitter (LAE; Murayama et al. 2007) and a Lyman Break Galaxy (LBG) which was selected for [CII] 158 μm and dust emission observations with ALMA based on its strong ultraviolet absorption features (Capak et al., 2015). We subsequently followed up HZ10 in [NII] 205 μm emission, and CO(2–1) (Chapter 6). These observations provide additional support to the interpretation that HZ10 appears to show a more "mature" and metal-rich inter-stellar medium (ISM) than other "typical" massive galaxies at $z > 5$ (Pavesi et al., 2016; Faisst et al., 2017). The new DSFG is also detected in *Herschel* observations. Its "red" color in the SPIRE 250 – 500 μm bands is consistent with its high redshift. We refer to this galaxy as COSMOS (FIR-)Red Line Emitter (CRLE, read "curly") in the following, after the methods that lead to its discovery.

In Section 4, we describe the spectroscopic observations that allowed the identification of CRLE as a dusty starburst at $z \sim 5.7$. An obstacle to any previous identification of this source may have been the presence of an unrelated foreground ($z \sim 0.3$), low-mass spiral galaxy, which covers the optical counterpart of CRLE[1], and therefore prevents detection in the visible and near-IR (NIR) bands. In Section 5, we detail our constraints on the potential contribution of gravitational lensing from the foreground galaxy to the observed properties of CRLE, finding that lensing may be negligible. In Section 6, we present the results of our line measurements and discuss their implications. In Section 7, we detail our attempt to separate the emission from CRLE from that of the foreground galaxy at observed-frame NIR wavelengths, we present the new continuum measurements and discuss the dust properties of CRLE and the evidence for a galaxy merger. Section 8 describes the UV-space dynamical modeling technique we utilized to investigate the [CII] observations from CRLE. In Section 9, we analyze public galaxy catalogs to identify and characterize a galaxy overdensity around CRLE, providing evidence for a galaxy protocluster. We conclude in Section 10. In this work, we adopt a Chabrier IMF and a flat, ΛCDM cosmology with $H_0 = 70\,\mathrm{km\ s^{-1}\ Mpc^{-1}}$ and $\Omega_M = 0.3$. Quoted lengths are proper sizes unless otherwise specified (for comoving distances).

[1]For this reason, and for its high sub-mm flux, CRLE may be considered "hidden in plain sight".

7.4 Observations

7.4.1 ALMA observations of [CII] and [NII]

The ALMA data containing the [CII] line for CRLE were first presented by Capak et al. (2015) as Cycle 1 observations of HZ10. A subsequent reprocessing of those data, together with a description of part of the Cycle 3 [NII] observations, was described in detail by Pavesi et al. (2016).

The Cycle-1 observations of [CII] were taken on 2013 November 16 in band 7 as part of a larger project (ID: 2012.1.00523.S; Capak et al. 2015). The pointing resulted in 56 min on source time with 25 usable antennas. The primary beam attenuation factor at the position of CRLE is $\sim$ 3. The correlator was set up to target the expected frequency of the [CII] line in HZ10 at 284.835 GHz, and to provide continuous coverage of the continuum emission in adjacent spectral windows (centered $\sim$ 2, 12, and 14 GHz above) with channels of 15.6 MHz width in Time Division Mode (TDM). The synthesized beam size is approximately $0''.6 \times 0''.5$, when adopting natural baseline weighting. We refer to Pavesi et al. (2016) for a complete description of the observations and the imaging product.

Cycle 3 observations of [NII] 205 μm targeting HZ10 and also covering CRLE were taken on 2016 January 1 and 5 in band 6, as part of two separate programs (2015.1.00928.S and 2015.1.00388.S; PIs: Pavesi and Lu, respectively) with one track each in a compact configuration (max. baseline $\sim$ 300 m). The two sets of observations resulted in 50 min, and 35 min on source with $\sim$41–45 usable 12 m antennas under good weather conditions at 1.3 mm. The first set of observations was previously described by Pavesi et al. (2016). For the second set

of observations, the nearby radio quasar J0948+0022 was observed regularly for amplitude and phase gain calibration, J1058+0133 was observed for bandpass calibration, and Callisto was used for flux calibration. We estimate the overall accuracy of the flux calibration to be within ~ 10%. The correlator was set up to cover two spectral windows of 1.875 GHz bandwidth each at 15.6 MHz (~ 20 km s^{-1}) resolution (dual polarization) in TDM, in each sideband.

We used the Common Astronomy Software Application (CASA) version 4.5 for data reduction and analysis. We combined data from all observations and produced all images with the CLEAN algorithm, using natural weighting for maximal sensitivity. Imaging these [NII] data results in a synthesized beam size of 1.6″ × 1.2″ at the redshifted [NII] frequency of CRLE and in the continuum map. The rms noise in the phase center is ~ 0.14 mJy $beam^{-1}$ in a 44 km s^{-1} wide channel. The final rms noise when averaging over the line-free spectral windows (i.e. over a total 7.1 GHz of bandwidth) is ~ 18 μJy $beam^{-1}$. The primary beam attenuation factor at the position of CRLE is ~ 1.8.

7.4.2 VLA observations of CO(2–1)

We observed the CO(2–1) transition line in CRLE (ν_{rest}=230.538 GHz, redshifted to ~34.58 GHz at z ~ 5.667), using NSF's Karl G. Jansky Very Large Array (VLA) in Ka band (project ID: 17A-011, PI: Pavesi). Observations were carried out between 2017 March 4 and April 6, with 27 antennas in the most compact array configuration (D; max. baseline ~ 950 m) under good to moderate weather conditions at 35 GHz (precipitable water vapor columns of 3–6 mm) for eight sessions. The pointing for these observations was centered on HZ10. The pri-

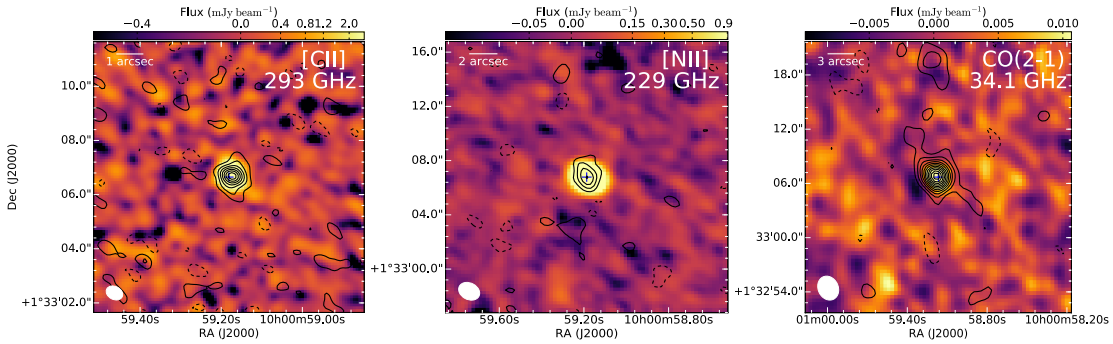

Figure 7.1: Continuum and integrated line maps for CRLE. The contours show the [CII] (left, observed with ALMA), [NII] (middle, observed with ALMA), and CO(2–1) (right, observed with the VLA) emission, while the background images show the continuum emission from the corresponding observations (frequencies are shown in the observed-frame). Blue crosses indicate the positions of the continuum peaks. The synthesized beam size is shown in the bottom left corner of each panel. Contours are multiples of 2σ, starting at $\pm 2\sigma$. The [CII] line, 158 μm continuum (corresponding to observed-frame 293 GHz), and 205 μm continuum (corresponding to observed-frame 229 GHz) emission are resolved. The [NII] line emission is marginally resolved.

mary beam attenuation factor at the position of CRLE is ~1.08. The combination of all data results in a total on-source time of 19.8 hr.

The nearby radio quasar J1041+0610 was observed regularly for amplitude and phase gain calibration. Also, 3C286 was observed for bandpass and flux calibration. We estimate the overall accuracy of the flux calibration to be within ~ 10%, since the phase calibrator flux was measured to be constant within < 5% across all sessions.

The VLA correlator was utilized in 8-bit mode for maximum sensitivity. In the first three sessions, the correlator was set up with two intermediate-frequency bands (IFs) of eight, 128 MHz-wide spectral windows each, centering one IF on the redshifted CO(2–1) line frequency in HZ10 and the other contiguously below to provide additional continuum sensitivity. The lower IF was

moved in the remaining five sessions, by centering it on the CO(2–1) line in CRLE (which otherwise fell onto a sub-band gap). While these overlapping sidebands limit the simultaneous bandwidth and hence the continuum sensitivity, they provide uninterrupted coverage of the CO(2–1) line in both galaxies. The channels in all spectral windows were chosen to provide 1 MHz ($\sim 9\,\mathrm{km\ s^{-1}}$) resolution (dual polarization) in each IF, to obtain a simultaneous bandwidth of 2.048 GHz for the first three sessions and 1.349 GHz for the remaining five sessions. Because of overlapping spectral coverage, the measurements in the two IFs are not independent. Therefore, we never combine their data, but rather only use the line IF for the analysis of CRLE.

We used CASA version 4.7 for data reduction and analysis. We calibrated the visibilities using the scripted VLA pipeline, supplemented by manual flagging through inspection of standard visibility plots. We combined data from all observations and imaged them with the CLEAN algorithm, using natural weighting for maximal sensitivity. The imaging of the CO(2–1) data results in a synthesized beam size of $2.7'' \times 2.3''$ at the redshifted CO(2–1) frequency and in the continuum map. The rms noise in the phase center is $\sim 45\,\mu\mathrm{Jy\ beam^{-1}}$ in a $35\,\mathrm{km\ s^{-1}}$ wide channel. The final rms noise when averaging over the line-free 1.92 GHz of bandwidth is $\sim 2.7\,\mu\mathrm{Jy\ beam^{-1}}$.

7.5 Constraining the effects of gravitational Lensing

The high apparent luminosity of CRLE, combined with the coincident spatial position with a foreground galaxy, raise questions concerning the relative importance of strong gravitational lensing. About 10% of the area of the segmen-

tation map in the *HST* H-band images we utilized to study CRLE is occupied by (mostly) local galaxies. Therefore, the coincidence of galaxies at different redshifts may not be uncommon. Using the method by Harris et al. (2012), we roughly estimate the magnification due to gravitational lensing, based on the apparent correlation between intrinsic CO luminosity and line width, finding $\mu = 0.9 \pm 0.2$. This may suggest that lensing is not expected to significantly boost the observed luminosity of CRLE. However, we note that the Harris et al. (2012) method relies on a proposed $L'_{\rm CO}$–FWHM$_{\rm CO}$ relation, which may only hold with large scatter (e.g., Sharon et al. 2016).

We also explore the potential lensing magnification by modeling the foreground galaxy with the commonly used approximation of a singular isothermal sphere (SIS). We confirm that the light distribution appears to be approximately proportional to the aperture radius, which implies that a "light traces mass" model would be approximately equivalent to the adopted SIS. By measuring the flux in the *HST*/WFC3 F160W image in apertures of varying radius, we deduce that 68% of light is included within 1″ radius, 37% within 0.5″ radius, 22% in 0.3″ radius. We assume that the total mass in the central regions of the foreground galaxy should be dominated by the stellar mass. Therefore, we adopt a total mass of $3.3 \times 10^9\ M_\odot$, as reported by the COSMOS2015 catalog (Laigle et al., 2016), in agreement with our *Cigale* SED modeling. A combination of the distance implied by the photometric redshift, the measured size, and the total mass suggests a velocity dispersion parameter for the SIS model of only 25–30 km s^{-1}. This velocity dispersion parameter corresponds to a very small Einstein radius of ∼0.02″–0.025″, at the lens and source distances derived by their redshifts. We measure a separation of the DSFG from the lens center of ∼0.3″. If we were to assume a point source model for the DSFG, we would estimate a magnification

of <10%. The relative positional uncertainty is dominated by the *HST* astrometric uncertainty, which we assume to be ~0.1″ (e.g., Gómez-Guijarro et al. 2018), dominating over the ALMA positional accuracy or the fitting uncertainty.

We use both our custom code and the publicly available code `gravlens` (Keeton, 2001) to constrain the effect of lensing in a model source distribution, obtaining equivalent answers. We fix the lens Einstein radius to 0.025″, the source spatial FWHM to 0.6″ based on the measured [CII] size, and a mean lens-source separation of 0.3″. We randomly vary this positional separation by adding independent, normally distributed spatial offsets along the two axes with standard deviation of 0.1″, representing the relative positional uncertainty. This results in an approximately normally distributed magnification of $\mu = 1.09 \pm 0.02$. Furthermore, since the Einstein radius is so small compared to the spatial extent of the source (< 5%), the effects of lensing are negligible both to the global flux but also to the observed kinematic structure within the uncertainty of our measurements. In addition, we also allow the source size and relative position to vary, and verify that a significantly smaller intrinsic source size is incompatible with the observed source size. The small Einstein radius implies that the observed source size can only be reproduced by a comparable intrinsic size, therefore significantly constraining the allowed magnification to the values reported above. We therefore assume that lensing does not measurably affect any of our conclusions based on the luminosity and spatial structure of CRLE.

Table 7.1: Measured line properties of CRLE.

	[CII]	[NII]	CO(2–1)
Component 1			
$\nu_{\rm obs}$(GHz)	284.892 ± 0.013	219.0298[a]	34.5604 ± 0.0017
$S_{\rm peak}$(mJy)	16 ± 3	1.2 ± 0.2	0.49 ± 0.04
FWHM (km s^{-1})	280 ± 40	280[a]	290 ± 30
I (Jy km s^{-1})	4.5 ± 0.9	0.33 ± 0.07	0.14 ± 0.02
Component 2			
$\nu_{\rm obs}$(GHz)	285.27 ± 0.07	219.3204[a]	34.613 ± 0.004
$S_{\rm peak}$(mJy)	9.6 ± 0.9	0.65 ± 0.13	0.25 ± 0.03
FWHM (km s^{-1})	610 ± 140	610[a]	420 ± 90
I (Jy km s^{-1})	6.3 ± 1.5	0.40 ± 0.13	0.11 ± 0.03
Total			
Mean redshift	5.6666 ± 0.0008		
I (Jy km s^{-1})	10.8 ± 1.2	0.73 ± 0.15	0.26 ± 0.02
L ($10^7 L_\odot$)	930 ± 100	49 ± 10	2.7 ± 0.2
Deconvolved size (FWHM)	(0″.63 ± 0″.03) × (0″.40 ± 0″.05)	(0″.98 ± 0″.18)	—
Physical size (kpc^2)	(3.7 ± 0.2) × (2.4 ± 0.3)	5.8 ± 1.1	—
L' (10^{10} K km s^{-1} pc^2)	4.3 ± 0.5	0.49 ± 0.10	7.0 ± 0.5

Note: We produced integrated line maps over the line FWHM and used CASA to fit a 2D Gaussian model. Then, we extracted aperture spectra utilizing the FWHM of the spatial Gaussian model, correcting the total flux by a factor of 2 to account for the flux outside the aperture. The deconvolved emission size was measured from Gaussian fitting to the visibilities. [a]: Fixed to the parameter values derived from the [CII] line.

7.6 Line emission properties

7.6.1 Results

We detect [CII], [NII] 205 μm and CO(2–1) line emission and the adjacent continuum toward CRLE at high significance (> 8σ; Figure 7.1), which provides an unambiguous redshift identification. Although a foreground galaxy ($z_{\rm phot} \sim 0.3$) is located along the line of sight to CRLE, potentially causing gravitational lensing of its emission, in the previous section we constrained the likely magnitude of this effect to be minor (< 10% flux magnification and negligible spatial distortion). Therefore, we simply extract aperture spectra and fit double Gaussians to the spectral profiles to measure the intrinsic line properties (Figure 7.2). We

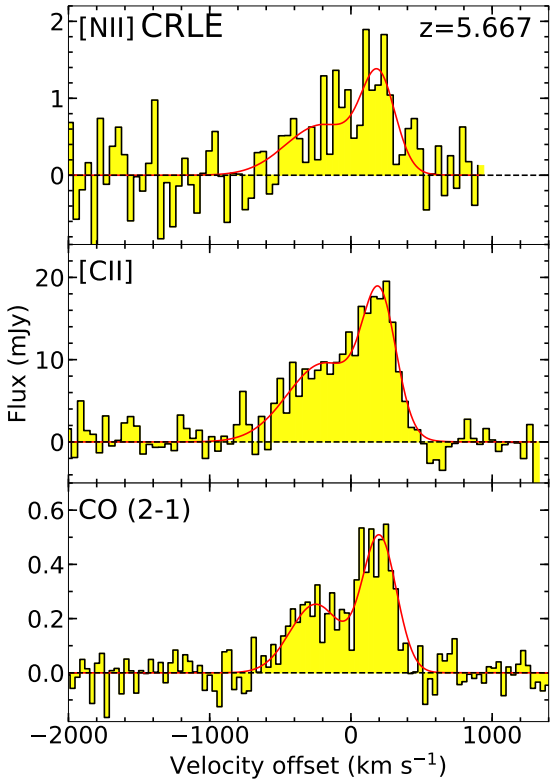

Figure 7.2: [NII], [CII], and CO(2–1) continuum-subtracted, aperture integrated line spectra for CRLE (histograms). Double Gaussian fits to the line emission are shown as red curves. A mean redshift of $z = 5.667$ was adopted as the velocity reference. The signal-to-noise ratio of the [NII] line does not allow fitting the central frequencies and the widths for the two velocity components. Therefore, these were fixed to the values measured for [CII]. The channel velocity widths are ~43, ~44 and ~35 km s^{-1} for the [NII], [CII] and CO(2–1) lines, respectively.

report the line properties in Table 7.1, while the continuum fluxes are listed together with the archival photometric measurements in Table 7.2.

We measure the deconvolved [CII] spatial FWHM size from UV plane modeling (see Section 8) to be 0″.46 ± 0″.08, which corresponds to 2.7 ± 0.5 kpc at $z = 5.667$. Using an isotropic virial estimator (Engel et al., 2010), and assuming a [CII] single-Gaussian fit line FWHM of 640 ± 60 km s^{-1} (which is also compatible with the broad velocity component), we derive a dynamical mass of

$(1.5 \pm 0.4) \times 10^{11}\ M_{\odot}$[2].

The [NII] emission is only slightly resolved. Using the CASA task UVMODELFIT, we measure a deconvolved FWHM major axis size of 0″.98 ± 0″.18, corresponding to 5.8 ± 1.1 kpc. We use the same technique to fit the size of the [CII] emission to provide an accurate comparison to the [NII] emission size, obtaining a result that is compatible with our more sophisticated UV plane modeling. The [NII] line emission appears to be marginally more extended (formally by a factor of 2.1 ± 0.5) than the [CII] emission, but higher resolution, and higher signal-to-noise [NII] observations are necessary to confirm this finding. In particular, a manual inspection of the UV-radial profile of the [NII] line visibilities appears compatible with the size of the [CII] emission. Neither the CO line nor the adjacent continuum emission are resolved. We fit the size of the continuum emission at 158 μm and 205 μm in the UV plane, and they are compatible with the same deconvolved size of (0″.39±0″.01)×(0″.31±0″.02). This implies that the size of the [CII] emitting region is more extended than the size of the dust continuum by $\sim (30 \pm 20)$%, in linear dimensions, suggesting that the observed dust continuum may not represent the full extent of the star-forming gas distribution (see also e.g., Riechers et al. 2014a; Chen et al. 2017b).

We find a [CII]/[NII] line luminosity ratio of 19 ± 4 in CRLE, which is comparable to the line ratio in the z = 5.3 DSFG AzTEC-3 of 22 ± 8 (Pavesi et al., 2016). This line ratio is sensitive to the fraction of [CII] emission coming from ionized gas, rather than photon-dominated regions (PDR), because the ionization energy of nitrogen, in contrast to carbon, is higher than that of hydrogen. This makes it a tracer of ionized gas only, and the [CII]/[NII] ratio is approximately

[2]We note that this estimate is subject to systematic uncertainties of the order of a factor of a few. In particular, a disk-like gas distribution would require an inclination correction.

constant in ionized gas (e.g., Oberst et al. 2006; Pavesi et al. 2016). Assuming a line ratio of 3 ± 0.5 in the ionized gas (Díaz-Santos et al., 2017), we calculate a fraction of the [CII] emission from PDRs of 84% ± 4% for CRLE and 86% ± 5% for AzTEC-3, respectively.

7.6.2 Origin of the [CII] emission

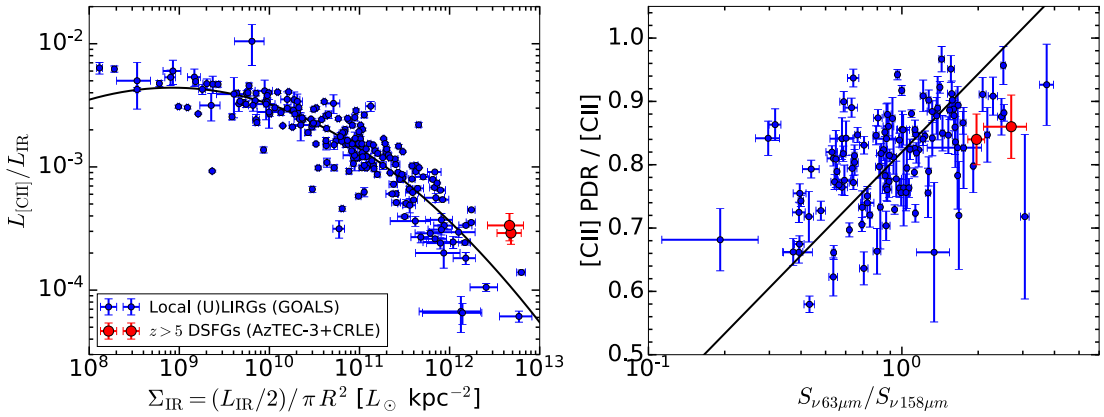

Figure 7.3: Left: [CII]-to-IR luminosity ratio as a function of IR luminosity surface density for CRLE and AzTEC-3 (red) and the GOALS sample of local (U)LIRGs (blue), adapted from Díaz-Santos et al. (2017). The black line shows the best fitting function reported by Díaz-Santos et al. (2017). Although the $z > 5$ DSFGs show low [CII] to IR luminosity ratios as expected for extreme starbursts, they appear to show more luminous [CII] emission than might be expected from the local relation. Right: Fraction of the [CII] luminosity coming from PDRs as a function of FIR color (rest-frame 63 μm to 158 μm; a proxy for dust temperature) for CRLE, AzTEC-3 and the GOALS sample (Díaz-Santos et al., 2017). The black line shows the best fitting function reported by Díaz-Santos et al. (2017). The FIR colors for the $z > 5$ DSFGs were inferred from the best-fitting modified-blackbody models. The PDR fraction of the [CII] emission was estimated from the [CII]/[NII] line ratio, assuming a line ratio of 3 ± 0.5 in the ionized gas, following Díaz-Santos et al. (2017). The $z > 5$ DSFGs appear to show a lower PDR fraction of the [CII] emission relative to the local trend with dust temperature.

CRLE exhibits approximately the same [CII]/[NII] ratio as AzTEC-3 (Pavesi et al., 2016). This ratio is compatible with the range observed in local (ultra)luminous infrared galaxies ((U)LIRGs). However, given the higher gas den-

sity and star formation rate surface density in high redshift DSFGs relative to most local (U)LIRGs, one might expect a lower fraction of the [CII] emission to come from the diffuse ionized gas, which is traced by [NII], relative to atomic and molecular PDRs and therefore a higher [CII]/[NII] ratio (Pavesi et al., 2016). Therefore, our observed line ratio suggests that high redshift DSFGs may host a significant reservoir of diffuse ionized gas, which may be more extended than the starbursting gas. The potentially larger size of the [NII] emitting region in CRLE, relative to [CII] (although with significant uncertainty), would provide support for this interpretation if confirmed. Recent measurements of both [NII] fine-structure lines at 205 μm (studied here), and 122 μm in local galaxies also support the interpretation of the [NII] emission predominantly coming from diffuse ionized gas, rather than compact HII regions (e.g., Herrera-Camus et al. 2016, 2018a,b; Díaz-Santos et al. 2017).

A well known decreasing trend of the [CII]/$L_{\rm IR}$ ratio with infrared luminosity surface density (a proxy for FUV field strength) offers insight into the origin of the [CII] emission. In particular, a decreasing trend is expected for PDR emission due to the saturation of [CII] line emission at higher FUV field strengths (e.g., Stacey et al. 1991). This trend is clearly observed in a sample of local dusty star-forming galaxies from the Great Observatories All-sky LIRG Survey (GOALS; Díaz-Santos et al. 2017). However, at the calculated infrared luminosity surface density for CRLE and AzTEC-3, their observed [CII]/$L_{\rm IR}$ ratios ($\sim 3 - 4 \times 10^{-4}$) lie significantly above the best-fit to the relation for the GOALS sample (Figure 7.3).

This may suggest an additional contribution besides PDRs to the [CII] emission. If we assume that the PDR contribution to the [CII] luminosity is uniquely

determined by the intensity of the radiation field as traced by the $L_{\rm IR}$ surface density, a more significant contribution from diffuse ionized gas may be a reason for this excess. Furthermore, the fraction of [CII] coming from PDR, rather than ionized gas (as traced by the [CII]/[NII] ratio), appears to be lower for CRLE and AzTEC-3 for their modeled FIR color, relative to the fitted relation for the GOALS sample (Figure 7.3). This quantifies the finding that the [CII]/[NII] ratio appears to be low, for the more extreme (i.e., higher dust temperature, Figure 7.3) gas conditions observed in these $z > 5$ DSFGs relative to local starbursts (Pavesi et al., 2016). As such, it appears to point towards a larger contribution from diffuse ionized gas to the [CII] emission than what is expected from local starbursts. This diffuse ionized gas may take the form of a gas halo, more extended than the star-forming region. We suggest that a potentially larger and more diffuse ionized gas component at $z > 5$ may be due to freshly accreted, inflowing gas, which is expected to play an important role in powering starbursts in the first billion years of cosmic time. Metallicity is unlikely to play a significant role in affecting the [CII]/[NII] line ratio, as we constrain $\alpha_{\rm CO}$ to be low, and the high dust mass for CRLE (see below) likely implies a solar or super-solar metallicity (Bolatto et al., 2013). Nonetheless, an important caveat to our conclusions is that variations in the carbon to nitrogen abundance ratio may affect our interpretation of the [NII] line emission properties.

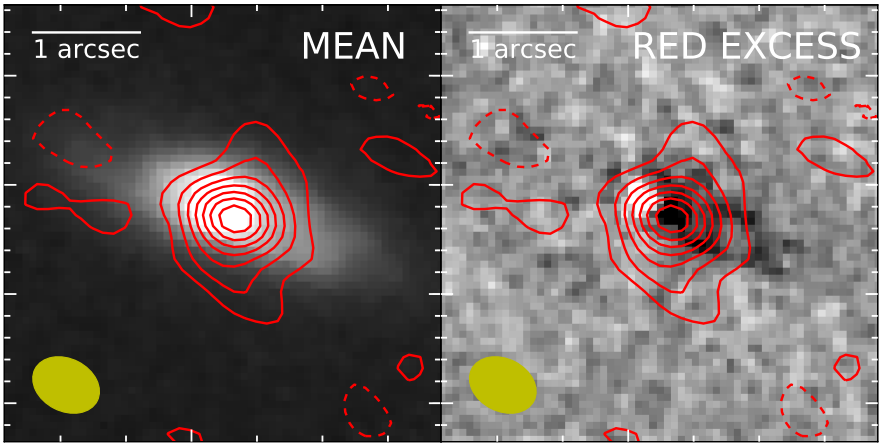

Figure 7.4: *HST* NIR band mean emission and red color excess, attempting to separate the emission from CRLE. Left: ALMA [CII] contours shown in steps of 2σ, overlaid on *HST* NIR mean image. To obtain the mean image, we averaged the emission detected in the three *HST*/WFC3 bands F105W, F125W and F160W. Right: Difference map of F160W and the mean image, showing F160W emission in excess from the mean.

7.7 Spectral Energy Distribution Analysis

7.7.1 HST foreground galaxy removal

In order to constrain the rest-frame optical emission from CRLE, we attempt different methods for removing the contamination of the *HST*/WFC3 NIR images due to the foreground galaxy. First, we attempt to separate the emission from CRLE from that of the foreground galaxy based on a color difference between the two galaxies (Figure 7.4). The mean NIR image (average of WFC3/F105W, F125W, and F160W) shows smooth emission due to the foreground disk galaxy but a F160W "excess" (relative to the mean NIR emission) shows a more red than average component to the northeast of the central position (corresponding to only $\sim$ 0.5% of the total F160W flux) and a deficit of F160W emission at the position of the CRLE [CII] emission peak. We may expect the rest-frame optical

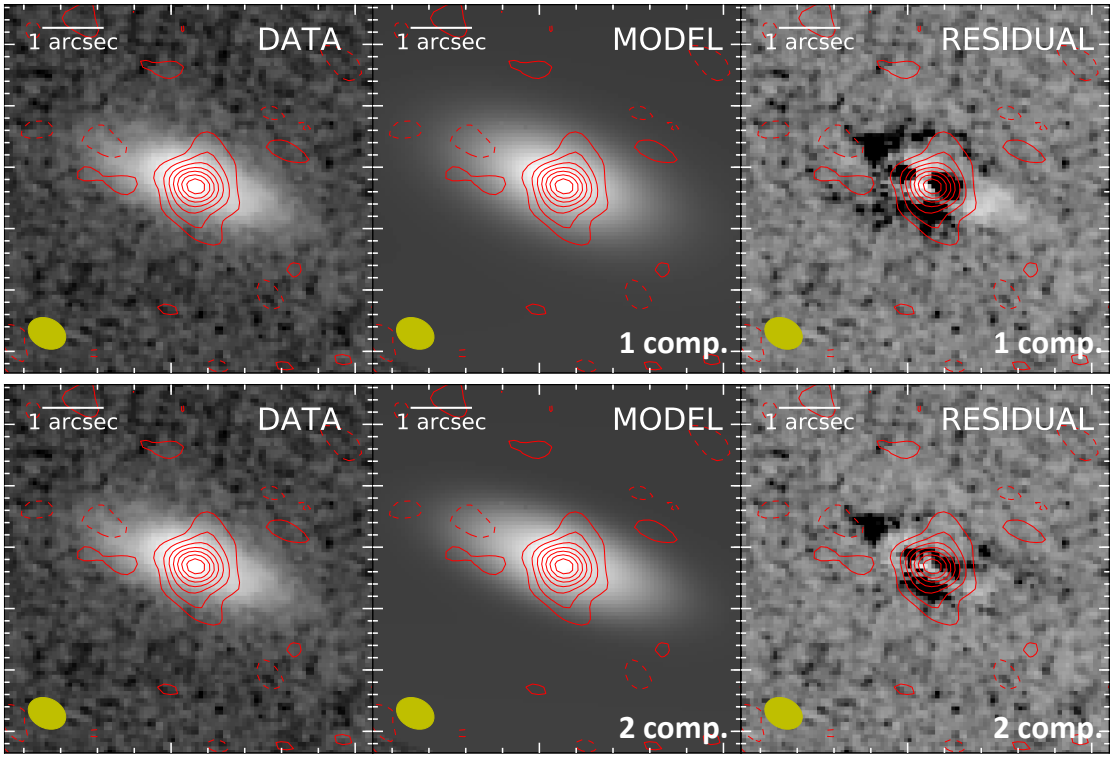

Figure 7.5: Top: Single Sérsic component model fit with *Galfit* to the *HST*/WFC3 F160W emission from the foreground galaxy. The low level residuals show a hint of emission (a few percent in flux) which may be associated with asymmetric structure in the foreground galaxy or CRLE itself (position indicated by the ALMA [CII] contours). Bottom: Two-component *Galfit* best-fit model and residuals, showing that no significant additional structure is present.

emission associated with CRLE to appear redder than that of the foreground galaxy. This tentative evidence may therefore suggest that the stellar emission from CRLE may be offset from the [CII] peak as frequently observed in high redshift DSFGs perhaps due to differential dust obscuration or an older stellar population offset from the young massive star-forming regions (e.g., Riechers et al. 2014a; Gómez-Guijarro et al. 2018). We also use *Galfit* to fit Sérsic profile emission models and remove the foreground emission from the F160W image (Peng et al., 2002). We first fit a single component model characterized by the center position, flux, radius, Sérsic index, axis ratio and position angle (Fig-

ure 7.5, top). We find a Sérsic index of ~ 1, compatible with an exponential disk, and a half-light radius of 0.82″. The total emission is not fit well by this model and shows positive residuals to the northeast of the center, which may or may not be associated with the "red" excess seen in Figure 7.4. The flux associated with this positive residual is only $\sim 1-2\%$ of the total F160W flux. Since part of the foreground galaxy emission to the west is apparent in the residuals, we do not consider these residuals to be sufficient to indicate an additional source of emission, beyond the imperfect model fit of an intrinsically not perfectly symmetric galaxy. In order to achieve a better fit to the foreground emission we also fit a two-component Sérsic profile (Figure 7.5, bottom). The residuals do not indicate significant additional structure. The second emission component may be associated with structure in the foreground galaxy or with emission from CRLE. In the main text, we neglect the contribution from CRLE to the emission at these wavelengths because it appears to represent, at most, a few percent of the total.

7.7.2 Optical-to-NIR SED

As described in the previous section, CRLE is located behind a local foreground spiral galaxy with a photometric redshift of ~ 0.35 and stellar mass of $3.3\times10^9\ M_\odot$ in the COSMOS2015 catalog (Laigle et al., 2016), which outshines its optical emission. The foreground galaxy is expected to dominate the total emission at optical-to-NIR wavelengths, at least up to observed-frame $\sim 2\,\mu$m. In order to constrain the contribution of CRLE to the total emission in the near to mid-IR, we use *Cigale* to carry out spectral energy distribution (SED) fitting of the optical and NIR emission (Noll et al., 2009; Serra et al., 2011). We fit the optical and NIR stellar emission with a delayed star formation history (with ages of the old-

Table 7.2: Measured continuum fluxes (foreground galaxy & CRLE).

Wavelength (μm)	Flux (μJy)	Band
0.4816	4.73 ± 0.03	*HSC* g
0.6234	10.49 ± 0.03	*HSC* r
0.7740	13.38 ± 0.04	*HSC* i
0.9125	17.44 ± 0.06	*HSC* z
0.9780	17.15 ± 0.12	*HSC* Y
1.0552	15.15 ± 0.07	*HST*/F105W
1.2501	17.20 ± 0.06	*HST*/F125W
1.5418	20.67 ± 0.08	*HST*/F160W
3.6	16.29 ± 0.17	*Spitzer*/IRAC
4.5	15.86 ± 0.18	—
5.8	19 ± 5	—
8.0	21 ± 4	—
24	70 ± 15	*Spitzer*/MIPS
100*	< 5,000	*Herschel*/PACS
160*	< 10,000	—
250*	12,000 ± 900	*Herschel*/SPIRE
350*	20,900 ± 1,300	—
500*	31,100 ± 1,400	—
850*	16,700 ± 2,000	SCUBA-2
1,024 (292.8 GHz)*	16,500 ± 900	ALMA
1,308 (229.2 GHz)*	8,650 ± 300	—
8,800 (34.069 GHz)*	22 ± 2	VLA

Note The *HST*/WFC3 fluxes measured with SExtractor, using the Kron mode. We report the *Herschel*/PACS non-detection as 3σ upper limits (Lutz et al., 2011). The SCUBA-2 flux was measured from the S2CLS images (Geach et al., 2017) and the other fluxes were obtained from the COSMOS2015 catalog (Laigle et al., 2016). *: Measurements expected to be dominated by emission from CRLE. Additional fluxes may be found in the publicly available COSMOS2015 catalog.

est stars ranging from 250 Myr to 12 Gyr, and an e-folding time ranging from 50 Myr to 8 Gyr), stellar population synthesis models with metallicity ranging from $1/50\,Z_\odot$ to $Z_\odot$ according to Bruzual & Charlot (2003) and a dust attenuation law according to Calzetti (2001). We determine a stellar mass of $(3.0 \pm 0.5) \times 10^9\,M_\odot$ and a star formation rate of $\sim 1.5\,M_\odot$ yr^{-1} for the foreground galaxy, confirming the catalog stellar mass value. We use the best fitting *Cigale* models to constrain the FIR luminosity of the foreground galaxy by adopting dust emission models

according to Draine & Li (2007). We find approximate predictions for the *Herschel*/SPIRE fluxes of 3.7, 2.0, and 0.8 mJy, in the 250, 350 and 500 μm bands, respectively. These are significantly lower than the measured fluxes in these bands. Therefore, we consider the FIR emission from the foreground galaxy to be subdominant to the emission from CRLE (Table 7.2).

The *Spitzer*/IRAC 5.8 and 8.0 μm and MIPS 24 μm fluxes are not fit well by the available SED models (Figure 7.6). We interpret this to be an indication of significant contamination by emission from CRLE toward the longer wavelengths. Although the IRAC1 and IRAC2 fluxes are compatible with expectations, the higher IRAC3 and IRAC4 fluxes are difficult to reproduce with the adopted dust emission models (Draine & Li, 2007). The best-fitting SED models were obtained by either including or excluding the MIPS 24 μm flux in the fitting (Figure 7.6). We find that best-fitting models to the IRAC points over-predict the 24μm flux when excluded, and that best-fitting models that include the 24μm measurement require strong PAH emission to fit the IRAC4 flux and they under-predict the IRAC3 flux at 5.8 μm by at least a factor $\sim$ 2. Even artificially reducing the measurement uncertainty on the IRAC3 flux does not improve the fit to this measurement. While it is unclear if the 24μm flux is dominated by emission from CRLE or from the foreground galaxy, we interpret these results as suggesting that perhaps a significant fraction of the flux at 5.8 μm may be due to CRLE. A potential caveat to this conclusion may arise in case the foreground galaxy contains an AGN, which could contribute additional flux at these wavelengths, and is presently unconstrained. We use *Cigale* to derive approximate constraints to the stellar mass in CRLE. If all the IRAC3 and IRAC4 emission were due to CRLE, the implied stellar mass would be of order $\sim 1-2\times10^{11}\,M_{\odot}$. This likely provides an upper limit to the actual stellar mass of

CRLE. A contribution of ~25%–50% of the emission may be plausible, yielding a best stellar mass estimate in the range of $\sim 2.5 - 10 \times 10^{10}\,M_{\odot}$.

7.7.3 FIR SED and modified blackbody fitting

In order to model the FIR SED of CRLE as measured by *Herschel*, ALMA, and JCMT/SCUBA-2, we use a modified blackbody, smoothly connected to a mid-IR power-law. We use *emcee* (Foreman-Mackey et al., 2013) to explore the posterior probability distribution of the parameters shown in Fig. 7.7. We employ uniform, non-constraining priors for the parameters (i.e., flux normalization at rest-frame 158 μm, dust temperature T_d, dust emissivity parameter β, rest-frame wavelength at which the optical depth becomes unity λ_0, and mid-IR power law index α; Table 7.3). By integrating between 42.5 and 122.5 μm, we find a FIR luminosity of $L_{\rm FIR} = (1.55 \pm 0.05) \times 10^{13}\,L_{\odot}$. By integrating between 8 and 1000 μm, we derive an IR luminosity of $L_{\rm IR} = (3.2 \pm 0.3) \times 10^{13}\,L_{\odot}$. Because the SED of CRLE is not constrained at mid-IR wavelengths, we follow the standard practice of estimating the star formation rate based on the FIR luminosity only, to provide a comparison to other $z > 5$ DSFGs (Riechers et al., 2014a). By adopting the standard conversion based on a Chabrier IMF (Carilli & Walter, 2013), we infer a star formation rate of $(1550 \pm 50)\,M_{\odot}$ yr^{-1}, with the caveat that the real star formation rate may be up to a factor of $\sim 2\times$ higher. Given the high level of dust obscuration in CRLE, we cannot exclude the presence of an obscured AGN. However, we expect that an AGN would only introduce minor contributions to the rest-frame $> 42.5\,\mu$m luminosity given the high dust-obscured star formation rate of CRLE (see, e.g., Kirkpatrick et al. 2015). As an example, the dust-obscured AGN in the $z = 4.05$ DSFG GN20 may dominate the mid-IR

luminosity, but its contribution to the total IR luminosity appears to be minor (Riechers et al., 2014b). Even for luminous high-redshift quasars, the contribution from AGN-heated, hot dust to the far-IR luminosity does not appear to exceed $\sim$ 20% (Leipski et al., 2013, 2014). By adopting standard (although uncertain) assumptions from Dunne et al. (2003), we find an estimated dust mass of $(1.3 \pm 0.3) \times 10^9\ M_\odot$.

The dust SED shape for CRLE appears to be intermediate between that of AzTEC-3 ($z \sim 5.3$) and ADFS-27 ($z \sim 5.7$; Figure 7.7, Riechers et al. 2014a, 2017). We also compare the measured FIR SED of CRLE to model templates of selected low- and high-redshift starbursts, spanning a range of physical conditions. A comparison to the template for local starbursts Arp 220 and M82 shows that CRLE resembles M82 more closely, suggesting a comparatively low dust optical depth[3] (Silva et al., 1998). A comparison to the ultra luminous $z = 6.34$ DSFG HFLS3 shows that CRLE appears to have a significantly lower dust temperature (Riechers et al., 2013; Ivison et al., 2016), as evidenced by the longer wavelength of the peak emission, while at the same time displaying a warmer dust temperature than is observed in the lower redshift ALESS sources (Swinbank et al., 2014). The SED of CRLE appears to closely resemble that of GN20, an extended $z \sim 4$ DSFG (Figure 7.7, e.g., Carilli et al. 2010; Magdis et al. 2011b; Hodge et al. 2012, 2015). Our reference SED templates suggest a potential redshift trend toward hotter dust in higher redshift DSFGs, as evidenced by the shorter wavelength SED peak in CRLE relative to the ALESS sample average (mostly in the range $z \sim 2-3$, Danielson et al. 2017), and the longer wavelength in comparison to HFLS3 (z=6.34, Riechers et al. 2013; Faisst et al. 2017). Heating

[3]The high optical depth in Arp 220 characteristically suppresses the emission at the short wavelengths, reducing the observable emission from the hot dust component (e.g., Scoville et al. 2017b).

Table 7.3: Results from modified blackbody fitting to the FIR SED of CRLE.

Percentile	Norm. (158 μm) (mJy)	T_d (K)	β	rest λ_0 (μm)	α
16th	13.25	38.95	1.537	1.659	1.430
50th	13.94	41.16	1.604	15.77	1.658
84th	14.65	47.49	1.674	80.08	1.938

from a warmer cosmic microwave background (CMB) may partly contribute to this tentative dust temperature trend (e.g., da Cunha et al. 2013c). However, selection effects may also be partly responsible for this trend, since most of these DSFGs were selected at fixed observed-frame wavelengths.

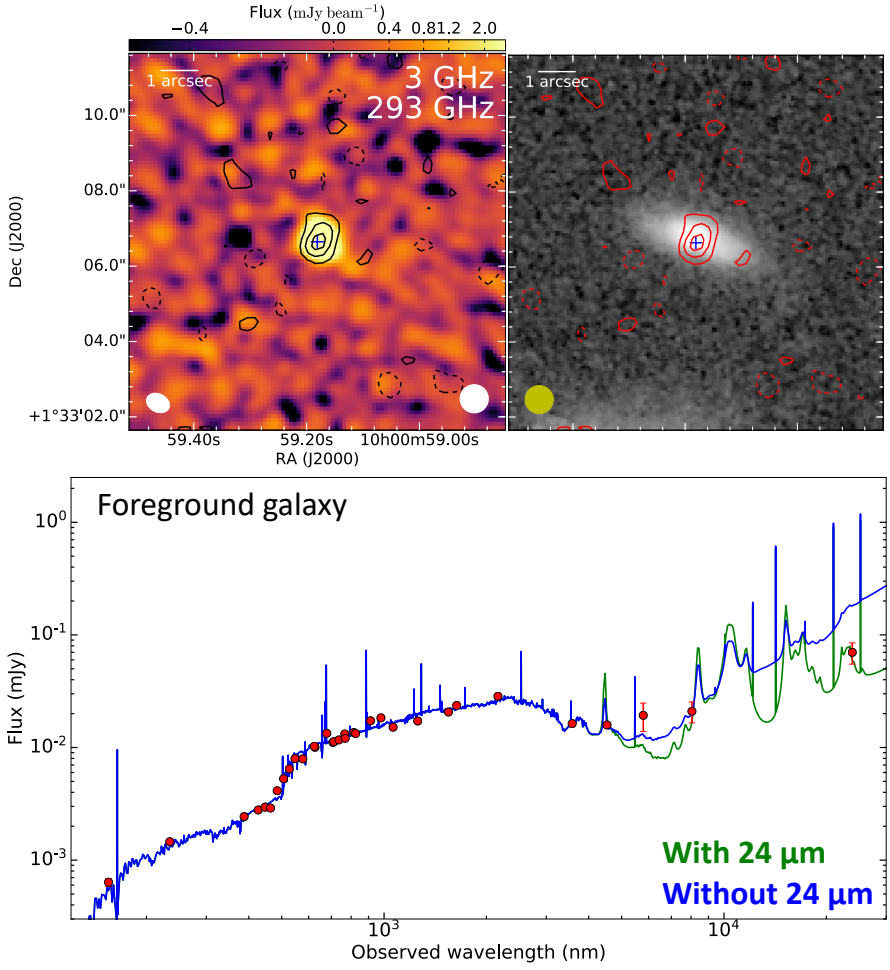

Figure 7.6: Top: 3 GHz observed-frame continuum emission from CRLE (contours; Smolčić et al. 2017a) on top of ALMA dust continuum from CRLE (left), and NIR emission from the foreground galaxy (right). Contours are shown in 2σ steps, starting from $\pm 2\sigma$. The blue cross represents the 158 μm dust emission peak. Top left: Color-scale, showing the rest-frame 158 μm continuum (corresponding to observed-frame 293 GHz). The beam sizes shown are for the 293 GHz data (left), and the 3 GHz data (right). Top right: Gray-scale *HST*/WFC3 F160W image from Barišić et al. (2017), showing the foreground disk galaxy at a photometric redshift $z \sim 0.35$. The contribution from CRLE cannot reliably be separated from the foreground galaxy at these wavelengths. Bottom: UV-NIR SED of the foreground galaxy and CRLE, fitted with *Cigale* models. The models do not provide a good fit to the measurement at 5.7 μm, suggesting that emission from CRLE may contribute a non-negligible fraction of, at least, the 5.7 μm flux.

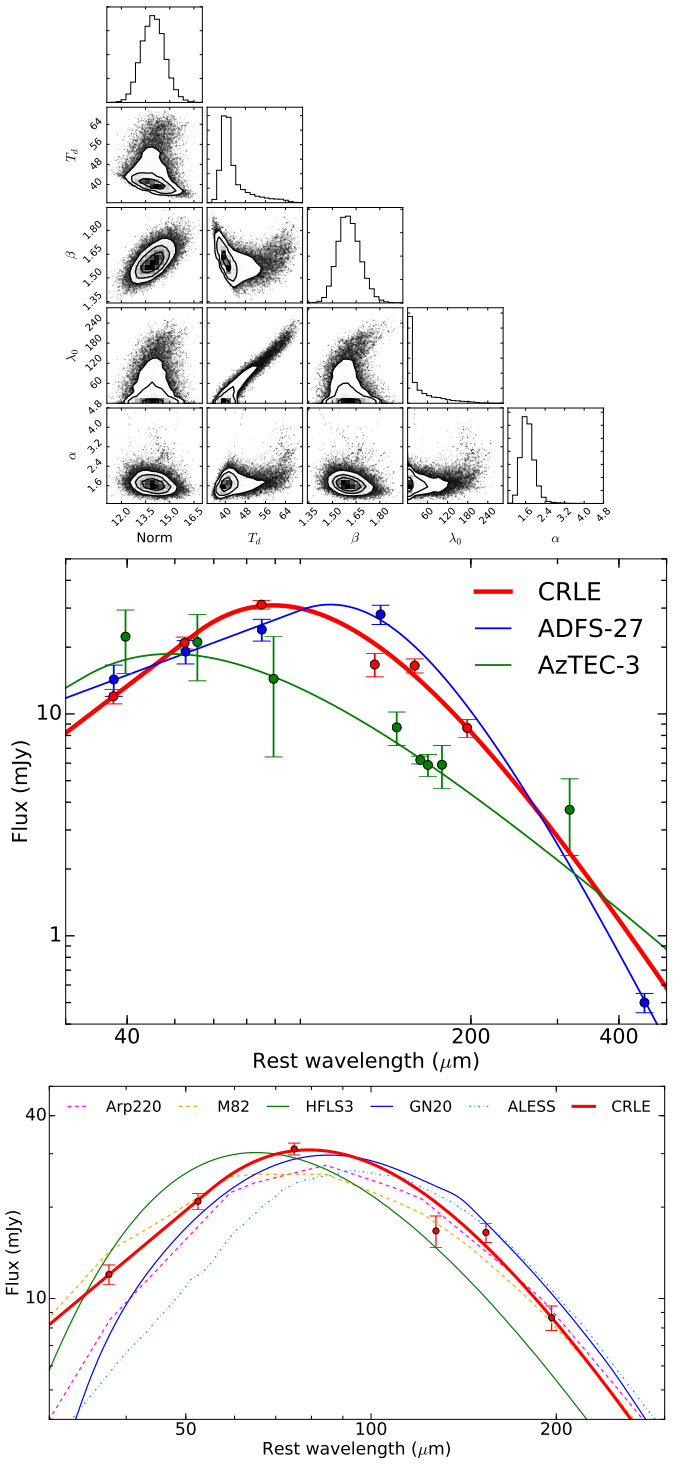

Figure 7.7: Modified blackbody (MBB) fits to the FIR SED in CRLE. Top: Corner plot of the model parameter posterior distribution. Middle: FIR SED comparison to other $z > 5$ DSFGs (AzTEC-3 and ADFS-27; Riechers et al. 2014a, 2017). CRLE shows peak emission at intermediate rest-wavelengths between the hot, compact starburst AzTEC-3 and the early-stage merger ADFS-27. Bottom: Comparison to other low and high redshift FIR SED templates (Silva et al., 1998; Riechers et al., 2013; Magdis et al., 2011b; Swinbank et al., 2014).

7.7.4 Radio continuum emission

CRLE is detected at 7σ significance in 3 GHz continuum emission ($24.3 \pm 3.8\,\mu$Jy; Smolčić et al. 2017a). The emission is not resolved at a synthesized beam size of 0.75″ and it is aligned with the dust continuum emission (Fig. 7.6). CRLE is also potentially weakly detected at 1.4 GHz at the 2.5σ level (Schinnerer et al., 2010). We conservatively adopt a 3σ limit of $< 84\,\mu$Jy at 1.4 GHz, which is consistent with a spectral index of -0.7. Sensitive low radio frequency observations also provide constraining non detections (Tisanić et al., in prep.). We derive 3σ upper limits of 320 μJy at 325 MHz and 150 μJy at 610 MHz. These imply constraints to the effective radio spectral index to observed-frame 3 GHz of > -1.16 and > -1.14 for the 325 MHz and 610 MHz limits, respectively.

Adopting the redshift-dependent FIR-radio correlation measured by Delhaize et al. (2017), we can convert our measured 3 GHz flux and the constraints to the 1.4 GHz flux to FIR luminosities. The FIR-radio correlation has been calibrated at a rest-frame frequency of 1.4 GHz, which corresponds to observed-frame 210 MHz for CRLE. This comparison therefore requires significant extrapolation from our measurement at 3 GHz, and it is sensitive to the spectral index. Adopting a radio power law index of -0.7 as in Delhaize et al. (2017), we use 3 GHz flux and 1.4 GHz flux upper limit to derive FIR luminosities of $4.0 \times 10^{12}\,L_{\odot}$ and $< 8.0 \times 10^{12}\,L_{\odot}$, respectively. This radio-inferred FIR luminosity is significantly lower than our direct measurement. We could reconcile these estimates with an effective spectral index of -1.2 between rest-frame 20 GHz and 1.4 GHz, but this would be in slight tension with our 325 and 610 MHz upper limits. Alternatively, Molnár et al. (2018) have suggested that the FIR-radio correlation may not evolve in star-forming, disk-dominated galaxies. If we assume

no redshift evolution, the 3 GHz flux and the 1.4 GHz flux upper limit would imply FIR luminosities of $\sim 2.7 \times 10^{13}\,L_{\odot}$ and $< 5.5 \times 10^{13}\,L_{\odot}$, in agreement with our direct measurement.

However, the observed radio emission may not be well described by a single power-law spectral index down to rest-frame 1.4 GHz. In particular, the analysis by Tabatabaei et al. (2017) suggests that approximately half of the radio flux at this frequency may be due to thermal free-free emission. Under this assumption, and adopting the relationship between thermal radio emission and star-formation rate by Murphy et al. (2011) for an HII region electron temperature of $T_e = 10^4\,K$, we would infer a SFR$\sim 4000\,M_{\odot}\,\mathrm{yr}^{-1}$ from the 3 GHz continuum flux, with large uncertainties due to assuming a thermal versus non-thermal fraction.

7.7.5 Star-forming gas properties

Low-J CO line luminosities are expected to provide a reliable estimate of the molecular gas mass (e.g., Bolatto et al. 2013). Here, we assume a brightness temperature ratio of $R_{21} = 1$ between the CO J=2–1 and 1–0 lines, due to the moderately high inferred dust temperature of CRLE (Table 7.3).[4] Another effect which may be relevant to the interpretation of the observed CO line flux is contrast against the warmer CMB, and the additional gas heating this provides at $z > 5$ (da Cunha et al., 2013c). While the effect this may introduce is difficult to estimate without additional CO excitation constraints, da Cunha et al. (2013c) suggest that for warm gas kinetic temperatures, and moderately high gas densities we may expect the observed CO line flux to be suppressed by ~0.5–0.8, at this

[4]Previous samples of DSFGs at lower redshift show nearly thermalized gas excitation up to the J=2–1 transition, justifying our assumption ($R_{21} \sim 0.85 - 0.95$; e.g., Carilli & Walter 2013).

redshift. We do not attempt to estimate a correction factor for this effect, but include it into the definition of $\alpha_{\rm CO}$ instead (i.e., a larger CMB correction would imply a higher $\alpha_{\rm CO}$). By assuming the dynamical mass to be completely accounted for by molecular gas, we can derive a conservative upper limit on the CO conversion factor of $\alpha_{\rm CO} < 2.1 \pm 0.6\, M_\odot\,(\mathrm{K\,km\,s^{-1}\,pc^2})^{-1}$. This conversion factor is conservative, because it does not include the stellar contribution to the dynamical mass. Our stellar mass estimate is too uncertain to provide a useful constraint in this context. Such low conversion factors are typically only observed in highly metal-enriched galaxies, which appears to suggest that metallicity is not a major source of uncertainty in the interpretation of line ratios (Bolatto et al., 2013). Furthermore, from the dust mass estimates presented in Section 4.2, we can adopt a gas-to-dust ratio in order to derive an independent estimate of $\alpha_{\rm CO}$. The gas-to-dust ratio may be assumed to follow the same dependence on metallicity as measured at lower redshift. Here, we follow Magdis et al. (2011b) by adopting a super-solar metallicity, expressed as 12+log(O/H), between 8.8 and 9.2. This implies a gas-to-dust mass ratio of 35–75, which is consistent with an average value for DSFGs of ~ 50 (Santini et al., 2010). This range implies a range of $\alpha_{\rm CO}$ from $0.65{\pm}0.16\, M_\odot\,(\mathrm{K\,km\,s^{-1}\,pc^2})^{-1}$ to $1.4{\pm}0.3\, M_\odot\,(\mathrm{K\,km\,s^{-1}\,pc^2})^{-1}$. These ranges are consistent with expectations from local ULIRGs, for which a conversion factor of $\alpha_{\rm CO} \sim 0.8\, M_\odot\,(\mathrm{K\,km\,s^{-1}\,pc^2})^{-1}$ was estimated (Downes & Solomon, 1998). In the following we adopt a conversion factor of $\alpha_{\rm CO} = 1\, M_\odot\,(\mathrm{K\,km\,s^{-1}\,pc^2})^{-1}$, which provides a conservative estimate of the molecular gas mass in CRLE[5]. We thus derive a total molecular gas mass of $M_{\rm gas} = (7.0 \pm 0.5) \times 10^{10}\, M_\odot$, corresponding to $\sim 50\%{\pm}15\%$ of the dynamical mass estimate. This gas mass estimate is similar to

[5]We note that there remain substantial systematic uncertainties regarding the appropriate CO conversion factor for high redshift DSFGs, as well as for local ULIRGs (e.g., Scoville et al. 2016, 2017b). Previous assumptions of $\alpha_{\rm CO}$ may also affect the adopted gas-to-dust ratios, and may therefore be partly responsible for the apparent consistency of our estimates.

the gas masses of other $z > 5$ DSFGs such as AzTEC-3 (~$5.3\times10^{10}\,M_{\odot}$) and HFLS3 (~$4.5\times10^{10}\,M_{\odot}$; Riechers et al. 2010b, 2013; Cooray et al. 2014). Our inferred $\alpha_{\rm CO}$ is compatible with model predictions by Vallini et al. (2018) at $z \sim 6$, which suggest $\alpha_{\rm CO} = (1.5 \pm 0.9)\,M_{\odot}\,({\rm K\,km\,s^{-1}\,pc^{2}})^{-1}$, despite the sub-solar metallicity of their simulated galaxy. They interpret this low conversion factor as the result of the high density and high turbulence in the molecular gas of their simulated galaxy. The measured [CII]/CO(2–1) line ratio in CRLE is also compatible with their model predictions, although we caution that their simulated galaxy targets the "normal" star-forming population with a star formation rate over an order of magnitude lower than CRLE (Vallini et al., 2018).

We also use single-wavelength, dust continuum emission measurements on the Rayleigh-Jeans tail to explore alternative methods to estimate the ISM mass of CRLE. Using the the rest-frame 205 μm and 1.3 mm observations, we follow Scoville et al. (2016, 2017a) to estimate total ISM masses of $1.1\times10^{12}\,M_{\odot}$ and $8.0\times10^{11}\,M_{\odot}$, respectively. This method was calibrated at a rest-frame wavelength of 850 μm, hence the latter estimate is expected to be more reliable, since the extrapolation is smaller. We also use rest-frame 500 and 250 μm fluxes in CRLE to infer a gas mass following Groves et al. (2015). The rest-frame 500 and 250 μm fluxes are estimated from our best-fitting modified black body model, and imply gas masses of $1.3\times10^{12}\,M_{\odot}$ and $2.4\times10^{11}\,M_{\odot}$, respectively. Therefore, these dust-based methods would imply very large ISM masses, exceeding our dynamical mass estimate and suggesting that hotter dust temperatures may affect these techniques making them less reliable for this type of high-redshift galaxy (e.g., Scoville et al. 2015).

Adopting the relationship between CO luminosity and star formation rate

(i.e., the star formation law) for local starburst galaxies (Kennicutt, 1998a; Carilli & Walter, 2013), we can convert the measured $L'_{\rm CO}$ to an IR luminosity of $L_{\rm IR} = 1.3 \times 10^{13}\,L_{\odot}$ with large uncertainties (the scatter of this relationship is a factor ~ 2.5). This is consistent with our measured IR luminosity, although apparently at the low end of the confidence interval. By adopting the fiducial values for the star formation rate and the molecular gas mass we derive a gas depletion time scale of 45 ± 4 Myr, which is comparable to estimates for other $z > 5$ DSFGs such as AzTEC-3 (~50 Myr) and HFLS3 (~36 Myr) (Riechers et al., 2010b, 2013, 2014a).

7.7.6 Merger stage of CRLE

As shown in Section 4.2, the dust SED in CRLE appears to be intermediate between those of other $z > 5$ DSFGs such as AzTEC-3 and ADFS-27 (Fig. 7.7; Riechers et al. 2010b, 2014a, 2017). A possible interpretation of these differences in the dust properties (e.g., temperature or optical depth) among these galaxies involves the merger stage. In particular, AzTEC-3 appears to be a dispersion dominated starburst with an exceptionally compact central density profile which is suggestive of a late stage merger, after coalescence (Riechers et al., in prep.). On the other hand, ADFS-27 is an interacting galaxy pair, where the individual galaxies are separated by just 9 kpc, and therefore may represent an early merger stage (Riechers et al., 2017). In the next section, we carry out dynamical modeling of the [CII] emission, which suggests that a simple rotating disk model does not provide a good fit to CRLE. This conclusion is also supported by the asymmetric profile visible in the line spectra (Fig. 7.2). We find evidence for a second dynamical component, which may suggest an overall dispersion dom-

inated system. This evidence appears to suggest an ongoing merger in CRLE, with a component separation of 2.0 ± 0.4 kpc (from the [CII] emission modeling). Therefore, we tentatively interpret the intermediate SED in CRLE as a reflection of its merger stage. However, the SED in CRLE also resembles that in GN20, which shows a coherently rotating massive gas disk and shows no evidence for a galaxy merger (Hodge et al., 2012).

7.8 Dynamical modeling

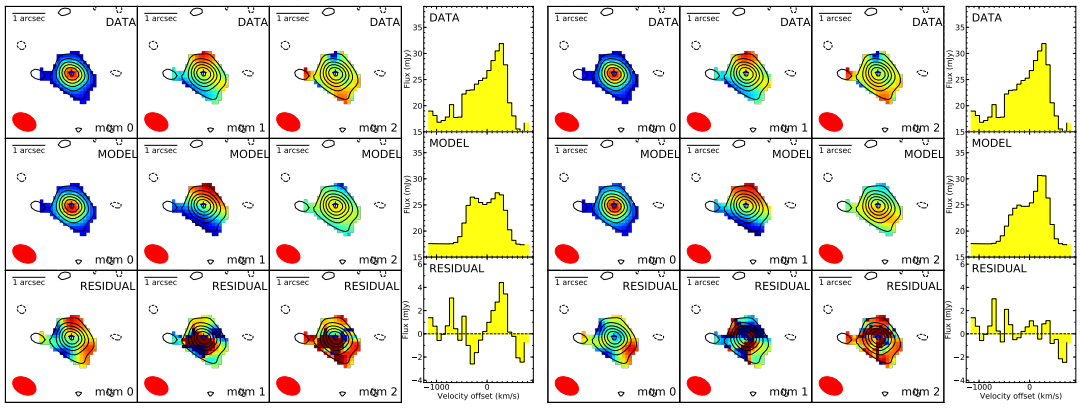

Figure 7.8: Visibility space dynamical modeling results for the [CII] line emission in CRLE. We show the "natural" weighting line moment 0 (intensity), 1 (velocity) and 2 (dispersion) maps and spectra for the data, the model, and the visibility residuals. Left: One component rotating disk model. Right: Two component model, with a spatially unresolved second dynamical component. Although a one component model provides an acceptable fit, the residuals show clear spectral structure, and the moment-2 map shows spatial structure hinting to a different dynamical component to the north. The residuals are significantly improved by the addition of a second model component, perhaps suggesting an ongoing galaxy merger.

In order to extract the most precise physical parameters for CRLE, we analyze the [CII] line data, which have the highest signal-to-noise ratio and angular resolution, by dynamical model fitting.

Table 7.4: Results of one- and two-component dynamical modeling.

Parameter (Units)	One component			Two component		
	16th perc.	50th perc.	84th perc.	16th perc.	50th perc.	84th perc.
Gas dispersion (km s^{-1})	98	105	112	118	129	141
Emission FWHM (arcsec)	0.43	0.45	0.47	0.68	0.71	0.75
Maximum velocity (km s^{-1})	640	800	1100	413	435	470
Velocity scale length (arcsec)	0.010	0.012	0.015	0.014	0.026	0.053
Inclination (degrees)	20	28	36	57	60	64
Position angle (degrees)	110	114	117	93	96	99
Continuum major FWHM (arcsec)	0.42	0.43	0.44	0.42	0.43	0.44
Continuum minor FWHM (arcsec)	0.26	0.27	0.29	0.26	0.27	0.29
Second component velocity FWHM (km s^{-1})	—	—	—	250	270	290

We have developed a novel implementation of dynamical model fitting, working directly on the visibilities. Carrying out the model comparison to data in the UV space, rather than in the image plane, makes our method independent of deconvolution and of choice of visibility weighting, and hence more robust. Furthermore, our method takes advantage of the well-behaved (i.e., independent and normally distributed) noise properties of measured visibilities, in comparison to the correlated noise affecting interferometric images.

Our method has general applicability for interferometric data with frequency structure, and is based on a Bayesian formulation of the model fitting problem. We use Markov Chain Monte Carlo (MCMC) and Nested Sampling techniques in the form of *emcee* (Foreman-Mackey et al., 2013) and *MultiNest* for `python` (Feroz et al., 2009; Buchner et al., 2014) to sample the posterior distribution for the model parameters, and to evaluate the model evidence (also called marginal likelihood), i.e., the integral of the posterior which gives the probability of the model given the data. We have verified that the parameter estimates derived from the samples produced by the two different techniques are well within the range of compatibility.

The first model fit to CRLE [CII] is a rotating disk model, generated through the publicly available code *KinMSpy* (Davis et al., 2013), superposed onto an el-

liptical 2D Gaussian continuum model. We choose this model to be described by disk center coordinates, systemic velocity, gas dispersion, FWHM size of the spatial light profile of the disk (assumed to be 2D Gaussian), maximum velocity and velocity scale length, inclination, position angle and line flux. The continuum flux and FWHM sizes of the continuum emission were separately fixed by fitting the line-free channels. We impose non-constraining priors. We choose uniform priors for additive parameters, logarithmic priors for scale parameters, and a sine prior for the inclination angle. The 1σ confidence intervals of the physically relevant parameters derived from our modeling are shown in Table 7.4, and the median model fit and the residuals are shown in Fig. 7.8.

Clear structure is visible in the single component model residuals by adopting median parameters, particularly in the spectrum, although the total residual flux has formally a low significance (Fig. 7.8). We explore a second model, with five additional parameters describing a second, unresolved component, which is designed to capture the narrow velocity component visible in the spectra and in the dispersion map. The additional parameters describe the second component center x and y coordinates, systemic velocity, integrated flux and line velocity width. As Fig. 7.8 shows, the model fit is significantly improved by this additional component. We characterize the improvement to the quality of the model fit achieved by the addition of the second component by the model evidence ratio evaluated through *MultiNest* of $e^{86} \sim 10^{37}$, which takes into account the additional parameter space available to the more general model. Therefore, we conclude that a single component rotating disk model is not sufficient to describe the [CII] emission in CRLE, and we find, instead, strong indication for a second component corresponding to the narrow line emission component also observed in the CO and [NII] lines. Higher resolution observations are required

in order to determine if coherent rotation may be important to the gas dynamics in this system, or whether the dynamics are dispersion dominated. The latter would provide stronger evidence in favor of a merging pair of galaxies, perhaps identified by the two separate dynamical components. However, strong shocks and winds may also be responsible for skewing the velocity profile, and could therefore contribute to the observed dynamics.

7.9 Galaxy Overdensity around CRLE

7.9.1 Overdensity characterization

The close association in the sky and in redshift space to HZ10 (z = 5.654, 13″ distance, corresponding to only 77 kpc, in projection and $\sim$ 580 km s^{-1} of relative radial velocity) suggests that CRLE may be located in an overdense galaxy environment. We follow the procedure described in Smolčić et al. (2017b) to evaluate a potential galaxy overdensity around CRLE. First, we analyze the small scale overdensity, around the DSFG in the COSMOS2015 catalog, making use of the photometric redshift information, as detailed in Smolčić et al. (2017b). Then, we apply a similar technique to also investigate the galaxy overdensity in the Lyman Alpha Emitter (LAE) catalog at $z \sim 5.7$, which may offer a higher accuracy in the redshift range selected (Murayama et al., 2007).

We do not apply the magnitude cut i^+ <25.5 of Smolčić et al. (2017b), because the i^+ magnitude of HZ10 is 26.45, which we know to have a redshift in the correct range. Based on the magnitude of HZ10, we also expect that even massive galaxies at this high redshift are likely to have an i^+ magnitude below

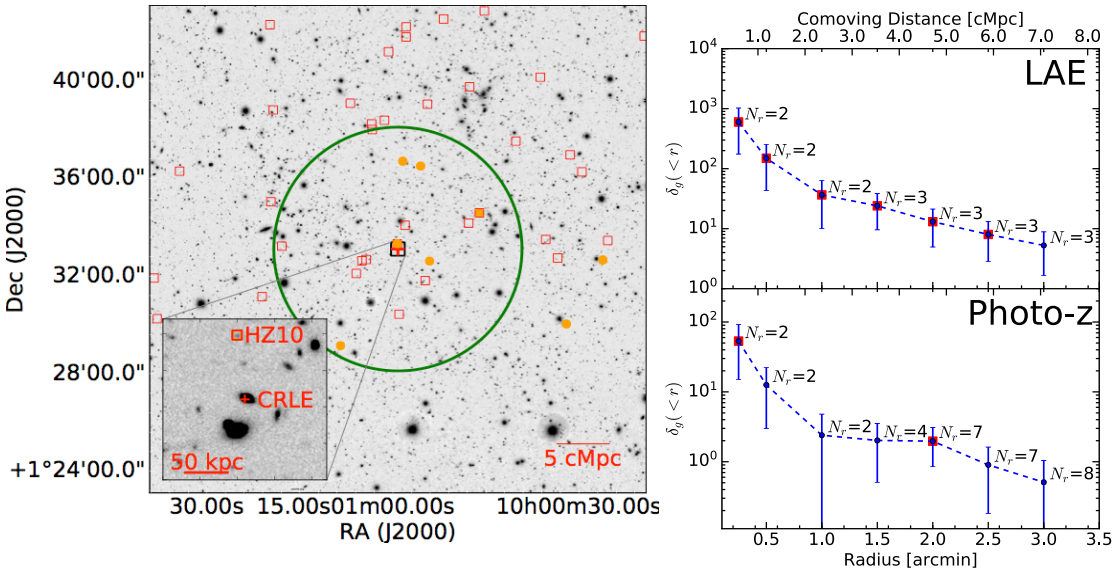

Figure 7.9: Left: Galaxy overdensity around CRLE (red cross), in the two galaxy catalogs considered. The grayscale shows the narrow-band Subaru/Suprime-Cam NB816 mosaic. Orange dots represent the position of Lyman Alpha Emitters (LAE; Murayama et al. 2007), and red squares represent galaxies from the photometric redshift catalog at the same redshift as CRLE (Laigle et al., 2016). The radius of the green circle is 5′, which corresponds to ∼ 12 cMpc. The inset shows the central 33″ of the image, showing the relative positions of CRLE (behind a foreground galaxy) and HZ10, to the north. Right: Overdensity parameter (δ_g) as a function of radius around CRLE, evaluated for the LAE (top) and the photometric redshift catalogs (bottom) following Smolčić et al. (2017b). We show the cumulative number of galaxies within the specified radius. Red squares indicate a significant overdensity, with a false positive rate below 5%.

the adopted threshold of Smolčić et al. (2017b). On the other hand, our choice to include fainter galaxies may limit the photometric redshift accuracy. We adopt their choice of redshift binning, which implies a photo-z range of $\Delta z = 0.64$ for the catalog "slice". Following Smolčić et al. (2017b) we define a galaxy overdensity parameter by $\delta_g(r) = \frac{N_r}{\Sigma_{\rm bg}\pi r^2} - 1$, where N_r is the number of galaxies in the catalog within a radius r of the DSFG (including the DSFG, itself), and $\Sigma_{\rm bg}$ is the mean galaxy surface density in the redshift "slice". We take into account masked regions when evaluating the surface area. We evaluate the overden-

sity parameter around CRLE, at radii of 0.25′ (to capture the overdensity due to HZ10 alone) and 0.5′ to 3′, in steps of 0.5′ in both the photometric redshift and LAE catalogs (Figure 7.9).

In order to evaluate the significance of the measured overdensity parameter values, we follow the procedure by Smolčić et al. (2017b), producing 10 mock random catalogs adopting the same masked regions with the same number of galaxies as the real ones, and measuring the overdensity around 1000 randomly placed centers. The rate of chance occurrence of the actual N_r profile (equivalently, of the overdensity parameter) can then be evaluated. We mark significantly over-dense radii by square markers in Figure 7.9, adopting the same 5% false-positive rate as Smolčić et al. (2017b).

In the COSMOS2015 photometric redshift catalog, we find that HZ10, due to its very close separation, constitutes a significant overdensity of > 50, and that at a radius of 2′, there is only a 1% probability of the observed overdensity (7 galaxies; corresponding to $\delta_g \sim 2-3$) to be produced by chance. The chance probability of at least one neighbor within 0.5′ is only 12% (the nearest, HZ10, is at 0.216′). This chance probability is comparable to that of having at least two neighbors within 1.05′ (i.e., the separation to the next galaxy) or of having at least three neighbors within 1.5′ (the following galaxy). In the LAE catalog, the overdensity is even more significant, due to the lower contamination from galaxies at incorrect redshifts. We find a significant overdensity at all radii up to 2.5′, with HZ10 already implying an overdensity of > 500 and, a second LAE within 1.5′ constituting an overdensity of ~ 30. The overdensity in the LAE catalog at a radius of 5′, including a total of 7 galaxies, is also > 4.

We also explore the second technique utilized by Smolčić et al. (2017b) in

order to study the larger scale overdensity. However, we are limited to scales of 4–5′ in the LAE catalog and 3′ in the photometric redshift catalog since CRLE is close to the southern edge of the catalog. This method utilizes a Voronoi tessellation analysis (VTA) in order to identify over-dense regions, and then determines an overdensity center by evaluating a barycenter for the "region". It then evaluates the significance of the overdensity parameter value as a function of radius around this newly found center. The VTA analysis in the case of CRLE indicates that, in both the photometric redshift and LAE catalogs, CRLE and HZ10 are in an over-dense region (i.e., above the 80th percentile of a randomized galaxy density distribution), due to the close proximity to the next galaxy neighbors. The overdensity center is evaluated to be approximately the mid-point between CRLE and HZ10. Because the overdensity center is close to CRLE, the overdensity evaluation for this method reproduces similar results to those of our previous analysis.

Four galaxies (all part of the LAE catalog) within 5′ have a spectroscopic redshift that place them in the overdensity (5.665, 5.674, 5.688, and HZ10 at 5.659 from Keck/DEIMOS, Capak et al., in prep.). The other two LAEs within this radius, have no known spectroscopic redshifts[6]. Of the four LAEs with spectroscopic redshift confirmation, two (including HZ10) are also part of the photometric redshift sample. No other photometric redshift candidates within 5′ have a spectroscopic redshift. If we expand the search radius to 17′, corresponding to 40 cMpc in the spectroscopic redshift catalog, we find 4 more galaxies with spectroscopic redshift between 5.5 and 6, which may potentially be part of the same overdensity (with spectroscopic redshifts of 5.682, 5.728, 5.663, 5.742).

[6]One of them, the closest LAE after HZ10, has an incorrect photometric redshift of 0.7688, the other one is not in the photometric catalog.

7.9.2 Discussion of the overdensity significance

Here we compare the galaxy overdensity around CRLE, with the cases of AzTEC-3 and other lower-redshift DSFGs (e.g., Walter et al. 2012; Smolčić et al. 2017b; Oteo et al. 2017b), with LAE overdensities at $z > 5$ (Higuchi et al., 2018), and in relation to theoretical expectations (e.g., Chiang et al. 2013, 2017).

The closest analog to the galaxy overdensity around CRLE is the protocluster around AzTEC-3 at $z = 5.3$, which is also located in the COSMOS field (Capak et al., 2011; Riechers et al., 2010b, 2014a). The close proximity of the "normal" LAE/LBG HZ10 to CRLE ($\sim$ 77 kpc away) is comparable to the close separation between the luminous DSFG AzTEC-3 and the "normal" galaxy LBG-1 ($\sim$ 95 kpc away; Riechers et al. 2014a). Capak et al. (2011) report a rich galaxy overdensity around AzTEC-3 with an overdensity parameter of $\gtrsim 11$ within a 2 cMpc radius. We also detect a comparable overdensity of LAEs of $\delta_g \gtrsim 10$ within a radius of $\sim$ 5 cMpc of CRLE. Because of the higher redshift of CRLE ($z \sim 5.667$) than AzTEC-3 ($z \sim 5.298$), catalogs contain significantly fewer galaxies. The overdensity is therefore associated with a smaller number of galaxies, and hence, is subject to larger uncertainties from random fluctuations. The "normal", "companion" galaxies LBG-1 and HZ10 are similar in terms of their stellar masses and UV luminosities, but the FIR luminosity in HZ10 is almost an order of magnitude higher, suggesting that the ISM in HZ10 may by substantially more enriched (Capak et al. 2015; Pavesi et al. 2016). Furthermore, the [CII]/[NII] ratio appears to suggest that the metallicity of HZ10 is compatible with local and high redshift starburst galaxies, while it suggests a lower metallicity for LBG-1 (Pavesi et al., 2016). The overdense environment experienced by HZ10 may be partly responsible for the particularly enriched ISM state in this

"normal" galaxy. In particular, it is possible that metal enriched material that was ejected by CRLE may have been accreted by HZ10. Also, it is likely that the local dark matter overdensity, as suggested by the galaxy overdensity, may be responsible for the early galaxy growth, by providing abundant gas fueling to the central regions. However, LBG-1 seems to be located in a similar environment and does not display a comparable level of enrichment. Capak et al. (2011) estimate that the dynamical time for LBG-1 to reach AzTEC-3 may be of order $\sim$ 0.5 Gyr, providing several dynamical times for a merger to occur by $z \sim 2$. A similar estimate applies to HZ10 and its likely eventual merger with CRLE, which may produce a central cluster galaxy.

Smolčić et al. (2017b) analyzed galaxy overdensities around previously known DSFGs in the COSMOS field at $z \sim 1 - 5.3$ and found an incidence of approximately $\sim 50\%$ when using similar methods to the ones employed here. They tentatively found a higher occurrence of DSFGs occupying overdense environments at $z > 3$, than at $z < 3$. This would be compatible with our finding of a high galaxy overdensity including CRLE at $z \sim 5.7$. A higher incidence of overdensities associated with the highest redshift DSFGs would be consistent with the idea that these massive galaxies may be associated with the highest peaks of the density field, tracing the most massive dark matter haloes at early cosmic epochs (e.g., Springel et al. 2005; Li et al. 2007; Overzier et al. 2009; Capak et al. 2011).

Recent observations with the Hyper-Suprime Cam on the Subaru telescope have yielded a deeper and wider catalog of LAEs in COSMOS at $z \sim 5.7$ than available for our analysis (Ouchi et al., 2017; Shibuya et al., 2017). These authors report numerous LAE overdensities at this redshift, showing that a significant

fraction of star forming galaxies at this epoch may be part of proto-cluster environments (Higuchi et al., 2018). In particular, these authors report an overdensity, HSC-z6PCC5, in the COSMOS field, with an overdensity parameter of $\delta \sim 10$. The reported overdensity center is located 44 cMpc away from CRLE, and at a redshift of $z = 5.686$, corresponding to only 9 cMpc of radial separation. It is therefore possible that CRLE, and its associated small scale galaxy overdensity, may also be associated with this significantly larger scale early cosmic structure.

Recent theoretical work suggests that proto-clusters may have dominated star formation in the first two billion years of cosmic time (Chiang et al., 2013, 2017). This is due to the fact that the fraction of the cosmic volume occupied by all future (proto)clusters increases by nearly three orders of magnitude from $z = 0$ to $z = 7$. More importantly, most models suggest that early galaxy formation may be dominated by the central regions of the most massive overdensities, and that star formation may evolve inside-out to galaxies in lower density environments (Chiang et al., 2017). These may be crucial predictions of structure formation in the early Universe. A quantification of the fraction of star formation in different environments as a function of cosmic time may be an important cosmological probe in the era of wide-area surveys. The physical processes associated with the "central" galaxy forming in a proto-cluster, which may be a DSFG at least during part of its life, may strongly affect the evolution of such proto-clusters, both by enriching the intra-cluster medium and by providing energy input through winds and radiation.

7.10 Conclusions

We have reported the serendipitous discovery of the bright, dusty, starbursting galaxy CRLE at $z = 5.667$ in the first billion years of cosmic time. This galaxy represents the highest redshift and brightest DSFG in the COSMOS field known to date, providing a higher redshift and brighter analog to the $z = 5.3$ massive starburst AzTEC-3. We report the detection of [CII], [NII], and CO(2–1) line emission, and we find properties that are common among the highest redshift DSFGs. CRLE displays a large molecular gas reservoir ($\sim 7 \times 10^{10}\,M_{\odot}$), a short gas depletion time scale of order ~ 50 Myr characterizing the intense starburst, and a high-intensity radiation field, as evidenced by a deep [CII] deficit. We find evidence for a significant fraction of the [CII] emission to be coming from ionized gas, similar to other high-redshift DSFGs. We suggest that this emission may be coming from a diffuse ionized medium not directly associated with the dense star-forming gas. We find dynamical evidence and dust emission properties consistent with an intermediate-stage merger. The physical proximity of the previously known "normal" Lyman Alpha Emitter (LAE) HZ10 to CRLE constitutes a high overdensity, and suggests that these two galaxies may coalesce in the future, forming a massive central cluster galaxy. We find further evidence for a galaxy overdensity, using both photometric redshift and LAE catalogs, which indicates the location of a likely proto-cluster analogous to the case of AzTEC-3. The presence of this likely proto-cluster supports the idea that such bright, extremely early starburst galaxies may commonly be associated with the most massive dark matter halos in the Universe at their respective epochs, providing the earliest sites of star formation of the most massive central cluster galaxies that we observe in the local Universe.

CHAPTER 8

SUMMARY AND OUTLOOK

8.1 Summary

In this thesis, we have used millimeter and Far-IR tracers of the interstellar medium to study the conditions of star formation in galaxies up to the first billion years of cosmic time. We have carried out the first unbiased, statistical survey of cold molecular gas at the peak cosmic epoch of star formation to better understand what is driving the observed intense rate of stellar mass growth. Our main result is a highly significant evolution in the shape of the cold gas mass function at $z = 2-3$, relative to previous determinations at $z \sim 0$. This measured evolution implies a considerable abundance of gas-rich galaxies (with gas masses an order of magnitude higher than in the local Universe) which are the sites of intense star formation. Through our search, we have not found any massive, gas-rich galaxies with very low star formation activity, although several of the galaxies in our sample appear to have lower star formation efficiency per unit gas mass, relative to traditional samples selected through sub-millimeter emission. The most gas-rich galaxies in our CO(1–0) sample (constituting a high fraction of the overall sample, at least 3 out of 5) are mergers of galaxies, with extended molecular gas reservoirs suggesting that mergers may host the most massive molecular gas reservoirs at high redshift. By stacking our data at the position and frequency of expected CO(1–0) emission from known galaxies with spectroscopic redshifts, we can push the sensitivity limits of our survey and look for emission from fainter galaxies. We detect a faint average CO line signal from a sample of 34 massive galaxies ($M_* > 10^{10}\,M_\odot$), which implies ~ 3–6 times lower

gas mass fractions than expected based on previous estimates for MS galaxies. This finding challenges our current understanding, and points the way to much deeper observations to explore the gas content and physical state of more typical galaxies. A possible caveat to such estimates comes from potential evolution in the CO conversion factor, and might suggest perhaps lower metallicity or a higher fraction of CO-dark molecular gas in Main Sequence galaxies at $z > 2$. Our analysis of the comparison between the cosmic gas density history and the star formation history shows that our constraints are compatible with a weak redshift dependence of the average star formation efficiency, with a possible increase in global efficiency toward higher redshift but likely ruling out major redshift evolution.

The COLDz survey also explored molecular gas content at $z \sim 5 - 7$ for the first time, by covering the CO(2–1) transition at those redshifts. Indeed, three of our secure CO detections belong to this high redshift bin. The non-targeted detection of two galaxies in this redshift bin in our wide field in GOODS-N suggests a significantly higher volume density than predicted by the latest models. The inferred volume density at the high gas masses is only slightly lower than our measurement at $z \sim 2 - 3$, suggesting a tantalizing lack of evolution at the high mass end between $z \sim 5$ and $z \sim 2$. In order to further study the evolution of the star-forming conditions at $z > 5$, we have carried out targeted measurements of the CO(2–1) luminosity in two "normal" galaxies, already finding a variety of conditions in this small sample. These are the deepest constraints at these redshifts, and by far the highest redshift detection of low-J CO emission from a normal galaxy, to date. One of the two galaxies hosts a massive molecular gas reservoir, traced by luminous CO emission, and suggests that star formation may proceed with the low efficiency which is similar to lower redshift, Main

Sequence disk galaxies. This finding is surprising and novel, because the very high inferred gas mass (perhaps up to an order of magnitude greater than the stellar mass) and the high expected degree of turbulence due to intense accretion in the first billion years of cosmic time might suggest more efficient star forming conditions, with shorter timescales for star formation in such early galaxies. On the other hand, the other target galaxy shows a deficiency of CO emission relative to its [CII] luminosity, which is indicative of low metallicity gas. This finding makes it difficult to infer a molecular gas mass from the CO luminosity because it requires the $\alpha_{\rm CO}$ conversion factor to be reassessed. Using atomic fine-structure line tracers we have investigated the relative importance of different phases of the ISM in "normal" galaxies on the star-forming Main Sequence. This provides the first constraints to the physical state of the ISM in what could be a completely different population of galaxies. That analysis has shown that low metallicity may be responsible for the observed evolution in ISM conditions at $z > 5$, accompanied and perhaps causing, a harder and more intense radiation field. Although lower metallicity may be expected at some point at high redshift because fewer stars have formed and had sufficient time to enrich the ISM with products of nuclear fusion, massive galaxies at the peak epoch of cosmic star formation ($z \sim 2$) typically appear to have metallicities compatible with solar. The latter observation is typically interpreted as evidence that galaxies which are already massive at redshift ~ 2 formed a large fraction of their final stellar mass at even higher redshift. However, our observations at $z > 5$ have found that massive galaxies in the first billion years of cosmic time may be forming their first generations of stars or, alternatively, that their ISM may be dominated by freshly accreted, pristine gas from the IGM. The latter interpretation is particularly interesting and may provide some of the first evidence for what is driving

the unprecedented early growth phase of galaxies observed in the first billion years of cosmic time (e.g., Faisst et al. 2016b). This brief summary of our conclusions was selected as representative of some of our most novel findings. They extend the reach of star-forming ISM studies by exploiting each of the most common, and best understood probes to some of the furthest regions of parameter space accessible by the latest telescopes. These results have been uniquely enabled by the latest technology powering such groundbreaking observatories as the upgraded VLA and ALMA.

8.2 Outlook

Future efforts can pursue multiple avenues in order to clarify and extend our findings, however they will require substantial investment of observing time and the development of entirely new facilities due to high sensitivity requirements to study "normal" galaxies.

In the immediate future, it is necessary to explore the physical gas properties of the first CO(1–0)-selected galaxies in greater detail with ALMA. Measurements of the CO excitation ladder in these galaxies are important not only to constrain the gas density and kinetic temperature in "normal" gas-rich galaxies, but also because they will inform the relationship between CO(1–0) and mid-J CO deep fields, which ALMA now routinely enables. In the medium term, larger samples of CO(1–0)-selected galaxies are needed in order to improve the statistical value of our luminosity function constraints. Although ALMA has higher sensitivity than the VLA, mid-J CO surveys in the 3 mm band have a low rate of $z > 2$ detections. In particular, VLA deep fields with comparable

sensitivity as the COLDz observations in the COSMOS field appear to yield the highest rate of discovered galaxies per observing hour. Larger samples will not only allow reducing the uncertainties on the luminosity function constraints, but will also strengthen the constraints on the abundance of gas-rich, low star formation galaxies which have not been detected to date. Stacking allowed us to derive puzzling constraints on the CO luminosity of "typical" MS galaxies at the peak epoch of star formation, suggesting that either their CO luminosity per unit gas mass might be significantly reduced (pointing to lower metallicity), or that they might be less gas-rich than their massive counterparts. However, deeper observations are needed targeting each line individually to clarify the origin of the low stacked luminosity. In particular, larger CO(1–0) samples of spectroscopically confirmed optical galaxies as well as low-luminosity sub-mm selected galaxies are necessary to accurately infer the star forming gas properties in normal galaxies. Similarly, constraints to the abundance of lower CO luminosity galaxies (i.e., the faint end of the luminosity function) need ultra-deep field observations (within the capabilities of the current VLA, although requiring very large observing time investments), which will probe into the lower mass regime where we expect metallicity might affect the CO conversion factor. In addition, targeted observations quantifying the conversion factor at the peak epoch of star formation are necessary and must be carried out through CO(1–0) to remove the contaminating effect of CO excitation. Such measurements of $\alpha_{\rm CO}$ are traditionally carried out partly by comparison to detailed dust emission modeling, and partly through estimates of dynamical masses, which must be accounted for completely by the galaxy mass budget.

Most of these future directions will require hundreds of hours from current and future facilities, just to double current sample sizes. Therefore large sam-

ples (tens to hundreds of CO(1–0) selected galaxies over cosmic time) will only be possible when the next generation of radio telescopes comes online, in future decades. In particular, the next-generation VLA (ngVLA; Carilli et al. 2015; Bolatto et al. 2017) currently represents the most compelling observatory proposal to expand the sensitivity and resolution of the VLA by an order of magnitude in that crucial frequency gap (~10-100 GHz) between ALMA and the Square Kilometer Array (SKA). The ngVLA, which is currently planned to come online in the 2030s, will be able to simultaneously detect CO(1–0) emission over a wide redshift range, with an order of magnitude higher sensitivity than the current VLA due to a similarly higher number of antennas (Selina et al., 2018a). This sensitivity will enable the blind discovery of several low-J CO emitters at high redshift ($z > 1$) every observation hour, allowing to achieve the large samples which are necessary to accurately constrain the luminosity function (Bolatto et al., 2017). However, the main revolution which will be brought forth by the ngVLA will lie in achieving the necessary sensitivity to resolve the CO(1–0) emission over tens of beams across normal galaxy disks at high redshift, corresponding to ~kpc scales, which are typical length-scales of galactic structures, such as spiral arms and giant gas clumps. These resolved CO studies will constrain the gas morphology and dynamics, and will probe the resolved "star formation law" within individual galaxies, identifying the physical factors driving variations in the star formation efficiency in the completely new star forming regime of massive gaseous disks which do not exist in the local Universe (Figure 8.1).

Although the epoch of "cosmic noon" is crucially important, the seeds for such intense activity are the physical processes shaping galaxies earlier on, such as during the epoch of rapid galaxy growth at $z > 4$. In the immediate future,

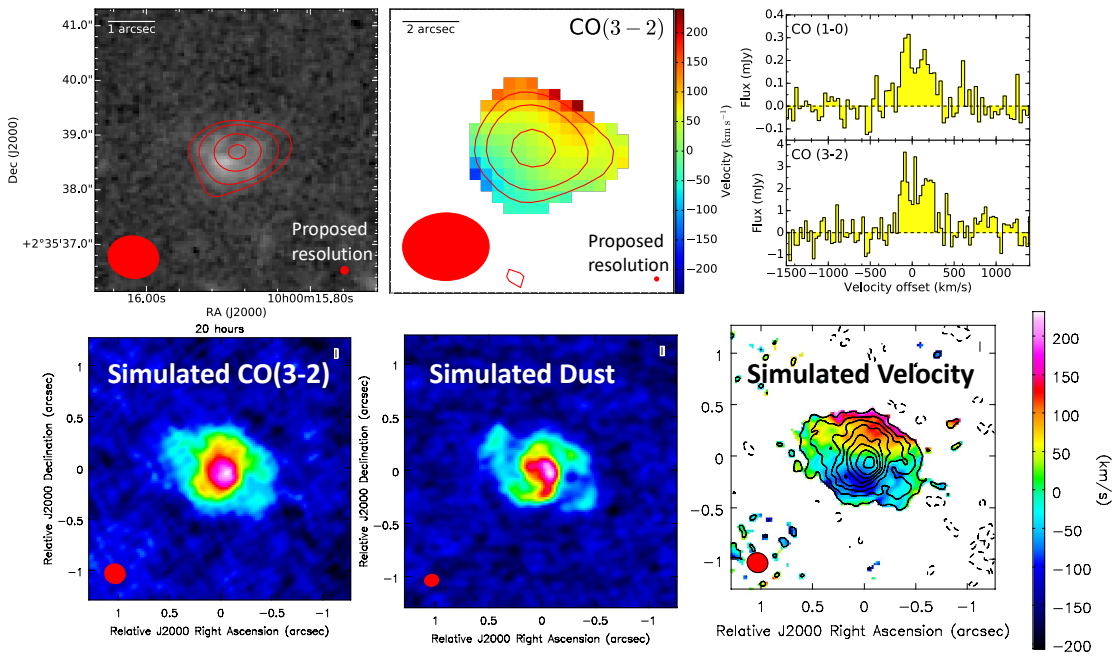

Figure 8.1: (At the top) ALMA detects the dust continuum and the CO(3–2) line emission in a COLDz galaxy, a "normal" gas-rich galaxy at $z \sim 3$. Dust continuum contours for COLDz.COS.1 overlaid on *HST* image showing the stellar mass distribution, and of the inferred gas kinematics shown by CO emission contours overlaid on the CO velocity map. (At the bottom) Simulation of what ALMA can achieve by observing this galaxy with higher sensitivity and resolution (simulated 20 hr on-source observation at 2 kpc resolution). Although the ngVLA will be necessary to carry out resolved CO(1–0) observations in large galaxy samples, ALMA can already investigate the gas morphology and dynamics, by targeting mid-*J* CO lines with sensitive, high resolution observations.

the landscape of star formation in "normal" galaxies at $z > 4$ will be revolutionized by the ALMA Large Program survey ALPINE, which is under way to measure the [CII] and dust continuum emission from a sample of ~120 "normal" galaxies at $4 < z < 6$. The main purpose of such a survey is to establish the statistical significance of our findings from previous, small sample studies. This survey will assess the prevalence of bright dust continuum emitters (similar to HZ10) among "normal" galaxies, i.e., galaxies which resemble lower redshift star-forming disks in which the ISM has been significantly enriched

of dust and metals by previous stellar populations. Characterizing the conditions in the remaining population is also key, as these galaxies appear to display young stellar populations and lower metallicity but little is known about how these conditions affect star formation. The ALPINE survey and higher resolution [CII] followup have the unique capability to measure the gas dynamics at $z > 4$ utilizing dynamical modeling techniques working directly with visibility data such as we have explored in this thesis. These studies will constrain the rotation curves and even the dark matter content of such early galaxies. One of the most useful output of such dynamical mass measurements will be the first accurate estimates of the gas mass content, thereby constraining the star formation efficiency up to the end of the epoch of reionization. Dedicated ALMA measurements at high frequency and complementary radio observations with the VLA (taking advantage of the radio-FIR correlation for star-forming galaxies) will be necessary to measure the dust obscured star formation rate, and to constrain the dust temperature in these galaxies. We have demonstrated that measurements of the [CII]/[NII] ratio provide a useful probe of the metallicity in these galaxies, which ALMA can explore in followup observations in order to explore the correlation with dust obscured star formation, dust temperature, [CII]/FIR ratio and, eventually, CO luminosity. These are all measurements which will require substantial investment of observing time from ALMA and the VLA, but which may be carried out over the next decade or less.

Extensive low-J CO observations at $z > 4$ will be needed to characterize CO as a tracer of molecular gas at such high redshift, and these will be afforded by the ngVLA. In particular, in order to establish CO as a tracer of molecular gas, the CO excitation, the fraction of CO-dark gas and the effect of a warmer CMB on CO emission are all key effects which need to be constrained if progress

is to be made in understanding the evolution of star formation up to the first galaxies. In order to select the best targets for the necessary sample studies with the VLA and ALMA over the next decade, large continuum survey single-dish telescopes such as the Large Millimeter Telescope in synergy with CCAT-p (combining the higher resolution of a 50 m aperture with the high frequency coverage of CCAT-p to extract redshift information) will be necessary. The continuum surveys enabled by such sensitive new observatories will collect large samples of "normal", moderately IR-luminous galaxies at $z > 4$ beyond the confusion limit which limited *Herschel* surveys. In following decades, new generation single-dish telescopes such as the Atacama Large Aperture Submm/mm Telescope (AtLAST) will enable tracing the complete history of dust-obscured star formation all the way to the formation of the first galaxies. In parallel to such continuum surveys, line emission studies will be limited by the available collecting area. In order to infer the clustering properties of the "normal" galaxy population at high redshift, CCAT-p will also carry out the [CII] intensity mapping measurement up to the epoch of reionization (Stacey et al., 2018). This measurement only captures the fluctuations in the average, large scale (~Mpc) [CII] emission field obtained by averaging over many galaxies due to low resolution. This measurement, specifically when compared to expectations for the Dark Matter clustering derived from simulations, will constrain how the [CII] emission tracing gas and star formation relates to different galaxy populations, and over a wide redshift range. Ultimately, achieving the measurement of the complete suite of fine-structure emission lines in large samples of individual high redshift galaxies will provide the physical detail to ISM studies of "normal" galaxies up to the first lights. In order to achieve this ambitious goal, the *Origins Space Telescope* is under design (OST), which will perform sensitive,

wide bandwidth spectroscopy in the Far-IR from space with enough resolution to avoid the confusion limit. The surveys enabled by the OST will measure, among other quantities, the ISM mass, chemical composition and phase breakdown, the age of the recent starburst, the hardness and intensity of the radiation field, the density of the ionized and atomic gas and the gas kinematics up to the earliest galaxies.

In the future, an ever more complete description of the gas components associated with galaxies and their evolution over cosmic time will shine light on the most important processes driving galaxy formation and evolution through star formation. In this thesis we have not discussed the role of black holes to galaxy evolution, but those are also believed to exert their influence to galaxy evolution by injecting energy and momentum into the gas supply of galaxies. Simulations of the physical processes shaping galaxies today are evolving rapidly and will soon successfully capture most large-scale gas processes, perfectly complementing observations in a regime which is difficult to probe (low gas density, ionized components of the galaxy halo and ISM). However, the processes taking place in the high density gas, where physical and chemical reactions take place over widely ranging time scales, and which crucially determine the conditions for star formation, may remain difficult to simulate over galaxy-scales in the near and medium term future. Therefore a better understanding of the gas drivers at the site of star formation, in all possible environmental conditions and over the course of cosmic time, will likely remain a primary focus of observational studies for decades to come if we want to achieve a deeper understanding of how the Universe came to look the way it does.

APPENDIX A

SEARCH FOR NEGATIVE FEATURES IN COLDZ AS POTENTIAL FORMALDEHYDE ABSORPTION

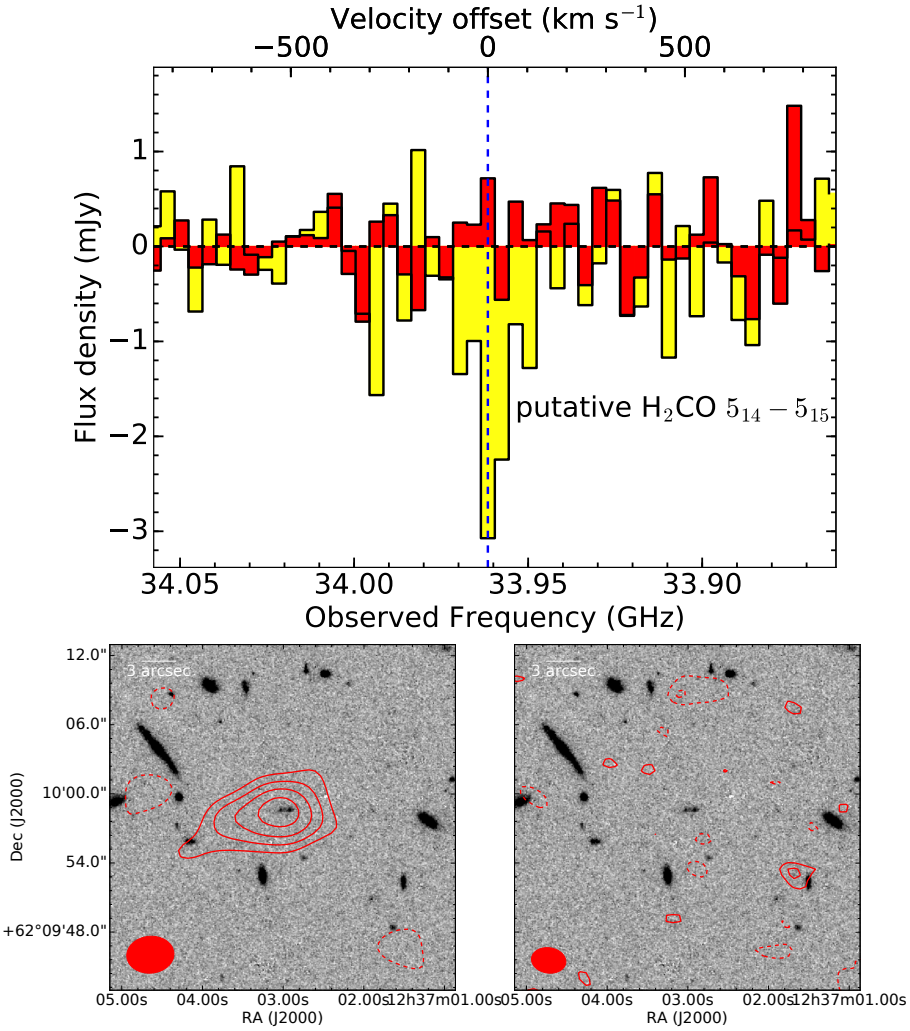

Figure A.1: Top: Aperture spectra of the most significant negative feature in the GOODS-N data in the original data (yellow histogram; where the feature was selected) and in the newer observations (red; pointing GN57). Bottom: The feature, a putative formaldehyde absorption line against the CMB (contours), appeared to be compatible with the 72.4 GHz (5_{14}–5_{15}) line of formaldehyde at the photo-z ~ 1.13 of the galaxies shown in the *HST* H-band image. The left image shows the line map in the original data, the right image shows the same frequency range in the newer data, where the line is not present, which suggests that it was simply due to noise. The contours are shown in steps of 1σ starting from $\pm 2\sigma$ with negative signal as solid contours to show absorption.

A.1 Putative feature

To better understand the characteristics of the noise in our survey data, we have also used our MF3D line searching algorithm to detect negative line features. In order to constrain spurious line features due to noise we take advantage of the symmetry around zero of interferometric noise, in the absence of strong sources in the field. Although negative line features can usually be assumed to be due to noise, line absorption against the uniform CMB has been suggested to be a potential source of such negative lines. In particular, formaldehyde in dense molecular gas in galaxies has been confirmed, at low-z, to have the potential to produce such absorption against the CMB (Zeiger & Darling, 2010; Darling & Zeiger, 2012).

The most significant negative feature in the initial GOODS-N data cube (pointings GN1–GN56) had a high significance of $\sim 6.6\sigma$, and it appeared to be coincident with a pair of local interacting galaxies, GOODS J123702.92+620959.0 with a photo-z of z=1.13 ± 0.05 (Fig. A.1). Intriguingly, the strong absorption feature would be consistent with the 72.4 GHz (5_{14}–5_{15}) line of formaldehyde (H_2CO) at z ~1.13. The energy-level structure of formaldehyde allows collisional population anti-inversion in dense molecular clouds, making the line excitation temperature lower than the CMB temperature and producing absorption against the CMB itself. Formaldehyde silhouettes of galaxies in absorption offer both a novel probe of cosmological size and distance, and a measurement of dense gas masses, density and excitation properties (Darling & Zeiger, 2012). Therefore, in order to investigate the possibility that our most significant negative feature may be a real absorption line against the CMB, we obtained additional VLA data, both at the same frequency (as an additional pointing, GN57

as part of our main survey) and at 22.6 GHz, in order to target the 4_{13}–4_{14} line of formaldehyde. We observed this additional tuning with the VLA K-band (project ID: 15B-370; PI: Pavesi) on 6 November 2015. The observations lasted approximately 3 hours (130 min on source) in D-array configuration, with a spectral setup consisting of a single tuning of the two 1-GHz 8-bit samplers (2 GHz total, dual polarization), with central frequencies of 21.58 GHz and 22.5815 GHz for the two intermediate frequencies (IFs), respectively. The same calibrators were observed as for the main survey observations. We calibrated the data using CASA v.4.5 using the VLA pipeline and minor manual flagging, and we imaged the visibilities using natural weighting. The data cube was produced with 1 MHz channels, corresponding to ~13 km s^{-1}, which is small compared to the expected linewidth. The data cube has a beam size of $4.4'' \times 3.4''$, and an *rms* noise of ~0.2 mJy beam^{-1} in 1 MHz-wide channels.

We did not detect the lower frequency line (Fig. A.2), and the new observations in pointing GN57 at the same frequency do not show any evidence for absorption at the same position and frequency (Fig. A.1). We therefore rule out the presence of an absorption line, and we conclude that the original feature was simply due to noise. By excluding the possibility that the most significant negative feature may correspond to real absorption we strengthen our confidence in the assumption that all (or at least most) negative line features are due to noise, which is crucial for the purity assessment of our positive line candidates.

A.2 H_2CO deep field limits

Our lack of detections of significant formaldehyde absorption lines allows us to place some of the first constraints on the cosmic abundance of such absorption lines. By assuming a line FWHM of 200 km s^{-1}, we derive median 6σ limits (with no negative line candidates found above this threshold) of 0.18 mJy $beam^{-1}$ and 0.55 mJy $beam^{-1}$ for the COSMOS and GOODS-N fields, respectively, corresponding to $\Delta T_{\rm Obs}$ of −0.03 K and −0.11 K, at the average frequency and beam size of our survey. We note that the beam size of our observations ($\sim 3''$) is likely to be larger than the absorbing molecular regions ($\sim 0''.25 - 1''.25$ at $z \sim 1$; Darling & Zeiger 2012), implying a dilution of the expected signal strength due to the beam filling factor of $\sim 0.025 - 0.1$. We use the absence of significant negative detections to infer a probability distribution for their space abundance, by assuming a uniform, uncorrelated distribution of sources over the cosmic volume covered by our survey, and therefore, a Poisson number count. The probability distribution for the space abundance is then an exponential distribution with a mode at zero, and a mean equal to the inverse of the volume sampled (the 68th percentile upper limit to the space density is listed in Table A.1). We use the model results from Darling & Zeiger (2012) to derive, from our $\Delta T_{\rm Obs}$ limit, a constraint on the line optical depth. These models imply that, at $z \sim 1$, the maximal expected temperature decrement with respect to the CMB is $\Delta T_{\rm Obs}/(1 - \exp^{-\tau}) \sim -1.2$ K, for the 5_{14}–5_{15} and 4_{13}–4_{14} lines covered by our survey. This implies limits on the line optical depth of $\tau \lesssim 0.025$ and 0.1 for the COSMOS and GOODS-N fields, respectively. Although these values are comparable to the optical depths previously measured for the lower frequency formaldehyde transitions, our results may be weaker by an order of magnitude

Table A.1: Formaldehyde Lines, Redshift Ranges and Volumes Covered by the COLDz Survey

Transition	ν_0 [GHz]	z_{min}	z_{max}	$\langle z \rangle$	Volume [Mpc^3]	$\Delta T_{\rm Obs}$ limit [K]	Volume density [Mpc^{-3}]
			COSMOS				
4_{13}–4_{14}	48.285	0.24	0.56	0.44	1,850	−0.03	$< 6.2 \times 10^{-4}$
5_{14}–5_{15}	72.409	0.86	1.34	1.12	9,253	−0.03	$< 1.2 \times 10^{-4}$
			GOODS-N				
4_{13}–4_{14}	48.285	0.27	0.61	0.47	13,690	−0.11	$< 8.3 \times 10^{-5}$
5_{14}–5_{15}	72.409	0.90	1.42	1.18	62,329	−0.11	$< 1.8 \times 10^{-5}$

The quoted $\Delta T_{\rm Obs}$ limits correspond to 6σ over a line FWHM of 200 km s^{-1}. The volume density limit represents the 68%-quantile of the probability distribution for the space abundance.

or more, due to the beam filling factor (Mangum et al., 2008; Darling & Zeiger, 2012; Mangum et al., 2013).

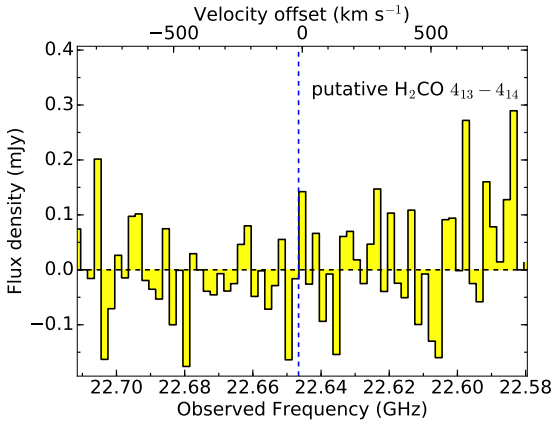

Figure A.2: VLA K-band spectrum at the expected redshifted frequency of the 48.3 GHz 4_{13}–4_{14} line of formaldehyde, at $z \sim 1.13$. If the absorption feature we detected in our original data had been a real formaldehyde absorption line we would expect to detect strong absorption, which is not seen.

APPENDIX B

DESCRIPTION OF THE INDIVIDUAL COLDZ LINE CANDIDATES

In this section, we briefly describe the remaining CO line candidates and potential counterpart associations. These candidates are currently not independently confirmed, and thus, are only used in our statistical analysis. Because we only expect a small fraction of these candidates to correspond to real CO line emission, we advise caution in interpreting these lower significance candidates on a per-source basis until they are independently confirmed. Quoted photometric redshift ranges are the 1σ uncertainties reported in the COSMOS2015 (Laigle et al., 2016) and the CANDELS catalogs (Brammer et al., 2012; Skelton et al., 2014; Momcheva et al., 2016). The positional search radius considered is 3″, which is dictated by the positional uncertainties (which are larger for extended sources) and the possibility of real physical offsets in the stellar emission, e.g., due to differential dust obscuration. The visual counterpart inspection was carried out utilizing *HST* (H-band in GOODS-N and I-band in COSMOS, where H-band was not available) and IRAC 3.6 μm images (band 1), which are shown in Figs. B.1 and B.2. We have also inspected images from the other IRAC bands and find no evidence for additional counterpart matches relative to IRAC band 1.

B.1 COSMOS

COLDz.COS.4: This is the highest signal-to-noise candidate in COSMOS without a secure counterpart. There is a potential match at 0.5″ ± 0.6″ to the NW in the COSMOS2015 catalog, with an uncertain photo-z=1.5–2.3, matching the CO(1–0) redshift of z=2.30. Two I-band and 3.6μm sources are aligned with the

Table B.1: Catalog of the line candidates identified in our analysis which have not been independently confirmed to date. Columns are: (1) Line ID. (2-3) Right ascension and declination (J2000). (4) Central frequency and uncertainty, based on Gaussian fitting. (5) CO(1–0) redshift and uncertainity, unless otherwise noted. (6) Velocity integrated line flux and uncertainty. (7) Line Full Width at Half Maximum (FWHM), as derived from a Gaussian fit. (8) SNR measured by MF3D. (9) Presence of a spatially coincident optical/NIR counterpart (10) Comments.

ID	RA (J2000.0)	Dec (J2000.0)	Frequency [GHz]	Redshift	Flux [Jy km s^{-1}]	FWHM [km s^{-1}]	S/N	Opt/NIR c.part?	Comments
(1)	(2)	(3)	(4)	(5)	(6)	(7)	(8)	(9)	(10)
COSMOS									
COLDz.COS.4	10:00:22.34	+02:34:14.0	34.887 ± 0.007	2.3041 ± 0.0007	0.12 ± 0.04	600 ± 150	5.71	possible	
COLDz.COS.5	10:00:17.63	+02:34:36.0	34.814 ± 0.005	2.3110 ± 0.0005	0.08 ± 0.03	360 ± 100	5.62	N	
COLDz.COS.6	10:00:23.27	+02:34:22.0	31.989 ± 0.003	2.6034 ± 0.0003	0.037 ± 0.013	250 ± 70	5.59	possible	
COLDz.COS.7	10:00:21.60	+02:33:56.0	35.823 ± 0.002	2.2178 ± 0.0002	0.12 ± 0.04	140 ± 40	5.56	possible?	extended
COLDz.COS.8	10:00:25.07	+02:35:56.0	35.291 ± 0.004	2.2663 ± 0.0004	0.24 ± 0.09	250 ± 70	5.56	N	extended
COLDz.COS.9	10:00:22.44	+02:36:16.0	36.593 ± 0.003	2.1501 ± 0.0003	0.13 ± 0.04	220 ± 50	5.57	N	extended
COLDz.COS.10	10:00:23.44	+02:36:29.0	34.132 ± 0.001	2.3772 ± 0.0001	0.11 ± 0.03	92 ± 18	5.56	possible	extended
COLDz.COS.11	10:00:20.43	+02:34:56.00	37.81 ± 0.002	2.0487 ± 0.0002	0.05 ± 0.02	120 ± 40	5.49	N	blended z=0.3, slightly extended
COLDz.COS.12	10:00:17.53	+02:35:11.00	35.354 ± 0.002	2.2605 ± 0.0002	0.025 ± 0.009	160 ± 40	5.43	N	
COLDz.COS.13	10:00:14.26	+02:35:02.50	32.423 ± 0.004	2.5552 ± 0.0004	0.09 ± 0.03	300 ± 90	5.43	N	
COLDz.COS.14	10:00:21.73	+02:35:57.00	35.005 ± 0.002	2.293 ± 0.0001	0.018 ± 0.008	90 ± 30	5.42	N	blended z=0.9
COLDz.COS.15	10:00:20.20	+02:35:31.50	34.681 ± 0.006	2.3237 ± 0.0005	0.033 ± 0.015	340 ± 110	5.41	possible	matched photo-z
COLDz.COS.16	10:00:25.50	+02:35:35.00	36.934 ± 0.004	2.121 ± 0.0004	0.07 ± 0.03	260 ± 80	5.34	possible	matched photo-z
COLDz.COS.17	10:00:19.70	+02:35:01.50	33.917 ± 0.007	2.3986 ± 0.0007	0.06 ± 0.02	570 ± 150	5.33	N	
COLDz.COS.18	10:00:24.60	+02:34:38.00	31.296 ± 0.002	2.6832 ± 0.0002	0.037 ± 0.012	180 ± 40	5.32	possible	matches photo-z, slightly extended
COLDz.COS.19	10:00:21.97	+02:34:54.50	37.083 ± 0.002	2.1085 ± 0.0002	0.046 ± 0.017	130 ± 30	5.29	N	M star nearby
COLDz.COS.20	10:00:17.03	+02:34:59.50	31.437 ± 0.002	2.6667 ± 0.0003	0.021 ± 0.008	170 ± 50	5.28	N	
COLDz.COS.21	10:00:23.47	+02:34:58.50	36.349 ± 0.004	2.1712 ± 0.0004	0.02 ± 0.02	110 ± 80	5.28	N	slightly extended
COLDz.COS.22	10:00:22.90	+02:34:10.00	35.301 ± 0.005	2.2653 ± 0.0004	0.12 ± 0.04	350 ± 90	5.27	possible	very uncertain photo-z, extended
COLDz.COS.23	10:00:20.57	+02:34:01.00	38.504 ± 0.001	1.9937 ± 0.0001	0.14 ± 0.04	60 ± 10	5.26	possible	matches photo-z, slightly extended
COLDz.COS.24	10:00:14.99	+02:35:41.00	35.362 ± 0.002	2.2597 ± 0.0002	0.07 ± 0.02	130 ± 30	5.25	possible	close separation and photo-z
COLDz.COS.25	10:00:21.07	+02:34:30.50	33.579 ± 0.005	2.4328 ± 0.0006	0.049 ± 0.018	410 ± 110	5.25	possible	close separation and photo-z, extended
GOODS-N									
COLDz.GN.1	12:36:59.79	+62:11:09.50	37.485 ± 0.003	2.0751 ± 0.0002	0.405 ± 0.137	200 ± 50	6.38	possible	slightly extended
COLDz.GN.2	12:36:27.94	+62:14:09.78	32.518 ± 0.002	2.5448 ± 0.0002	0.109 ± 0.033	210 ± 50	6.14	N	
COLDz.GN.4	12:36:54.77	+62:17:28.00	35.937 ± 0.002	2.2076 ± 0.0002	0.382 ± 0.12	180 ± 40	6.08	N	extended
COLDz.GN.5	12:37:00.00	+62:15:21.00	37.229 ± 0.005	2.0962 ± 0.0005	0.283 ± 0.073	520 ± 100	6.06	N	photo-z at lower z
COLDz.GN.6	12:37:01.50	+62:12:35.50	32.878 ± 0.003	2.5059 ± 0.0003	0.116 ± 0.038	260 ± 60	6.0	possible	
COLDz.GN.7	12:36:28.89	+62:13:00.80	30.615 ± 0.002	2.7652 ± 0.0003	0.189 ± 0.047	290 ± 50	5.97	N	
COLDz.GN.8	12:36:37.31	+62:15:03.39	37.737 ± 0.004	2.0546 ± 0.0003	0.823 ± 0.272	270 ± 70	5.89	possible	close photo-z, very extended
COLDz.GN.9	12:36:56.35	+62:18:19.50	36.348 ± 0.001	2.1713 ± 0.0001	0.077 ± 0.022	100 ± 20	5.88	possible	
COLDz.GN.10	12:36:33.87	+62:15:29.36	32.841 ± 0.002	2.51 ± 0.0002	0.143 ± 0.05	120 ± 30	5.83	possible	slightly extended
COLDz.GN.11	12:36:53.20	+62:14:34.49	35.073 ± 0.001	2.2866 ± 0.0001	0.323 ± 0.101	90 ± 20	5.81	N	extended
COLDz.GN.12	12:37:03.50	+62:12:52.00	37.93 ± 0.007	2.039 ± 0.0006	0.317 ± 0.114	490 ± 130	5.81	possible	photo-z=4
COLDz.GN.13	12:36:43.18	+62:14:22.44	36.743 ± 0.005	2.1372 ± 0.0005	0.199 ± 0.071	390 ± 100	5.8	N	
COLDz.GN.14	12:36:59.07	+62:14:48.00	34.133 ± 0.006	2.3771 ± 0.0006	0.605 ± 0.192	490 ± 120	5.65	possible	very close photo-z, extended
COLDz.GN.15	12:36:41.67	+62:15:47.93	33.34 ± 0.009	2.4574 ± 0.0009	0.178 ± 0.069	640 ± 190	5.64	possible	blended photo-z ~3
COLDz.GN.16	12:36:49.42	+62:12:17.98	32.807 ± 0.002	2.5136 ± 0.0002	0.062 ± 0.022	140 ± 40	5.63	possible	local foreground?
COLDz.GN.17	12:37:01.22	+62:13:04.50	33.2 ± 0.002	2.472 ± 0.0002	0.084 ± 0.036	140 ± 50	5.63	N	
COLDz.GN.18	12:36:51.12	+62:15:54.99	36.938 ± 0.003	2.1206 ± 0.0003	0.152 ± 0.043	270 ± 60	5.62	possible	matched photo-z
COLDz.GN.19	12:37:08.45	+62:14:23.48	36.017 ± 0.002	2.2005 ± 0.0002	0.207 ± 0.09	120 ± 40	5.61	N	local foreground, extended
COLDz.GN.20	12:37:04.88	+62:17:44.49	30.727 ± 0.003	2.7514 ± 0.0003	0.205 ± 0.062	280 ± 60	5.6	possible	close photo-z
COLDz.GN.21	12:36:54.93	+62:11:29.50	35.265 ± 0.004	2.2687 ± 0.0004	0.194 ± 0.057	390 ± 90	5.6	N	
COLDz.GN.22	12:37:00.14	+62:11:58.50	33.441 ± 0.003	2.447 ± 0.0003	0.075 ± 0.037	140 ± 50	5.59	N	
COLDz.GN.23	12:36:56.71	+62:13:19.50	37.925 ± 0.002	2.0394 ± 0.0002	0.156 ± 0.051	160 ± 40	5.59	N	
COLDz.GN.24	12:36:46.85	+62:12:18.97	31.165 ± 0.008	2.6988 ± 0.0009	0.222 ± 0.095	560 ± 180	5.56	N	slightly extended
COLDz.GN.25	12:37:03.35	+62:08:59.00	35.598 ± 0.002	2.2381 ± 0.0002	0.119 ± 0.043	130 ± 30	5.55	possible	close photo-z
COLDz.GN.26	12:37:00.29	+62:16:31.50	36.733 ± 0.006	2.1381 ± 0.0005	0.169 ± 0.056	490 ± 120	5.54	possible	very faint counterpart
COLDz.GN.27	12:36:45.09	+62:18:00.46	37.373 ± 0.001	2.0843 ± 0.0001	0.096 ± 0.025	90 ± 20	5.54	possible	close photo-z
COLDz.GN.28	12:36:47.77	+62:12:57.47	32.289 ± 0.003	2.57 ± 0.0003	0.113 ± 0.04	210 ± 60	5.51	N	different spec-z, z=2.932, slightly extended
COLDz.GN.29	12:37:06.38	+62:16:34.49	32.861 ± 0.002	2.5078 ± 0.0002	0.089 ± 0.027	190 ± 40	5.51	possible	
COLDz.GN.30	12:36:50.43	+62:10:29.48	31.297 ± 0.002	2.6832 ± 0.0002	0.236 ± 0.088	150 ± 40	5.51	N	slightly extended

elongated CO candidate emission (Fig. B.1).

COLDz.COS.5: No counterpart is found in the COSMOS2015 catalog or the images at the position of this candidate.

COLDz.COS.6: The images show an IRAC 3.6μm source 3″ ± 0.2″ to the SE of the candidate which has a photo-z=2.9–3 and might therefore be associated with our candidate although the offset appears significant (the CO(1–0) redshift is z=2.60). At the CO position there is an I-band source with photo-z=0.44–0.48, although its 3.6μm image is contaminated by the brighter, higher-z galaxy. It is unclear if the CO candidate may be related.

COLDz.COS.7: The CO(1–0) redshift of this candidate is z=2.22. It is at the position of an *HST* I-band source, which is not in the COSMOS2015 catalog, and is not visible in the 3.6μm image.

COLDz.COS.8: Candidate is at the position of a faint *HST* I-band and IRAC 3.6μm source, which is listed in the COSMOS2015 catalog 2.3″ ± 0.4″ to the N (z_{phot}=0.2–0.7).

COLDz.COS.9: Candidate shows spatially extended CO emission, centered on an *HST* I-band source with a photo-z=0.1–0.8, which is therefore unlikely to be associated with the candidate.

COLDz.COS.10: Candidate is spatially extended and is co-spatial with multiple faint *HST* I-band galaxies. The COSMOS2015 catalog only reports a faint galaxy 1.3″ ± 0.7″ to the SW, with a very uncertain photo-z of 0.8–4.3, which may be associated with our candidate.

COLDz.COS.11: Candidate is near the position of a low-z galaxy (z_{phot}=0.32–

0.35). There is a brighter IRAC 3.6μm source 1.6″ ±0.4″ to the NW, (z_{phot}=1.5–1.6), which may be related to the CO candidate with a CO redshift of 2.0.

COLDz.COS.12: No counterpart is found in the COSMOS2015 catalog or the images at the position of this candidate.

COLDz.COS.13: No counterpart is found in the COSMOS2015 catalog or the images at the position of this candidate.

COLDz.COS.14: Candidate is affected by foreground contamination which prevents any counterpart assessment. In particular, there is a bright photo-z=0.9 galaxy at 1.6″ ± 0.3″ to the NW.

COLDz.COS.15: Candidate has a potential counterpart match. The COSMOS2015 catalog lists a galaxy 1.8″ ± 0.4″ to the NW with a photo-z=1.8–2.8, which is very faint in the I band and IRAC 3.6μm images. Assuming CO(1–0) would place this candidate at z=2.32.

COLDz.COS.16: Candidate has a potential counterpart match, but it appears confused with a bright galaxy 1.6″ to the SE, with a photo-z=1.0–1.2. The potential counterpart has photo-z=1.3–2.6 and is located about 2″ ± 0.5″ to the NE.

COLDz.COS.17: No counterpart is found in the COSMOS2015 catalog or the images.

COLDz.COS.18: Candidate has a potential counterpart match, 1.6″ ± 0.4″ to the N, with a photo-z=2.4–2.5; assuming CO(1–0) would place it at z=2.68. This candidate is contaminated by a local bright galaxy to the NE.

COLDz.COS.19: Candidate does not appear to have a counterpart. An M star is located 0.8″ ± 0.7″ to the NE, and partly prevents counterpart identification.

COLDz.COS.20: Candidate does not have a counterpart. The COSMOS2015 catalog lists two galaxies at separations of 2.2″ ± 0.3″ and 2.3″ ± 0.3″, respectively. The first galaxy has a photo-z=0.6–0.9 and the second one is at photo-z =1.9–2.5. This latter galaxy may be associated with our candidate, which has a CO(1–0) redshift of z_{10}=2.67.

COLDz.COS.21: No counterpart is found in the COSMOS2015 catalog or the images, at the position of this spatially extended candidate, but the IRAC 3.6μm images are contaminated by bright nearby stars and galaxies.

COLDz.COS.22: A faint galaxy is visible in the *HST* I-band image, 1.5″ ± 0.7″ to the NW, which may be associated with our line candidate. The catalog lists a very uncertain photo-z=1.5–5.5, which is compatible with the CO(1–0) redshift of z_{10}=2.27.

COLDz.COS.23: Candidate has a potential counterpart association. This is a galaxy 1.5″ ± 0.5″ to the SW, which is compatible with the position of at least part of the slightly spatially extended line emission. The photometric redshift for this galaxy is photo-z=1.7–2.8, which is compatible with the CO(1–0) redshift of z_{10}=1.99.

COLDz.COS.24: Candidate has a potential counterpart association. The potential counterpart is only 0.8″ ± 0.9″ to the N and has a photometric redshift of $z_{\rm phot}$=1.9–2.0 which is close to the CO(1–0) redshift of z_{10}=2.26. A second galaxy is seen, 1.6″ ± 0.9 to the E, which has a photometric redshift of photo-z=0.89–0.92

and which contaminates the emission in the IRAC 3.6μm images.

COLDz.COS.25: This spatially extended candidate has a potential counterpart. This potential counterpart is 1.4″ ± 0.7″ to the SE and has a photometric redshift of photo-z=2.6–3.0 which is close to the CO(1–0) redshift of z_{10}=2.43. The IRAC 3.6μm images are contaminated by a nearby star, which makes it difficult to identify faint sources reliably.

B.2 GOODS-N

COLDz.GN.1: This spatially extended line candidate has potential counterpart matches. There are multiple galaxies which are compatible with the line emission position, blended in the IRAC 3.6μm image but visible in *HST* H-band, with photometric redshifts in the CANDELS catalog (Skelton et al., 2014). The closest catalog match has a separation of only 0.4″ ± 0.6″ to the NE and has an uncertain photo-z=0.8–2.2. The catalog lists three more galaxies within 3″ (separations of 1.3″ ± 0.6″, 2″ ± 0.6″ and 2.6″ ± 0.6″), with photo-zs of 1.5–1.7, 0.9–2.5 and 1.1–1.8 respectively. The CO(1–0) redshift of our candidate is z_{10}=2.08, which makes it compatible with at least two of these potential counterparts.

COLDz.GN.2: This is the highest SNR candidate in GOODS-N without a clear counterpart. The CANDELS catalog lists a faint source 2.6″ ± 0.3″ to the SE, with uncertain photo-z=1.0–2.0 Skelton et al. (2014). The CO(1–0) redshift of our candidate (z=2.54) makes it a possible, although unlikely counterpart.

COLDz.GN.4: Candidate is unlikely to have a counterpart. There are no galaxies in the CANDELS catalog within 3″, and no galaxies are visible in the

HST H-band or IRAC 3.6μm images.

COLDz.GN.5: There are two galaxies in the images within 2″ of the line candidate, with separations of 1.5″ ± 0.3″ and 1.7″ ± 0.3″, respectively. They are unlikely to be counterparts because they have photometric redshifts of z_{phot} =1.1–1.3 and 0.4–0.5 respectively, while the CO(1–0) redshift of our candidate is z_{10}=2.1.

COLDz.GN.6: Candidate has a potential match 2.8″ ± 0.4″ to the SE, in the direction where the CO emission is slightly spatially extended. The catalog lists a photo-z of 2.4–2.5 which is compatible with the CO(1–0) redshift of z_{10}=2.51, suggesting a possible counterpart match.

COLDz.GN.7: Candidate has an unlikely, but possible match 2.9″ ± 0.3″ to the SE, which appears to be at a significant offset. The galaxy has a photo-z=1.8–2.0, which is not compatible with the CO(1–0) redshift of z_{10}=2.76, therefore we do not consider this to be a match.

COLDz.GN.8: This spatially extended CO candidate has a possible match 3.0″ ± 0.8″ to the SE, with an uncertain photo-z of 1.4–2.4 which is compatible with the CO(1–0) redshift of z_{10}=2.05. This is a potential match, because the line emission appears to be very spatially extended, and may be compatible with coming from a dust-obscured part of the optical galaxy.

COLDz.GN.9: Candidate is unlikely to have a counterpart. It appears near a spec-z=0.516 galaxy, which is 2.8″ ± 0.3″ to the NW. The catalog also lists a faint, photo-z=1.9–2.1 galaxy 2.4″ ± 0.3″ to the SW (which appears to be significantly offset from the CO line emission), which could be consistent with the CO(1–0) redshift of z_{10}=2.17.

COLDz.GN.10: This slightly spatially extended candidate is unlikely to have a counterpart. The closest catalog association is 1.5″ ± 0.5″ to the NE and has a photo-z of 4.4–5. The CO(2–1) redshift for our candidate would be z_{21}=6.0, and is therefore an unlikely match. The CANDELS catalog lists two more galaxies, just below 3″ to the NE with photo-zs of 1.7–2.0 and 1.9–2.4, respectively, which may be compatible with the CO(1–0) redshift of z_{10}=2.51.

COLDz.GN.11: Candidate appears spatially extended and elongated. No objects are seen in the *HST* H-band and IRAC 3.6 μm images. The CANDELS catalog lists a galaxy 1.8″ ± 0.7″ to the NW which has a photo-z of 0.6–1.6. This is inconsistent with the CO(1–0) redshift of z_{10}=2.29, so a match is unlikely.

COLDz.GN.12: Candidate has no likely match. The catalog lists a faint galaxy, 1.7″ ± 0.4″ to the NE, with photo-z=4.1–4.4, which may potentially be associated. The counterpart status is difficult to evaluate due to blending with the bright local (spec-z=0.784) galaxy at a separation of just 2.4″ ± 0.4″.

COLDz.GN.13: Candidate is spatially extended and elongated, and is unlikely to have a counterpart association. The CANDELS catalog lists two potential matches within 3″, with separation 1.7″ ± 0.5″ and 3″ ± 0.5″, respectively. The photometric redshifts listed by the catalog are z_{phot} =0.2–0.4 and 0.6–1.4, respectively, which make them unlikely counterparts given the CO(1–0) redshift of our candidate (z_{10}=2.14).

COLDz.GN.14: This is a spatially extended CO candidate, and it has a possible counterpart, which is faint but visible in the IRAC 3.6 μm image. We identify this counterpart with the catalog listing of a photo-z=2.4–2.7 galaxy which is displaced by 2.8″ ± 0.7″ to the SW. This counterpart is compatible with the CO(1–0)

redshift of z_{10}=2.38. The offset may not be significant, because the IR-detected galaxy appears to be compatible with the position of this spatially extended candidate.

COLDz.GN.15: Candidate may have a counterpart. The 3.6 μm image is partly blended with a spec-z=0.453 galaxy 2.3″ ± 0.6″ to the W which makes the identification difficult. The catalog lists two possible counterparts, with photo-z=1.6–1.8 and 3.1–3.9, offset respectively 0.9″ ± 0.6″ and 1.7″ ± 0.6″ to the NW and NE, which are not compatible with the CO(1–0) redshift of z_{10}=2.46.

COLDz.GN.16: Candidate may have a counterpart. The image is partly blended with a spec-z=0.961 galaxy 2.3″ ± 0.6″ to the NE, which makes identification difficult. The CANDELS catalog lists three more galaxies within 2″ and 3″ from our candidate, with photo-z=0.9–2.0, 2.2–2.4 and 1.4–2.3, all of which may be compatible with the CO(1–0) redshift of z_{10}=2.51.

COLDz.GN.17: Candidate appears spatially extended and elongated. The catalog lists a galaxy 1.5″ ± 0.5″ to the SE, which is visible in the IRAC 3.6 μm images. This galaxy has a photo-z of 1.2–1.9, which is only somewhat inconsistent with the CO(1–0) redshift of z_{10}=2.47. Therefore a counterpart association cannot be ruled out.

COLDz.GN.18: Candidate appears to be closely associated with other, lower significance, candidates which are visible in the line maps. It has a potential match, a faint galaxy with photo-z=1.3–2.2 only 0.8″ ± 0.5″ to the SE, which is compatible with the CO(1–0) redshift of z_{10}=2.12. The catalog also lists three galaxies 0.4″ ± 0.5″, 1.8″ ± 0.5″ and 2.7″ ± 0.5″ to the SE, with photo-zs of 0.3–0.9, 2.5–2.8 and 4.3–5.2, respectively, which may be associated in case of incorrect

photometric redshifts.

COLDz.GN.19: This spatially extended candidate is blended with a local foreground galaxy at z=0.564. No continuum emission is detected in our data at this position and therefore we exclude the possibility that the line candidate may be spurious and due to noise superposed to continuum emission. The presence of the bright foreground contaminates the *HST* H-band and the IRAC 3.6 μm images making it difficult to evaluate the counterpart status. Lensing of a faint z=2.20 galaxy by the foreground galaxy is a possibility.

COLDz.GN.20: Candidate may have a counterpart. It appears close to a foreground galaxy, which partly contaminates the IRAC 3.6 μm image. The *HST* H-band image shows a potential match which the catalog identifies as a galaxy 1.16″ ± 0.3 to the NW with a photo-z of 1.6–2.5. The association is not ruled out by our CO(1–0) redshift of z_{10}=2.75.

COLDz.GN.21: Candidate is unlikely to have a counterpart. The images show a galaxy 1.0″ ± 0.6″ to the NE, which has a grism-z of 0.86–0.94 from Momcheva et al. (2016). This makes it incompatible with the CO(1–0) redshift of z_{10}=2.27.

COLDz.GN.22: No counterpart is found in the images or the CANDELS catalog at the position of this candidate.

COLDz.GN.23: No counterpart is found in the images or the CANDELS catalog at the position of this candidate.

COLDz.GN.24: This spatially extended candidate may have a counterpart, which is visible in the IRAC 3.6 μm image but not in the *HST* H-band image. The

separation is 2.9″ ± 0.5″ to the S, but this may not be significant due to the extent of the emission. The photo-z is uncertain and ranges from 0.9 to 2.3, therefore an association is not strongly ruled out by our CO(1–0) redshift of z_{10}=2.7.

COLDz.GN.25: Candidate has a potential counterpart, 1.7″ ± 0.7″ to the NE. The galaxy is well visible in H-band and IRAC 3.6 μm images and has a photo-z of 1.9–2.2, which is compatible with the CO(1–0) redshift of z_{10}=2.24.

COLDz.GN.26: This spatially extended CO candidate has potential matches, which appear very faint in the IRAC 3.6 μm image. The catalog lists two galaxies at 1.8″ ± 0.5″ and 1.9″ ± 0.5″ to the NE, with uncertain photo-zs of 0.6–4.2 and 2.1–3.7 respectively, which makes them compatible with the CO(1–0) redshift of z_{10}=2.14. The spatial offset may not be significant because of the spatial extent of the emission, and these are therefore potential counterpart matches.

COLDz.GN.27: Candidate has three potential counterparts in the catalog with close photo-zs. The first is 2.3″ ± 0.4″ to the SE, with a photo-z of 1.5–2.3. The second is 2.7″ ± 0.4″ to the SE, with a photo-z of 1.5–2. Both of these are compatible with the CO(1–0) redshift of z_{10}=2.08. The third potential counterpart is located 2.9″ ± 0.4″ to the NE and has a photo-z in the range 5.2–5.7 which is consistent with the CO(2–1) redshift of z_{21}=5.16.

COLDz.GN.28: The *HST* H-band and IRAC 3.6 μm images show a potential match 1.6″ ± 0.3″ to the S, but this galaxy was reported to have a spec-z=2.932 (Skelton et al., 2014). Assuming CO(1–0) would imply z_{10}=2.57, which implies either a lack of counterpart or an incorrect spectroscopic redshift.

COLDz.GN.29: Candidate has a possible counterpart. Both the *HST* H-band

and the IRAC 3.6 μm images show multiple sources within 2″. The catalog lists two faint galaxies, with photo-z=0.8–3.5 and 1.1–1.7 just 1.4″±0.4″ and 1.5″±0.4″ to the SE and NE respectively. The first of these is compatible with the CO(1–0) redshift of z_{10}=2.51.

COLDz.GN.30: This spatially extended candidate does not appear to have counterparts. The IRAC 3.6 μm image is blended with a bright foreground galaxy, and the only catalog association (offset by 2.7″ ± 0.9″ to the SW) has a photo-z=0.7–0.9, which is incompatible with the CO(1–0) redshift of z_{10}=2.68.

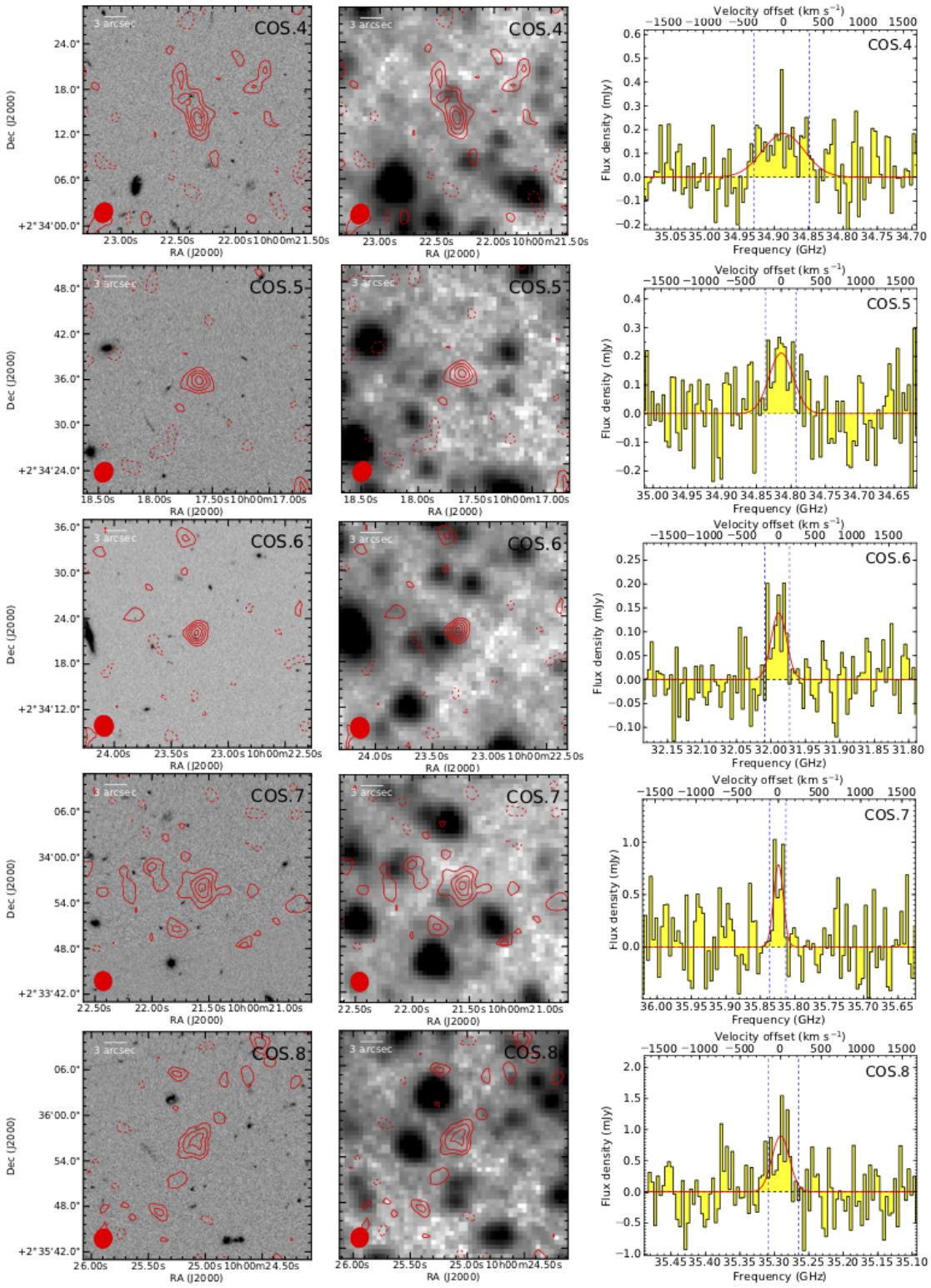

Figure B.1: Additional candidate integrated line map overlays (contours) over *HST* I-band (left) and IRAC channel 1 images (middle) from SPLASH (grayscale; Steinhardt et al. 2014). Contours are shown in steps of 1σ starting at $\pm 2\sigma$. Right: Line candidate aperture spectra ("histograms") and Gaussian fits (red curves) to the line features. The observed frequency resolution is the same as in Fig. 3.7. The velocity range used for the overlays is shown by the dashed blue lines.

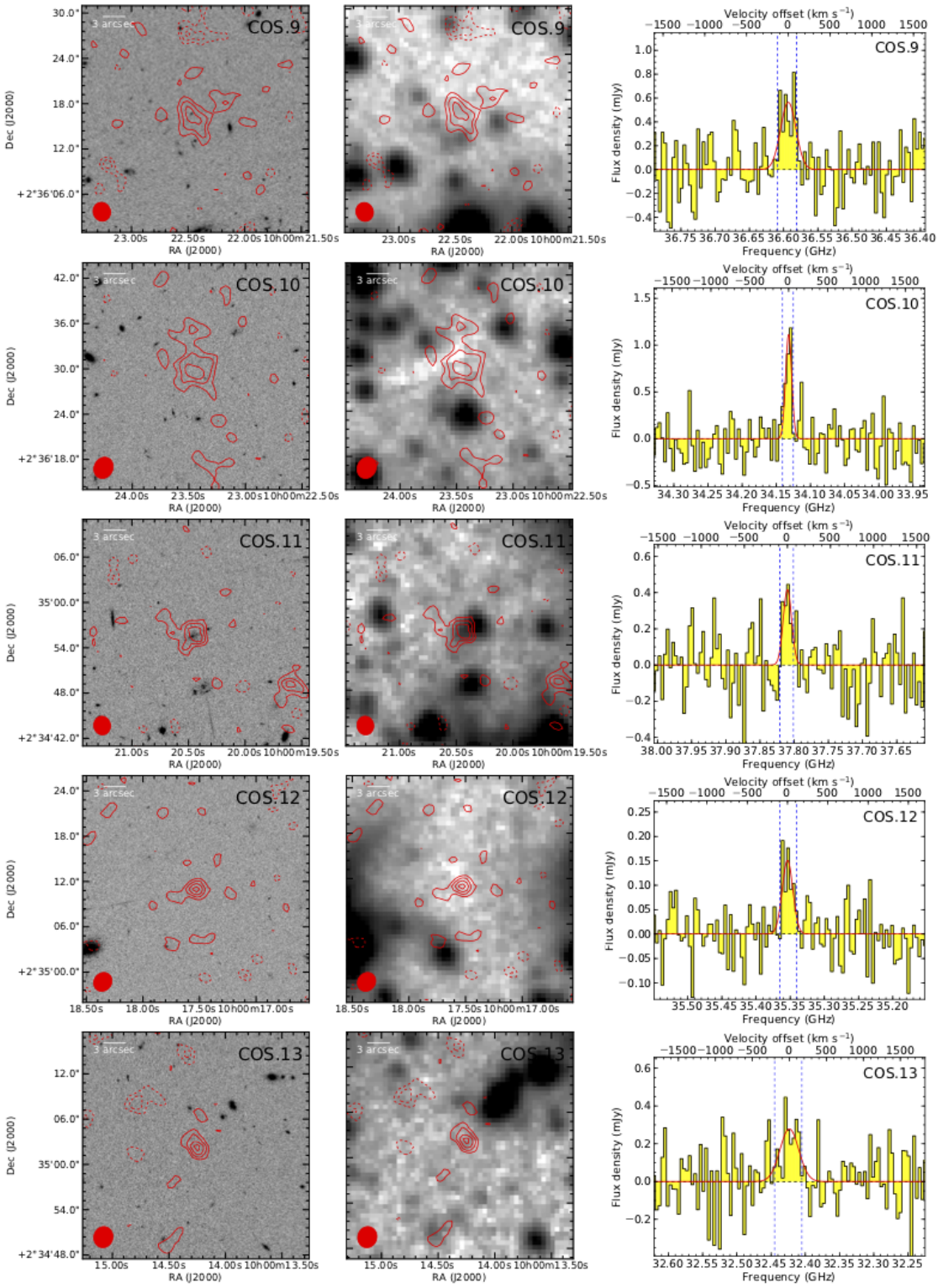

Figure B.1: (continued)

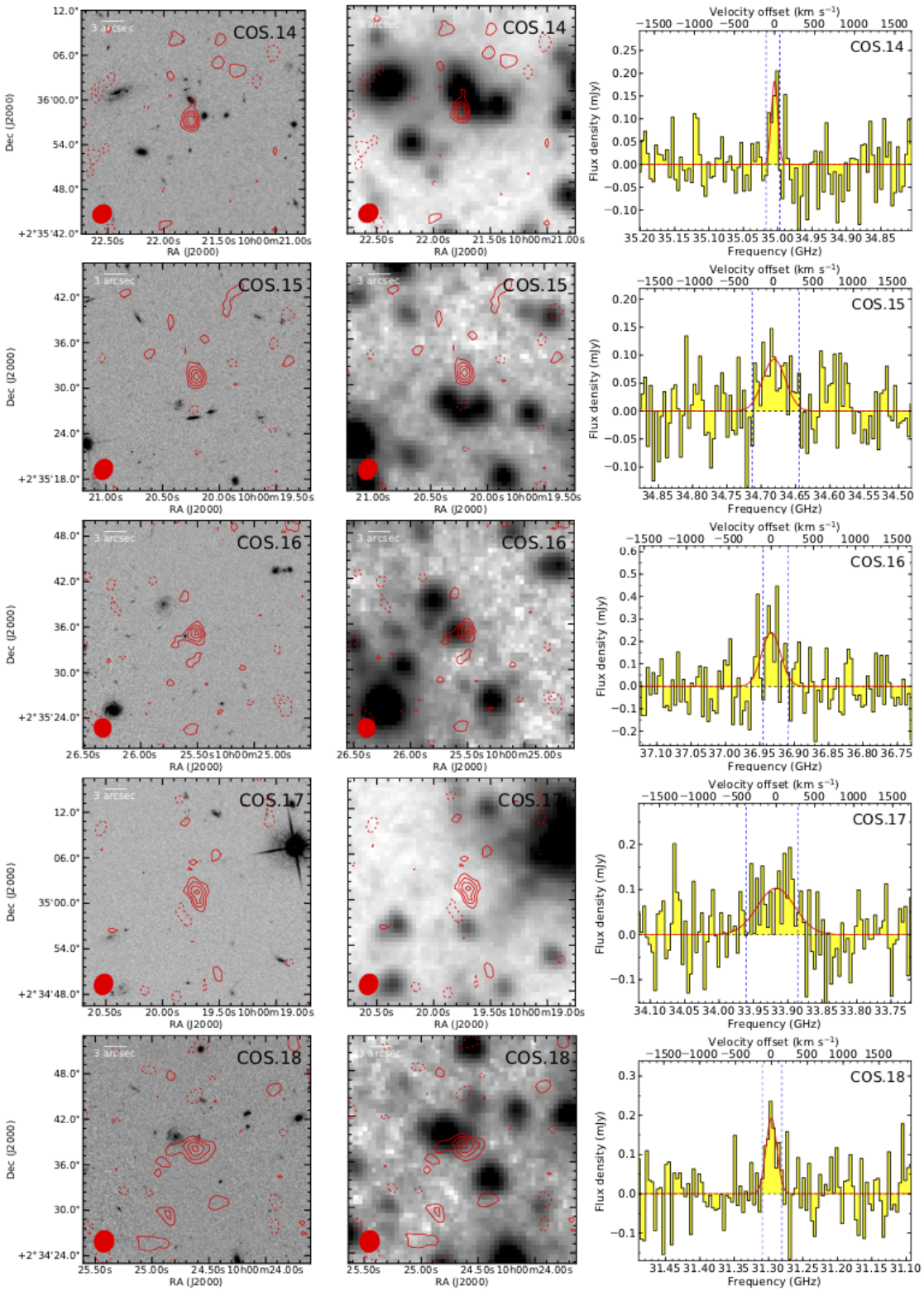

Figure B.1: (continued)

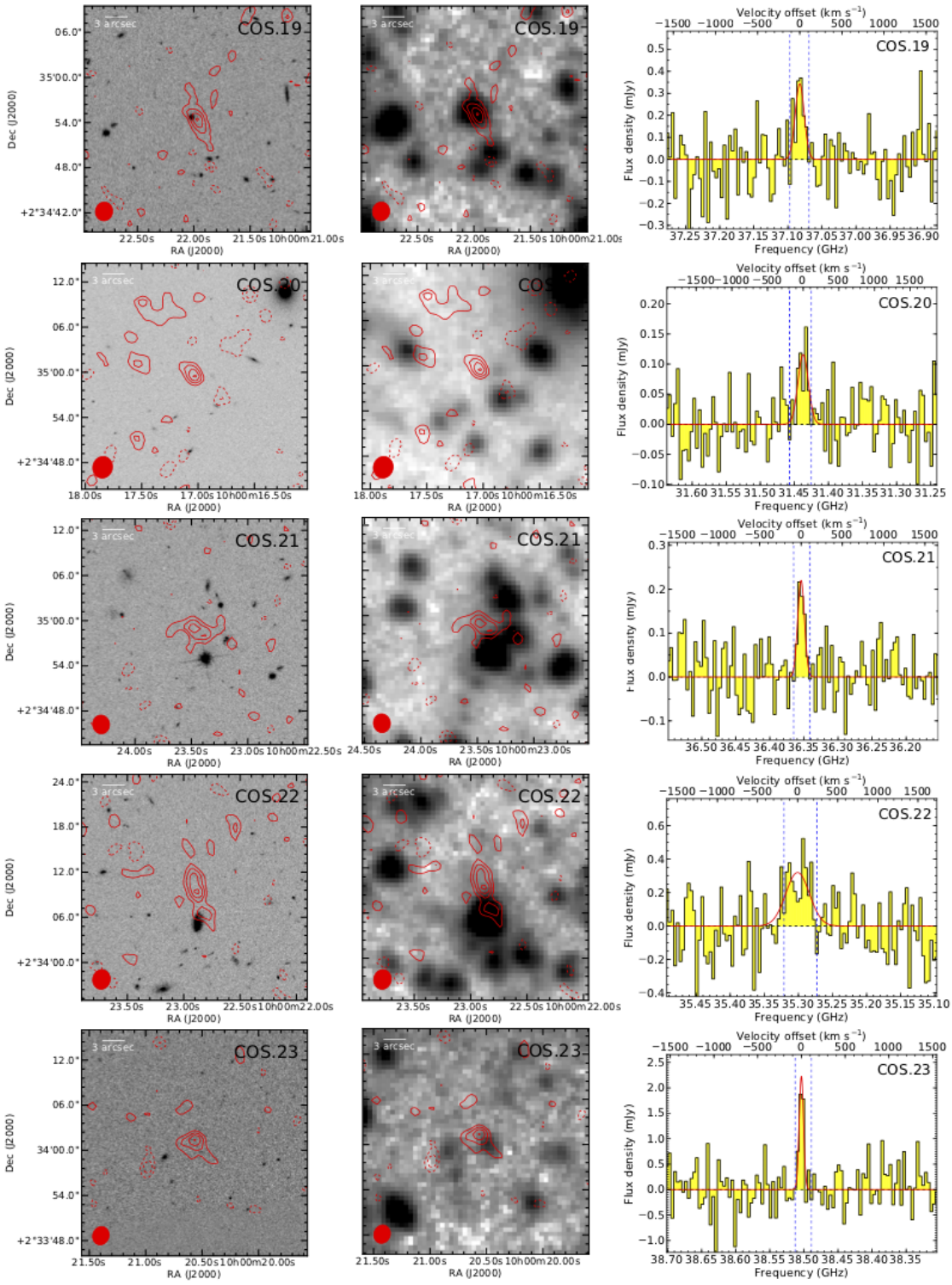

Figure B.1: (continued)

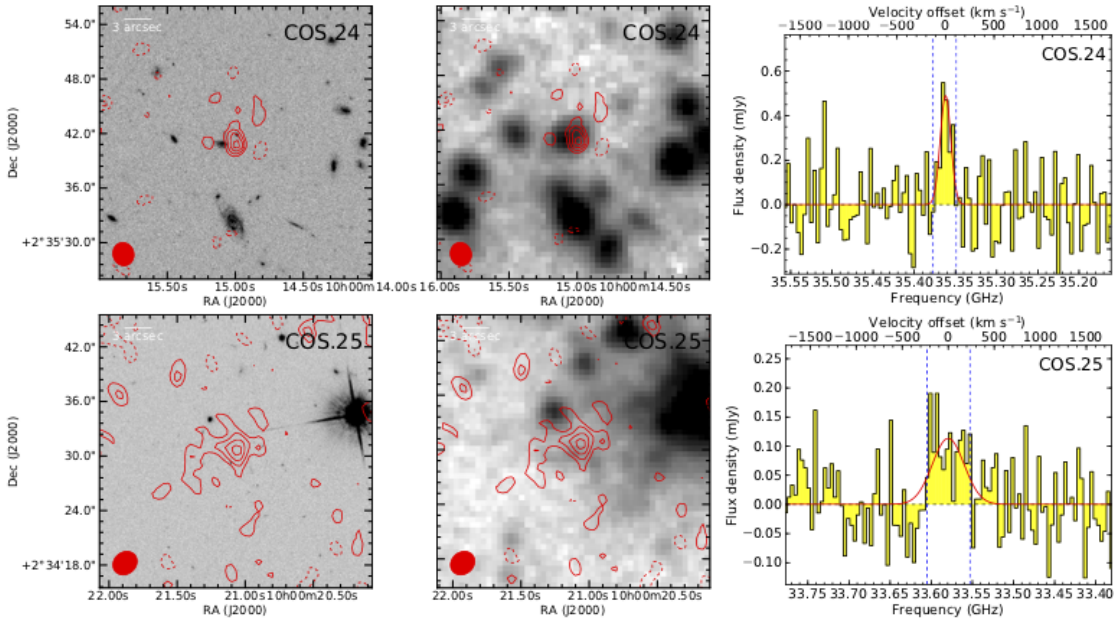

Figure B.1: (continued)

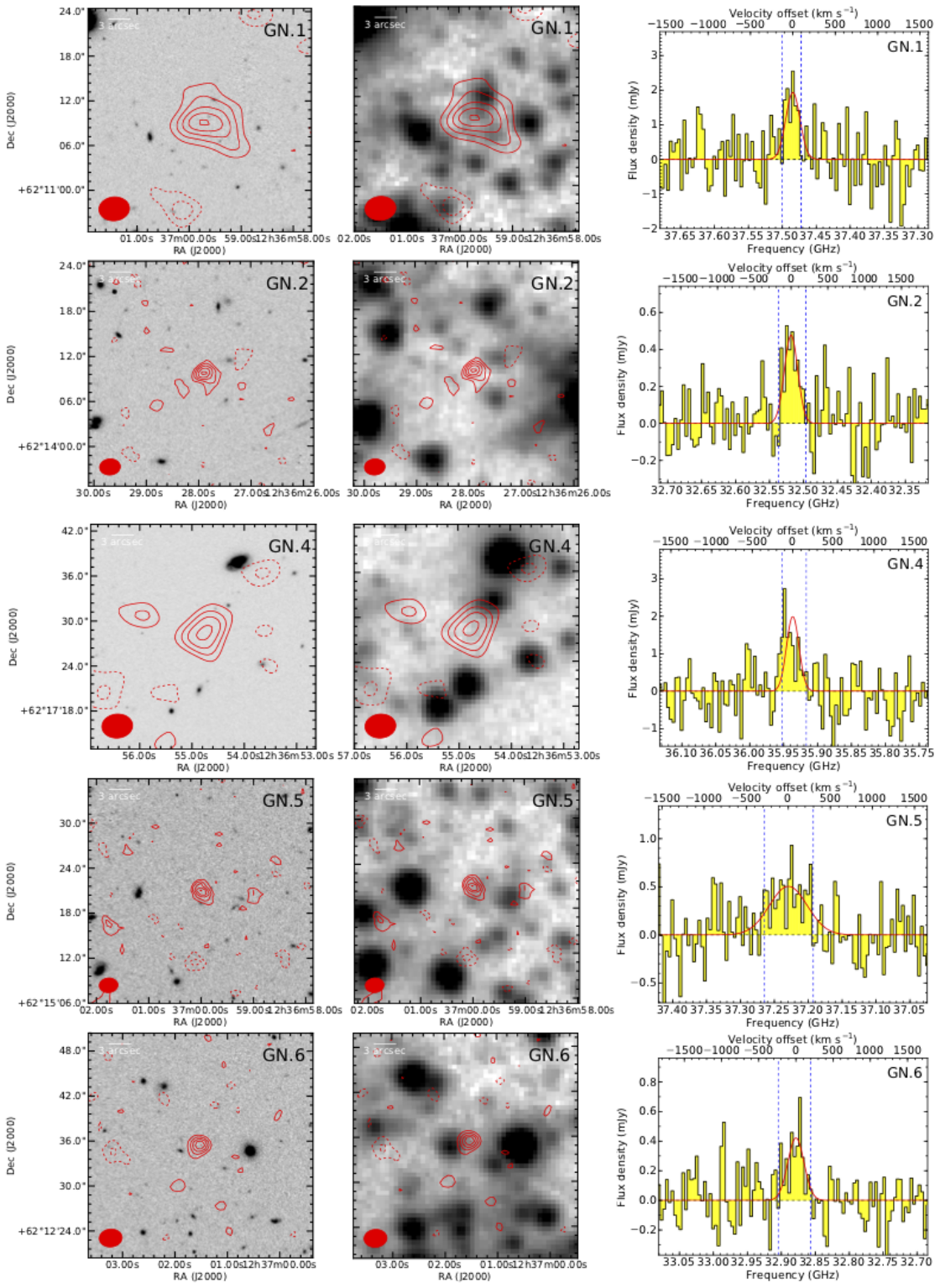

Figure B.2: Additional candidate integrated line map overlays (contours) over *HST* H-band (left) and IRAC channel 1 images (middle; grayscale). The CO line data were taken from the Natural-mosaic or Smoothed-mosaic when the line emission is unresolved/resolved, respectively. Contours are shown in steps of 1σ starting at $\pm 2\sigma$. Right: Line candidate single-pixel/aperture spectra ("histograms"; for unresolved/resolved emission) and Gaussian fits to the line features (red curves). The observed frequency resolution is the same as in Fig. 3.7. The velocity range used for the overlays is shown by the dashed blue lines.

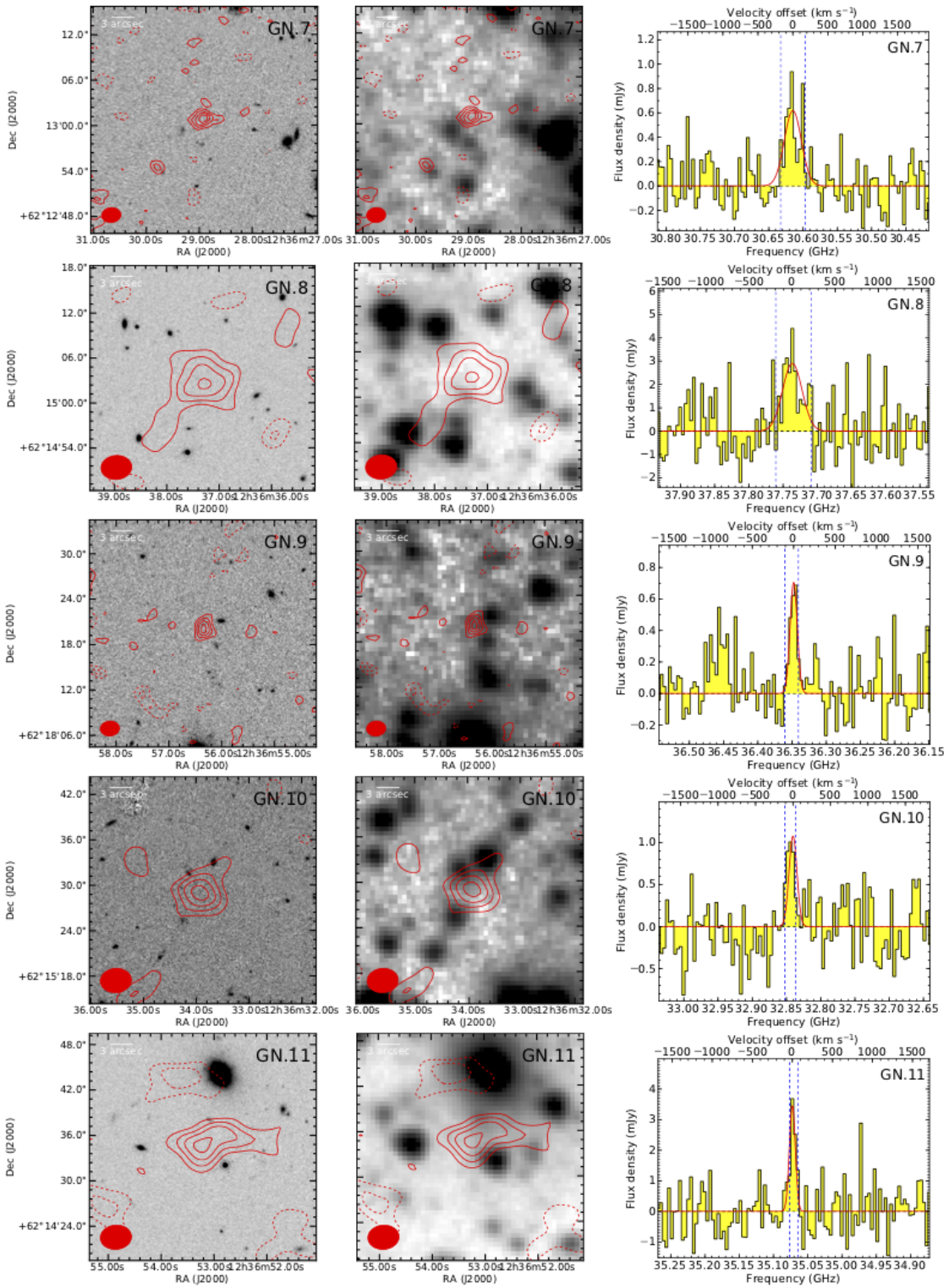

Figure B.2: (continued)

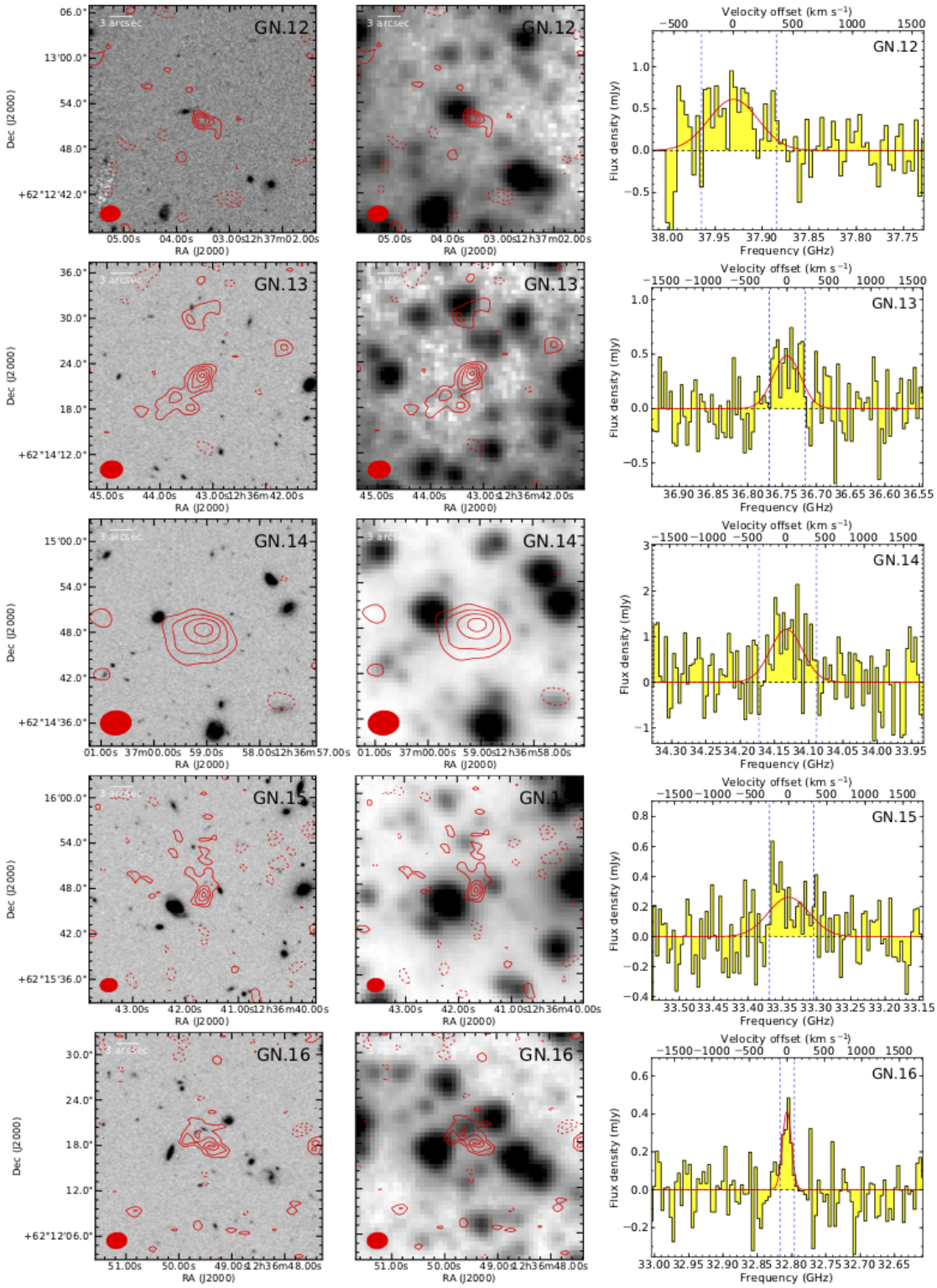

Figure B.2: (continued)

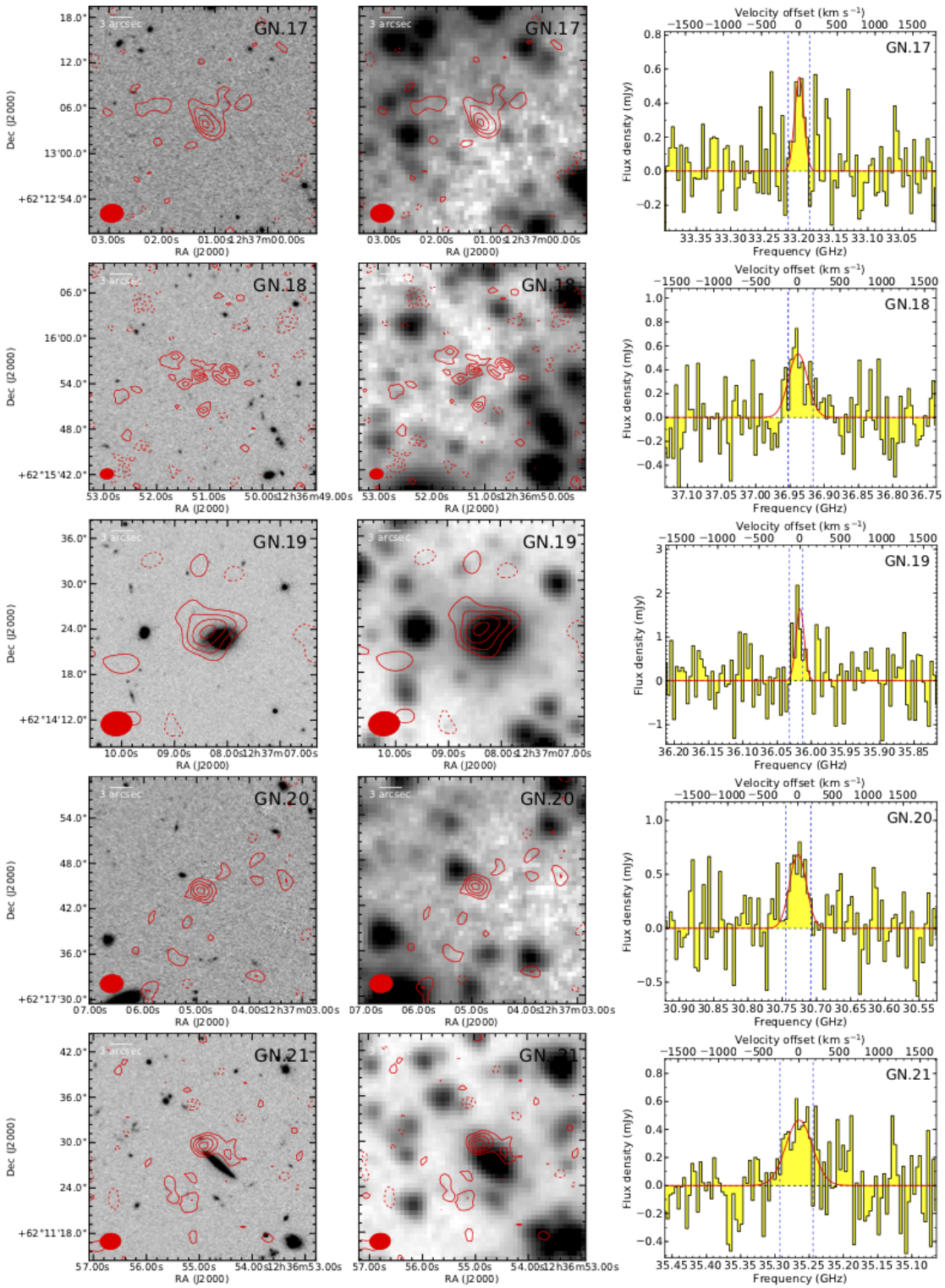

Figure B.2: (continued)

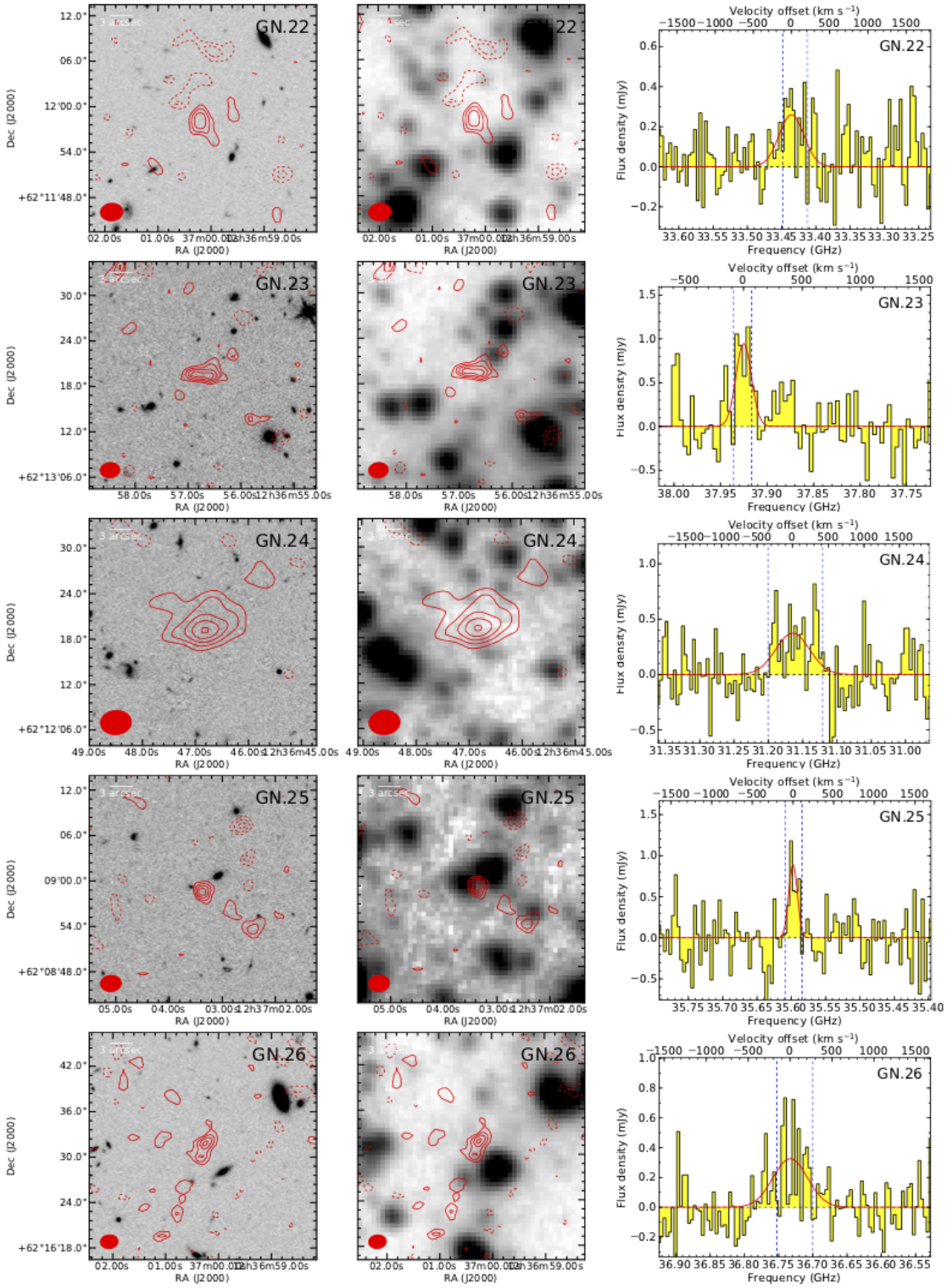

Figure B.2: (continued)

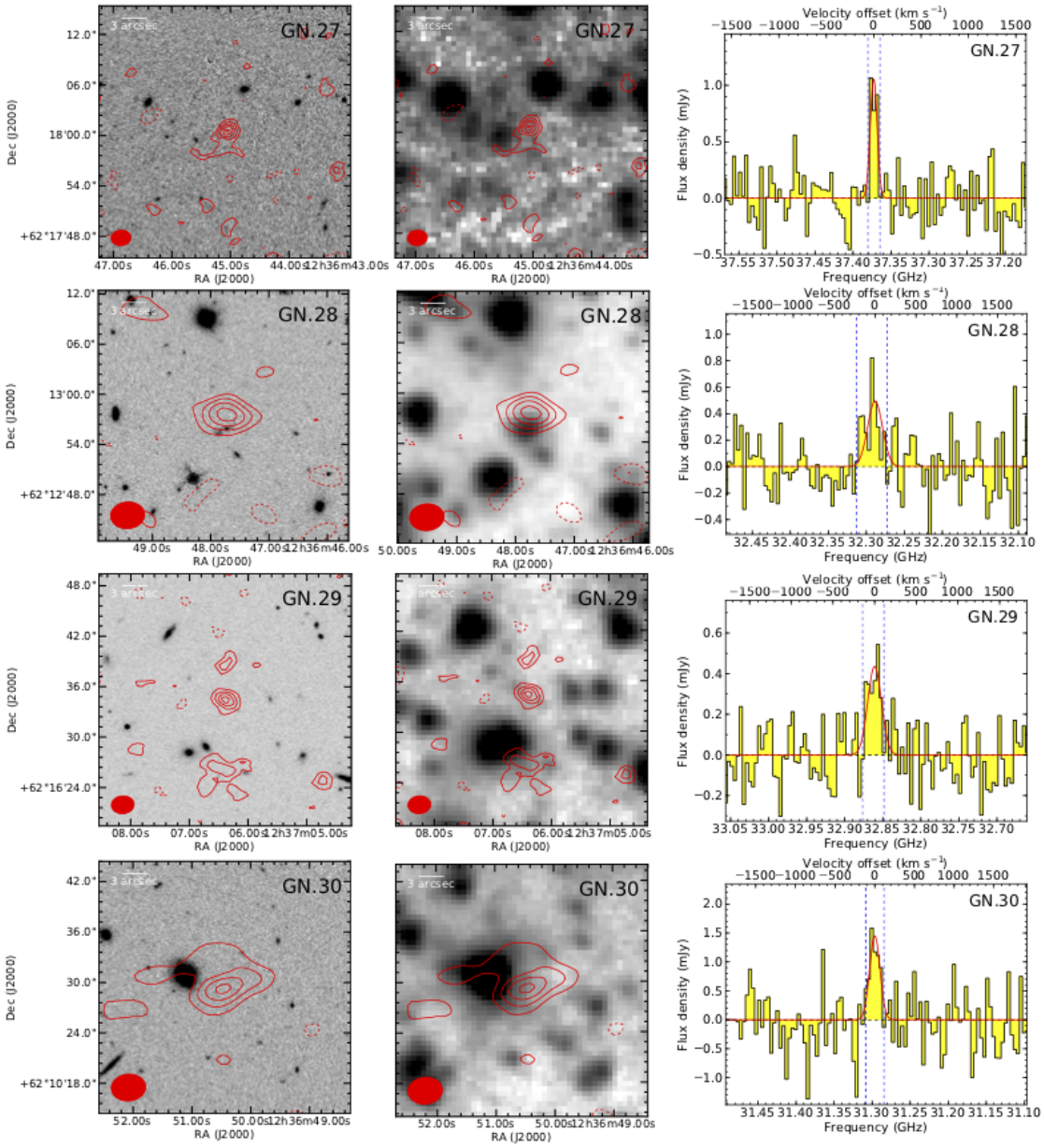

Figure B.2: (continued)

BIBLIOGRAPHY

Amvrosiadis, A., Valiante, E., Gonzalez-Nuevo, J., et al. 2018, MNRAS, 2881

Aravena, M., Carilli, C., Daddi, E., et al. 2010a, ApJ, 718, 177

Aravena, M., Bertoldi, F., Carilli, C., et al. 2010b, eapj@ApJLetters, 708, L36

Aravena, M., Carilli, C. L., Salvato, M., et al. 2012, MNRAS, 426, 258

Aravena, M., Hodge, J. A., Wagg, J., et al. 2014, MNRAS, 442, 558

Aravena, M., Decarli, R., Walter, F., et al. 2016, ApJ, 833, 68

Ashby, M. L. N., Willner, S. P., Fazio, G. G., et al. 2013, ApJ, 769, 80

Baker, A. J., Tacconi, L. J., Genzel, R., Lehnert, M. D., & Lutz, D. 2004, ApJ, 604, 125

Baldry, I. K., Glazebrook, K., Brinkmann, J., et al. 2004, ApJ, 600, 681

Bardeen, J. M., Bond, J. R., Kaiser, N., & Szalay, A. S. 1986, ApJ, 304, 15

Barišić, I., Faisst, A. L., Capak, P. L., et al. 2017, ApJ, 845, 41

Bastian, N., Covey, K. R., & Meyer, M. R. 2010, Annual Review of Astronomy and Astrophysics, 48, 339

Becker, G. D., Rauch, M., & Sargent, W. L. W. 2009, ApJ, 698, 1010

Behroozi, P., Wechsler, R., Hearin, A., & Conroy, C. 2018, ArXiv e-prints, arXiv:1806.07893

Behroozi, P. S., Wechsler, R. H., & Conroy, C. 2013, ApJ, 770, 57

Berta, S., Lutz, D., Genzel, R., Förster-Schreiber, N. M., & Tacconi, L. J. 2016, A&A, 587, A73

Bertin, E., & Arnouts, S. 1996, A&AS, 117, 393

Béthermin, M., De Breuck, C., Gullberg, B., et al. 2016, A&A, 586, L7

Bigiel, F., Leroy, A., Walter, F., et al. 2008, AJ, 136, 2846

Bigiel, F., Leroy, A. K., Walter, F., et al. 2011, ApJ, 730, L13

Blain, A. W., Smail, I., Ivison, R. J., Kneib, J.-P., & Frayer, D. T. 2002a, Phys. Rep., 369, 111

—. 2002b, Phys. Rep., 369, 111

Bolatto, A. D., Wolfire, M., & Leroy, A. K. 2013, ARA&A, 51, 207

Bolatto, A. D., Warren, S. R., Leroy, A. K., et al. 2015, ApJ, 809, 175

Bolatto, A. D., Chatterjee, S., Casey, C. M., et al. 2017, ArXiv e-prints, arXiv:1711.09960

Bolton, J. S., & Haehnelt, M. G. 2007, MNRAS, 382, 325

Bond, J. R., & Efstathiou, G. 1987, MNRAS, 226, 655

Boselli, A., Cortese, L., Boquien, M., et al. 2014, A&A, 564, A66

Bothwell, M. S., Chapman, S. C., Tacconi, L., et al. 2010, MNRAS, 405, 219

Bothwell, M. S., Smail, I., Chapman, S. C., et al. 2013, MNRAS, 429, 3047

Bouché, N., Cresci, G., Davies, R., et al. 2007, ApJ, 671, 303

Bouché, N., Dekel, A., Genzel, R., et al. 2010, ApJ, 718, 1001

Bournaud, F., Daddi, E., Weiß, A., et al. 2015, A&A, 575, A56

Bournaud, F., Perret, V., Renaud, F., et al. 2014, ApJ, 780, 57

Bourne, N., Dunne, L., Bendo, G. J., et al. 2013, MNRAS, 436, 479

Bouwens, R. J., Illingworth, G. D., Oesch, P. A., et al. 2015, ApJ, 803, 34

Bouwens, R. J., Aravena, M., Decarli, R., et al. 2016, ApJ, 833, 72

Brammer, G. B., van Dokkum, P. G., Franx, M., et al. 2012, ApJS, 200, 13

Brinchmann, J., Charlot, S., White, S. D. M., et al. 2004, MNRAS, 351, 1151

Bruzual, G., & Charlot, S. 2003, MNRAS, 344, 1000

Buchner, J., Georgakakis, A., Nandra, K., et al. 2014, A&A, 564, A125

Buckley, M. R., & Peter, A. H. G. 2017, ArXiv e-prints, arXiv:1712.06615

Bussmann, R. S., Riechers, D., Fialkov, A., et al. 2015, ApJ, 812, 43

Bussmann, S., Leung, T. K. ., & Conley, A. 2016, uvmcmcfit: Parametric models to interferometric data fitter, Astrophysics Source Code Library, , , ascl:1606.006

Calzetti, D. 2001, PASP, 113, 1449

Cameron, E., & Pettitt, A. N. 2012, MNRAS, 425, 44

Cantiello, M., Yoon, S. C., Langer, N., & Livio, M. 2007, A&A, 465, L29

Capak, P. L., Riechers, D., Scoville, N. Z., et al. 2011, Nature, 470, 233

Capak, P. L., Carilli, C., Jones, G., et al. 2015, Nature, 522, 455

Caputi, K. I., Deshmukh, S., Ashby, M. L. N., et al. 2017, ApJ, 849, 45

Carilli, C. L., Riechers, D., Walter, F., et al. 2013, ApJ, 763, 120

Carilli, C. L., & Walter, F. 2013, ARA&A, 51, 105

Carilli, C. L., Daddi, E., Riechers, D., et al. 2010, ApJ, 714, 1407

Carilli, C. L., McKinnon, M., Ott, J., et al. 2015, ArXiv e-prints, arXiv:1510.06438

Carilli, C. L., Chluba, J., Decarli, R., et al. 2016, ApJ, 833, 73

Carniani, S., Maiolino, R., Pallottini, A., et al. 2017, A&A, 605, A42

Casey, C. M., Narayanan, D., & Cooray, A. 2014a, Phys. Rep., 541, 45

—. 2014b, Phys. Rep., 541, 45

Casey, C. M., Scoville, N. Z., Sanders, D. B., et al. 2014c, ApJ, 796, 95

Casey, C. M., Hodge, J. A., Lacy, M., et al. 2015, ArXiv e-prints, arXiv:1510.06411

Castellano, M., Pentericci, L., Vanzella, E., et al. 2018, ApJ, 863, L3

Chen, C.-C., Hodge, J. A., Smail, I., et al. 2017a, ApJ, 846, 108

—. 2017b, ApJ, 846, 108

Chiang, Y.-K., Overzier, R., & Gebhardt, K. 2013, ApJ, 779, 127

Chiang, Y.-K., Overzier, R. A., Gebhardt, K., & Henriques, B. 2017, eapj@ApJLetters, 844, L23

Choi, J.-H., & Nagamine, K. 2010, MNRAS, 407, 1464

Clark, P. C., Bonnell, I. A., & Klessen, R. S. 2008, MNRAS, 386, 3

Colombi, S., Davis, O., Devriendt, J., Prunet, S., & Silk, J. 2011, MNRAS, 414, 2436

Combes, F., Rex, M., Rawle, T. D., et al. 2012, A&A, 538, L4

Condon, J. J. 1997, PASP, 109, 166

Condon, J. J., Cotton, W. D., Greisen, E. W., et al. 1998, AJ, 115, 1693

Cooray, A., Calanog, J., Wardlow, J. L., et al. 2014, ApJ, 790, 40

Coppin, K. E. K., Swinbank, A. M., Neri, R., et al. 2007, ApJ, 665, 936

Cormier, D., Madden, S. C., Lebouteiller, V., et al. 2014, A&A, 564, A121

—. 2015, A&A, 578, A53

Cox, D. P. 2005, Annual Review of Astronomy and Astrophysics, 43, 337

Csáki, C., Goodman, J., Pavesi, R., & Shirman, Y. 2014, Phys. Rev. D, 89, 055005

da Cunha, E., Charlot, S., & Elbaz, D. 2008, MNRAS, 388, 1595

da Cunha, E., Groves, B., Walter, F., et al. 2013a, ApJ, 766, 13

da Cunha, E., Walter, F., Decarli, R., et al. 2013b, ApJ, 765, 9

da Cunha, E., Groves, B., Walter, F., et al. 2013c, ApJ, 766, 13

da Cunha, E., Walter, F., Smail, I. R., et al. 2015a, ApJ, 806, 110

—. 2015b, ApJ, 806, 110

Daddi, E., Cimatti, A., Renzini, A., et al. 2004, ApJ, 617, 746

Daddi, E., Dannerbauer, H., Elbaz, D., et al. 2008, eapj@ApJLetters, 673, L21

Daddi, E., Dannerbauer, H., Krips, M., et al. 2009a, eapj@ApJLetters, 695, L176

Daddi, E., Dickinson, M., Morrison, G., et al. 2007, ApJ, 670, 156

Daddi, E., Dannerbauer, H., Stern, D., et al. 2009b, ApJ, 694, 1517

Daddi, E., Bournaud, F., Walter, F., et al. 2010a, ApJ, 713, 686

Daddi, E., Elbaz, D., Walter, F., et al. 2010b, eapj@ApJLetters, 714, L118

Daddi, E., Dannerbauer, H., Liu, D., et al. 2015, A&A, 577, A46

Danielson, A. L. R., Swinbank, A. M., Smail, I., et al. 2017, ApJ, 840, 78

Dannerbauer, H., Walter, F., & Morrison, G. 2008, eapj@ApJLetters, 673, L127

Darling, J., & Zeiger, B. 2012, eapj@ApJLetters, 749, L33

Davé, R., Finlator, K., & Oppenheimer, B. D. 2011, MNRAS, 416, 1354

—. 2012a, MNRAS, 421, 98

—. 2012b, MNRAS, 421, 98

Davé, R., Rafieferantsoa, M. H., Thompson, R. J., & Hopkins, P. F. 2017, MNRAS, 467, 115

Davis, T. A., Alatalo, K., Bureau, M., et al. 2013, MNRAS, 429, 534

De Breuck, C., Williams, R. J., Swinbank, M., et al. 2014, A&A, 565, A59

De Looze, I., Cormier, D., Lebouteiller, V., et al. 2014, A&A, 568, A62

Decarli, R., Walter, F., Carilli, C., et al. 2014a, ApJ, 782, 78

—. 2014b, ApJ, 782, L17

Decarli, R., Walter, F., Aravena, M., et al. 2016a, ApJ, 833, 69

—. 2016b, ApJ, 833, 70

Decarli, R., Walter, F., Venemans, B. P., et al. 2017, Nature, 545, 457

Dekel, A., & Birnboim, Y. 2006, MNRAS, 368, 2

Dekel, A., & Krumholz, M. R. 2013, MNRAS, 432, 455

Dekel, A., Sari, R., & Ceverino, D. 2009a, ApJ, 703, 785

Dekel, A., Zolotov, A., Tweed, D., et al. 2013, MNRAS, 435, 999

Dekel, A., Birnboim, Y., Engel, G., et al. 2009b, Nature, 457, 451

Delhaize, J., Smolčić, V., Delvecchio, I., et al. 2017, A&A, 602, A4

Dessauges-Zavadsky, M., Zamojski, M., Schaerer, D., et al. 2015, A&A, 577, A50

Dessauges-Zavadsky, M., Zamojski, M., Rujopakarn, W., et al. 2017, A&A, 605, A81

Díaz-Santos, T., Armus, L., Charmandaris, V., et al. 2013, ApJ, 774, 68

—. 2017, ApJ, 846, 32

Donnari, M., Pillepich, A., Nelson, D., et al. 2019, MNRAS, 690

Dopcke, G., Glover, S. C. O., Clark, P. C., & Klessen, R. S. 2013, ApJ, 766, 103

Downes, D., & Solomon, P. M. 1998, ApJ, 507, 615

Draine, B. T. 2011, Physics of the Interstellar and Intergalactic Medium

Draine, B. T., & Li, A. 2007, ApJ, 657, 810

Driver, S. P., & Robotham, A. S. G. 2010, MNRAS, 407, 2131

Dunne, L., Eales, S. A., & Edmunds, M. G. 2003, MNRAS, 341, 589

Eales, S., Smith, M. W. L., Auld, R., et al. 2012, ApJ, 761, 168

Eales, S., Smith, D., Bourne, N., et al. 2018, MNRAS, 473, 3507

Elbaz, D., Daddi, E., Le Borgne, D., et al. 2007, A&A, 468, 33

Elbaz, D., Dickinson, M., Hwang, H. S., et al. 2011, A&A, 533, A119

Eldridge, J. J., Langer, N., & Tout, C. A. 2011, MNRAS, 414, 3501

Eldridge, J. J., & Stanway, E. R. 2012, MNRAS, 419, 479

Elmegreen, D. M., Elmegreen, B. G., Marcus, M. T., et al. 2009, ApJ, 701, 306

Elmegreen, D. M., Elmegreen, B. G., Ravindranath, S., & Coe, D. A. 2007, ApJ, 658, 763

Engel, H., Tacconi, L. J., Davies, R. I., et al. 2010, ApJ, 724, 233

Fabian, A. C. 2012, Annual Review of Astronomy and Astrophysics, 50, 455

Faisst, A. L., Capak, P. L., Davidzon, I., et al. 2016a, ApJ, 822, 29

Faisst, A. L., Capak, P., Hsieh, B. C., et al. 2016b, ApJ, 821, 122

Faisst, A. L., Capak, P. L., Yan, L., et al. 2017, ApJ, 847, 21

Fan, X., Carilli, C. L., & Keating, B. 2006, Annual Review of Astronomy and Astrophysics, 44, 415

Farrah, D., Lebouteiller, V., Spoon, H. W. W., et al. 2013, ApJ, 776, 38

Faucher-Giguère, C.-A., Kereš, D., & Ma, C.-P. 2011, MNRAS, 417, 2982

Ferland, G. J., Porter, R. L., van Hoof, P. A. M., et al. 2013, Rev. Mexicana Astron. Astrofis., 49, 137

Feroz, F., Hobson, M. P., & Bridges, M. 2009, MNRAS, 398, 1601

Ferrara, A. 2016, in Understanding the Epoch of Cosmic Reionization: Challenges and Progress, ed. A. Mesinger, Vol. 423, 163

Ferrara, A., Hirashita, H., Ouchi, M., & Fujimoto, S. 2017, MNRAS, 471, 5018

Ferraro, S. 2015, PhD thesis, Princeton University

Field, G. B., Goldsmith, D. W., & Habing, H. J. 1969, ApJ, 155, L149

Finlator, K. 2017, in Astrophysics and Space Science Library, Vol. 430, Gas Accretion onto Galaxies, ed. A. Fox & R. Davé, 221

Finlator, K., & Davé, R. 2008, MNRAS, 385, 2181

Foreman-Mackey, D., Hogg, D. W., Lang, D., & Goodman, J. 2013, PASP, 125, 306

Förster Schreiber, N. M., Genzel, R., Lehnert, M. D., et al. 2006, ApJ, 645, 1062

Förster Schreiber, N. M., Genzel, R., Bouché, N., et al. 2009, ApJ, 706, 1364

Förster Schreiber, N. M., Renzini, A., Mancini, C., et al. 2018, The Astrophysical Journal Supplement Series, 238, 21

Furlong, M., Bower, R. G., Theuns, T., et al. 2015, MNRAS, 450, 4486

Geach, J. E., Smail, I., Moran, S. M., et al. 2011, ApJ, 730, L19

Geach, J. E., Dunlop, J. S., Halpern, M., et al. 2017, MNRAS, 465, 1789

Genel, S., Bouché, N., Naab, T., Sternberg, A., & Genzel, R. 2010, ApJ, 719, 229

Genzel, R., Tacconi, L. J., Gracia-Carpio, J., et al. 2010, MNRAS, 407, 2091

Genzel, R., Newman, S., Jones, T., et al. 2011, ApJ, 733, 101

Genzel, R., Tacconi, L. J., Combes, F., et al. 2012, ApJ, 746, 69

Genzel, R., Tacconi, L. J., Lutz, D., et al. 2015, ApJ, 800, 20

Giavalisco, M., Steidel, C. C., Adelberger, K. L., et al. 1998, ApJ, 503, 543

Giavalisco, M., Ferguson, H. C., Koekemoer, A. M., et al. 2004, eapj@ApJLetters, 600, L93

Goldsmith, P. F., Yıldız, U. A., Langer, W. D., & Pineda, J. L. 2015, ApJ, 814, 133

Gómez-Guijarro, C., Toft, S., Karim, A., et al. 2018, ArXiv e-prints, arXiv:1802.07751

González-López, J., Bauer, F. E., Aravena, M., et al. 2017, ArXiv e-prints, arXiv:1704.03007

Gowardhan, A., Riechers, D. A., Daddi, E., et al. 2017, ApJ, 838, 136

Gregory, P. 2010, Bayesian Logical Data Analysis for the Physical Sciences

Gregory, P. C., & Loredo, T. J. 1992, ApJ, 398, 146

Greve, T. R., Bertoldi, F., Smail, I., et al. 2005, MNRAS, 359, 1165

Grogin, N. A., Kocevski, D. D., Faber, S. M., et al. 2011, ApJS, 197, 35

Groves, B. A., Schinnerer, E., Leroy, A., et al. 2015, ApJ, 799, 96

Guidetti, D., Bondi, M., Prandoni, I., et al. 2017, ArXiv e-prints, arXiv:1705.03766

Gullberg, B., De Breuck, C., Vieira, J. D., et al. 2015, MNRAS, 449, 2883

Harikane, Y., Ouchi, M., Shibuya, T., et al. 2018, ApJ, 859, 84

Harrington, K. C., Yun, M. S., Magnelli, B., et al. 2018, MNRAS, 474, 3866

Harris, A. I., Baker, A. J., Frayer, D. T., et al. 2012, ApJ, 752, 152

Hashimoto, T., Inoue, A. K., Tamura, Y., et al. 2018a, ArXiv e-prints, arXiv:1811.00030

Hashimoto, T., Inoue, A. K., Mawatari, K., et al. 2018b, ArXiv e-prints, arXiv:1806.00486

Hashimoto, T., Laporte, N., Mawatari, K., et al. 2018c, Nature, 557, 392

Hasinger, G., Capak, P., Salvato, M., et al. 2018, ApJ, 858, 77

Haynes, M. P., Giovanelli, R., Kent, B. R., et al. 2018, ApJ, 861, 49

Hayward, C. C., & Hopkins, P. F. 2017, MNRAS, 465, 1682

Herrera-Camus, R., Bolatto, A., Smith, J. D., et al. 2016, ApJ, 826, 175

Herrera-Camus, R., Sturm, E., Graciá-Carpio, J., et al. 2018a, ArXiv e-prints, arXiv:1803.04419

—. 2018b, ArXiv e-prints, arXiv:1803.04422

Heyer, M., & Dame, T. M. 2015, Annual Review of Astronomy and Astrophysics, 53, 583

Higuchi, R., Ouchi, M., Ono, Y., et al. 2018, ArXiv e-prints, arXiv:1801.00531

Hildebrand, R. H. 1983, Quarterly Journal of the Royal Astronomical Society, 24, 267

Hodge, J. A., Carilli, C. L., Walter, F., et al. 2012, ApJ, 760, 11

Hodge, J. A., Riechers, D., Decarli, R., et al. 2015, eapj@ApJLetters, 798, L18

Hodge, J. A., Karim, A., Smail, I., et al. 2013, ApJ, 768, 91

Hodge, J. A., Swinbank, A. M., Simpson, J. M., et al. 2016, ApJ, 833, 103

Hogg, D. W., Myers, A. D., & Bovy, J. 2010, ApJ, 725, 2166

Hollenbach, D. J., & Tielens, A. G. G. M. 1997, Annual Review of Astronomy and Astrophysics, 35, 179

Hopkins, P. F., Kereš, D., Oñorbe, J., et al. 2014, MNRAS, 445, 581

Hopkins, P. F., Quataert, E., & Murray, N. 2012, MNRAS, 421, 3522

Hu, W., & Dodelson, S. 2002, Annual Review of Astronomy and Astrophysics, 40, 171

Hubble, E. P. 1926, ApJ, 64, 321

Inoue, A. K., Tamura, Y., Matsuo, H., et al. 2016, Science, 352, 1559

Ishida, E. E. O., Vitenti, S. D. P., Penna-Lima, M., et al. 2015, Astronomy and Computing, 13, 1

Ivison, R. J., Papadopoulos, P. P., Smail, I., et al. 2011, MNRAS, 412, 1913

Ivison, R. J., Swinbank, A. M., Smail, I., et al. 2013, ApJ, 772, 137

Ivison, R. J., Lewis, A. J. R., Weiss, A., et al. 2016, ApJ, 832, 78

Jameson, K. E., Bolatto, A. D., Wolfire, M., et al. 2018, ApJ, 853, 111

Jones, G. C., Carilli, C. L., Shao, Y., et al. 2017, ApJ, 850, 180

Kamenetzky, J., Rangwala, N., Glenn, J., Maloney, P. R., & Conley, A. 2016, ApJ, 829, 93

Kaufman, M. J., Wolfire, M. G., Hollenbach, D. J., & Luhman, M. L. 1999, ApJ, 527, 795

Keating, G. K., Marrone, D. P., Bower, G. C., et al. 2016, ApJ, 830, 34

Keating, G. K., Bower, G. C., Marrone, D. P., et al. 2015, ApJ, 814, 140

Keeton, C. R. 2001, ArXiv Astrophysics e-prints, astro-ph/0102340

Kennicutt, R. C., & Evans, N. J. 2012, ARA&A, 50, 531

Kennicutt, Jr., R. C. 1998a, ApJ, 498, 541

—. 1998b, ApJ, 498, 541

Keres, D., Yun, M. S., & Young, J. S. 2003, ApJ, 582, 659

Kewley, L. J., Maier, C., Yabe, K., et al. 2013, ApJ, 774, L10

Kirkpatrick, A., Pope, A., Sajina, A., et al. 2015, ApJ, 814, 9

Koekemoer, A. M., Faber, S. M., Ferguson, H. C., et al. 2011, ApJS, 197, 36

Kogut, A., Fixsen, D. J., Chuss, D. T., et al. 2011, JCAP, 7, 025

Kogut, A., Chuss, D. T., Dotson, J., et al. 2014, in Proc. SPIE, Vol. 9143, Space Telescopes and Instrumentation 2014: Optical, Infrared, and Millimeter Wave, 91431E

Koprowski, M. P., Dunlop, J. S., Michałowski, M. J., et al. 2017, MNRAS, 471, 4155

Krumholz, M. R. 2012, ApJ, 759, 9

—. 2013, MNRAS, 436, 2747

Krumholz, M. R., Burkhart, B., Forbes, J. C., & Crocker, R. M. 2018, MNRAS, 477, 2716

Krumholz, M. R., McKee, C. F., & Tumlinson, J. 2009, ApJ, 699, 850

Krumholz, M. R., & Thompson, T. A. 2007, ApJ, 669, 289

Lacey, C. G., Baugh, C. M., Frenk, C. S., et al. 2010, MNRAS, 405, 2

Lagos, C. D. P., Baugh, C. M., Lacey, C. G., et al. 2011, MNRAS, 418, 1649

Lagos, C. d. P., Bayet, E., Baugh, C. M., et al. 2012, MNRAS, 426, 2142

Lagos, C. d. P., Crain, R. A., Schaye, J., et al. 2015, MNRAS, 452, 3815

Laigle, C., McCracken, H. J., Ilbert, O., et al. 2016, ApJS, 224, 24

Langer, W. D., Goldsmith, P. F., & Pineda, J. L. 2016, A&A, 590, A43

Laporte, N., Ellis, R. S., Boone, F., et al. 2017, eapj@ApJLetters, 837, L21

Leipski, C., Meisenheimer, K., Walter, F., et al. 2013, ApJ, 772, 103

—. 2014, ApJ, 785, 154

Leitherer, C., Schaerer, D., Goldader, J. D., et al. 1999, The Astrophysical Journal Supplement Series, 123, 3

Lentati, L., Wagg, J., Carilli, C. L., et al. 2015, ApJ, 800, 67

Leroy, A. K., Walter, F., Brinks, E., et al. 2008, AJ, 136, 2782

Leroy, A. K., Walter, F., Bigiel, F., et al. 2009, AJ, 137, 4670

Leroy, A. K., Bolatto, A., Gordon, K., et al. 2011, ApJ, 737, 12

Leroy, A. K., Walter, F., Sandstrom, K., et al. 2013, AJ, 146, 19

Lewis, A. J. R., Ivison, R. J., Best, P. N., et al. 2018, ApJ, 862, 96

Li, Y., Hernquist, L., Robertson, B., et al. 2007, ApJ, 665, 187

Lilly, S. J., Carollo, C. M., Pipino, A., Renzini, A., & Peng, Y. 2013, ApJ, 772, 119

Liu, D., Daddi, E., Dickinson, M., et al. 2017, ArXiv e-prints, arXiv:1703.05281

Lu, N., Zhao, Y., Xu, C. K., et al. 2015, ApJ, 802, L11

Lu, N., Cao, T., Díaz-Santos, T., et al. 2018, ApJ, 864, 38

Luhman, M. L., Satyapal, S., Fischer, J., et al. 2003, ApJ, 594, 758

—. 1998, ApJ, 504, L11

Lutz, D., Poglitsch, A., Altieri, B., et al. 2011, A&A, 532, A90

Ma, X., Hopkins, P. F., Garrison-Kimmel, S., et al. 2018, MNRAS, 478, 1694

Madau, P., & Dickinson, M. 2014, ARA&A, 52, 415

Madden, S. C., Poglitsch, A., Geis, N., Stacey, G. J., & Townes, C. H. 1997, ApJ, 483, 200

Magdis, G. E., Daddi, E., Elbaz, D., et al. 2011a, eapj@ApJLetters, 740, L15

—. 2011b, eapj@ApJLetters, 740, L15

Magdis, G. E., Daddi, E., Béthermin, M., et al. 2012a, ApJ, 760, 6

—. 2012b, ApJ, 760, 6

Magnelli, B., Saintonge, A., Lutz, D., et al. 2012, A&A, 548, A22

Magnelli, B., Popesso, P., Berta, S., et al. 2013, A&A, 553, A132

Maiolino, R., Caselli, P., Nagao, T., et al. 2009, A&A, 500, L1

Maiolino, R., Cox, P., Caselli, P., et al. 2005, A&A, 440, L51

Malhotra, S., Kaufman, M. J., Hollenbach, D., et al. 2001, ApJ, 561, 766

Maloney, P., & Black, J. H. 1988, ApJ, 325, 389

Mangum, J. G., Darling, J., Henkel, C., & Menten, K. M. 2013, ApJ, 766, 108

Mangum, J. G., Darling, J., Menten, K. M., & Henkel, C. 2008, ApJ, 673, 832

Marrone, D. P., Spilker, J. S., Hayward, C. C., et al. 2018, Nature, 553, 51

Masters, D., Faisst, A., & Capak, P. 2016, ApJ, 828, 18

McKinnon, M., Carilli, C., & Beasley, T. 2016, in Proc. SPIE, Vol. 9906, Ground-based and Airborne Telescopes VI, 990627

McMullin, J. P., Waters, B., Schiebel, D., Young, W., & Golap, K. 2007, in Astronomical Society of the Pacific Conference Series, Vol. 376, Astronomical Data Analysis Software and Systems XVI, ed. R. A. Shaw, F. Hill, & D. J. Bell, 127

Meurer, G. R., Heckman, T. M., & Calzetti, D. 1999, ApJ, 521, 64

Meynet, G., Maeder, A., Schaller, G., Schaerer, D., & Charbonnel, C. 1994, Astronomy and Astrophysics Supplement Series, 103, 97

Miettinen, O., Novak, M., Smolčić, V., et al. 2017, A&A, 602, A54

Miller, T. B., Hayward, C. C., Chapman, S. C., & Behroozi, P. S. 2015, MNRAS, 452, 878

Miller, T. B., Chapman, S. C., Aravena, M., et al. 2018, Nature, 556, 469

Molnár, D. C., Sargent, M. T., Delhaize, J., et al. 2018, MNRAS, 475, 827

Momcheva, I. G., Brammer, G. B., van Dokkum, P. G., et al. 2016, ApJS, 225, 27

Morrison, G. E., Owen, F. N., Dickinson, M., Ivison, R. J., & Ibar, E. 2010, ApJS, 188, 178

Moster, B. P., Naab, T., & White, S. D. M. 2018, MNRAS, 477, 1822

Moster, B. P., Somerville, R. S., Newman, J. A., & Rix, H.-W. 2011, ApJ, 731, 113

Muratov, A. L., Kereš, D., Faucher-Giguère, C.-A., et al. 2015, MNRAS, 454, 2691

Murayama, T., Taniguchi, Y., Scoville, N. Z., et al. 2007, ApJS, 172, 523

Murphy, E. J., Condon, J. J., Schinnerer, E., et al. 2011, ApJ, 737, 67

Myers, A. T., Krumholz, M. R., Klein, R. I., & McKee, C. F. 2011, ApJ, 735, 49

Nagao, T., Maiolino, R., De Breuck, C., et al. 2012, A&A, 542, L34

Nagao, T., Maiolino, R., Marconi, A., & Matsuhara, H. 2011, A&A, 526, A149

Narayanan, D., Davé, R., Johnson, B. D., et al. 2018, MNRAS, 474, 1718

Narayanan, D., & Krumholz, M. R. 2014, MNRAS, 442, 1411

Narayanan, D., Turk, M., Feldmann, R., et al. 2015, Nature, 525, 496

Noeske, K. G., Weiner, B. J., Faber, S. M., et al. 2007, ApJ, 660, L43

Noll, S., Burgarella, D., Giovannoli, E., et al. 2009, A&A, 507, 1793

Oberst, T. E., Parshley, S. C., Nikola, T., et al. 2011, ApJ, 739, 100

Oberst, T. E., Parshley, S. C., Stacey, G. J., et al. 2006, eapj@ApJLetters, 652, L125

Obreschkow, D., Heywood, I., Klöckner, H.-R., & Rawlings, S. 2009, ApJ, 702, 1321

Oliver, S. J., Bock, J., Altieri, B., et al. 2012, MNRAS, 424, 1614

Orr, M. E., Hayward, C. C., Hopkins, P. F., et al. 2018, MNRAS, 478, 3653

Osterbrock, D. E., & Ferland, G. J. 2006, Astrophysics of gaseous nebulae and active galactic nuclei

Oteo, I., Ivison, R. J., Dunne, L., et al. 2016, ApJ, 827, 34

—. 2017a, ArXiv e-prints, arXiv:1709.02809

—. 2017b, ArXiv e-prints, arXiv:1709.02809

Ouchi, M., Shimasaku, K., Furusawa, H., et al. 2003, ApJ, 582, 60

Ouchi, M., Shimasaku, K., Akiyama, M., et al. 2005, ApJ, 620, L1

—. 2008, The Astrophysical Journal Supplement Series, 176, 301

Ouchi, M., Harikane, Y., Shibuya, T., et al. 2017, ArXiv e-prints, arXiv:1704.07455

Overzier, R. A., Guo, Q., Kauffmann, G., et al. 2009, MNRAS, 394, 577

Pannella, M., Carilli, C. L., Daddi, E., et al. 2009, ApJ, 698, L116

Partridge, R. B., & Peebles, P. J. E. 1967, ApJ, 147, 868

Pavesi, R., Riechers, D. A., Capak, P. L., et al. 2016, ApJ, 832, 151

Pavesi, R., Riechers, D. A., Sharon, C. E., et al. 2018a, ApJ, 861, 43

Pavesi, R., Sharon, C. E., Riechers, D. A., et al. 2018b, ApJ, 864, 49

Pawlik, A. H., Schaye, J., & van Scherpenzeel, E. 2009, MNRAS, 394, 1812

Peng, C. Y., Ho, L. C., Impey, C. D., & Rix, H.-W. 2002, AJ, 124, 266

Peng, Y., Maiolino, R., & Cochrane, R. 2015, Nature, 521, 192

Pineda, J. L., Langer, W. D., Velusamy, T., & Goldsmith, P. F. 2013, A&A, 554, A103

Planck Collaboration, Aghanim, N., Akrami, Y., et al. 2018, arXiv e-prints, arXiv:1807.06209

Pope, A., Scott, D., Dickinson, M., et al. 2006, MNRAS, 370, 1185

Popping, A., Jurek, R., Westmeier, T., et al. 2012, PASA, 29, 318

Popping, G., Pérez-Beaupuits, J. P., Spaans, M., Trager, S. C., & Somerville, R. S. 2014a, MNRAS, 444, 1301

Popping, G., Somerville, R. S., & Trager, S. C. 2014b, MNRAS, 442, 2398

Popping, G., van Kampen, E., Decarli, R., et al. 2016, MNRAS, 461, 93

Pullen, A. R., Chang, T.-C., Doré, O., & Lidz, A. 2013, ApJ, 768, 15

Rawle, T. D., Egami, E., Bussmann, R. S., et al. 2014, ApJ, 783, 59

Reddy, N. A., Erb, D. K., Pettini, M., Steidel, C. C., & Shapley, A. E. 2010, ApJ, 712, 1070

Reddy, N. A., Steidel, C. C., Fadda, D., et al. 2006, ApJ, 644, 792

Reddy, N. A., Oesch, P. A., Bouwens, R. J., et al. 2018, ApJ, 853, 56

Rémy-Ruyer, A., Madden, S. C., Galliano, F., et al. 2013, A&A, 557, A95

Riechers, D. A., Carilli, C. L., Walter, F., & Momjian, E. 2010a, eapj@ApJLetters, 724, L153

Riechers, D. A., Hodge, J., Walter, F., Carilli, C. L., & Bertoldi, F. 2011a, eapj@ApJLetters, 739, L31

Riechers, D. A., Walter, F., Carilli, C. L., et al. 2006a, ApJ, 650, 604

—. 2006b, ApJ, 650, 604

Riechers, D. A., Capak, P. L., Carilli, C. L., et al. 2010b, eapj@ApJLetters, 720, L131

Riechers, D. A., Carilli, C. L., Maddalena, R. J., et al. 2011b, eapj@ApJLetters, 739, L32

Riechers, D. A., Carilli, L. C., Walter, F., et al. 2011c, eapj@ApJLetters, 733, L11

Riechers, D. A., Bradford, C. M., Clements, D. L., et al. 2013, Nature, 496, 329

Riechers, D. A., Carilli, C. L., Capak, P. L., et al. 2014a, ApJ, 796, 84

Riechers, D. A., Pope, A., Daddi, E., et al. 2014b, ApJ, 786, 31

Riechers, D. A., Leung, T. K. D., Ivison, R. J., et al. 2017, ApJ, 850, 1

Riechers, D. A., Pavesi, R., Sharon, C. E., et al. 2018, ArXiv e-prints, arXiv:1808.04371

Righi, M., Hernández-Monteagudo, C., & Sunyaev, R. A. 2008, A&A, 489, 489

Rodighiero, G., Cimatti, A., Gruppioni, C., et al. 2010, A&A, 518, L25

Rodighiero, G., Daddi, E., Baronchelli, I., et al. 2011, ApJ, 739, L40

Röllig, M., Simon, R., Güsten, R., et al. 2016, A&A, 591, A33

Rosenberg, M. J. F., van der Werf, P. P., Aalto, S., et al. 2015, ApJ, 801, 72

Rubio, M., Elmegreen, B. G., Hunter, D. A., et al. 2015, Nature, 525, 218

Rudnick, G., Hodge, J., Walter, F., et al. 2017, ApJ, 849, 27

Ryan-Weber, E. V., Pettini, M., Madau, P., & Zych, B. J. 2009, MNRAS, 395, 1476

Saintonge, A., Lutz, D., Genzel, R., et al. 2013, ApJ, 778, 2

Saintonge, A., Catinella, B., Tacconi, L. J., et al. 2017, ApJS, 233, 22

Sandstrom, K. M., Leroy, A. K., Walter, F., et al. 2013a, ApJ, 777, 5

—. 2013b, ApJ, 777, 5

Santini, P., Maiolino, R., Magnelli, B., et al. 2010, A&A, 518, L154

Sargent, M. T., Béthermin, M., Daddi, E., & Elbaz, D. 2012, eapj@ApJLetters, 747, L31

Sargent, M. T., Daddi, E., Béthermin, M., et al. 2014, ApJ, 793, 19

Savage, B. D., & Sembach, K. R. 1996, Annual Review of Astronomy and Astrophysics, 34, 279

Schinnerer, E., Sargent, M. T., Bondi, M., et al. 2010, ApJS, 188, 384

Schinnerer, E., Groves, B., Sargent, M. T., et al. 2016, ApJ, 833, 112

Schmidt, M. 1959, ApJ, 129, 243

Schruba, A., Leroy, A. K., Walter, F., et al. 2011, AJ, 142, 37

Scott, K. S., Lupu, R. E., Aguirre, J. E., et al. 2011, ApJ, 733, 29

Scoville, N., Aussel, H., Brusa, M., et al. 2007, ApJS, 172, 1

Scoville, N., Arnouts, S., Aussel, H., et al. 2013, ApJS, 206, 3

Scoville, N., Sheth, K., Walter, F., et al. 2015, ApJ, 800, 70

Scoville, N., Sheth, K., Aussel, H., et al. 2016, ApJ, 820, 83

Scoville, N., Lee, N., Vanden Bout, P., et al. 2017a, ApJ, 837, 150

Scoville, N., Murchikova, L., Walter, F., et al. 2017b, ApJ, 836, 66

Scoville, N. Z. 2013, Evolution of star formation and gas, ed. J. Falcón-Barroso & J. H. Knapen, 491

Selina, R., Murphy, E., McKinnon, M., et al. 2018a, ArXiv e-prints, arXiv:1810.08197

Selina, R. J., Murphy, E. J., McKinnon, M., et al. 2018b, ArXiv e-prints, arXiv:1806.08405

Serra, P., Amblard, A., Temi, P., et al. 2011, ApJ, 740, 22

Shapley, A. E. 2011, Annual Review of Astronomy and Astrophysics, 49, 525

Shapley, A. E., Steidel, C. C., Pettini, M., & Adelberger, K. L. 2003, ApJ, 588, 65

Sharda, P., Federrath, C., da Cunha, E., Swinbank, A. M., & Dye, S. 2018, MNRAS, 477, 4380

Sharon, C. E., Riechers, D. A., Hodge, J., et al. 2016, ApJ, 827, 18

Shibuya, T., Ouchi, M., Konno, A., et al. 2017, PASJ, arXiv:1704.08140

Silk, J., & Mamon, G. A. 2012, Research in Astronomy and Astrophysics, 12, 917

Silk, J., & Rees, M. J. 1998, A&A, 331, L1

Silva, L., Granato, G. L., Bressan, A., & Danese, L. 1998, ApJ, 509, 103

Silverman, J. D., Daddi, E., Rodighiero, G., et al. 2015, ApJ, 812, L23

Silverman, J. D., Rujopakarn, W., Daddi, E., et al. 2018, ApJ, 867, 92

Simcoe, R. A. 2006, ApJ, 653, 977

Simpson, J. M., Smail, I., Swinbank, A. M., et al. 2015, ApJ, 807, 128

Skelton, R. E., Whitaker, K. E., Momcheva, I. G., et al. 2014, ApJS, 214, 24

Smith, J. D. T., Croxall, K., Draine, B., et al. 2017, ApJ, 834, 5

Smolčić, V., Novak, M., Bondi, M., et al. 2017a, A&A, 602, A1

Smolčić, V., Miettinen, O., Tomičić, N., et al. 2017b, A&A, 597, A4

Sofue, Y., & Rubin, V. 2001, Annual Review of Astronomy and Astrophysics, 39, 137

Somerville, R. S., & Davé, R. 2015, ARA&A, 53, 51

Sparre, M., Hayward, C. C., Feldmann, R., et al. 2017, MNRAS, 466, 88

Speagle, J. S., Steinhardt, C. L., Capak, P. L., & Silverman, J. D. 2014a, ApJS, 214, 15

—. 2014b, ApJS, 214, 15

Spilker, J. S., Bezanson, R., Marrone, D. P., et al. 2016, ApJ, 832, 19

Spinoglio, L., Pereira-Santaella, M., Dasyra, K. M., et al. 2015, ApJ, 799, 21

Spitzer, L. 1978, Physical processes in the interstellar medium, doi:10.1002/9783527617722

Springel, V., & Hernquist, L. 2003, MNRAS, 339, 289

Springel, V., White, S. D. M., Jenkins, A., et al. 2005, Nature, 435, 629

Stacey, G. J. 2011, IEEE Transactions on Terahertz Science and Technology, 1, 241

Stacey, G. J., Geis, N., Genzel, R., et al. 1991, ApJ, 373, 423

Stacey, G. J., Hailey-Dunsheath, S., Ferkinhoff, C., et al. 2010, ApJ, 724, 957

Stacey, G. J., Aravena, M., Basu, K., et al. 2018, in Society of Photo-Optical Instrumentation Engineers (SPIE) Conference Series, Vol. 10700, Ground-based and Airborne Telescopes VII, 107001M

Steidel, C. C., Shapley, A. E., Pettini, M., et al. 2004, ApJ, 604, 534

Steidel, C. C., Strom, A. L., Pettini, M., et al. 2016, ApJ, 826, 159

Steidel, C. C., Rudie, G. C., Strom, A. L., et al. 2014, ApJ, 795, 165

Steinhardt, C. L., Speagle, J. S., Capak, P., et al. 2014, eapj@ApJLetters, 791, L25

Strandet, M. L., Weiss, A., Vieira, J. D., et al. 2016, ApJ, 822, 80

Strandet, M. L., Weiss, A., De Breuck, C., et al. 2017, eapj@ApJLetters, 842, L15

Strom, A. L., Steidel, C. C., Rudie, G. C., Trainor, R. F., & Pettini, M. 2017a, ArXiv e-prints, arXiv:1711.08820

Strom, A. L., Steidel, C. C., Rudie, G. C., et al. 2017b, ApJ, 836, 164

Swinbank, A. M., Simpson, J. M., Smail, I., et al. 2014, MNRAS, 438, 1267

Tabatabaei, F. S., Schinnerer, E., Krause, M., et al. 2017, ApJ, 836, 185

Tacchella, S., Bose, S., Conroy, C., Eisenstein, D. J., & Johnson, B. D. 2018, ArXiv e-prints, arXiv:1806.03299

Tacconi, L. J., Neri, R., Chapman, S. C., et al. 2006, ApJ, 640, 228

Tacconi, L. J., Genzel, R., Smail, I., et al. 2008, ApJ, 680, 246

Tacconi, L. J., Genzel, R., Neri, R., et al. 2010, Nature, 463, 781

Tacconi, L. J., Neri, R., Genzel, R., et al. 2013, ApJ, 768, 74

Tacconi, L. J., Genzel, R., Saintonge, A., et al. 2018, ApJ, 853, 179

Tamura, Y., Mawatari, K., Hashimoto, T., et al. 2018, ArXiv e-prints, arXiv:1806.04132

Tan, Q., Daddi, E., Sargent, M., et al. 2013, ApJ, 776, L24

Tan, Q., Daddi, E., Magdis, G., et al. 2014, A&A, 569, A98

Tazzari, M., Beaujean, F., & Testi, L. 2018, MNRAS, 476, 4527

Tielens, A. G. G. M., & Hollenbach, D. 1985, ApJ, 291, 722

Tremonti, C. A., Heckman, T. M., Kauffmann, G., et al. 2004, ApJ, 613, 898

Umehata, H., Matsuda, Y., Tamura, Y., et al. 2017, eapj@ApJLetters, 834, L16

Utomo, D., Sun, J., Leroy, A. K., et al. 2018, ApJ, 861, L18

Vallini, L., Gallerani, S., Ferrara, A., & Baek, S. 2013, MNRAS, 433, 1567

Vallini, L., Gruppioni, C., Pozzi, F., Vignali, C., & Zamorani, G. 2016, MNRAS, 456, L40

Vallini, L., Pallottini, A., Ferrara, A., et al. 2018, MNRAS, 473, 271

Vincenzo, F., Belfiore, F., Maiolino, R., Matteucci, F., & Ventura, P. 2016, MNRAS, 458, 3466

Vio, R., & Andreani, P. 2016, A&A, 589, A20

Vio, R., Vergès, C., & Andreani, P. 2017, A&A, 604, A115

Wagg, J., Carilli, C. L., Wilner, D. J., et al. 2010, A&A, 519, L1

Walter, F., Riechers, D., Cox, P., et al. 2009, Nature, 457, 699

Walter, F., Decarli, R., Carilli, C., et al. 2012, Nature, 486, 233

Walter, F., Decarli, R., Sargent, M., et al. 2014, ApJ, 782, 79

Walter, F., Decarli, R., Aravena, M., et al. 2016, ApJ, 833, 67

Weiß, A., Downes, D., Walter, F., & Henkel, C. 2005, A&A, 440, L45

Weiß, A., De Breuck, C., Marrone, D. P., et al. 2013, ApJ, 767, 88

Westmeier, T., Popping, A., & Serra, P. 2012, PASA, 29, 276

Weyant, A., Schafer, C., & Wood-Vasey, W. M. 2013, ApJ, 764, 116

Whitaker, K. E., van Dokkum, P. G., Brammer, G., & Franx, M. 2012, ApJ, 754, L29

Whitaker, K. E., Franx, M., Leja, J., et al. 2014, ApJ, 795, 104

Whiting, M. T. 2012, MNRAS, 421, 3242

Williams, R. J., Wagg, J., Maiolino, R., et al. 2014, MNRAS, 439, 2096

Willott, C. J., Carilli, C. L., Wagg, J., & Wang, R. 2015, ApJ, 807, 180

Wisnioski, E., Förster Schreiber, N. M., Wuyts, S., et al. 2015, ApJ, 799, 209

Wolfire, M. G., Hollenbach, D., & Tielens, A. G. G. M. 1989, ApJ, 344, 770

Wolfire, M. G., McKee, C. F., Hollenbach, D., & Tielens, A. G. G. M. 2003, ApJ, 587, 278

Wolfire, M. G., Tielens, A. G. G. M., & Hollenbach, D. 1990, ApJ, 358, 116

Wuyts, S., Förster Schreiber, N. M., Lutz, D., et al. 2011, ApJ, 738, 106

Xie, L., De Lucia, G., Hirschmann, M., Fontanot, F., & Zoldan, A. 2017, MNRAS, 469, 968

Yoon, S. C., & Langer, N. 2005, A&A, 443, 643

Zavala, J. A., Montaña, A., Hughes, D. H., et al. 2018, Nature Astronomy, 2, 56

Zeiger, B., & Darling, J. 2010, ApJ, 709, 386

Zhao, Y., Lu, N., Xu, C. K., et al. 2013, ApJ, 765, L13

—. 2016, ApJ, 819, 69